

# SUMMARY OF ACTIVITIES 2023

Geoscience BC Report 2024-01



**Geoscience BC**

## *Unearthing Opportunities*

Energy  
Carbon Capture, Utilization and Storage  
Critical Minerals  
Geothermal

[canadiandiscovery.com](http://canadiandiscovery.com)

### RECENT BRITISH COLUMBIA PROJECTS

---

Northeast BC Geological  
Carbon Capture and  
Storage Atlas  
*January 2023*

Northeast BC Lithium  
Formation Water Database  
*February 2024*

---

*Trusted advisors for resource  
assessment and development*



NEBC Geological  
CCS Atlas  
Download Available

# **GEOSCIENCE BC SUMMARY OF ACTIVITIES 2023**

© 2024 by Geoscience BC.

All rights reserved. Electronic edition published 2024.

This publication is also available, free of charge, as colour digital files in Adobe Acrobat® PDF format from the Geoscience BC website: <https://www.geosciencebc.com/updates/summary-of-activities/>.

Every reasonable effort is made to ensure the accuracy of the information contained in this report, but Geoscience BC does not assume any liability for errors that may occur. Source references are included in the report and the user should verify critical information.

When using information from this publication in other publications or presentations, due acknowledgment should be given to Geoscience BC. The recommended reference is included on the title page of each paper. The complete volume should be referenced as follows:

Geoscience BC (2024): Geoscience BC Summary of Activities 2023; Geoscience BC, Report 2024-01, 114 p.

Summary of Activities (Geoscience BC)

Annual publication

ISSN 2817-8556 (Print)

ISSN 2817-8564 (Online)

Geoscience BC

1101–750 West Pender Street

Vancouver, British Columbia V6C 2T7

Canada

**Front cover photo and credit:** K. Powers, M.Sc. student at The University of British Columbia, undertaking a 3-D scan of a pyroclastic rock outcrop in the Golden Triangle, east of Stewart, British Columbia. Photo by K. Rubingh.

**Back cover photos and credits:**

**(Left)** Bluebunch wheatgrass (*Pseudoroegneria spicata*) growing in pots filled with mine tailings from the historical Afton mine tailings storage facility and covered by subsoil, topsoil and different amendments (i.e., zeolite, leonardite and compost), Thompson Rivers University Research Greenhouse, Kamloops, British Columbia. Photo by B. Bahroudi.

**(Centre)** J. Dlugosz, M.Sc. student at The University of British Columbia Okanagan, observes an outcrop on the Burgundy Ridge prospect, north-central British Columbia. Photo by C. Beno.

**(Right)** Sunset over Giga Metals Corporation’s Turnagain camp, north-central British Columbia. Photo by K. Broda.

## Foreword

Geoscience BC is pleased to once again present results from our ongoing projects and scholarship recipients in our annual *Summary of Activities* publication. This year, we have combined our minerals, energy and water research into one volume, which is available in print and online via [www.geosciencebc.com](http://www.geosciencebc.com). The papers are divided into three sections, based on Geoscience BC's current research themes:

- 1) Critical Minerals and Metals
- 2) Cleaner Energy
- 3) Geological Carbon Capture and Storage (CCS)

The 'Critical Minerals and Metals' section starts off with Höy and Jackaman introducing a Geoscience BC–BC Geological Survey collaboration to complete geological compilation and selective mapping work in the West Kootenay area. This is followed by Abdale et al. examining the Mount Grace carbonatite and the Cottonbelt Pb-Zn deposit in southeastern British Columbia (BC). Two projects consider exploration for critical metals in north-central BC, with Xu et al. examining hostrocks and alteration at the Lorraine alkalic Cu-Au porphyry deposit, and Broda et al. detailing controls on Ni mineralization at the Alaskan-type Turnagain deposit. Another three papers relate to mineral exploration in BC's highly active northwestern region, with Powers et al. refining stratigraphic classifications within the Hazelton Group, Dlugosz et al. reporting on trace-element mapping of sulphide minerals from the Burgundy Ridge Cu-Au prospect and Johnston et al. considering the stratigraphy of the Stuhini Group in the Galore Creek area. Pamparana et al. investigate high-pressure grinding roll pilot-scale tests and the relationship between operational variables, and Bahroudi et al. investigate the influence of soil amendments and compost, and their potential for improving plant growth and soil fertility in tailings-storage facilities.

The 'Cleaner Energy' section features a paper by Hormozzade Ghalati et al. examining geothermal systems at Mount Meager. Finally, the 'Geological Carbon Capture and Storage (CCS)' section features an update by Nazemi on considerations for CO<sub>2</sub> sequestration in BC's Lower Mainland.

## New Projects in 2024

In 2023, Geoscience BC was able to significantly move forward several of our 'Project Concepts' that were introduced previously (Figure 1). Below is a summary of Geoscience BC's projects that will start in early 2024, and Project Concepts that will move ahead as funding is secured.

### Critical Minerals and Metals in BC Mine Tailings and Wasterock

Critical minerals and metals are essential to Canada's economic security and essential for the transition to a net-zero emissions economy. Canada's critical minerals list includes 31 minerals and metals, 21 of which are produced in Canada, with potential for further resource development (Government of Canada, 2023). Mine tailings and wasterock resulting from production at current and historical mine sites may contain economic concentrations of critical minerals and metals that were not recoverable or considered valuable at the time of extraction.

This program will selectively test tailings and wasterock to identify if there are economic opportunities to extract further value from these mining byproducts while potentially addressing environmental liabilities. It supports responsible development by industry and is closely aligned with provincial and federal critical minerals objectives, including the 2022 Auditor General's report calling for innovative mechanisms to fund reclamation activities (Auditor General of British Columbia, 2022). It will also incorporate the needs of many Indigenous groups and communities.

The program aims to

- identify suitable mine tailings and wasterock facilities in BC to undertake lab and field-scale studies for critical minerals and metals;
- attract investment to BC by demonstrating an innovative approach to critical minerals and metals research and the collaboration between industry, governments, Indigenous groups, academia and communities;
- foster collaboration, expand research expertise and build capacity and training opportunities across mineral systems and the mining lifecycle; and
- engage the broader minerals industry, from geoscience and exploration to mine development, mineral processing/metallurgy and reclamation.

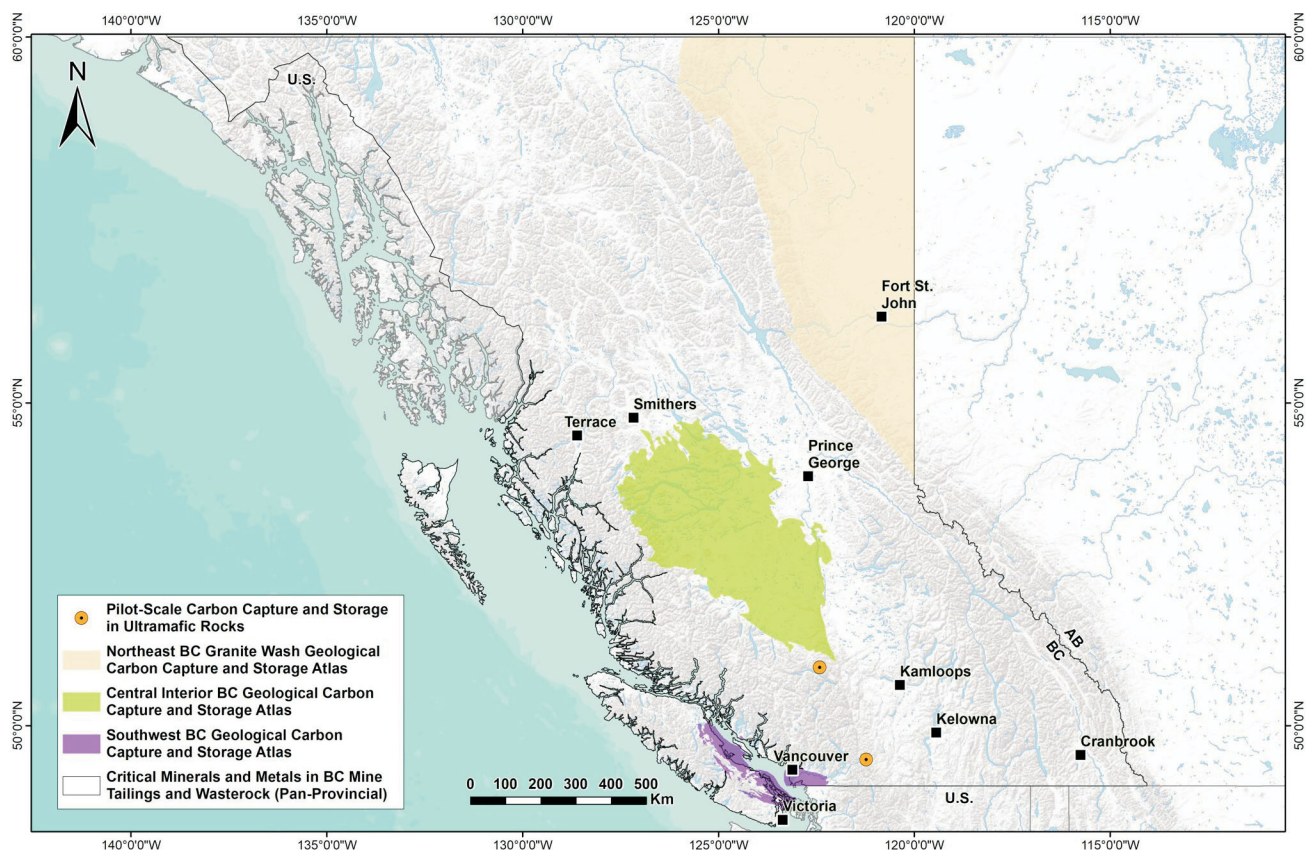


Figure 1. Geoscience BC's 'Project Concepts' under development in 2023.

The first phase of the program will compile information related to legacy and operating minesites across BC. Targeted information will include deposit type, geology, alteration, geochemistry, metallurgy, mineralogy, known infrastructure and proxy studies. First Nations input will be sought and integrated with technical criteria where possible, and guidance will be provided by Geoscience BC's Indigenous Relations and Reconciliation Advisory Council. Outcomes of the first phase include a public GIS database and report, identification of priority sites (approximately four) for technical investigation, and scoping for later phases, which will include collecting new data to support the development of site investigation models, and evaluating and recommending economic and environmental approaches that could be taken at each site.

Geoscience BC is planning to launch this program in January 2024. The first phase will be funded by Arca, New Gold Inc. and Geoscience BC, and supported with in-kind resources provided by government and academic partners. Future phases will depend on securing additional funding and in-kind resource support.

#### Northeast BC Granite Wash Geological Carbon Capture and Storage Atlas

The Northeast BC Granite Wash Geological CCS Atlas project will assess the carbon-storage potential of the Granite Wash, with a focus on the geology in the Peace River arch (Fort St. John and Dawson Creek areas in northeastern BC). The primary focus of the project is to identify and map the regional distribution, reservoir characteristics and deep saline aquifer CCS storage potential of the Granite Wash clastic rocks, particularly in the Peace River arch and its northern flank region. The results will help determine to what extent northeastern BC has a CCS sequestration zone equivalent in reservoir characteristics and CO<sub>2</sub> potential storage capacity to the Basal Cambrian Sands used for storage at Shell Canada Limited's Quest CCS project in Alberta. The project will identify and catalogue all relevant geoscience reports; identify and review all available well logs and well data; acquire, where possible, regional seismic data to tie to well data and assist with mapping; generate regional mapping of the Granite Wash; assess Granite Wash CO<sub>2</sub> potential storage capacity; and provide a preliminary public report and atlas (similar to our completed Northeast BC Geological Carbon Capture and Storage Atlas project) for use by industry, governments, Indigenous groups, academia and communities to guide decisions and further research requirements.

Foundational funding for this project has been provided by the BC Ministry of Energy, Mines and Low Carbon Innovation. A critical component of the project is industry collaboration and in-kind support in the form of seismic data to allow regional mapping of the sparsely drilled Granite Wash. Geoscience BC is planning to publicly launch this project in early 2024, with findings released in March 2026.

### Central Interior BC Geological Carbon Capture and Storage Atlas

A CCS atlas is also in the works for BC's central interior. The first phase of the Central Interior BC Geological Carbon Capture and Storage Atlas project will be to undertake a preliminary assessment of the geological CCS potential of the ~75 000 km<sup>2</sup> Nechako Basin, including assessing technical risks and identifying data gaps (BC Ministry of Energy, Mines and Low Carbon Innovation, 2002). The project will identify and catalogue all pertinent existing geoscience data and studies, and provide a preliminary public report and atlas for use by industry, governments, Indigenous groups, academia and communities. The primary focus of the project is to assess the CCS storage potential of deep saline aquifers. The structural and sedimentary framework of the basin will be characterized by compiling and re-interpreting existing geoscience data and reports for the Nechako Basin, including data from previous Geoscience BC-supported and other public geoscience research, predominantly focused on seismic, gravity and magnetotelluric studies. The project will build on previous research done by Petrel Robertson Consulting Limited for the BC government (Hayes, 2002). A key deliverable is a preliminary atlas identifying and quantifying CCS potential, similar to the *Northeast BC Geological Carbon Capture and Storage Atlas*, which is being used to inform CCS decisions and potential investment in northeastern BC. There is a shortage of existing data for the Nechako Basin, so it is expected that this phase will also recommend further research. Foundational funding for this project has been provided by the BC Ministry of Energy, Mines and Low Carbon Innovation and, at the time of writing, we have preliminary commitments of funding from Enbridge Inc. and Foresight Canada. Geoscience BC is planning to publicly launch this project in early 2024, with findings made public in late 2024 or early 2025.

## Ongoing Project Concepts in 2024

### Pilot-Scale Carbon Capture and Storage in Ultramafic Rocks

Storing CO<sub>2</sub> through mineralization has many advantages over sequestration in sedimentary basins, most notably the permanency of storage because, once the CO<sub>2</sub> reacts with the rock below surface, it forms a mineral that is stable over geological timescales. The process of mineralizing CO<sub>2</sub> is also extremely safe. In Iceland, it has been demonstrated that the CO<sub>2</sub> dissolved in water reaches instant solubility, trapping upon contact with basalt, and more than 95% of the CO<sub>2</sub> turns into carbonate minerals in less than two years. Therefore, it cannot leak back up to surface and long-term monitoring is therefore unnecessary (e.g., Snæbjörnsdóttir et al., 2020).

This project concept would demonstrate the feasibility of using ultramafic rocks for storage via shallow injection and carbon mineralization. Technical partners on the proposed project include Carbfix hf. and The University of British Columbia's (UBC) CarbMin Lab. Altered ultramafic rocks, specifically serpentinites, have high potential for carbon mineralization as they contain reactive minerals and high amounts of Mg that bind with CO<sub>2</sub> to form stable carbonate minerals. Current and previous work, including models, experiments and natural analogues, show that serpentinites can sequester high amounts of CO<sub>2</sub> (e.g., 0.0563 Gt CO<sub>2</sub>/km<sup>3</sup> of serpentinite; Mitchinson et al., 2020). Serpentinites may provide a closer-to-emission-source alternative to other geological CO<sub>2</sub> storage options for emitters.

Two candidate locations (each one the site of a different ultramafic unit) for a pilot-scale test have been identified in BC by K. Steinhorsdottir (UBC). This project would select one of these locations, work with the BC Energy Regulator to permit project activities, drill injection and monitoring wells, and run a test injection for up to three months to mineralize up to 500 t of CO<sub>2</sub>. Monitoring and verification of the mineralization will be tracked for up to two years. Design of the injection program could be supported through the collection of airborne geophysical data, downhole sampling and analysis of the injection well, and baseline environmental data.

Geoscience BC would also undertake an engagement program with First Nations, communities, industry and governments to both educate and develop an understanding of the potential of carbon mineralization and its application to inform development decisions. Geoscience BC and FortisBC have committed funding to the project, and Geoscience BC has applied for a significant funding contribution from Natural Resources Canada.

## Southwest BC Geological Carbon Capture and Storage Atlas

Geoscience BC is also looking to partner on potential carbon-storage research activities in BC's Lower Mainland region. The Georgia Basin overlies up to 6 km of sedimentary strata that have been partially evaluated for hydrocarbon potential and natural-gas-storage projects, but with no major development. These same strata are prospective for deep-saline-aquifer CCS but, at present, the understanding of their potential is limited. There is a need to gather, analyze, interpret and model existing available geoscience data to understand the sequestration potential of southwestern BC.

The Lower Mainland region has significant sources of greenhouse-gas emissions. Identifying and technically assessing viable CO<sub>2</sub>-sequestration capacity in the region, coupled with potential clean-energy geothermal technology, close to high-volume emission sites, would provide critical missing information to help inform decision-making by government, Indigenous groups, communities and industry to achieve net-zero goals.

### Geoscience BC Publications in 2023

Geoscience BC released the following six reports in 2023:

- Eight technical papers in the **Geoscience BC Summary of Activities 2022: Minerals** volume (Geoscience BC Report 2023-01)
- Seven technical papers in the **Geoscience BC Summary of Activities 2022: Energy and Water** volume (Geoscience BC Report 2023-02)
- **Drift Prospecting in the Central Interior Copper-Gold Research Projects Area**, by D.A. Sacco, W. Jackaman and B. Janzen (Geoscience BC Report 2023-03)
- **Northeast BC Geological Carbon Capture and Storage Atlas**, by Canadian Discovery Ltd. (Geoscience BC Report 2023-04)
- **Kootenay Lake Geothermal Project - Phase Two: Geological, Geochemical and Geospatial Investigations into the Geothermal Potential of the East Shore of Kootenay Lake – Summary Report, January 2023**, by G. MacMahon, R. McQuarrie, D. Gatto and S. Humphries (Geoscience BC Report 2023-06)
- **Geochemical Reanalysis of Archived Till Samples, CICGR Project, Interior Plateau, Central BC (parts of NTS 093A, B, G, J, K, O)**, by W. Jackaman, D.A. Sacco and R.E. Lett (Geoscience BC Report 2023-07)

In addition, the following journal articles and theses related to Geoscience BC projects were published this year:

- **Compositional signatures of gold from different deposit types in British Columbia, Canada**, by R. Chapman, J.K. Mortensen and R. Murphy (Minerals, v. 13, no. 8)
- **Arthropod recovery in post-mine reclaimed sites**, by C. Gervan (M.Sc. thesis, Thompson Rivers University)
- **Response of soil geochemical properties and microbial communities to long-term storage in two mine operations in the Interior of British Columbia**, by A. Fischer (M.Sc. thesis, Thompson Rivers University)
- **The use of the Roben Jig for preparation of clean coal samples of Western Canadian coals via density separation**, by M. Mackay, M. Holuszko, R. Leeder, J. Halko, H. Dexter and V. Barwaj (CIM Journal, v. 14, no. 2)
- **Analysis of fluid flow pathways in the Mount Meager Volcanic Complex, southwestern Canada, utilizing AMT and petrophysical data**, by F. Hormozzade Ghalati, J.A. Craven, D. Motazedian, S.E. Grasby, E. Roots, V. Tschirhart, Z. Chen and X. Liu (Geochemistry, Geophysics, Geosystems, v. 24, no. 3)
- **A 500 ka record of volcanism and paleoenvironment in the northern Garibaldi Volcanic Belt, British Columbia**, by M.A. Harris, J.K. Russell, A. Wilson and B. Jicha (Canadian Journal of Earth Sciences, v. 60, no. 4)
- **Magnetotelluric imaging of the magmatic and geothermal systems beneath Mount Meager, southwestern Canada**, by C. Hanneson and M.J. Unsworth (Canadian Journal of Earth Sciences, v. 60, no. 10)

All releases of Geoscience BC reports, maps and data, as well as related external publications, can be found through our website. Most final reports and data can also be viewed or accessed through our Earth Science Viewer at <https://gis.geosciencebc.com/esv/?viewer=esv>.

### Membership

Geoscience BC membership opportunities make it easy for a wide range of partners to learn about new project concepts, as well as support, provide input, network and stay up to date on Geoscience BC minerals, energy and water research. Corporate, Individual, Student and Associate memberships provide a variety of opportunities to suit industry, academia, commu-

nities, Indigenous groups and governments as we work toward shared goals. Geoscience BC launched the membership program early in 2022 and, as of mid-December 2023, has more than 180 members.

## Acknowledgments

Geoscience BC would like to thank all authors and reviewers of the *Summary of Activities* for their contributions to this volume. RnD Technical is also acknowledged for its work in editing and assembling this volume.

Geoscience BC would like to thank all members, project sponsors and advocates for their ongoing support of Geoscience BC's independent public geoscience. Teck Resources Limited, in particular, is thanked for their sponsorship of the 2023 Geoscience BC Scholarship program. As well, Geoscience BC would like to express our appreciation for the leaders and volunteers in British Columbia's mineral exploration, mining, clean energy and CCS sectors who support our organization through their guidance and their use and recognition of the data and information that we collect and distribute.

Christa Pellett  
Vice President, Minerals  
Geoscience BC  
www.geosciencebc.com

## References

- Auditor General of British Columbia (2022): Oversight of major mines: policies and procedures to address environmental risks; Office of the Auditor General of British Columbia, 39 p., URL <<https://www.bcauditor.com/sites/default/files/publications/reports/BCOAG-Oversight-Major-Mines-Report-June-2022.pdf>> [December 2023].
- BC Ministry of Energy, Mines and Low Carbon Innovation (2002): Nechako Basin: oil and gas opportunities in central British Columbia; BC Ministry of Energy, Mines and Low Carbon Innovation, information brochure, URL <[https://www2.gov.bc.ca/assets/gov/farming-natural-resources-and-industry/natural-gas-oil/petroleum-geoscience/nechako\\_basin\\_interior.pdf](https://www2.gov.bc.ca/assets/gov/farming-natural-resources-and-industry/natural-gas-oil/petroleum-geoscience/nechako_basin_interior.pdf)> [December 2023].
- Government of Canada (2023): Critical minerals: an opportunity for Canada; Government of Canada, URL <<https://www.canada.ca/en/campaign/critical-minerals-in-canada/critical-minerals-an-opportunity-for-canada.html>> [December 2023].
- Hayes, B. (2002): Petroleum exploration potential of the Nechako Basin, British Columbia; BC Ministry of Energy, Mines and Low Carbon Innovation, Petroleum Geology Special Paper 2002-3, 64 p.
- Mitchinson, D., Cutts, J., Fournier, D., Naylor, A., Dipple, G., Hart, C.J.R., Turvey, C., Rahimi, M. and Milidragovic, D. (2020): The carbon mineralization potential of ultramafic rocks in British Columbia: a preliminary assessment; Geoscience BC, Report 2020-15 and The University of British Columbia, MDRU Publication 452, 27 p., URL <[https://cdn.geosciencebc.com/project\\_data/GBCReport2020-15/Geoscience%20BC%20Report%202020-15%20-%20CaMP%20v2022-07\\_11v2.pdf](https://cdn.geosciencebc.com/project_data/GBCReport2020-15/Geoscience%20BC%20Report%202020-15%20-%20CaMP%20v2022-07_11v2.pdf)> [December 2023].
- Snæbjörnsdóttir, S.Ó., Sigfússon, B., Marieni, C., Goldberg, D., Gislason, S.R. and Oelkers, E.H. (2020): Carbon dioxide storage through mineral carbonation; Nature Reviews Earth & Environment, v. 1, p. 90–102, URL <<https://doi.org/10.1038/s43017-019-0011-8>>.



## Contents

### Critical Minerals and Metals

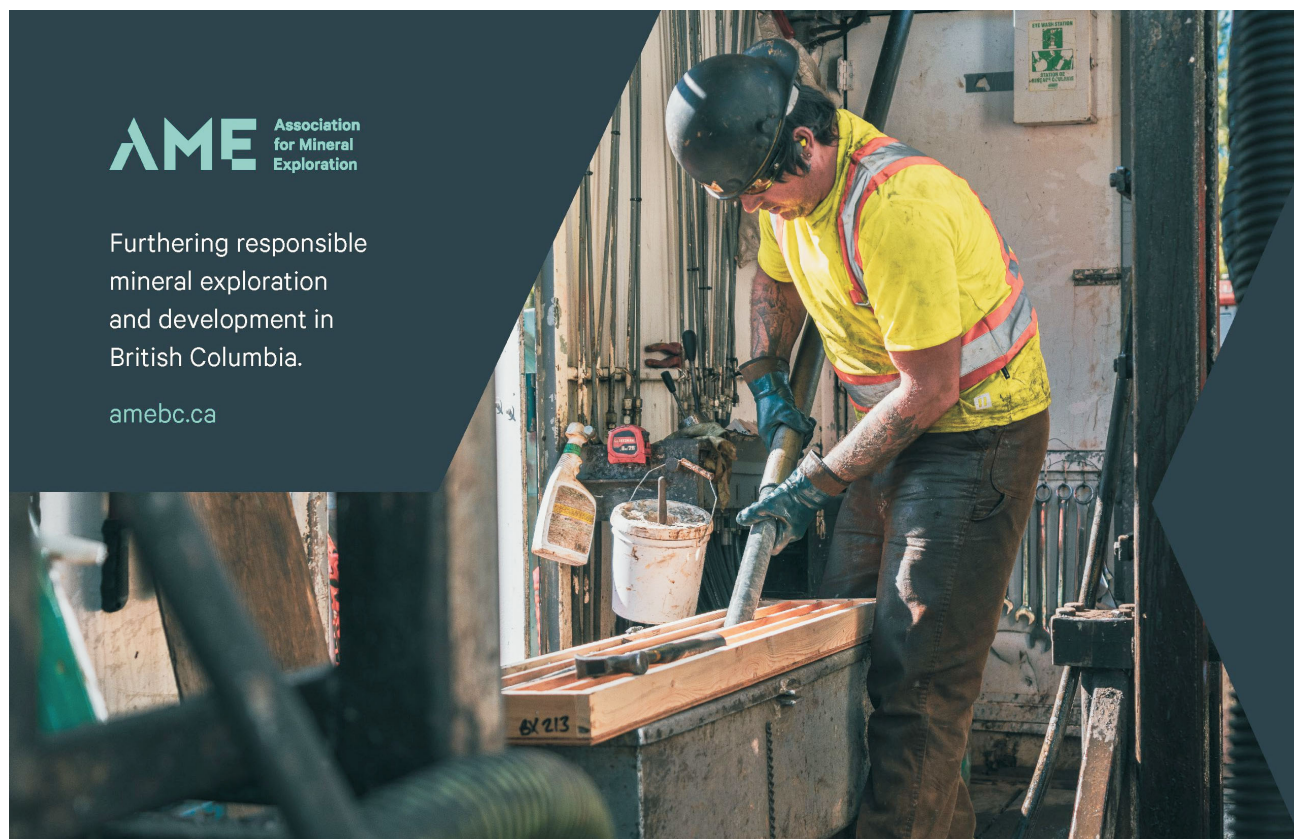
- T. Höy and W. Jackaman:** Geology of the West Kootenay area, southern British Columbia: regional compilation and mineral potential. . . . . 1
- L. Abdale, J. Nelson and L.A. Groat:** Testing the relationship between the Cottonbelt lead-zinc deposit and the carbonatite-syenite province of the Frenchman Cap dome area, southeastern British Columbia. . . . . 3
- H. Xu, S. Barker, F. Bouzari, C. Harraden and M. Manor:** Characterizing hostrocks and alteration footprints at the Lorraine alkalic copper-gold porphyry deposit, north-central British Columbia . . . . . 11
- K.R. Broda, A.E. Williams-Jones and O.V. Vasyukova:** Controls on the nickel mineralization of the Alaskan-type Turnagain deposit, north-central British Columbia . . . . . 23
- K.M. Powers, K.E.L. Rubingh and S.L.L. Barker:** Stratigraphic classification and geochronology within the Hazelton Group, Stewart mining camp, northwestern British Columbia . . . . . 33
- J. Dlugosz, K.P. Larson, C.J.M. Lawley, C.J. Beno and D.C. Petts:** Trace-element mapping by laser ablation–inductively coupled plasma–mass spectrometry of sulphide minerals from the Burgundy Ridge copper-gold alkalic porphyry prospect in the Golden Triangle, northwestern British Columbia . . . . 47
- R.J. Johnston, L.A. Kennedy, K.A. Hickey and B.I. van Straaten:** Revisiting the stratigraphy of the alkalic Stuhini Group in the Galore Creek area, northwestern British Columbia . . . . . 59
- G. Pamparana, B. Klein and M.G. Bergerman:** Effect of the specific pressing force, material moisture content and roll speed on throughput of the high-pressure grinding roll: pilot-scale test on Copper Mountain mine ore, south-central British Columbia . . . . . 67
- B. Bahroudi, J. Singh and L.H. Fraser:** Application of zeolite, leonardite and compost as a tool for mine reclamation: a greenhouse study using tailings from the historical Afton mine in south-central British Columbia. . . . . 79

### Cleaner Energy

- F. Hormozzade Ghalati, J.A. Craven, D. Motazedian and S.E. Grasby:** Petrophysical analysis of geothermal systems at Mount Meager, southwestern British Columbia. . . . . 93

### Geological Carbon Capture and Storage (CCS)

- M. Nazemi:** Key considerations for carbon dioxide sequestration in the Lower Mainland, southwestern British Columbia . . . . . 101



**AME** Association  
for Mineral  
Exploration

Furthering responsible  
mineral exploration  
and development in  
British Columbia.

[amebc.ca](http://amebc.ca)



# Geology of the West Kootenay Area (West Half of NTS 082F), Southern British Columbia: Regional Compilation and Mineral Potential

T. Höy, Geological Consultant, Sooke, British Columbia, thoy@shaw.ca

W. Jackaman, Consultant, Jordan River, British Columbia, wjackamn@shaw.ca

---

Höy, T. and Jackaman, W. (2024): Geology of the West Kootenay area (west half of NTS 082F), southern British Columbia: regional compilation and mineral potential; *in* Geoscience BC Summary of Activities 2023, Geoscience BC, Report 2024, p. 1–2.

## Introduction

The West Kootenay Geology Project (Geoscience BC Project 2023-003), a collaborative research project between Geoscience BC and the BC Geological Survey, involves geological compilation and selective geological mapping in the four western 1:50 000 scale maps of the west half of the Nelson area (NTS 082F; Figure 1). The project is an extension to the east of the recently completed Boundary Project (Geoscience BC Project 2016-004) that completed the geological mapping, compilation and publication of six 1:50 000 scale maps in the east half of the Pentiction area (NTS 082E), which included the Greenwood, Franklin and Beaverdell mining camps (Höy and Jackaman, 2019).

This project includes compilation of geological data sourced from published maps, university theses and industry assessment reports. The digital compilation will be integrated into the BC Geological Survey's Digital Geology database and made available on the survey's MapPlace 2. As well, this project will include publication of individual 1:50 000 scale geological maps, suitable for mineral exploration companies, prospectors, resource-based field workers, Indigenous groups and others interested in the region's geology and mineral potential.

The West Kootenay area has an extensive history of mineral exploration and mining activity, and continues to be actively explored by both individuals and exploration companies. It includes the historical Rossland gold-copper camp (Höy and Dunne, 2001) that produced approximately 85 900 kilograms of gold and 109 500 kilograms of silver between 1894 and 1941. The Slocan silver camp, and the base- and precious-metal Nelson, Ymir and Salmo camps, lie immediately east of the project area and are planned as a second phase of the project (Figure 1).

## Conclusion

In summary, the first phase of the project, scheduled for completion in 2024, has four main aims:

- Compilation of the geology of four 1:50 000 scale maps (NTS 082F/04, 05, 12, 13), extending eastward from the recently completed Boundary Project, augmented locally by geological mapping and potentially radiometric dating in key areas.
- Digital compilation of all locations, geological units and features that will be tied to the map compilations.
- Digitization of all linework, regional structural data, mineral occurrence data, radiometric dates and other geological data according to a format supplied by the BC Geological Survey and Geoscience BC, for inclusion in the BC Digital Geology database and available on MapPlace 2.
- Publication of individual 1:50 000 scale maps.

Compilation and publication of geological data will help define areas for new geological mapping and provide a focus for mineral-exploration target areas. This will aid in guiding responsible development in an area that has seen renewed mineral exploration in recent years.

A proposed second phase of the project could extend geological compilation and MapPlace 2 updates into the eastern 1:50 000 scale maps (NTS 082F/03, 06, 11, 13) of the west half of the Nelson map area (Figure 1).

## Acknowledgments

A regional geological compilation and metallogenic study is based, in large part, on the work of previous geological mappers, including those in government, numerous university graduate students and their advisors, and geologists in the mineral-exploration industry. It is difficult to acknowledge all of these, but some notable workers include H. Little of the Geological Survey of Canada (GSC), who published a regional 'one inch to four miles' map of the west half of the Nelson map area (Little, 1960). The first comprehensive study of the Rossland camp, by C.W. Drysdale of the GSC, formed the template for all subsequent work there (Drysdale, 1915). Mapping of the Rossland gold camp by J. Fyles of the BC Geological Survey (BCGS; Fyles, 1984) formed the basis of a more detailed study of the camp by the senior author and K. Dunne, summarized in a 2001 BCGS bulletin (Höy and Dunne, 2001). P. Simony

---

*This publication is also available, free of charge, as colour digital files in Adobe Acrobat® PDF format from the Geoscience BC website: <https://geosciencebc.com/updates/summary-of-activities/>.*

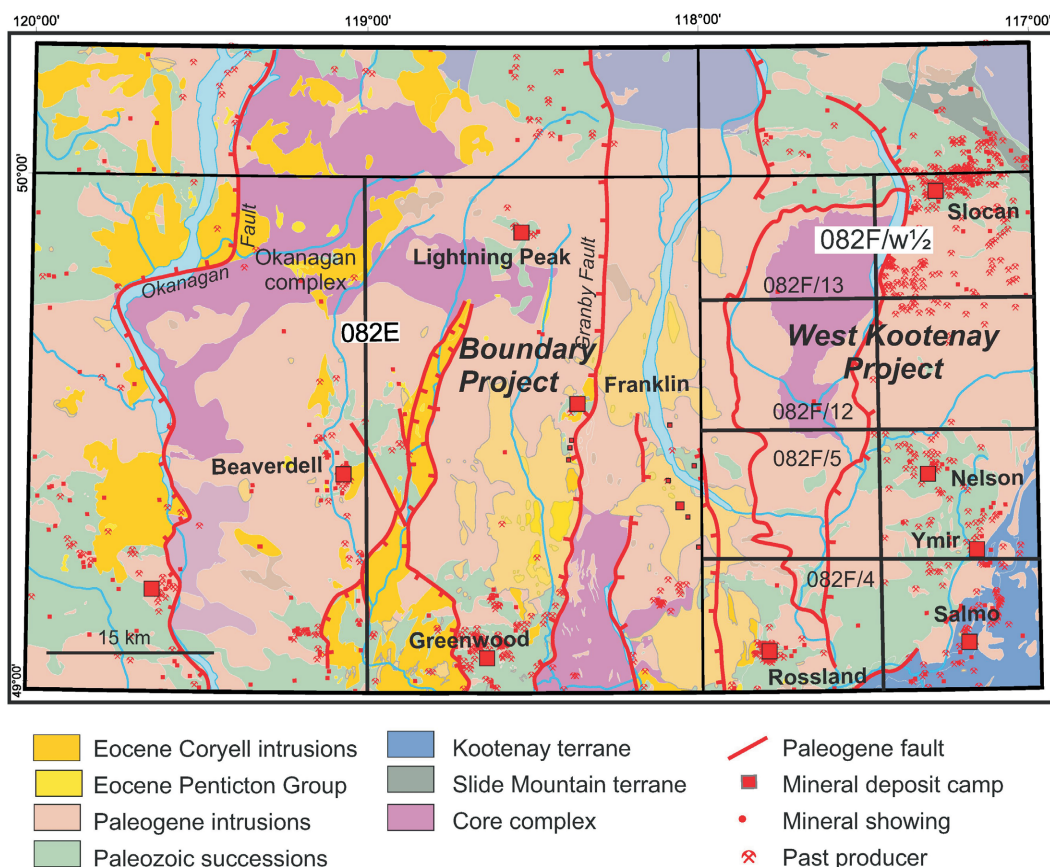


**Figure 1.** Regional geology and tectonic map showing location of the proposed project and the recently completed Boundary Project. Also shown are the main base- and precious-metal camps, as well as Paleogene extensional faults.

of the University of Calgary, and a number of his graduate students, played a key role in unravelling the structure of the area immediately north and east of Rossland, and contributed both published and unpublished maps to the authors' later work. Much of the northern part of the area (NTS 082F/12, 13) was mapped and compiled by S. Carr (Carr, 1986), a graduate student at Carleton University and now a professor in the Department of Earth Sciences at Carleton. Numerous others have contributed to the geological history of the Nelson, Rossland and Slovan mining camps and, although not referenced, their work is gratefully acknowledged.

Finally, the authors would like to acknowledge and thank Geoscience BC, and the BC Geological Survey of the Ministry of Energy, Mines and Low Carbon Innovation, for their financial and logistical support of this project.

## References

Carr, S. (1986): The Valkyr shear zone and the Slovan Lake fault zone: Eocene structures that bound the Valhalla gneiss

dome, southeastern British Columbia; M.Sc. thesis, Carleton University.

Drysdale, C.W. (1915): Geology and ore deposits of Rossland, British Columbia; Geological Survey of Canada, Memoir 77.

Fyles, J.T. (1984): Geological setting of the Rossland mining camp; BC Ministry of Mines and Petroleum Resources, Bulletin 74.

Höy, T. and Dunne, K.P.E. (2001): Metallogeny and mineral deposits of the Nelson-Rossland map area: part II: the early Jurassic Rossland Group, southeastern British Columbia; BC Ministry of Energy and Mines, Bulletin 109, 195 p.

Höy, T. and Jackaman, W. (2019): Geology of the Pentiction map sheet (082E), east-half; Geoscience BC Map 2019-04 (revised 2022), scale 1:150 000, URL <[https://www.geosciencebc.com/i/project\\_data/GBCR2018-11/GBC%20Map%202019-04%20Revised%202022%20-%20Pentiction%20Map%20Sheet%20east%20half%20NTS%20082E01%2C02%2C07%2C08%2C09%2C10%2C15%2C16.pdf](https://www.geosciencebc.com/i/project_data/GBCR2018-11/GBC%20Map%202019-04%20Revised%202022%20-%20Pentiction%20Map%20Sheet%20east%20half%20NTS%20082E01%2C02%2C07%2C08%2C09%2C10%2C15%2C16.pdf)> [October 2023].

Little, H.W. (1960): Nelson map-area, west-half, British Columbia; Geological Survey of Canada, Memoir 308, 205 p.

# Testing the Relationship between the Cottonbelt Lead-Zinc Deposit and the Carbonatite-Syenite Province of the Frenchman Cap Dome Area, Southeastern British Columbia (NTS 082M/06, 07, 10)

L. Abdale<sup>1</sup>, Department of Earth, Ocean and Atmospheric Sciences, The University of British Columbia, Vancouver, British Columbia, labdale@eoas.ubc.ca

J. Nelson, British Columbia Geological Survey, Victoria, British Columbia

L.A. Groat, Department of Earth, Ocean and Atmospheric Sciences, The University of British Columbia, Vancouver, British Columbia

---

Abdale, L., Nelson, J. and Groat, L.A. (2024): Testing the relationship between the Cottonbelt Pb-Zn deposit and the carbonatite-syenite province of the Frenchman Cap dome area, southeastern British Columbia (NTS 082M/6, 7, 10); *in* Geoscience BC Summary of Activities 2023, Geoscience BC, Report 2024-01, p. 3–10.

## Introduction

This paper is an introduction to the lead author's Ph.D. research on the relationship between the Cottonbelt Pb-Zn deposit and the carbonatite-syenite province of the Frenchman Cap dome area in southeastern British Columbia (BC) that will be undertaken during the next 1–2 years. This paper presents the study's background information, as analytical results are not yet available. The overall goal of the study is to address an age conundrum between the extrusive Mount Grace carbonatite (MGC) and the Cottonbelt Pb-Zn deposit in southeastern BC. The specific objectives are to obtain and compare  $^{207}\text{Pb}/^{204}\text{Pb}$  and  $^{206}\text{Pb}/^{204}\text{Pb}$  ratios of regional intrusive units with those of the Cottonbelt deposit. The Pb in the Cottonbelt deposit may have come from Cambrian miogeoclinal sediments, a lower crust–upper mantle source or a mixture of the two.

## Regional Geology

The MGC and the Cottonbelt deposit occur as thin, laterally discontinuous stratabound layers in the Monashee Mountains, northwest of Revelstoke, on the northwest flank of the Frenchman Cap dome (Figures 1, 2; Höy and Kwong, 1986; Höy, 1987; Pell, 1994). Both layers have been traced and projected for at least 5 km along the strike of an east-verging fold nappe named the Mount Grace syncline (Figures 1, 2). The MGC and Cottonbelt layers occur on the northeastern overturned limb of the Mount Grace syncline (Figures 1, 2). A similar mineralized layer appears on the southwest upright limb of the syncline, where it is referred to as the McLeod and Complex showings. These may represent the same depositional system (Figures 1, 2).

The MGC and the Cottonbelt deposit occur in the Monashee Complex (MC). The MC is the deepest exposed structural level in the southern Omineca belt; it includes exposed basement rocks in the Frenchman Cap dome in the north and the Thor-Odin dome in the south, bounded by the Selkirk parautochthonous terrane in the west and the Columbia River fault in the east (Figure 1; Okulitch, 1984; Parrish and Scammell, 1988; Johnson, 1994). The MC consists of basement migmatitic paragneiss and granitoid orthogneiss of Paleoproterozoic age and basal quartzite overlain by metasedimentary cover rocks of Paleozoic age (Crowley 1997; Kuiper et al., 2014). In the Jurassic, allochthonous terranes amalgamated and were thrust and obducted over the North American margin (Brown et al., 1993), resulting in tectonic transport of parautochthonous sequences of the outer margin (e.g., Selkirk allochthon) and culminating in maximal crustal thickening and regional uplift during the mid-Cretaceous (Brown et al., 1986).

The uppermost MC rocks, the Monashee cover sequence, consist of quartzite, pelitic schist, silicate gneiss, calcsilicate gneiss and marble, all of which unconformably overlie basement paragneiss and orthogneiss of probable Proterozoic age (Reesor and Moore, 1971; Armstrong and Ward, 1991; Parkinson, 1991; Crowley, 1997). The base of the Monashee cover sequence sedimentary package contains a laterally extensive quartzite of variable thickness and purity with local crossbedding and grading, providing the only top-up indicators (Höy, 1987). The quartzite underlies a sequence of dominantly calcareous and pelitic schists with minor amphibolite, impure quartzite and quartz-feldspar-biotite gneiss interlayers. Topping this is a thinly bedded unit of interlayered calcsilicate gneiss, kyanite and sillimanite schist and gneiss, calcitic and dolomitic marble, amphibolite and thin scapolite-rich marble layers; this section hosts the MGC and the Cottonbelt deposit.

---

<sup>1</sup>The lead author is a 2023 Geoscience BC Scholarship recipient.

This publication is also available, free of charge, as colour digital files in Adobe Acrobat® PDF format from the Geoscience BC website: <https://geosciencebc.com/updates/summary-of-activities/>.

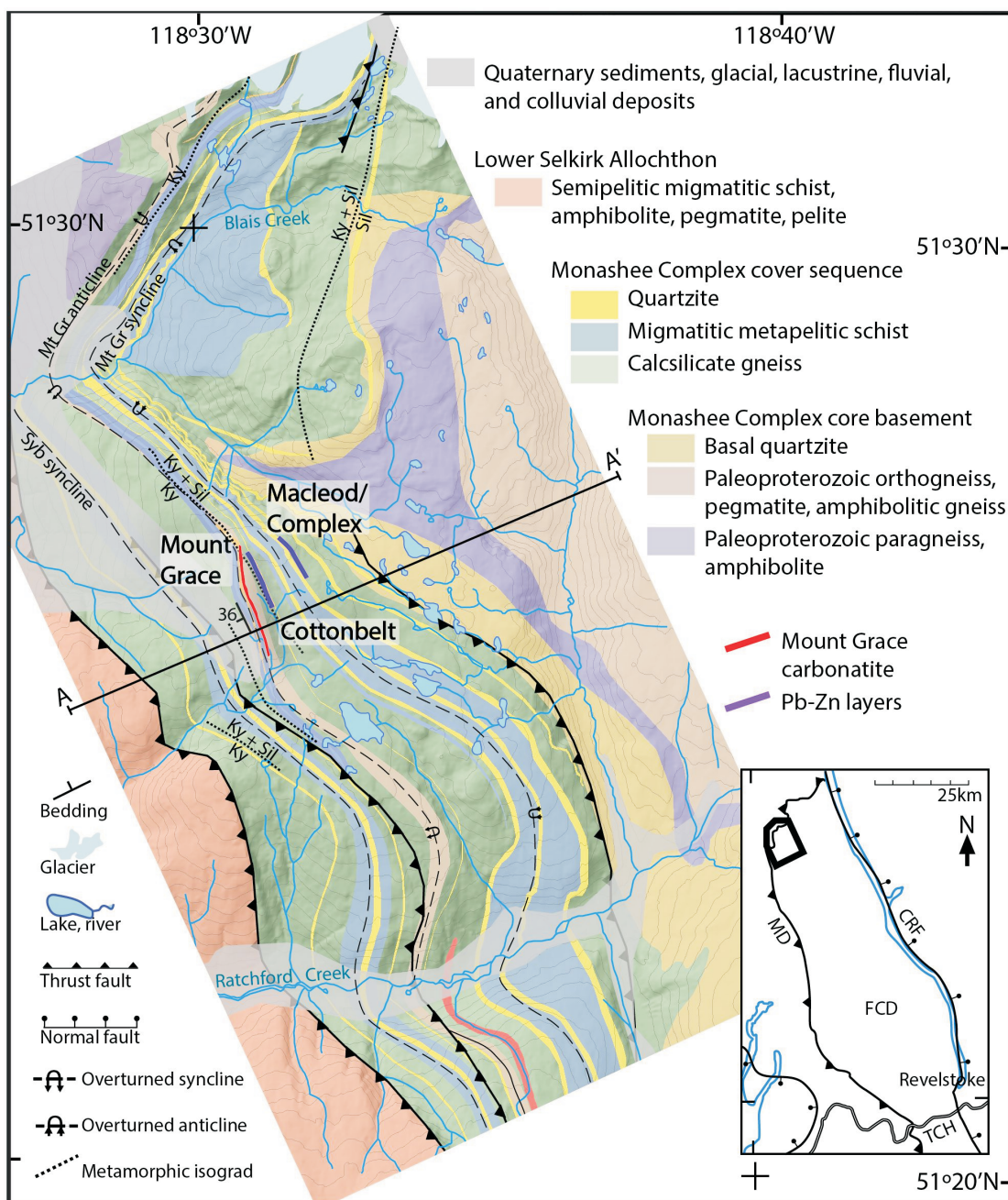


**Figure 1.** Generalized geology of the northwest flank of the Frenchman Cap dome, showing regional geology, Mount Grace carbonatite, Cottonbelt and Macleod/Complex Pb-Zn layers, structural features and metamorphic isograds (modified from Wheeler, 1965; McMillan, 1970; Höy & McMillan, 1979; Brown, 1980; Pell, 1994; Crowley, 1997; Journeay et al., 2000a, b; Lund, 2008; Millonig et al., 2012; Gervais, 2019). Abbreviations: CRF, Columbia River fault; FCD, Frenchman Cap dome; MD, Monashee Décollement; Ky, kyanite; Mt Gr, Mount Grace; Sil, sillimanite; TCH, Trans Canada Highway.

Previous authors have interpreted the sedimentary package of the Monashee cover sequence to represent a transgressive marine sequence deposited on a low-relief basement complex (McMillan, 1973; Höy and McMillan, 1979; Höy and Kwong, 1986). Coarse fluvial sandstone, conglomerate and perhaps marine sands overlying a regional unconformity pass upward into fine-grained, calcareous muds and siltstones, likely deposited on extensive tidal flats. The

tremendous lateral extent of a metasedimentary marble unit and its relative purity (with trace amounts of scapolite), as well as its stratigraphic relationship in a package with quartzites and schists, is consistent with the deposition of marine carbonate on a flat, stable continental shelf (Höy, 1987). A more recent study of the metasedimentary marble unit (Dzikowski et al., 2014) assesses the low Sr contents and their positive correlation with CaO to be consistent with a non-

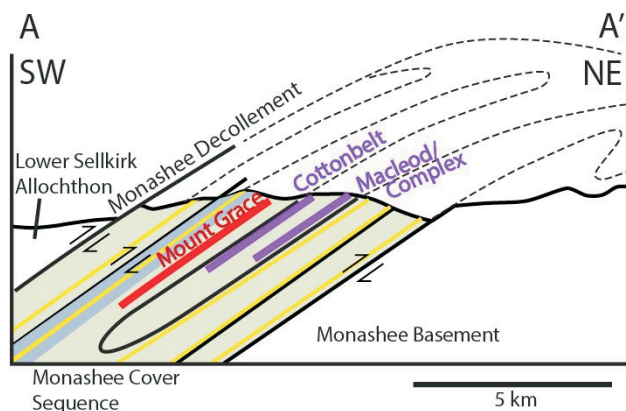


**Figure 2.** Generalized cross-section (A-A' in Figure 1) showing the structural relationship between the Mount Grace carbonatite and the Cottonbelt and Macleod/Complex strata.

evaporitic origin, and the isotopic, major- and trace-element composition of the marble to correspond with shales or marls derived from platform sediments.

### Mount Grace Carbonatite

The MGC is a deformed, recrystallized, lithic clast-bearing impure marble (Figure 3). Previous authors inferred an extrusive origin for the carbonatite based on a lack of fenitized margins, an abundance of included lithic clasts and the deposit's tremendous lateral extent (Figure 1; Höy and Kwong, 1986). In the field, the MGC is recognized by its unusual pale to medium brown weathering colour; prominent matrix grains of dark brown phlogopite, colourless apatite and black (weathered) amphibole crystals; and the widespread occurrence of white, matrix-supported, lithic clasts (Figure 3a). The deposit commonly contains one main, thick (up to 5 m) layer of tuff breccia interbedded with finer grained, lithic clast-poor, massive or laminated carbonatite layers (Figure 3a). The MGC layer averages 2–4 m in thickness and locally narrows to less than a metre (Pell, 1994). The original thickness of the MGC is unknown, as it was likely thinned in the limbs of the major folds.

### Cottonbelt Pb-Zn Layer

Cottonbelt is a sulphide-magnetite layer, 15 cm to approximately 3 m thick, that has been traced or projected for approximately 4 km along strike (Figures 1 and 3b). The Cottonbelt consists predominantly of thickly banded to massive olivine-, pyroxene-, amphibole- and carbonate-bearing calcisilicate gneiss with variable amounts of sphalerite, galena and magnetite. The mineralized zones occur as thick beds, occasionally with thin interbedded layers of metasedimentary marble, calcisilicate gneiss or pelitic schist (Figure 3b). The marble layers contain disseminated sphalerite, galena and trace amounts of pyrrhotite and magnetite. The depositional environment of the Cottonbelt deposit was through sedimentary deposition on the seafloor.

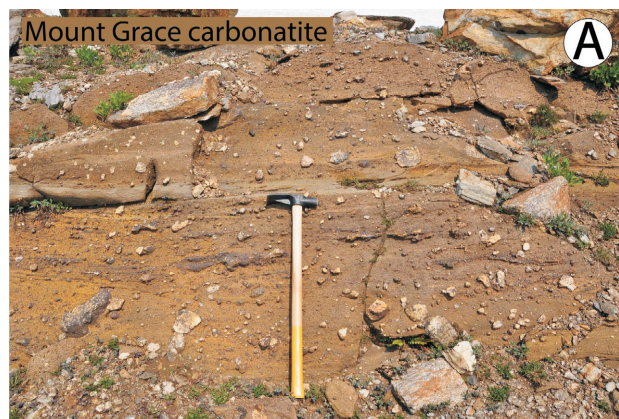


**Figure 3.** Field photos displaying **a)** the main tuff breccia units of the Mount Grace carbonatite, and **b)** the Cottonbelt sphalerite-galena-magnetite mineralization within the metasedimentary marble. 75 cm GeoTool for scale.

A synsedimentary origin for Cottonbelt is indicated by the crude to finely bedded nature, the large lateral extent, the association with chert of probable exhalative origin and the presence of disseminated sulphides in the associated marble.

### Justification of Methodology

The absolute age of the Mount Grace carbonatite is currently in dispute. Millonig et al. (2012) analyzed 28 zircons from the MGC that yielded U-Pb and Th-Pb (from zircons with low U contents) weighted mean ages of ca. 360 Ma, interpreted as its eruptive age. Zircon U-Pb dating by Parrish (1995) of the intrusive Three Valley Gap (TVG) carbonatite, located approximately 20 km southeast of the MGC, yielded a similar age of ca. 360 Ma and may represent the intrusive equivalent to the MGC. Millonig et al. (2012) also dated zircons from the Trident River syenite, located approximately 30 km northeast of the MGC, at ca. 360 Ma. Kuiper et al. (2014) identified a detrital zircon grain from regional pelitic schist (that hosts the MGC) with a zircon U-Pb age of 357 Ma and a CA-TIMS age of 396 Ma. The Devonian age for the MGC conflicts with the Cambrian-Pb model age that Höy and Godwin (1988) assigned to the Cottonbelt Pb-Zn magnetite layer, which structurally and probably stratigraphically overlies the MGC (Höy, 1987; Pell, 1994). The Cottonbelt galena Pb model age uses Pb

isotopic comparison with values on the Shale Curve of Godwin and Sinclair (1982), which was developed based on galena-bearing SEDEX deposits within strata of the Canadian Cordilleran miogeocline.

The  $^{207}\text{Pb}/^{204}\text{Pb}$  vs.  $^{206}\text{Pb}/^{204}\text{Pb}$  ratios of K-feldspar (from syenite), pyrite and pyrrhotite (from carbonatite) and galena (from Cottonbelt) will be plotted, along with reference terrestrial Pb-growth curves (Stacey and Kramers, 1975) to determine if the nearby carbonatites and syenites played a role in Cottonbelt mineralization, which would discredit the model age. Due to the abundance of xenolithic material and the fine-grained nature of only trace amounts of sulphides in the Mount Grace carbonatite, it was not possible to separate enough suitable grains for Pb isotopic analysis from this rock type. However, an overlap or mixing trend in Pb isotopes between Cottonbelt galena and regional magmatic units would still discredit an upper crustal Pb source.

The study will obtain and compare Pb isotopes from the Trident River and Three Valley Gap syenite feldspars and Three Valley Gap carbonatite sulphides (pyrite and pyrrhotite) to test if magmatic activity contributed to Cottonbelt mineralization. Common Pb is any Pb incorporated into a mineral or rock during formation; this signature reflects the primary Pb composition of the source, and the common Pb isotopic ratio is the product of the fractionation history of the source material (Zametzer et al., 2022). Minerals such as feldspars and sulphides incorporate very little initial U in their structure, meaning minimal Pb isotopic evolution after crystallization (Woodhead, 2009; Flowerdew et al., 2012). Similarly, the original Pb isotopic ratios in Pb ore galena (PbS) inform on the source and timing of metal deposits (Doe and Stacey 1974; Huston et al., 2014). The Pb-isotope compositions of some ‘conformable’ stratabound Pb-Zn ore deposits can be accounted for by a growth curve from the formation of the Earth to the known emplacement age of dated ores (Stanton and Russell, 1959). The resulting model age for undated ore deposits is an apparent age calculated from measured isotopic abundances (Stanton and Russell, 1959). The Holmes-Houtermans Pb-growth curve model assumes a chemically closed environment and a single-stage system (Houtermans 1946; Holmes 1946, 1947, 1949). The Stacey and Kramers (1975) model for the evolution of terrestrial Pb involves two stages. Godwin and Sinclair (1982) expanded on the Stacey and Kramers (1975) model by constructing a three-stage growth curve that represents the Pb isotopic evolution of sediments deposited on the western margin of North America that were derived primarily from upper crustal rocks derived from erosion of the western Canadian Shield (Figure 3; Godwin et al., 1988; Nelson, 1991; Mortensen et al., 2006).

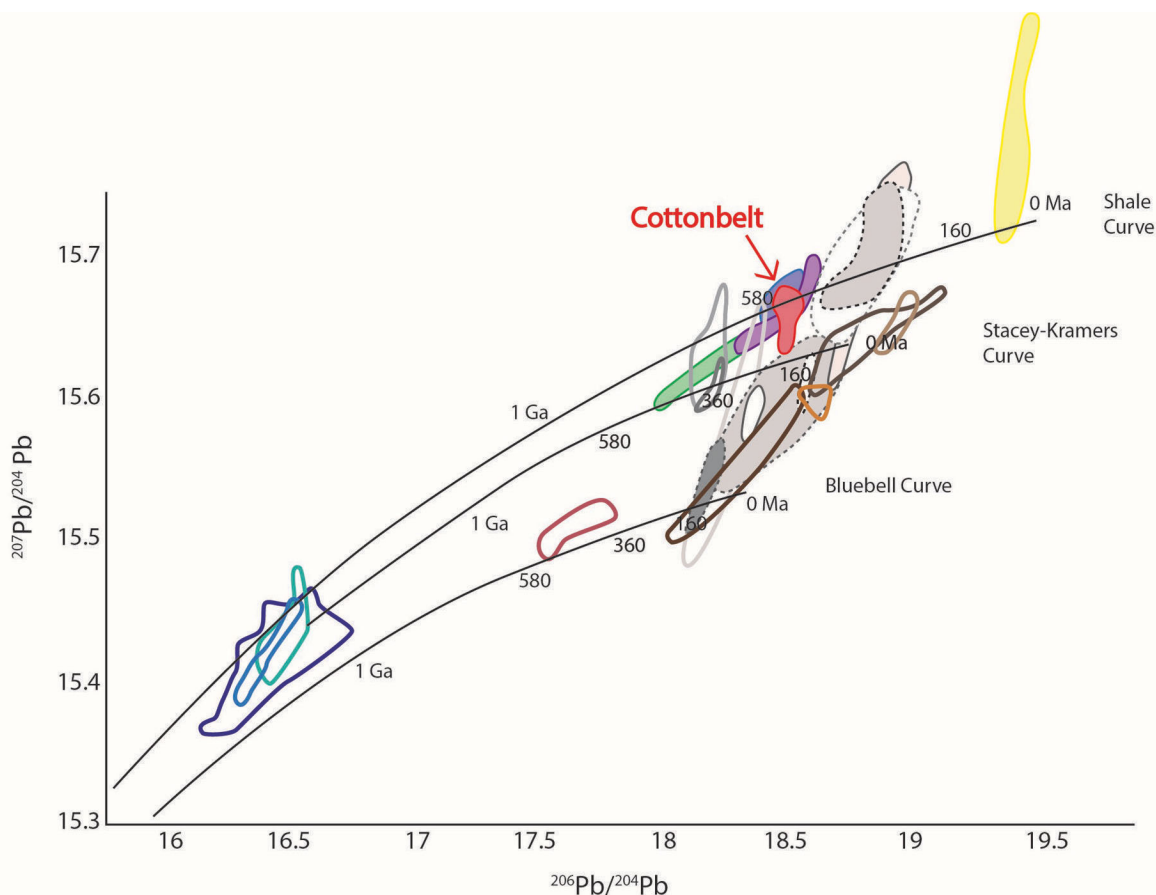
Andrew et al. (1984) plotted galena-Pb from Pb deposits in southeastern BC (Figure 3) on the shale-growth curve of Godwin and Sinclair (1982). Lead data from Pb-Zn deposits that plot off the shale curve in steep linear arrays represent mixing lines between two Pb sources: upper continental crust represented by the Shale Curve and another source more depleted in U with a low  $\mu$  ( $^{238}\text{U}/^{204}\text{Pb}$ ) value from the lower crust/upper mantle batholith (Nelson batholith; Figure 3). Lead data that plot off the Shale Curve and overlap with Ag-rich veins from the Nelson batholith indicate that the Pb deposit is also related to the nearby intrusion rather than being syngenetic (Figure 3). Höy and Godwin (1988) plotted Pb-isotope ratios of galena from the Cottonbelt deposit on the Shale Curve of Godwin and Sinclair (1982) to infer an Early Cambrian model age (Figure 3).

Höy (2002) noted the unusual metal content of the Cottonbelt deposit compared to more typical sedimentary-exhalative (SEDEX) deposits, involving a magnetite host and skarn mineralogy, with high overall Fe-Mn-Pb contents that may require a magmatic input generating hydrothermal fluids similar to a volcanogenic massive sulphide (VMS) deposit (Figure 4). Dusel-Bacon et al. (2012) noted the overlap of Pb-isotope compositions between sulphides from the Bonifield VMS deposit in east-central Alaska with those of feldspars from nearby Late Devonian to Early Mississippian felsic igneous rocks, indicating a common source for the Pb in both minerals and a syngenetic origin for the deposit (Figure 5).

Lead isotopes for this study will be measured on an Element II High Resolution ICP-MS (HR-ICP-MS, Thermo Scientific) at The University of British Columbia’s Pacific Centre for Isotopic and Geochemical Research. Solution MC-ICP-MS was chosen because high precision ( $<0.5\%$   $2\sigma$ ) is critical, but the spatial resolution (i.e., LA-ICP-MS) is less important. The  $^{207}\text{Pb}/^{204}\text{Pb}$  and  $^{206}\text{Pb}/^{204}\text{Pb}$  errors of  $<0.5\%$  ( $2\sigma$ ) produce Shale Curve model Pb ages with errors generally less than 0.05 m.y., sufficient for determining isotopic overlap.

## Expected Outcomes and Impact

This study will plot Pb-isotope ratios and their corresponding analytical errors (displayed as  $2\sigma$ ) from Trident River syenite feldspar, Three Valley Gap syenite feldspar, Three Valley Gap carbonatite pyrite and pyrrhotite, and Cottonbelt galena on a Pb-Pb plot, along with the Stacey-Kramers Curve (Stacey and Kramers, 1975) and the Shale Curve (Godwin and Sinclair, 1982). Overlapping Pb isotopes may indicate that one (or two) magmatic events played a role in Cottonbelt mineralization. Any mixing trends (similar to results from Andrew et al., 1984) may indicate that both upper crustal miogeoclinal sediments and magmatic fluids affected Cottonbelt mineralization. Either scenario would also preclude using a terrestrial growth curve to date the



From Nelson et al. (2006):

- Finlayson District
- Alaska Range
- Eagle Bay
- Ecstall Belt
- Tulsequah Chief
- Brooks Range
- Foremore
- Ambler
- Iberian pyrite belt
- Meggen, Rammelsberg

From Theny (2016):

- Anvil (Höy and Godwin, 1988)
- Wig Wam and Ruddock Creek (Sinclair, 1964; LeCouteur, 1973; Theny et al., 2015)
- Jordan River (LeCouteur, 1973)
- Big Ledge (Cummings and Gudjurgis, 1973)
- Cottonbelt (Höy and Godwin, 1988)

From Andrew et al. (1984):

- Devonian Slocan
- Tillicum
- Carmi
- Mesozoic group (Zartman and Stacey, 1971)
- Bluebell-Ainsworth
- Precambrian group (Zartman and Stacey, 1971)
- Sullivan-Moyie
- Precambrian Slocan

**Figure 4.** Lead isotopic data for sulphide minerals from sedimentary exhalative (SEDEX)-type deposits and K-feldspar from granitic intrusions (after Sinclair, 1964; Stacey and Kramers, 1975; Godwin et al., 1988; Nelson, 1991; Mortensen et al., 2006; Nelson et al., 2006; Theny, 2016).

Cottonbelt deposit. If there are no isotopic overlaps, then additional studies will be needed to address the age problem of an underlying Devonian pyroclastic carbonatite and overlying Cambrian SEDEX deposit (such as isotopic resetting in the Devonian carbonatite zircons or the presence of an unconformity between the two deposits).

This study illustrates the importance of having a local frame of reference to interpret Pb data and provide a method for dating epigenetic and syngenetic or pencon-temporaneous mineralization in the Omineca crystalline belt. Determining accurate age estimates and a potential genetic relationship for the extrusive Mount Grace carbonatite and the Cottonbelt deposit will also have important im-

plications for paleotectonics, as both deposit types indicate rifting. In addition, any influence by carbonatite magmatism on Cottonbelt mineralization would be a world first and any influence by alkaline magmatism would be unique. Only a handful of volcanogenic massive sulphide deposits are associated with peralkaline magmatic rocks and all of these examples (e.g., Cottonbelt) occurred in the Devonian–Mississippian age range on the paleo–western margin of Laurentia (Mortensen & Godwin, 1982; Gibson et al., 1999; Dusel-Bacon et al., 2012).

### Acknowledgments

The authors are grateful for support from Geoscience BC (in the form of a Geoscience BC Scholarship to the lead au-

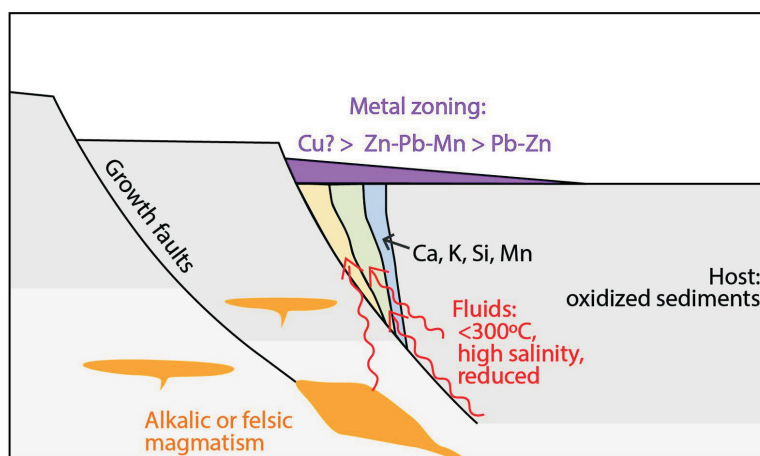


**Figure 5.** Schematic model of the Cottonbelt deposit (modified from Höy, 2002).

thor) and the Natural Sciences and Engineering Research Council of Canada (in the form of a Discovery Grant to the third author) The lead author thanks E. Ye for assistance in the field. The authors also thank M. Parker for reading and reviewing various versions of this document.

## References

- Andrew, A., Godwin, C.I. and Sinclair, A.J. (1984): Mixing line isochrons: a new interpretation of galena lead isotope data from southeastern British Columbia; *Economic Geology*, v. 79, no. 5, p. 919–932, URL <<https://doi.org/10.2113/gsecongeo.79.5.919>>.
- Armstrong, R.L. and Ward, P. (1991): Evolving geographic patterns of Cenozoic magmatism in the North American Cordillera: the temporal and spatial association of magmatism and metamorphic core complexes; *Journal of Geophysical Research: Solid Earth*, v. 96, no. B8, p. 13201–13224, URL <<https://doi.org/10.1029/91JB00412>>.
- Brown, R.L. (1980): Frenchman Cap Dome, Shuswap Complex, British Columbia; Geological Survey of Canada, Paper 80-1A, p. 47–51, URL <<https://doi.org/10.4095/106181>>.
- Brown, R.L., Beaumont, C. and Willett, S.D. (1993): Comparison of the Selkirk fan structure with mechanical models: implications for interpretation of the southern Canadian Cordillera; *Geology*, v. 21, no. 11, p. 1015–1018, URL <[https://doi.org/10.1130/0091-7613\(1993\)021<1015:COTSFS>2.3.CO;2](https://doi.org/10.1130/0091-7613(1993)021<1015:COTSFS>2.3.CO;2)>.
- Brown, R.L., Journeay, J.M., Lane, L.S., Murphy, D.C. and Rees, C.J. (1986): Obduction, backfolding and piggy-back thrusting in the metamorphic hinterland of the southeastern Canadian Cordillera; *Journal of Structural Geology*, v. 8, no. 3–4, p. 255–268, URL <[https://doi.org/10.1130/0091-7613\(1993\)021<1015:COTSFS>2.3.CO;2](https://doi.org/10.1130/0091-7613(1993)021<1015:COTSFS>2.3.CO;2)>.
- Crowley, J.L. (1997): U-Pb geochronologic constraints on the cover sequence of the Monashee complex, Canadian Cordillera: Paleoproterozoic deposition on basement; *Canadian Journal of Earth Sciences*, v. 34, no. 7, p. 1008–1022, URL <<https://doi.org/10.1139/e17-083>>.
- Cumming, G.L. and Gudjurgis, P.J. (1973): Alteration of trace lead isotopic ratios by postore metamorphic and hydrothermal activity; *Canadian Journal of Earth Sciences*, v. 10, no. 12, p. 1782–1789, URL <<https://doi.org/10.1139/e73-174>> [November 2023].
- Doe, B.R. and Stacey, J.S. (1974): The application of lead isotopes to the problems of ore genesis and ore prospect evaluation: a review; *Economic Geology*, v. 69, no. 6, p. 757–776, URL <<https://doi.org/10.2113/gsecongeo.69.6.757>>.
- Dusel-Bacon, C., Foley, N.K., Slack, J.F., Koenig, A.E. and Oscarson, R.L. (2012): Peralkaline- and calc-alkaline-hosted volcanogenic massive sulphide deposits of the Bonfield District, east-central Alaska; *Economic Geology*, v. 107, p. 1403–1432, URL <<https://doi.org/10.2113/econgeo.107.7.1403>>.
- Dzikowski, T.J., Cempírek, J., Groat, L.A., Dipple, G.M. and Giuliani, G. (2014): Origin of gem corundum in calcite marble: the Revelstoke occurrence in the Canadian Cordillera of British Columbia; *Lithos*, v. 198, p. 281–297, URL <<https://doi.org/10.1016/j.lithos.2014.03.030>>.
- Flowerdew, M.J., Tyrrell, S., Riley, T.R., Whitehouse, M.J., Mulvaney, R., Leat, P.T. and Marschall, H.R. (2012): Distinguishing East and West Antarctic sediment sources using the Pb isotope composition of detrital K-feldspar; *Chemical Geology*, v. 292–293, p. 88–102, URL <<https://doi.org/10.1016/j.chemgeo.2011.11.006>>.
- Gervais, F. (2019): Three modes of isograd formation in the northern Monashee Complex of the Canadian Cordillera; Geological Society, London, Special Publications, v. 478, no. 1, p. 373–388. URL <<https://doi.org/10.1144/SP478.7>>.
- Gibson, A.M., Holbek, P.M. and Wilson, R.G. (1999): The Wolf property—1998 update: volcanogenic massive sulphides hosted by rift-related, alkaline, felsic volcanic rocks, Pelly Mountains, Yukon; *in* Yukon Exploration and Geology 1998, C.F. Roots and D.S. Emond (ed.), Exploration and Geological Services Division, Yukon, Indian and Northern Affairs Canada, p. 237–242, URL <[https://emrlibrary.gov.yk.ca/ygs/yeg/1998/1998\\_p237-242.pdf](https://emrlibrary.gov.yk.ca/ygs/yeg/1998/1998_p237-242.pdf)> [October 2023].
- Godwin, C.I. and Sinclair, A.J. (1982): Average lead isotope growth curves for shale-hosted zinc-lead deposits, Canadian Cordillera; *Economic Geology*, v. 77, p. 675–690, URL <<https://doi.org/10.2113/gsecongeo.77.3.675>>.
- Godwin, C.I., Gabites, J.E. and Andrew, A. (1988): Leadtable — a galena lead isotope database for the Canadian Cordillera, with a guide to its use by explorationists; BC Ministry of Energy, Mines and Low Carbon Innovation, Geological Survey Branch, Paper 1988-4, 188 p. [October 2023].

- Holmes, A. (1946): An estimate of the age of the earth; *Nature*, v. 157, 680–684, URL <<https://doi.org/10.1038/157680a0>>.
- Holmes, A. (1947): A revised estimate of the age of the earth; *Nature*, v. 159, p. 127–128, URL <<https://doi.org/10.1038/159127b0>>.
- Holmes, A. (1949): Lead isotopes and the age of the earth; *Nature*, v. 163, p. 453–456, URL <<https://doi.org/10.1038/163453a0>>.
- Höy, T. (1987): Geology of the Cottonbelt lead-zinc-magnetite layer, carbonatites and alkalic rocks in the Mount Grace area, Frenchman Cap dome, southeastern British Columbia; BC Ministry of Energy, Mines and Low Carbon Innovation, Bulletin 80, 99 p., URL <[https://cmscontent.nrs.gov.bc.ca/geoscience/PublicationCatalogue/Bulletin/BCGS\\_B080.pdf](https://cmscontent.nrs.gov.bc.ca/geoscience/PublicationCatalogue/Bulletin/BCGS_B080.pdf)>.
- Höy, T. (2002): BHT and SEDEX deposits of the Kootenay Terrane; BC Ministry of Energy, Mines and Low Carbon Innovation, GeoFile 2002-4, URL <[https://cmscontent.nrs.gov.bc.ca/geoscience/PublicationCatalogue/GeoFile/BCGS\\_GF2002-04.pdf](https://cmscontent.nrs.gov.bc.ca/geoscience/PublicationCatalogue/GeoFile/BCGS_GF2002-04.pdf)> [November 2023].
- Höy, T. and Godwin, C.I. (1988): Significance of a Cambrian date from galena lead-isotope data for the stratiform Cottonbelt deposit in the Monashee Complex, southeastern British Columbia; *Canadian Journal of Earth Sciences*, v. 25, no. 9, p. 1534–1541, URL <<https://doi.org/10.1139/e88-145>>.
- Höy, T. and Kwong, Y.T.J. (1986): The Mount Grace carbonatite: a Nb and light rare earth element–enriched marble of probable pyroclastic origin in the Shuswap complex, southeastern British Columbia; *Economic Geology*, v. 81, no. 6, p. 1374–1386, URL <<https://doi.org/10.2113/gsecongeo.81.6.1374>>.
- Höy, T. and McMillan, W.J. (1979): Geology in the vicinity of Frenchman Cap Gneiss Dome, BC; *in* Geological Fieldwork, 1978, BC Ministry of Energy, Mines and Low Carbon Innovation, Paper 1979-1, p. 25–20, URL <[https://cmscontent.nrs.gov.bc.ca/geoscience/publicationcatalogue/Paper/BCGS\\_P1979-01.pdf#page=24](https://cmscontent.nrs.gov.bc.ca/geoscience/publicationcatalogue/Paper/BCGS_P1979-01.pdf#page=24)> [November 2023].
- Houtermans, F.G. (1946): The isotope ratios in natural lead and the age of uranium; *Naturwissenschaften*, v. 33, p. 185–186.
- Huston, D.L., Champion, D.C. and Cassidy, K.F. (2014): Tectonic controls on the endowment of Neoproterozoic cratons in volcanic-hosted massive sulfide deposits: evidence from lead and neodymium isotopes; *Economic Geology*, v. 109, no. 1, p. 11–26, URL <<https://doi.org/10.2113/econgeo.109.1.11>>.
- Johnson, B.J. (1994): Structure and tectonic setting of the Okanagan Valley fault system in the Shuswap Lake area, southern British Columbia; Ph.D. thesis, Carleton University, 266 p.
- Journeay, J.M., Williams, S.P. and Wheeler, J.O. (2000a): Tectonic assemblage map, Kootenay Lake, British Columbia–Alberta–U.S.A.; Geological Survey of Canada, Open File 2948b, scale 1:1 000 000.
- Journeay, J.M., Williams, S.P. Wheeler, J.O. (2000b): Tectonic assemblage map, Lesser Slave Lake, Alberta–British Columbia; Geological Survey of Canada, Open File 2948f, scale 1:1 000 000.
- Kuiper, Y.D., Shields, C.D., Tubret, M.N., Bennett, V. and Buchwaldt, R. (2014): Age and provenance of a Paleoproterozoic to Devonian Canadian Cordilleran sequence of metasedimentary rocks, Thor-Odin dome, southeastern British Columbia; *GSA Bulletin*, v. 126, no. 9–10, p. 1259–1274, URL <<https://doi.org/10.1130/B31031.1>>.
- LeCouteur, P.C. (1973): Study of lead isotopes from mineral deposits in southeastern British Columbia and from the Anvil range, Yukon Territory; Ph.D. thesis, The University of British Columbia, <<https://dx.doi.org/10.14288/1.0302659>> [November 2023].
- Lund, K. (2008): Geometry of the Neoproterozoic and Paleozoic rift margin of western Laurentia: implications for mineral deposit settings; *Geosphere* v. 4, no. 2, p. 429–1444, URL <<https://doi.org/10.1130/GES00121.1>>.
- McMillan, W.J. (1970): West Flank, Frenchman Cap Gneiss Dome, Shuswap Terrane, British Columbia, *in* Structure of the Canadian Cordillera; Geological Association of Canada, Special Paper 6, p. 99–106.
- McMillan, W.J. (1973): Petrology and structure of the west flank, Frenchman’s Cap dome, near Revelstoke, British Columbia; Geological Survey of Canada, Paper 71-29, 88 p., 2 maps, URL <<https://doi.org/10.4095/102277>>.
- Millonig, L.J., Gerdes, A. and Groat, L.A. (2012): U-Th-Pb geochronology of meta-carbonatites and meta-alkaline rocks in the southern Canadian Cordillera: a geodynamic perspective; *Lithos*, v. 152, p. 202–217, URL <<https://doi.org/10.1016/j.lithos.2012.06.016>> .
- Mortensen, J.K., Dusel-Bacon, C., Hunt, J.A. and Gabites, J. (2006): Lead isotopic constraints on the metallogeny of Middle and Late Paleozoic syngenetic base-metal occurrences in the Yukon-Tanana and Slide Mountain/Seventymile terranes and adjacent portions of the North American miogeocline; *in* Paleozoic Evolution and Metallogeny of Pericratonic Terranes at the Ancient Pacific Margin of North America, Canadian and Alaskan Cordillera, M. Colpron and J.L. Nelson (ed.), Geological Association of Canada, Special Paper 45, p. 261–279, URL <<https://doi.org/10.2113/gsecongeo.77.5.1225>>.
- Mortensen, J.K. and Godwin, C.I. (1982): Volcanogenic massive sulfide deposits associated with highly alkaline rift volcanics in the southeastern Yukon Territory; *Economic Geology*, v. 77, no. 5, p. 1225–1230.
- Nelson, J.L. (1991): Carbonate-hosted lead-zinc (±silver, gold) deposits of British Columbia; *in* Ore Deposits, Tectonics and Metallogeny in the Canadian Cordillera, W.J. McMillan, Coordinator, BC Ministry of Energy, Mines and Low Carbon Innovation, Paper 1991-3, 71–88.
- Nelson, J.L., Colpron, M., Piercey, S.J., Dusel-Bacon, C., Murphy, D.C. and Roots, C.F. (2006): Paleozoic tectonic and metallogenic evolution of the pericratonic terranes in Yukon, northern British Columbia and eastern Alaska; *in* Paleozoic Evolution and Metallogeny of Pericratonic Terranes at the Ancient Pacific Margin of North America, Canadian and Alaskan Cordillera, M. Colpron and J.L. Nelson (ed.), Geological Association of Canada, Special Paper 45, p. 323–360.
- Okulitch, A.V. (1984): The role of the Shuswap metamorphic complex in Cordilleran tectonism: a review; *Canadian Journal of Earth Sciences*, v. 21, no. 10, p. 1171–1193, URL <<https://doi.org/10.1139/e84-123>>.
- Parkinson, D. (1991): Age and isotopic character of early Proterozoic basement gneisses in the southern Monashee Complex, southeastern British Columbia; *Canadian Journal of Earth Sciences*, v. 28, no. 8, p. 1159–1168, URL <<https://doi.org/10.1139/e91-106>>.
- Parrish, R.R. (1995): Thermal evolution of the southeastern Canadian Cordillera; *Canadian Journal of Earth Sciences*, v. 32, p. 1618–1642, URL <<https://doi.org/10.1139/e95-130>>.
- Parrish, R.R. and Scammell, R.J. (1988): The age of the Mount Copeland syenite gneiss and its metamorphic zircons,

- Monashee complex, southeastern British Columbia; *in* Radiogenic Age and Isotopic Studies, Geological Survey of Canada, Paper 88-2, p. 21–28.
- Pell, J. (1994): Carbonatites, nepheline syenites, kimberlites and related rocks in British Columbia; BC Ministry of Energy, Mines and Low Carbon Innovation, Bulletin 88.
- Reesor J.E. and Moore, J.M. Jr. (1971): Petrology and structure of Thor-Odin gneiss dome, Shuswap metamorphic complex, British Columbia; Geological Survey of Canada, Paper 195, 149 p.
- Sinclair, A.J. (1964): A lead isotope study of mineral deposits in the Kootenay Arc; Ph.D. thesis, The University of British Columbia.
- Stacey, J.S. and Kramers, J.D. (1975): Approximation of terrestrial lead evolution by a two-stage model; *Earth and Planetary Science Letters*, v. 26, p. 207–221, URL <[https://doi.org/10.1016/0012-821X\(75\)90088-6](https://doi.org/10.1016/0012-821X(75)90088-6)>.
- Stanton, R.L. and Russell, R.D. (1959): Anomalous leads and the emplacement of lead sulfide ores; *Economic Geology*, v. 54, no. 4, p. 588–607, URL <<https://doi.org/10.2113/gsecongeo.54.4.588>>.
- Theny, L.M. (2016): Age, formation and tectonism of the Neoproterozoic Ruddock Creek zinc-lead deposit and host Windermere Supergroup, northern Monashee Mountains, southern Canadian Cordillera; M.Sc. thesis, Simon Fraser University.
- Wheeler, J.O. (1965): Big Bend map-area, British Columbia; Geological Survey of Canada, Paper 64-32, 37 p., 1 map, URL <<https://doi.org/10.4095/101007>>.
- Zametzer, A., Kirkland, C.L., Hartnady, M.I., Barham, M., Champion, D.C., Bodorkos, S., Hugh Smithis, R. and Johnson, S.P. (2022): Applications of Pb isotopes in granite K-feldspar and Pb evolution in the Yilgarn Craton; *Geochimica et Cosmochimica Acta*, v. 320, p. 279–303, URL <<https://doi.org/10.1016/j.gca.2021.11.029>>.
- Zartman, R.E., and Stacey, J.S. (1971): Lead isotopes and mineralization ages in Belt Supergroup rocks, northwestern Montana and northern Idaho; *Economic Geology*, V. 66, no.6, p. 849–860, URL <<https://doi.org/10.2113/gsecongeo.66.6.849>> [November 2023].

# Characterizing Hostrocks and Alteration Footprints at the Lorraine Alkalic Copper-Gold Porphyry Deposit, North-Central British Columbia (Part of NTS 093N/14)

H. Xu<sup>1</sup>, Department of Earth, Ocean and Atmospheric Sciences, The University of British Columbia, Vancouver, British Columbia, dxu@eoas.ubc.ca

S. Barker, Department of Earth, Ocean and Atmospheric Sciences, The University of British Columbia, Vancouver, British Columbia

F. Bouzari, Department of Earth, Ocean and Atmospheric Sciences, The University of British Columbia, Vancouver, British Columbia

C. Harraden, Department of Earth, Ocean and Atmospheric Sciences, The University of British Columbia, Vancouver, British Columbia

M. Manor, NorthWest Copper Corp. and Department of Earth, Ocean and Atmospheric Sciences, The University of British Columbia, Vancouver, British Columbia

---

Xu, H., Barker, S., Bouzari, F., Harraden, C. and Manor, M. (2024): Characterizing hostrocks and alteration footprints at the Lorraine alkalic copper-gold porphyry deposit, north-central British Columbia (part of NTS 093N/14); *in* Geoscience BC Summary of Activities 2023, Geoscience BC, Report 2024-01, p. 11–22.

## Introduction

Copper is currently one of the most widely used metals, essential to the construction of infrastructure and the production of electronics, vehicles and renewable energy systems (Schlesinger et al., 2011; Mudd et al., 2013). In the 20<sup>th</sup> century, copper demand increased dramatically and copper resources will become even more critical for future society, due to the global promotion of the green energy transition (Schipper et al., 2018). The increase in demand will require the discovery of new copper resources. Porphyry copper-gold deposits are considered one of the primary repositories of global copper resources (Mudd et al., 2013; Mudd and Jowitt., 2018). Porphyry deposits are generally associated with a series of oxidized calcalkalic or alkalic subvolcanic intrusions at convergent margins that exhibit distinctive hydrothermal alteration zonation patterns (Cooke et al., 2007; Sillitoe, 2010). Although alkalic deposits typically have a smaller footprint than calcalkalic deposits, alkalic porphyry deposits play an important role in copper exploration due to their high metal grades (Bissig and Cooke, 2014; Müller and Groves, 2019; Kwan and Müller, 2020). The alkalic porphyry province in British Columbia (BC), includes several world-famous deposits (Figure 1) such as Galore Creek, Mount Milligan, Mount Polley and Lorraine (Lang et al., 1995; Cooke et al., 2007; Bouzari et al., 2016).

The Lorraine porphyry Cu-Au deposit is located about 300 km northwest of Prince George and is among several deposits that highlight the significant base- and precious-metal endowment of the Canadian Cordillera. The resource comprises the Lower Main zone, the Upper Main zone and the Bishop zone. Previous studies have focused mainly on the Lower Main zone (Bath et al., 2014; Devine et al., 2014) but less work has been conducted on the other two zones. These zones are hosted by a wide range of felsic to ultramafic rocks, which are variably altered and mineralized. The aim of this study is to characterize different rock types and alteration assemblages across the three zones to fill the knowledge gaps from previous work and contribute to exploration of the Lorraine deposit.

## Geological Setting

The Lorraine alkalic porphyry Cu-Au deposit is located in the Triassic–Jurassic Quesnel arc of north-central BC (Figure 2). The area around the Lorraine deposit is composed of volcanic and sedimentary rocks of the Late Triassic Takla Group and intruded by Late Triassic to mid-Cretaceous plutons of the Hogen batholith (Nixon and Peatfield, 2003; Bath et al., 2014; Devine et al., 2014; Ootes et al., 2020).

The Hogen batholith around the Lorraine area is subdivided into five suites comprising, from oldest to youngest: 1) Late Triassic to Early Jurassic Hogen granodiorite in the central area; 2) Late Triassic to Early Jurassic diorite, monzodiorite and quartz monzodiorite of the Thane and Detni plutons; 3) the Early Jurassic Duckling Creek syenite complex, which hosts the Lorraine deposit; 4) Early to mid-Cretaceous granodiorite and granite of the Osilinka intrusions in the northern section of the Hogen batholith; and

---

<sup>1</sup>The lead author is a 2023 Geoscience BC Scholarship recipient.

This publication is also available, free of charge, as colour digital files in Adobe Acrobat® PDF format from the Geoscience BC website: <https://geosciencebc.com/updates/summary-of-activities/>.

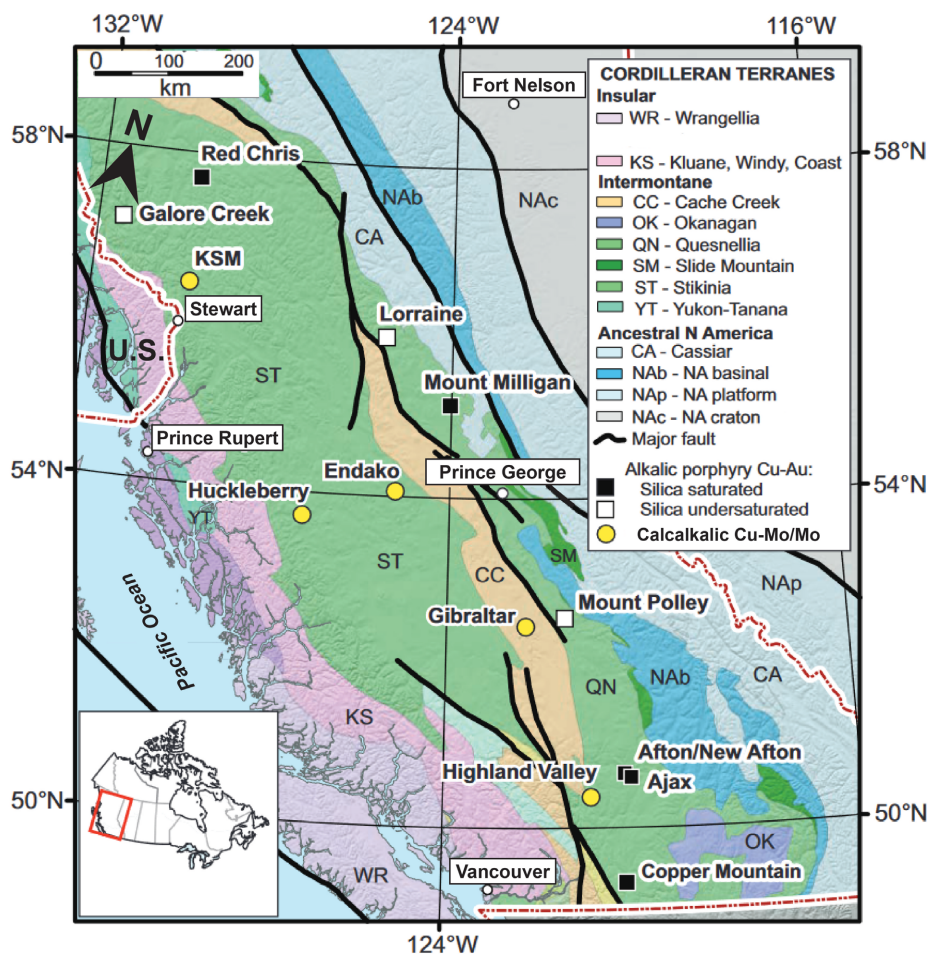


**Figure 1.** Tectonostratigraphic terranes and location of major porphyry deposits in British Columbia (modified from Bouzari et al., 2016).

5) Early to mid-Cretaceous granodiorite, quartz diorite and monzodiorite of the Mesilinka pluton in the northwestern part of the Hogem batholith (Figure 2; Nixon and Peatfield, 2003; Bath, 2010; Bath et al., 2014).

The Duckling Creek syenite complex is a multiphase alkalic intrusive complex that trends generally northwest and is approximately 30 km long by 5 km wide. Its southeastern boundary is the north-northwest-trending Duckling fault, to the east of which lie the Rhonda-Dorothy gabbro-diorite and Takla Group volcanic rocks. The Duckling Creek syenite complex is composed of syenite, pyroxenite, monzonite and diorite. Previous studies (Bath, 2010; Bath et al., 2014; Devine et al., 2014) have classified these rock types into three phases based on the relative timing of emplacement with respect to mineralization. Phase 1 rocks are regarded as the hostrock for mineralization and are composed of silica-undersaturated syenite and pyroxenite. Devine et al. (2014) proposed that phase 1 rocks dip southwest due to tilting following the main stage of mineralization. Phase 2 rocks exhibit similar mineralogy to phase 1 rocks and are composed of unmineralized silica-undersaturated syenite

and pyroxenite. Late unmineralized phase 3 silica-saturated leucosyenite and pegmatitic dikes are compositionally distinct from phase 1 and 2 units. According to previous studies (Bath, 2010; Bath et al., 2014; Devine et al., 2014), the sulphide zones (Figure 3) are defined by bornite-chalcocite cores, ringed by chalcopyrite-dominant zones, with outer pyrite-dominant zones. The alteration assemblages were interpreted by Devine et al. (2014) as pervasive K-feldspar-biotite alteration (potassic alteration) in the core surrounded by albite-diopside-magnetite alteration (calcipotassic alteration). Distinctive patterns of sulphide and alteration zonation at the Lorraine deposit have been documented in previous work, in which it is further classified as a tilted alkalic porphyry-style deposit.

## Methodology

Thin-section analysis to characterize rock types and alteration assemblages to better understand the characteristics of the Lorraine deposit is the focus of this study. Thin sections were provided by the sponsor company, NorthWest Copper Corp., and were cut from company-selected

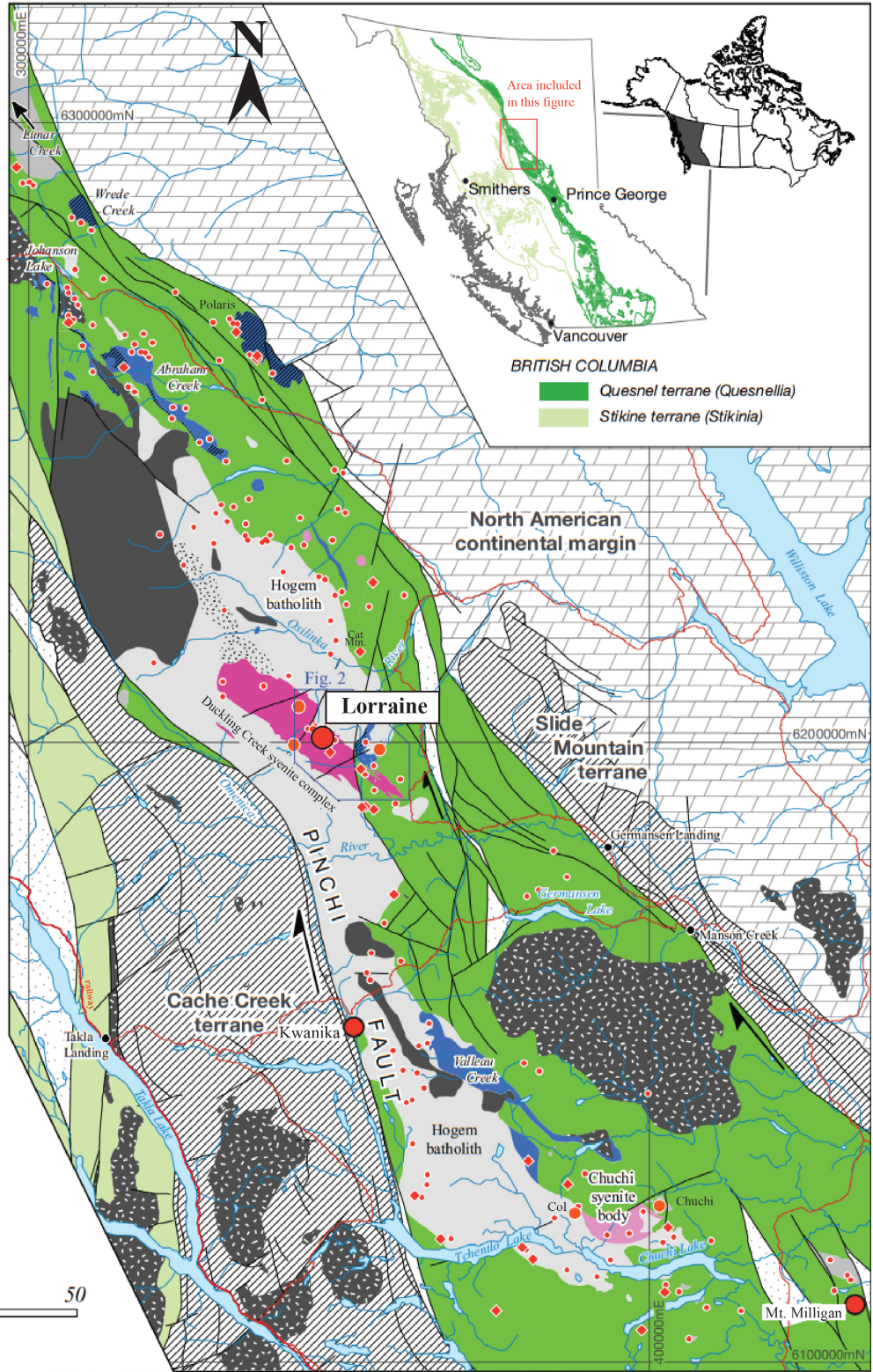
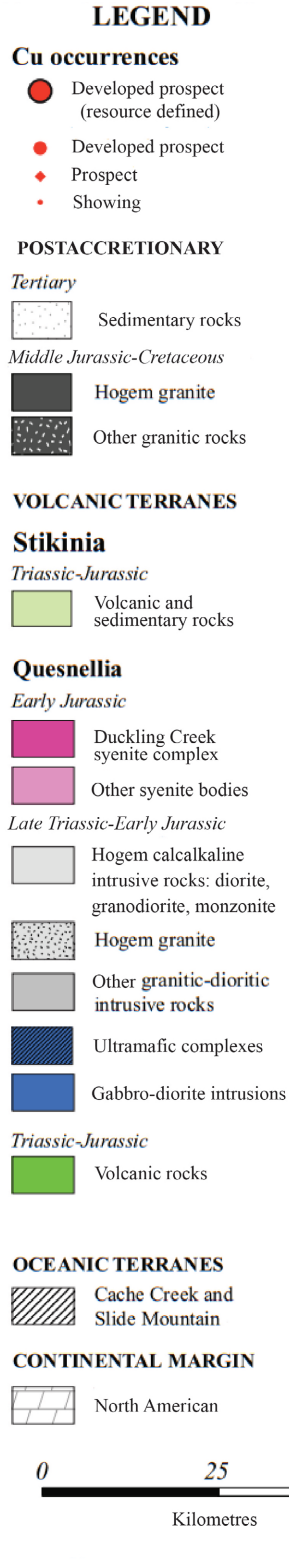


**Figure 2.** Geology of the central Quesnel terrane, highlighting the Hogen batholith, the Duckling Creek syenite complex and the Lorraine deposit (modified from Devine et al., 2014). The term 'Tertiary' used in this figure is a historical term. The International Commission on Stratigraphy recommends using 'Paleogene' (comprising the Paleocene to Oligocene epochs) and 'Neogene' (comprising the Miocene and Pliocene epochs). The author used the term 'Tertiary' because it was used in the source material for this figure. All co-ordinates are in UTM Zone 10, NAD 83.

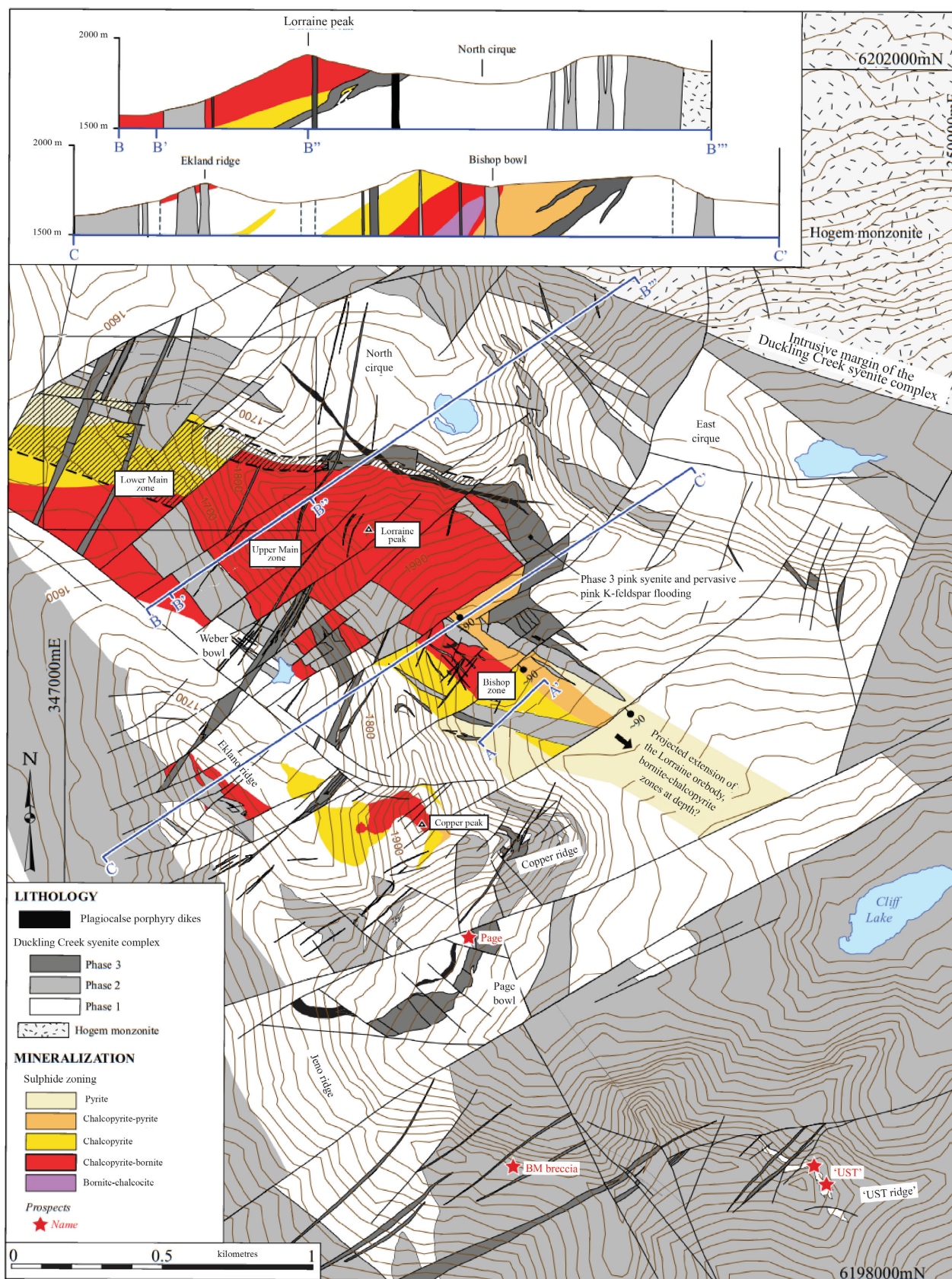


**Figure 3.** Geology and cross-sections of the Lorraine deposit, highlighting the distribution of different phases of intrusion and sulphide-alteration zonation (modified from Devine et al., 2014). Place names with the generic in lower case are unofficial. All co-ordinates are in UTM Zone 10, NAD 83.

**Table 1.** Selected drillholes and number of thin sections selected from each drillhole in the Lower Main zone, Upper Main zone and Bishop zone of the Lorraine deposit.

Lower Main zone		Upper Main zone		Bishop zone	
Hole ID	Thin sections	Hole ID	Thin sections	Hole ID	Thin sections
LOR-01-56	2	LOR-01-50	5	LOR-91-07	2
LOR-01-60	3	LOR-01-51	3	LOR-91-11	1
LOR-02-66	1	LOR-22-132	1	LOR-94-06	1
		LOR-22-133	1	LOR-96-43	6
		LOR-22-136	2	LOR-96-44	2
Total	6	Total	12	Total	12

**Table 2.** Classification of pyroxenite and syenite, with corresponding mineral modal abundance determined from the analysis of thin sections from drillcore samples from the Lorraine deposit.

Pyroxenite				
	diopside	biotite	K-feldspar	Accessory minerals (Ap, Mag, Ttn)
Biotite clinopyroxenite	60–85%	5–40%	0–20%	<20%
Feldspathic biotite	40–60%	10–35%	20–40%	<20%
Syenite				
	diopside + biotite	plagioclase	K-feldspar	Accessory minerals (Ap, Mag, Ttn)
Melanocratic syenite	40–60%	0–5%	40–60%	<20%
Mesocratic syenite	15–40%	0–10%	60–75%	<15%
Leucocratic syenite	0–15%	0–10%	85–95%	<5%

drillcore samples collected from three drillholes in the Lower Main zone, five holes in the Upper Main zone and five holes in the Bishop zone (Table 1). Thirty thin sections with various grades of mineralization were selected from these thirteen drillholes (Figure 4), including six thin sections from the Lower Main zone, twelve thin sections from the Upper Main zone and twelve thin sections from the Bishop zone. These samples include examples of different rock types from different zones at the Lorraine deposit, which will help develop further understanding of the lithological relationships across the three zones.

The selected samples were digitally scanned at the Mineral Deposit Research Unit of The University of British Columbia (UBC) using the Zeiss Axioscan 7 Geo automated petrography system at 5x magnification. Digital images exhibit the complete optical view of thin sections for precise mineral abundance estimation and help to illustrate mineral texture at a coarser scale. The digital thin-section images were analyzed using the ZEN lite software (3.8 version) from Zeiss. Selected thin sections were sent to the UBC microbeam and X-ray laboratory to map major elements using scanning electron microscopy (SEM). All SEM images were obtained using an energy level of 20 kV, at a working distance of 10 mm, a map resolution of 750 by 750 pixels and a pixel size of 3 µm.

## Rock-Type Characterization

According to the ultramafic rock classification scheme from Le Maitre (2002), pyroxenite samples from Lorraine are classified as clinopyroxenite due to the presence of diopside and the absence of olivine and orthopyroxene (Bath, 2010). Based on the abundance of feldspars in digital thin-section images the clinopyroxenite can be subdivided into biotite clinopyroxenite and feldspathic biotite clinopyroxenite (Table 2).

Biotite clinopyroxenite (Figure 5a, b) contains 60–85% green, cumulus, euhedral to subhedral diopside; 5–40% yellow to dark brown, pleochroic, intercumulus, subhedral to anhedral biotite; 0–20% fine-grained intercumulus, anhedral K-feldspar; and <5% subhedral to anhedral plagioclase. Accessory minerals are euhedral apatite (3–15%), magnetite (5–10%) and subhedral to anhedral titanite (0–7%). Disseminated bornite-chalcopyrite is locally present in biotite clinopyroxenite. Two thin sections are classified as biotite clinopyroxenite, one from the Upper Main zone and the other from the Bishop zone.

Feldspathic biotite clinopyroxenite (Figure 5c, d) is differentiated from biotite clinopyroxenite by the abundance of K-feldspar. It is characterized by 40–60% euhedral to subhedral diopside, 20–40% medium-grained anhedral K-feldspar, 10–35% subhedral to anhedral intercumulus biotite and 2–7% subhedral to anhedral plagioclase. Accessory

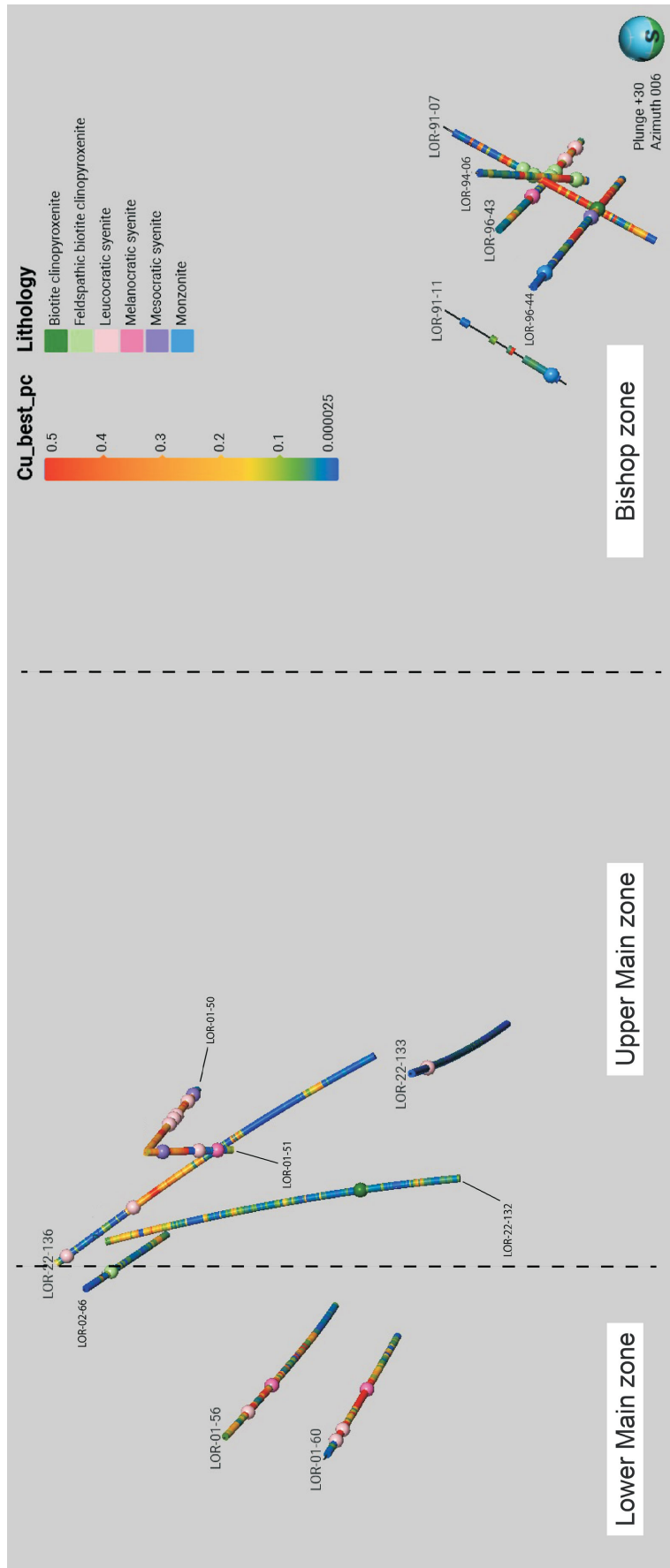


**Figure 4.** Geospatial distribution of selected drillholes at the Lorraine deposit; with the different rock types represented by the coloured nodes and the amount of mineral present (Cu\_best\_pc) represented by the coloured drillhole segments between the nodes (copper content ranging between 0.000025 and 0.5 %).

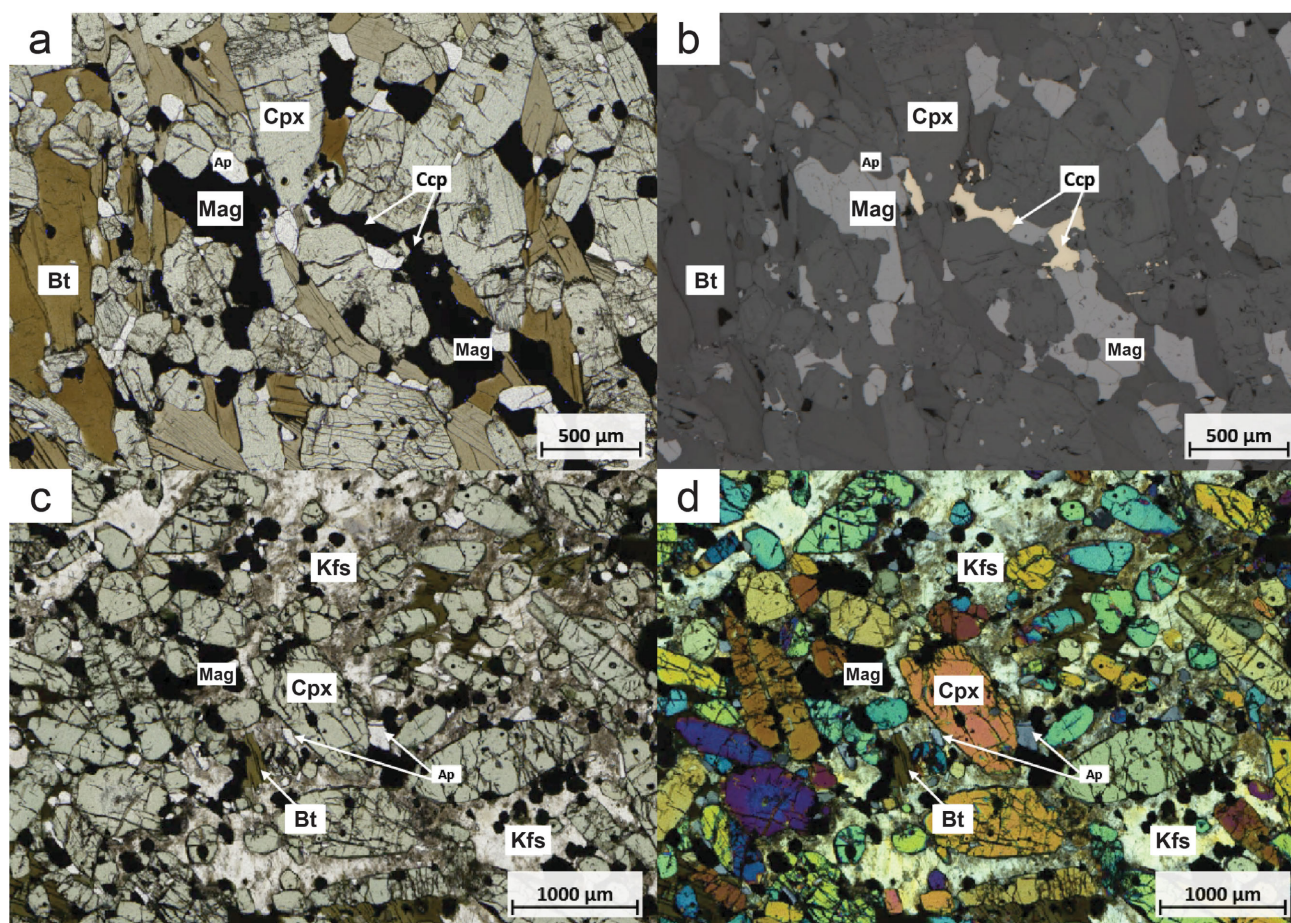


**Figure 5.** Photomicrographs of clinopyroxenite in thin sections from drillcore samples from the Lorraine deposit: **a)** image in plain-polarized light of biotite and diopside showing cumulus texture from biotite clinopyroxenite (sample 4653387, drillhole LOR-22-132 at 279.8 m, Upper Main zone); **b)** same image as (a) in reflected light; **c)** image in plane-polarized light of cumulus diopside with intercumulus K-feldspar and biotite from feldspathic biotite clinopyroxenite (sample 4653564, drillhole LOR-02-66 at 49.8 m, Lower Main zone); **d)** same image as (c) in cross-polarized light. Abbreviations: Ap, apatite; Bt, biotite; Ccp, chalcopyrite; Cpx, clinopyroxene; Kfs, K-feldspar; Mag, magnetite.

minerals comprise euhedral apatite (3–10%), magnetite (3–8%) and subhedral to anhedral titanite (<3%). Potassium-feldspar commonly has turbid boundaries. The cumulate texture of both types of clinopyroxenite is consistent across all three zones at the Lorraine deposit.

In mineralized clinopyroxenite, copper sulphides precipitate interstitially to form primary diopside and biotite and replace K-feldspar. The diopside and biotite grains that are in contact with sulphides are commonly unaltered and have sharp grain boundaries. Six thin sections are classified as feldspathic biotite clinopyroxenite. Five of these came from the Bishop zone and a single one from the Lower Main zone.

According to the felsic rock classification scheme of Le Maitre (2002), syenite at Lorraine is divided into three groups (Table 2) based on the abundance of mafic minerals (diopside and biotite): leucocratic syenite, mesocratic syenite and melanocratic syenite. Leucocratic syenite (Figure 6a, b) is characterized by 85–95% cumulus

anhedral K-feldspar, 0–10% euhedral to subhedral diopside, 0–8% anhedral biotite and <10% subhedral to anhedral plagioclase, with accessory magnetite (<5%). Mesocratic syenite (Figure 6c) is characterized by 60–75% anhedral K-feldspar, 15–30% euhedral to subhedral diopside, 8–15% anhedral biotite and 3–8% subhedral to anhedral plagioclase, with minor magnetite (5–7%) and apatite (3–5%). Melanocratic syenite (Figure 6d) is characterized by 40–60% K-feldspar, 35–55% euhedral to subhedral diopside, 10–25% anhedral biotite and <5% plagioclase, with accessory magnetite (<10%) and euhedral apatite (5–8%). Trace titanite, rutile and zircon are present in some of the syenite samples. Sulphides are observed in all three types of syenite, mostly as disseminated chalcopyrite-pyrite. Bornite-chalcopyrite is also observed in some of the thin sections. Disseminated chalcopyrite (2–3 vol %) is commonly found in leucocratic syenite but is less common (<1 vol %) in mesocratic and melanocratic syenite. The sample suite includes thirteen leucocratic syenite samples, three mesocratic syenite samples and four melanocratic

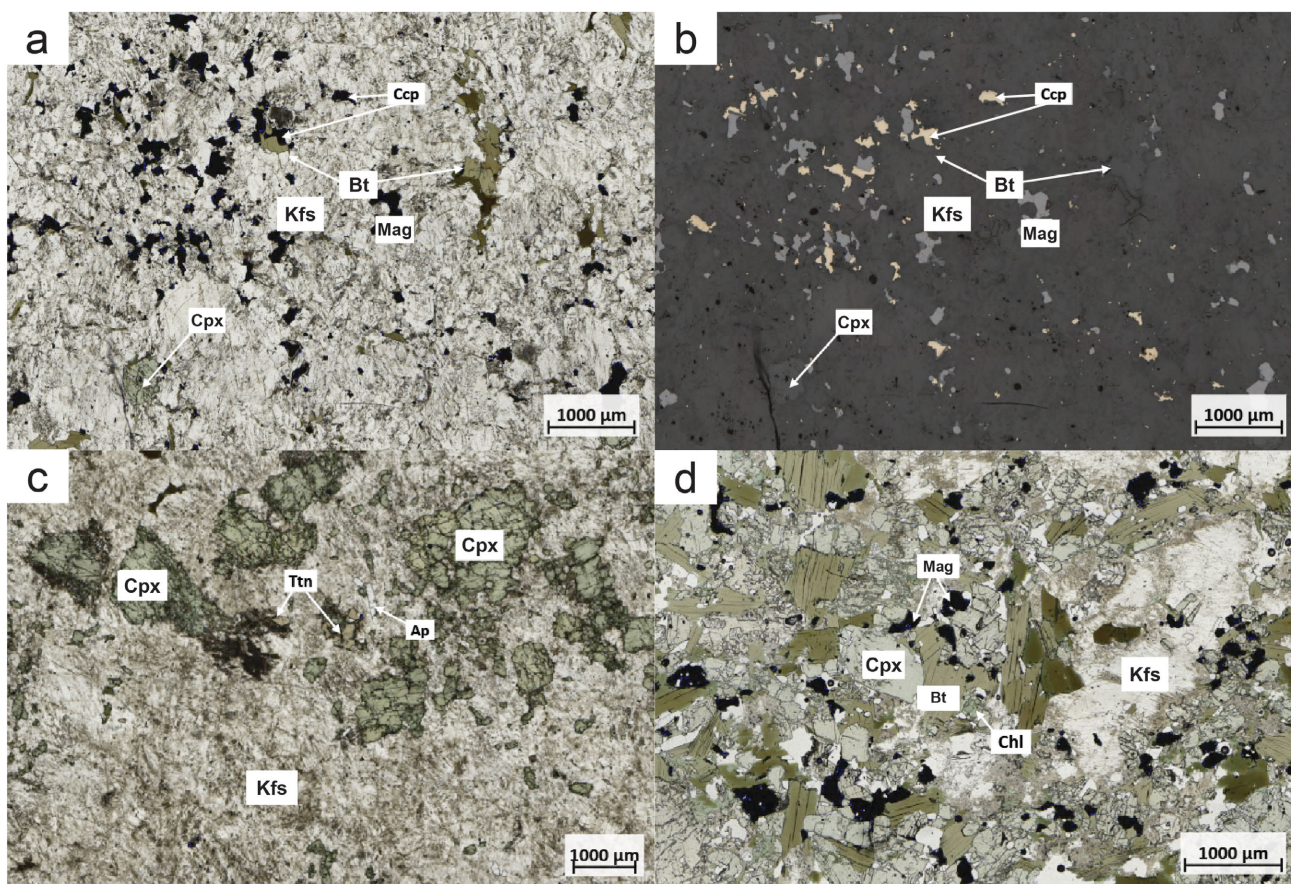


**Figure 6.** Photomicrographs of syenite in thin sections from drillcore samples from the Lorraine deposit: **a)** image in plane-polarized light of leucocratic syenite with <10% of mafic minerals (sample 4653394, drillhole LOR-96-43 at 167.6 m, Bishop zone); **b)** same image as (a) in reflected light; **c)** image in plane-polarized light of mesocratic syenite with 10–50% of mafic minerals (drillhole LOR-01-50 at 154.7 m, Upper Main zone); **d)** image in plane-polarized light of melanocratic syenite with >50% of mafic minerals (sample 4653596, drillhole LOR-01-51 at 84.3 m, Upper Main zone). Abbreviations: Ap, apatite; Bt, biotite; Ccp, chalcopyrite; Chl, chlorite; Cpx, clinopyroxene; Kfs, K-feldspar; Ttn, titanite.

syenite samples. Leucocratic syenite samples are mostly from the Lower Main zone and Upper Main zone except for two samples from the Bishop zone. Mesocratic syenites are mostly from the Upper Main zone, except for one sample from the Bishop zone. Two melanocratic syenite samples came from the Lower Main zone, whereas the other two samples came from the Upper Main zone and the Bishop zone, respectively (Figure 4).

### Alteration Minerals

Four alteration minerals were studied: biotite, epidote, garnet and albite. In the selected thin-section suite, biotite is divided into three types. The first, Bt 1, is commonly present in pyroxenite, and in mesocratic and melanocratic syenites (Figure 7a). This type of biotite is commonly medium grained, subhedral to anhedral to locally poikilitic, with diopside and apatite chadacrysts, yellow to dark brown pleochroic and sometimes exhibits perfect cleavages, whereas Bt 2 is very fine grained and lacks visible cleavages. Diopside along fractures is most commonly replaced by Bt 2 as

thin biotite veinlets and along diopside grain boundaries as biotite patches before being subsequently partially to completely replaced by chlorite (Figure 7a). Results from semi-quantitative SEM analysis indicate that coarse-grained biotite has higher Fe (27–29%) and Ti (2.9–5.2%) contents but a lower Mg content (11.9–13.4%) than the very fine-grained biotite, which has lower Fe (about 23%) and Ti (0.5–0.7%) contents but a higher Mg (15.9–18%) content. Finally, Bt 3 is present in some leucocratic syenite samples (Figure 7b). This third type of biotite is fine grained, yellow to reddish-brown pleochroic and has imperfect cleavages in some cases; it is commonly associated with euhedral chalcopyrite-pyrite.

Garnet and epidote are commonly present in mineralized feldspathic biotite clinopyroxenite and mineralized syenite at the Lorraine deposit. The garnet is fine grained, light brown (Figure 8a), euhedral to subhedral, of high relief, zoned, optically anisotropic, with first-order grey to yellow interference colours (Figure 8b), and is typically associated with epidote. Garnet appears to replace both intercumulus

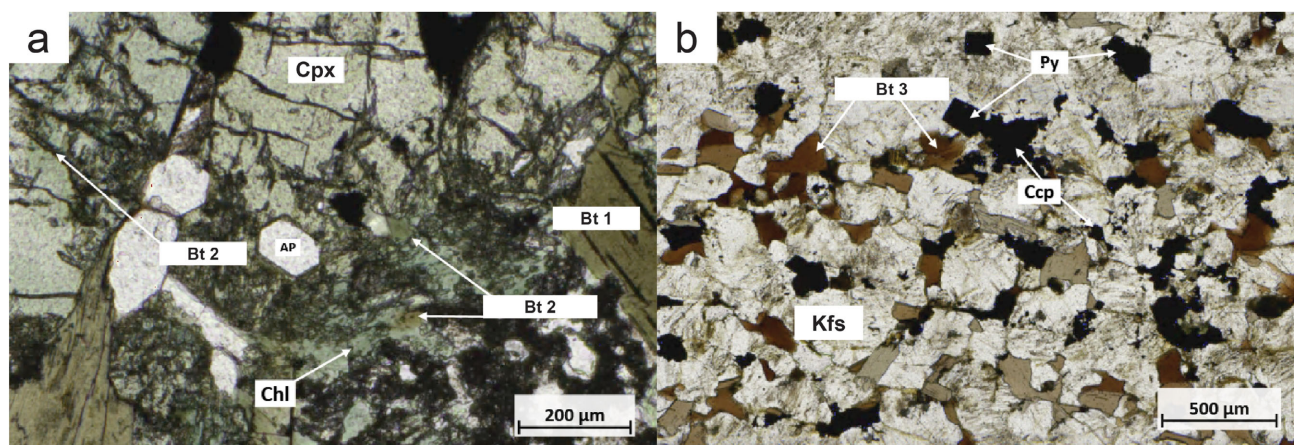


**Figure 7.** Photomicrographs of biotite alteration in thin sections from drillcore samples from the Lorraine deposit: **a)** image in plane-polarized light of melanocratic syenite with two types of biotite, the first (Bt 1) being medium grained, euhedral to subhedral and exhibiting perfect cleavages, whereas the second (Bt 2) grows along diopside grain fractures and along diopside grain boundaries to form biotite veinlets and biotite patches before being subsequently altered to chlorite (drillhole LOR-96-43 at 83.8 m, Bishop zone); **b)** image in cross-polarized light of leucocratic syenite with reddish-brown biotite (Bt 3) closely associated with chalcopyrite and pyrite (sample 3678951, drillhole LOR-22-136 at 102.6 m, Upper Main zone). Abbreviations: Ap, apatite; Bt, biotite; Ccp, chalcopyrite; Chl, chlorite; Cpx, clinopyroxene; Kfs, K-feldspar; Py, pyrite.

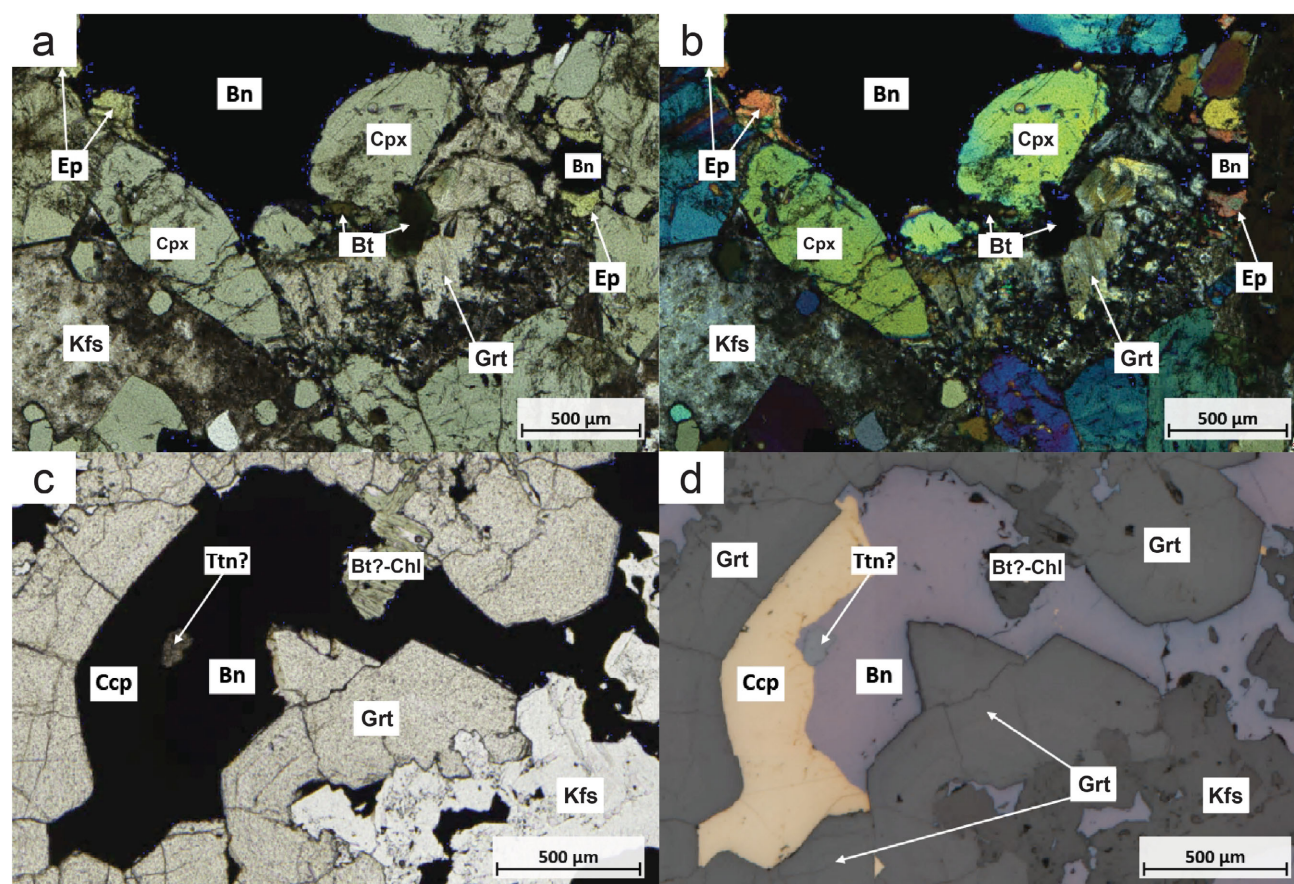


**Figure 8.** Photomicrographs of epidote-garnet alteration in thin sections from drillcore samples from the Lorraine deposit: **a)** image in plane-polarized light of feldspathic biotite clinopyroxenite with epidote-garnet assemblage, characterized by light brown, high-relief garnets that replace intercumulus K-feldspar and epidote in contact with bornite as well as weakly altered surrounding diopside (sample 4653542, drillhole LOR-91-07 at 89.3 m, Bishop zone); **b)** same image as (a) in cross-polarized light; **c)** image in plane-polarized light of bornite-chalcopyrite filling open space and sharp contacts with surrounding hydrothermal garnet, which indicates that epidote-garnet alteration is pre- or synmineralization (drillhole LOR-91-11 at 120.2 m, Bishop zone); **d)** same image as (c) in reflected light. Abbreviations: Ap, apatite; Bt, biotite; Bn, bornite; Ccp, chalcopyrite; Chl, chlorite; Cpx, clinopyroxene; Ep, epidote; Grt, garnet; Kfs, K-feldspar; Ttn, titanite.

K-feldspar in pyroxenite and K-feldspar in syenite to form irregular contacts with surrounding K-feldspar (Figure 8a, b). Garnet-associated copper sulphides tend to have sharp contacts with the surrounding garnet, exhibiting void-filling textures (Figure 8c, d). Epidote is euhedral, fine grained, of moderate relief and is yellow pleochroic to transparent (Figure 8a, b). Epidote overprints both K-feldspar and diopside in pyroxenite and syenite. Garnet is commonly associated with epidote in mineralized samples,

but epidote also occurs where sulphide mineralization is not present.

Alteration albite is difficult to identify petrographically because it is optically similar to primary K-feldspar (Figure 9a); in pyroxenite, the presence of albite was only detected by SEM analysis. Albite commonly replaces intercumulus K-feldspar to form albite patches (Figure 9a, b). In mineralized pyroxenite, albite locally replaces

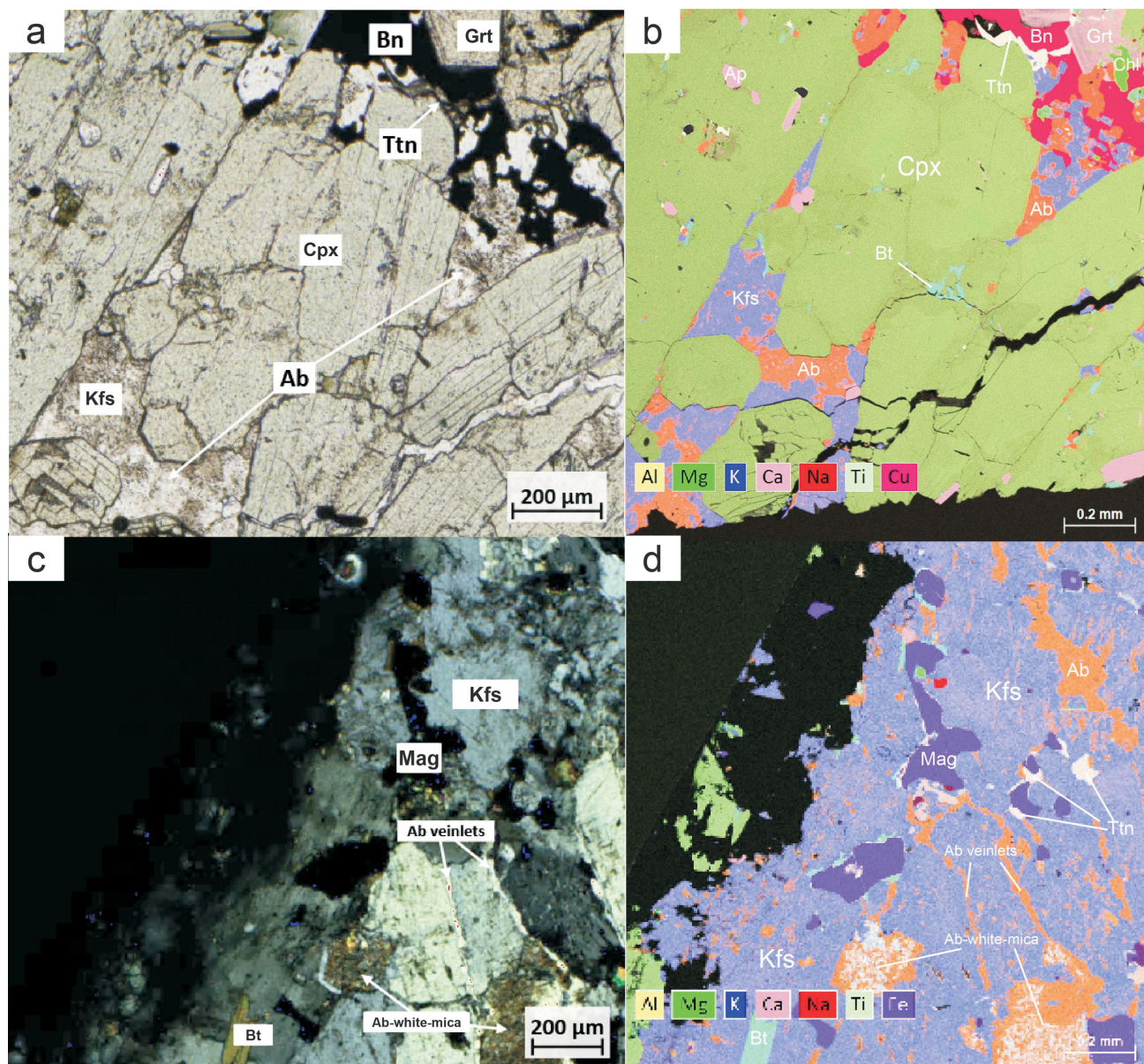


**Figure 9.** Photomicrographs and scanning electron microscope (SEM) images of albite alteration in thin sections from drillcore samples from the Lorraine deposit: **a)** image in plane-polarized light of feldspathic biotite clinopyroxenite with both garnet alteration and albite alteration, which is difficult to identify due to its similarity to primary K-feldspar (sample 4653542, drillhole L91-07 at 89.3 m, Bishop zone); **b)** same image as (a) but showing, as detected by SEM, that albite altered intercumulus K-feldspar and overprinted garnet have blurry contacts with bornite; **c)** image in cross-polarized light of leucocratic syenite with albite alteration (optically identified due to the relatively higher relief and interference colour) that commonly occurs along K-feldspar grain boundaries and at times within K-feldspar grains, whereas plagioclase is shown to be strongly to completely altered to albite-white mica (sample 4653394, drillhole LOR-96-43 at 167.6 m, Bishop zone.); **d)** SEM image of (c). Abbreviations: Ab, albite; Ap, apatite; Bt, biotite; Bn, bornite; Chl, chlorite; Cpx, clinopyroxene; Grt, garnet; Kfs, K-feldspar; Ttn, titanite.

garnet alteration (Figure 9b, upper right corner). In syenite, albite has relatively higher relief and first-order birefringence compared to surrounding K-feldspar. It commonly occurs along K-feldspar grain boundaries as albite veinlets and can be identified from both photomicrographs and SEM images (Figure 9c, d). The albite veinlets are thin (about 20–50 µm wide), and the contacts with K-feldspar are usually indistinct. The K-feldspar is also weakly altered to form fine albite patches within grains, whereas plagioclase (identified by remnants of polysynthetic twinning) is strongly to completely altered by albite and white mica.

## Discussion

The aim of this study is to characterize the mineralogy of pyroxenite and syenite at the Lorraine deposit; texturally and geochemically evaluate the origins of minerals; and assess the relationship between different types of alteration and mineralization. In previous studies of the area (Bath et al., 2014; Devine et al., 2014), it was proposed that pervasive biotite alteration is the most common alteration style and that it is closely associated with mineralization. The petrography reported herein indicates that biotite from leucocratic syenite (Bt 3, Figure 7b) correlates strongly with mineralization, whereas biotite in pyroxenite, mesocratic syenite and melanocratic syenite (Bt 1 and Bt 2, Figure 7a) shows less spatial correlation with mineralization. Although the three types of biotite identified in this study are texturally and geochemically distinct from each other, the current results are too sparse to determine if they were formed by igneous or hydrothermal processes. There is insufficient evidence to support the assumption that Bt 1 and Bt 2 are associated with mineralization, whereas Bt 3 is strongly correlated with copper sulphide in leucocratic syenite.

Epidote-garnet alteration was documented in previous studies (Devine et al., 2014) as two separate alteration types. Devine et al. (2014) proposed that albite-epidote alteration was present in postmineralized intrusions and that garnet alteration locally occurred in distal postmineralization melanocratic syenite. Observations from the present study suggest that epidote-garnet alteration is more common than previously documented and closely correlates with mineralization. The uncommon anisotropic garnet detected by SEM analysis shows similar optical properties to hydrothermal garnet from the Oslo Rift of southern Norway documented in Jamtveit (1991) and Jamtveit et al. (1995), which implies a hydrothermal origin for the grossular-andradite garnet at the Lorraine deposit. The sharp contacts between copper sulphides and garnet (Figure 8c, d) indicate that garnet alteration is pre- or syn-mineralization. Although garnet and epidote are strongly associated with each other in mineralized samples, epidote is also associated with mineralization in areas where no garnet is present. This suggests that there are two separate

phases of alteration at the Lorraine deposit: epidote-garnet alteration and epidote-only alteration. Bath (2010) proposed that albite alteration is present in distal zones and relatively uncommon in the proximal area. According to petrographic and SEM results, albite is present in all different rock types with different grades of mineralization. Albite alteration overprints the previous garnet alteration (Figure 9b, upper right corner), which suggests that albite alteration postdates garnet alteration. The relationships between mineralization and albite alteration in different rock types are currently uncertain due to the ubiquitous nature of albite alteration across all rock types.

## Future Work

The other two major rock types at the Lorraine deposit are monzonite and monzodiorite; these should also be characterized using the same process as relied upon in this study. More detailed petrographic and geochemical analysis on alteration minerals should be completed to help define the origins of different generations of alteration minerals and their relationships to mineralization. Summarizing the characteristics of each alteration type in each of the different rock types will help to unravel the magmatic and hydrothermal processes that led to the formation of the Lorraine deposit.

## Conclusions

Pyroxenite and syenite were classified in this study based on the proportion of K-feldspar, diopside and other mafic minerals. Pyroxenite is subdivided into biotite clinopyroxenite and feldspathic biotite clinopyroxenite. Syenite is subdivided into leucocratic, mesocratic and melanocratic syenite. Several possible alteration minerals are characterized and compared with previous studies:

- Biotite is subdivided into three texturally and geochemically different types; only the biotite present in leucocratic syenite is suggested to correlate with mineralization.
- Epidote-garnet alteration is more common than previously documented and, when compared with previous studies, shows strong correlations with mineralization. Characteristics of this alteration are most consistent with pre- or syn-mineralization timing and the epidote-garnet assemblage might prove to be a new vector for copper exploration at the Lorraine deposit.
- Albite alteration is ubiquitous in all rock types, with albite replacing garnet, but the timing relative to mineralization is uncertain.

## Acknowledgments

The authors would like to thank Geoscience BC, Teck Resources Limited, NorthWest Copper Corp. and the Mineral Deposit Research Unit of the University of British Columbia for financially supporting this project. They would also

like to thank J. Lang, G. Titley and S. Peacock for reviewing the manuscript.

## References

- Bath, A.B. (2010): Geology, geochronology and alteration of the Lorraine alkalic porphyry Cu-Au deposit, British Columbia, Canada; Ph.D. thesis, University of Tasmania, 299 p., URL <<https://doi.org/10.25959/23234834.v1>>.
- Bath, A.B., Cooke, D.R., Friedman, R.M., Faure, K., Kamenetsky, V.S., Tosdal, R.M. and Berry, R.F. (2014): Mineralization, U-Pb geochronology, and stable isotope geochemistry of the Lower Main zone of the Lorraine deposit, north-central British Columbia: a replacement-style alkalic Cu-Au porphyry; *Economic Geology*, v. 109, no. 4, p. 979–1004, URL <<https://doi.org/10.2113/econgeo.109.4.979>>.
- Bissig, T. and Cooke, D.R. (2014): Introduction to the Special Issue devoted to alkalic porphyry Cu-Au and epithermal Au deposits; *Economic Geology*, v. 109, no. 4, p. 819–825, URL <<https://doi.org/10.2113/econgeo.109.4.819>>.
- Bouzari, F., Hart, C.J.R., Bissig, T. and Barker, S. (2016): Hydrothermal alteration revealed by apatite luminescence and chemistry: a potential indicator mineral for exploring covered porphyry copper deposits; *Economic Geology*, v. 111, no. 6, p. 1397–1410, URL <<https://doi.org/10.2113/econgeo.111.6.1397>>.
- Cooke, D.R., Wilson, A.J., House, M.J., Wolfe, R.C., Walshe, J.L., Lickfold, V. and Crawford, A.J. (2007): Alkalic porphyry Au–Cu and associated mineral deposits of the Ordovician to Early Silurian Macquarie Arc, New South Wales; *Australian Journal of Earth Sciences*, v. 54, no. 2–3, p. 445–463, URL <<https://doi.org/10.1080/08120090601146771>>.
- Devine, F.A.M., Chamberlain, C.M., Davies, A.G.S., Friedman, R. and Baxter, P. (2014): Geology and district-scale setting of tilted alkalic porphyry Cu-Au mineralization at the Lorraine deposit, British Columbia; *Economic Geology*, v. 109, no. 4, p. 939–977, URL <<https://doi.org/10.2113/econgeo.109.4.939>>.
- Kwan, K. and Müller, D. (2020): Mount Milligan alkalic porphyry Au-Cu deposit, British Columbia, Canada, and its AEM and AIP signatures: implications for mineral exploration in covered terrains; *Journal of Applied Geophysics*, v. 180, art. 104131, URL <<https://doi.org/10.1016/j.jappgeo.2020.104131>>.
- Lang, J.R., Stanley, C.R., Thompson, J.F.H. and Dunne, K.P.E. (1995): Na-K-Ca magmatic-hydrothermal alteration in alkalic porphyry Au-Cu deposit, British Columbia; *Mineralogical Association of Canada, Short Course Handbook*, v. 23, p. 339–366.
- Jamtveit, B. (1991): Oscillatory zonation patterns in hydrothermal grossular-andradite garnet: nonlinear dynamics in regions of immiscibility; *American Mineralogist*, v. 76, no. 7–8, p. 1319–1327.
- Jamtveit, B., Agnarsdottir, K.V. and Wood, B.J. (1995): On the origin of zoned grossular-andradite garnets in hydrothermal systems; *European Journal of Mineralogy*, v. 7, no. 6, p. 1399–1410, URL <<https://doi.org/10.1127/ejm/7/6/1399>>.
- Le Maitre, R.W. (2002): *Igneous rocks: a classification and glossary of terms—recommendations of the International Union of Geological Sciences, Subcommittee on the Systematics of Igneous Rocks (2<sup>nd</sup> edition)*; R.W. Le Maitre, A. Streckeisen, B. Zanettin, M.J. Le Bas, B. Bonin and P. Bateman (ed.), Cambridge University Press, p. 22–28, URL <<https://doi.org/10.1017/CBO9780511535581>>.
- Mudd, G.M. and Jowitt, S.M. (2018): Growing global copper resources, reserves and production: discovery is not the only control on supply; *Economic Geology*, v. 113, no. 6, p. 1235–1267, URL <<https://doi.org/10.5382/econgeo.2018.4590>>.
- Mudd, G.M., Weng, Z. and Jowitt, S.M. (2013): A detailed assessment of global Cu resource trends and endowments; *Economic Geology*, v. 108, no. 5, p. 1163–1183, URL <<https://doi.org/10.2113/econgeo.108.5.1163>>.
- Müller, D. and Groves, D.I. (2019): *Implications for mineral exploration in arc environments; in Potassic Igneous Rocks and Associated Gold-Copper Mineralization*, D. Müller and D. I. Groves (ed.), Springer International Publishing, p. 337–354, URL <[https://doi.org/10.1007/978-3-319-92979-8\\_10](https://doi.org/10.1007/978-3-319-92979-8_10)>.
- Nixon, G.T. and Peatfield, G.R. (2003): Geological setting of the Lorraine Cu-Au porphyry deposit, Duckling Creek syenite complex, north-central British Columbia; BC Ministry of Energy, Mines and Low Carbon Innovation, BC Geological Survey, Open File 2003-4, 24 p.
- Ootes, L., Bergen, A.L., Milidragovic, D., Jones, G.O., Camacho, A. and Friedman, R. (2020): An update on the geology of northern Hogen batholith and its surroundings, north-central British Columbia; *in Geological Fieldwork 2019*, BC Ministry of Energy, Mines and Low Carbon Innovation, BC Geological Survey, Paper 2020-01, p. 25–47.
- Schlesinger, M.E., King, M.J., Sole, K.C. and Davenport, W.G. (2011): Production and use; Chapter 2 *in Extractive Metallurgy of Copper (5<sup>th</sup> edition)*, M.E. Schlesinger, M.J. King, K.C. Sole and W.G. Davenport (ed.), Elsevier, p. 13–30, URL <<https://doi.org/10.1016/B978-0-08-096789-9.10002-2>>.
- Schipper, B.W., Lin, H.-C., Meloni, M.A., Wansleben, K., Heijungs, R. and van der Voet, E. (2018): Estimating global copper demand until 2100 with regression and stock dynamics; *Resources, Conservation and Recycling*, v. 132, p. 28–36, URL <<https://doi.org/10.1016/j.resconrec.2018.01.004>>.
- Sillitoe, R.H. (2010): Porphyry copper systems; *Economic Geology*, v. 105, no. 1, p. 3–41, URL <<https://doi.org/10.2113/gsecongeo.105.1.3>>.

# Controls on the Nickel Mineralization of the Alaskan-Type Turnagain Deposit, North-Central British Columbia (Parts of NTS 104I/07, 10)

K.R. Broda<sup>1</sup>, Department of Earth and Planetary Sciences, McGill University, Montréal, Quebec, kiera.broda@mail.mcgill.ca

A.E. Williams-Jones, Department of Earth and Planetary Sciences, McGill University, Montréal, Quebec

O.V. Vasyukova, Department of Earth and Planetary Sciences, McGill University, Montréal, Quebec

---

Broda, K.R., Williams-Jones, A.E. and Vasyukova, O.V. (2024): Controls on the nickel mineralization of the Alaskan-type Turnagain deposit, north-central British Columbia (parts of NTS 104I/07, 10); in Geoscience BC Summary of Activities 2023, Geoscience BC, Report 2024-01, p. 23–32.

## Introduction

Alaskan-type complexes constitute a distinct class of ultramafic–mafic igneous rocks formed through the emplacement and fractional crystallization of a hydrous, magnesium-rich basaltic magma derived from partial melting of the mantle wedge at convergent plate margins (Irvine, 1963; Naldrett and Cabri, 1976; Himmelberg and Loney, 1995; Naldrett, 2004). The presence of hydrous minerals (hornblende), absence of orthopyroxene and their plate-tectonic setting distinguish Alaskan-type complexes from other ultramafic–mafic complexes. They are zoned from a core of dunite outward to wehrlite, clinopyroxenite, hornblendite, gabbro and diorite, and are considered to represent cumulates of olivine, clinopyroxene and hornblende (Irvine, 1959, 1963, 1974; Naldrett and Cabri, 1976; Naldrett, 2004; Thakurta et al., 2008; Thakurta, 2018). Because of their relatively oxidized nature and depth of formation, Alaskan-type magmas are undersaturated with respect to sulphide (Mavrogenes and O’Neil, 1999) and, consequently, do not generally host significant sulphide mineralization (Irvine, 1963, 1974; Naldrett and Cabri, 1976; Naldrett, 2004; Thakurta, 2018).

The Turnagain complex in north-central British Columbia (BC) is an unusual example of an Alaskan-type complex that contains a potentially economic body of magmatic nickel-sulphide mineralization. It comprises a core of dunite and wehrlite surrounded by clinopyroxenite and hornblendite (Clark, 1980; Scheel, 2007; Jackson-Brown, 2017). Pentlandite ( $[\text{Ni}, \text{Fe}]_9\text{S}_8$ ) is the principal nickel-ore mineral (25 to 35 wt. % Ni), although a significant proportion of nickel is also present in olivine (mean 1400 ppm), serpentine (mean 800 ppm) and pyrrhotite (mean 400 ppm; Blue Coast Research Ltd., unpublished reports, 2019,

2020). The complex has experienced variable but extensive serpentinization, leading to the replacement of the olivine by serpentine minerals and the remobilization of sulphur. Because of the presence of nickel in both sulphide and silicate minerals, and the intricate interplay between magmatic and hydrothermal processes, the nickel-to-sulphur ratios within the deposit display extreme variability, posing challenges for the metallurgical recovery of the nickel. The Turnagain complex has the highest known endowment of nickel sulphide of any Alaskan-type ultramafic complex (1574 Mt of ore grading 0.21 wt. % Ni; Giga Metals Corporation, 2023) and therefore represents an ideal natural laboratory, in which to investigate the processes that lead to economic concentrations of nickel-sulphide mineralization in such complexes.

A detailed petrographic and geochemical study of a suite of representative samples from the Horsetrail-Northwest zone of the Turnagain complex (Figure 1) has been initiated to unravel the history of nickel-sulphide mineralization in the complex. Preliminary results from that study are presented in this paper.

## The Geology of the Turnagain Complex

The Turnagain complex is situated in north-central BC, approximately 65 km east of Dease Lake (Figure 1) and is part of a belt of Alaskan-type intrusions of Early Jurassic age 250 km long located between Turnagain in the north and the Polaris intrusion in the south (Nixon et al., 2020). It is an elliptical body of intrusive mafic to ultramafic rocks approximately 8 km long by 3.5 km wide in plan, with a northwest-trending long axis that roughly parallels the regional structural trend (Scheel, 2007; Jackson-Brown et al., 2017; Nixon et al., 2020). The magma that formed the complex intruded into Middle to Late Paleozoic graphitic phyllite and metasedimentary-volcanic rocks with Yukon-Tanana or Quesnellia terrane affinity between 189 and 185 Ma, during the initial accretion of arc-related terranes onto the ancient North American continental margin (Nixon et al., 2020). The Turnagain complex is fault-bounded and juxta-

---

<sup>1</sup>The lead author is a 2023 Geoscience BC Scholarship recipient.

This publication is also available, free of charge, as colour digital files in Adobe Acrobat® PDF format from the Geoscience BC website: <https://geosciencebc.com/updates/summary-of-activities/>.

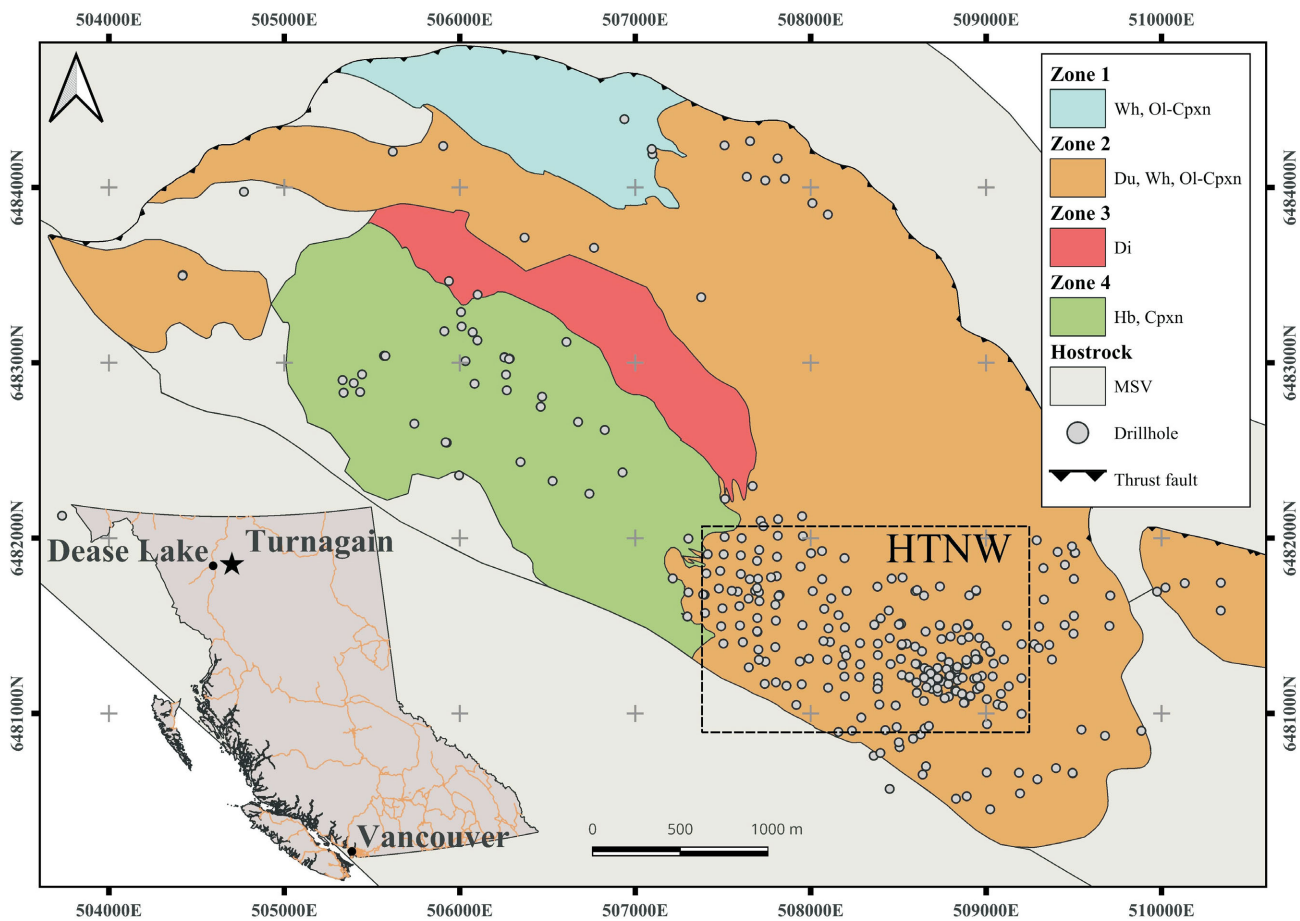


**Figure 1.** Location (inset) and generalized geology of the Turnagain complex. The study area, the Horsetrail-Northwest resource zone (HTNW), is outlined by the rectangle in the southeastern part of the complex. Zones 1 through 4 represent distinct intrusive bodies composed of different lithological assemblages. Abbreviations: Cpxn, clinopyroxenite; Di, diorite; Du, dunite; Hb, hornblendite; MSV, metasedimentary-volcanic; Ol-Cpxn, olivine-clinopyroxenite; Wh, wehrlite. All co-ordinates are in UTM Zone 9N, NAD 83.

posed against pyrite-bearing graphitic phyllite on its northern and eastern margins, whereas on its southern boundary it is in intrusive contact with metavolcanic and metasedimentary rocks (Scheel, 2007; Jackson-Brown, 2017; Nixon et al., 2020).

The Turnagain complex has been subdivided into four zones, with each zone representing a separate intrusive body defined by sharp intrusive contacts (Figure 1). Zone 1 is a body in the north-northwestern sector of the complex, composed primarily of wehrlite (Wh) and olivine-clinopyroxenite (Ol-Cpxn) and minor dunite (Du). Zone 2, which hosts the deposit, comprises dunite and wehrlite, with minor olivine-clinopyroxenite (Ol-Cpxn). Hornblendite (Hb) occurs as rare crosscutting dikes. Zone 3 is a small diorite (Di) lens that occurs in the centre of the complex and intrudes part of zone 2. Finally, zone 4 comprises a body of clinopyroxenite and hornblendite, with minor wehrlite that intruded zone 3 to the north and zone 2 to the east. All the intrusive rocks have undergone varying degrees of alteration (Nixon et al., 2020). Enclaves of pyrite-

bearing graphitic phyllite and metavolcanic rock occur within zones 1, 2 and 4.

The nickel-sulphide deposit, the Horsetrail-Northwest zone, occurs in the southern part of the zone 2 intrusive body (Figure 1), which, as mentioned above, consists dominantly of dunite and wehrlite. However, a feature that distinguishes the Horsetrail-Northwest zone from other parts of zone 2 is that it contains numerous enclaves of pyrite-rich graphitic phyllite. Moreover, it is evident from examination of drillcore that the sulphide content of the dunite and wehrlite is markedly higher proximal to these enclaves. Alteration, mainly serpentinization of the olivine, varies from incipient to intense. Pyrrhotite ( $Fe_{1-x}S$  [ $x = 0-0.2$ ]) is the main sulphide mineral and has a disseminated-interstitial to net-textured mode of occurrence. It is accompanied by pentlandite ( $[Ni, Fe]_9S_8$ ), trace proportions of chalcopyrite ( $CuFeS_2$ ) and the secondary sulphides, heazlewoodite ( $Ni_3S_2$ ) and millerite ( $NiS$ ). The sulphides typically make up 0.5 to 1 wt. % of the rock, but lenses (<20 cm in length) of net-textured to semi-massive sulphides containing up to 30 wt. % sulphide occur locally.

## Methodology

Drillcore samples ( $n = 140$ ) representative of the altered and unaltered silicate rocks of the Horsetrail-Northwest zone and their sulphide ores were collected for petrographic, mineral, chemical and bulk-rock analyses. A subset of ten samples was selected for preliminary petrographic examination and analysis. The petrographic analysis was conducted at the Earth and Planetary Sciences Department of McGill University on polished thin sections of these samples using an Olympus BX51-P polarizing microscope and a Hitachi High-Tech Canada, Inc. SU5000 field-emission scanning electron microscope, equipped with an X-Max<sup>N</sup> 80 silicon drift detector from Oxford Instruments plc. This ensured reliable identification of the minerals and accurate determination of the textural relationships among them.

A set of 110 samples was analyzed by SGS Minerals Services (Burnaby, BC) and a set of 30 samples was analyzed by Activation Laboratories Ltd. (Ancaster, Ontario) for their bulk-rock chemical composition using lithium borate fusion for the major and trace elements, sodium peroxide fusion for their trace elements (SGS Minerals Services) and infrared combustion for total sulphur. The loss-on-ignition (LOI) was also determined.

As many of the samples had undergone moderate to intense alteration (mainly serpentinization), the whole-rock data were used to help distinguish the primary igneous rock types. The MgO concentration in the silicate fraction (normalized to anhydrous MgO, CaO and SiO<sub>2</sub>, and corrected for Fe in sulphide, assuming that all the sulphide was present as pyrrhotite) was used for this purpose. Samples containing >53 wt. % MgO were classified as dunite, samples containing between 34 and 53 wt. % MgO were classified as wehrlite, and samples containing between 19 and 34 wt. % MgO were classified as olivine-clinopyroxenite. These groupings were calculated assuming end-member compositions of rock types and minerals dunite (100–90 vol. % forsterite and 0–10 vol. % diopside modal abundance), wehrlite (90–40 vol. % forsterite and 10–60 vol. % diopside modal abundance) and olivine-clinopyroxenite (40–10 vol. % forsterite and 60–90 vol. % diopside modal abundance).

## Results

### Primary Silicate Minerals and Their Textures

The Horsetrail-Northwest rocks are composed primarily of olivine and clinopyroxene. The olivine, which displays an obvious cumulate texture, occurs as euhedral to anhedral crystals and is typically equigranular (1–3 mm), although olivine crystals up to 15 mm in diameter may be observed locally. In many samples, the olivine crystals exhibit kink banding that appears as undulatory extinction; these crystals

commonly exhibit two angles of parting (at 90°) that gives the appearance of cleavage. The olivine exhibits two types of fractures, specifically random fractures within crystals and fractures that crosscut several crystals.

The clinopyroxene occurs interstitially to olivine and, locally, as cumulates. In rare cases, the interstitial clinopyroxene is oikocrystic, with numerous inclusions of olivine and chromite (<15 mm). Cumulate clinopyroxene occurs as 1–3 mm subhedral crystals and exhibits a moderate to strong prismatic cleavage. Locally, there are thin (2–5 mm) layers of interlocking clinopyroxene crystals.

Chromite is an important accessory mineral and occurs as small (<1 mm) subhedral to euhedral crystals that may be isolated or form clusters interstitial to cumulate clinopyroxene. Locally, chromite occurs as inclusions in olivine and clinopyroxene or as thin chromite schlieren (observed in drillcore). The chromite crystals are commonly rimmed by a second chromite phase, distinguished by its lighter colour in reflected light.

### Sulphide Minerals and Their Textures

The sulphide mineralization in the Horsetrail-Northwest zone is generally disseminated or net textured, but locally replaced olivine. The principal sulphide minerals are pyrrhotite and pentlandite, with pentlandite being the main nickel-ore mineral; chalcopyrite is present in trace proportions.

Pyrrhotite occurs as disseminated aggregates of subhedral to euhedral crystals (typically 50 to 500 µm), with or without pentlandite. As the sulphide content and the interconnectivity of sulphides in the interstitial space increase, the pyrrhotite becomes net textured. Locally, pyrrhotite contains exsolution lamellae of pentlandite (Figure 2a) and may occur as inclusions in olivine, clinopyroxene and chromite. These inclusions are commonly composed of a single pyrrhotite crystal ± pentlandite.

Pentlandite occurs in both the disseminated-interstitial and net-textured pyrrhotite aggregates and has two main modes of occurrence, namely as the exsolution lamellae mentioned above and as discrete crystals or clusters of crystals that occur within pyrrhotite aggregates or in isolation (Figure 2a–c). Both the discrete crystals and those in the pentlandite aggregates are euhedral to subhedral and range in diameter from <20 to 150 µm; the pentlandite aggregates range in diameter from <100 to >1500 µm. Locally, pentlandite fills the space at the triple junctions of cumulate olivine crystals (Figure 2b). Where pentlandite occurs in isolation from pyrrhotite, it is the only sulphide mineral present, whereas, if it occurs with pyrrhotite, the ratio of pyrrhotite to pentlandite ranges from approximately 90:10 to approximately 10:90. Locally, pentlandite may occur as

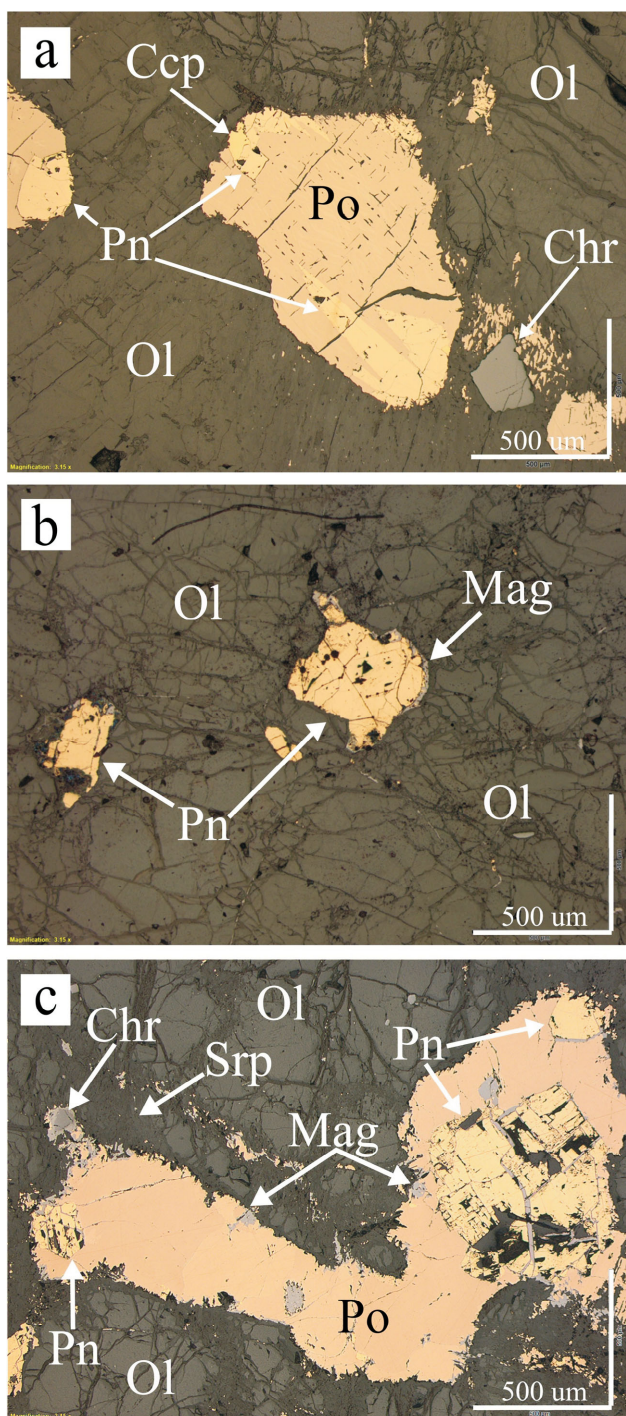


**Figure 2.** Photomicrographs of magmatic sulphide textures of samples from the Turnagain deposit taken under reflected light: **a**) pyrrhotite (Po) with crystallographically controlled exsolved pentlandite (Pn) and local chalcopyrite (Ccp) interstitial to cumulate olivine (Ol) and chromite (Chr), as well as traces of serpentine along the fractures (note the serpentine intergrowths at the edges of the sulphide aggregate, which are suggestive of partial dissolution and mobilization of sulphide and replacement by serpentine); **b**) pentlandite interstitial to olivine, with traces of serpentine along the fractures and the pentlandite showing evidence of minor replacement by magnetite along its edges; **c**) pyrrhotite, blocky pentlandite interstitial to olivine and chromite, with minor serpentinization along fractures and the pyrrhotite showing evidence of minor replacement by magnetite.

both exsolution lamellae and discrete crystals in the same sulphide mass.

### Alteration

Serpentinization has affected olivine to varying degrees in all parts of the Horsetrail-Northwest zone and, where it was intense, left no relicts of this mineral (Figure 3a). Thus, some dunite samples now consist almost entirely of serpentine. This alteration proceeded primarily along fractures and grain boundaries. In weakly altered rocks, the serpentine typically grew perpendicular to the olivine crystal boundaries, whereas in more strongly serpentinized samples, serpentine forms pseudomorphs of olivine, in some cases outlined by thin mantles of magnetite. Magnetite produced during the serpentinization of olivine also occurs as disseminated anhedral grains. Rarely, alteration of the olivine led to the crystallization of brucite. In contrast to olivine, the clinopyroxene altered to tremolite and locally to serpentine minerals.

The main effect of alteration on the sulphide minerals was the replacement of pyrrhotite by magnetite (Figure 3b). Sulphide alteration is also evident from the occurrence of heazlewoodite and millerite, which are inferred to be breakdown products of pentlandite. In one sample, heazlewoodite was observed to have replaced pentlandite in contact with olivine that had been altered to brucite and serpentine group minerals. Finally, olivine was altered locally to serpentine group minerals and pyrrhotite, with rare pentlandite (Figure 3c, d).

### Bulk-Rock Geochemistry

The bulk-rock geochemistry results for silicate rocks ( $n = 140$ ) in the Horsetrail-Northwest zone are summarized in Table 1. For all rock types, the CaO content increases as MgO decreases, ranging from 0.01 to 1 wt. % in dunites (>53 wt. % MgO;  $n = 61$ ), 0.07 to 12 wt. % in wehrlites (34 and 53 wt. % MgO) and 7 to 22 wt. % in olivine-clinopyroxenites (19–34 wt. % MgO; Figure 4a). Sulphur concentrations show no relationship with MgO content or rock type, ranging from 0.02 to 8 wt. % in dunites, 0.06 to 8 wt. % in wehrlites and 0.15 to 10 wt. % (with one outlier at 24 wt. %) in olivine-clinopyroxenites (Figure 4b). Nickel concentrations, on the other hand, increase with increasing MgO content, and range from 0.02 to 0.3 wt. % (with an outlier at 1.2 wt. %) in olivine-clinopyroxenites, 0.01 to 1.2 wt. % in wehrlites, and 0.1 to 1 wt. % in dunites (Figure 4c). Thus, nickel-to-sulphur ratios are weakly correlated with MgO, displaying ranges from <0.01 to 1.2 ( $R = 0.27$ ) for olivine-clinopyroxenites, 0.04 to 2.5 ( $R = 0.32$ ) for wehrlites and 0.05 to 14.2 ( $R = 0.32$ ) for dunites (Figure 4d). Loss-on-ignition (LOI) appears to be unrelated to rock chemistry, ranging from 2 to 17 wt. % in dunites, 1 to 23 wt. % in wehrlites and 2 to 10 wt. % in olivine-clinopyroxenites (Table 1).

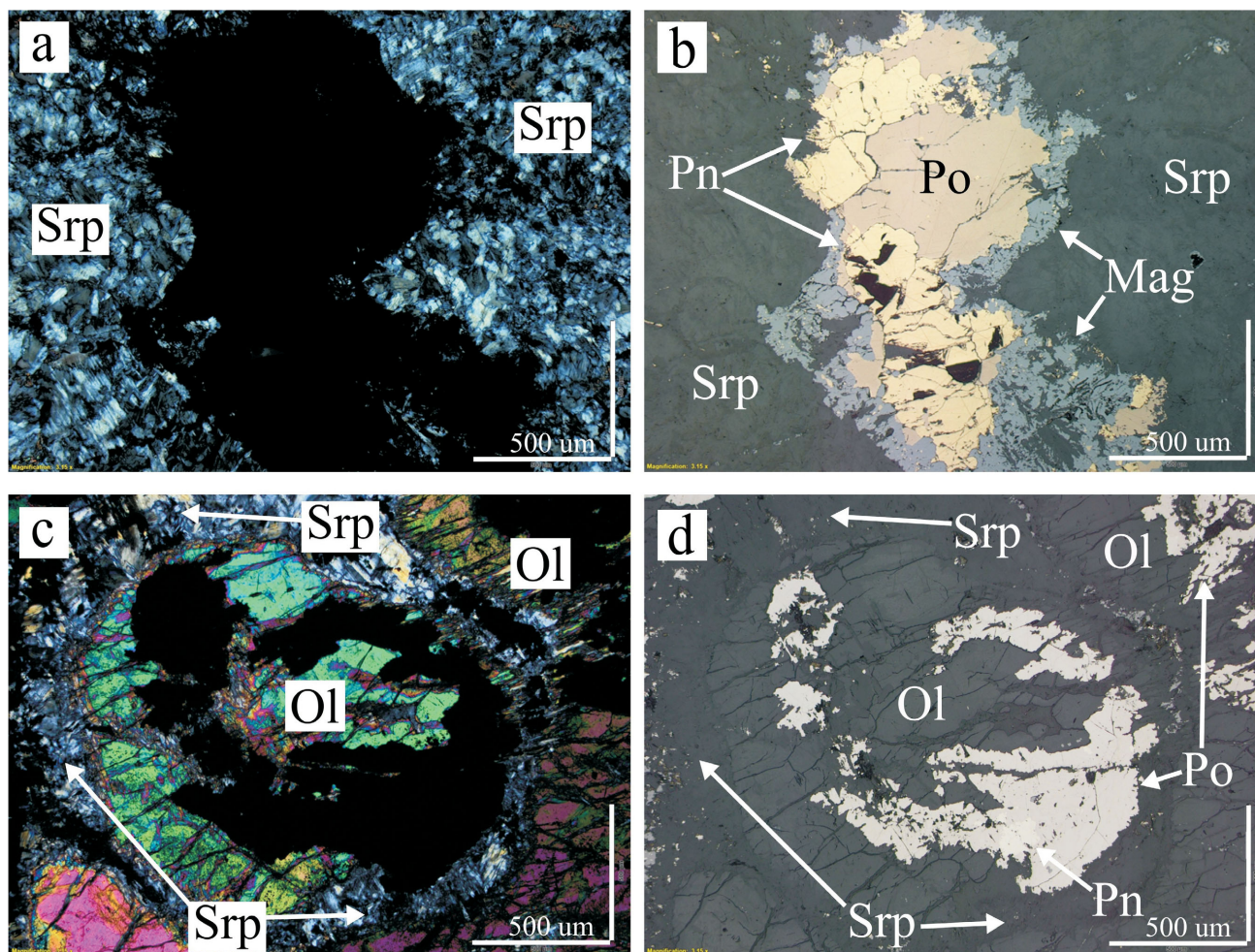


**Figure 3.** Photomicrographs of silicate and sulphide alteration textures of samples from the Turnagain deposit: **a)** image in cross-polarized light of serpentine (Srp) that has completely replaced olivine; **b)** same image as (a) in reflected light showing magnetite (Mag) that has partially replaced an aggregate of pyrrhotite (Po), pentlandite (Pn); **c)** image in cross-polarized light of olivine (Ol) partially pseudomorphed by serpentine; **d)** same image as (c) in reflected light showing olivine partially pseudomorphed by pyrrhotite and pentlandite.

**Table 1.** Summary statistics for bulk-rock geochemical analysis of samples from the Turnagain deposit. Abbreviation: LOI, loss-on-ignition.

	MgO <sup>1</sup> (wt. %)	CaO (wt. %)	S (wt. %)	Ni (wt. %)	Ni vs S	LOI (wt. %)
<b>Dunite (n = 61)</b>						
Minimum	53	0.01	0.02	0.1	0.05	2
Maximum	56	1	8	1	14.2	17
Mean	54.3	0.3	1.6	0.3	1.6	5.4
Median	54.3	0.2	0.6	0.3	0.4	4.9
<b>Wehrlite (n = 66)</b>						
Minimum	35	0.07	0.06	0.01	0.04	1
Maximum	53	12	8	1.2	2.5	23
Mean	47.2	3.2	1.6	0.3	0.5	7.3
Median	49.1	2.3	1.0	0.2	0.2	5.8
<b>Olivine-clinopyroxenite (n = 13)</b>						
Minimum	21	7	0.15	0.02	0.01	2
Maximum	33	22	24	1.2	1.2	10
Mean	28.7	14.0	4.7	0.2	0.2	5.8
Median	30.1	14.5	1.5	0.1	0.03	5.2

<sup>1</sup>Minimum and maximum values do not refer to the limits used in grouping the three rock types (see 'Methodology') but the actual values of the samples analyzed.

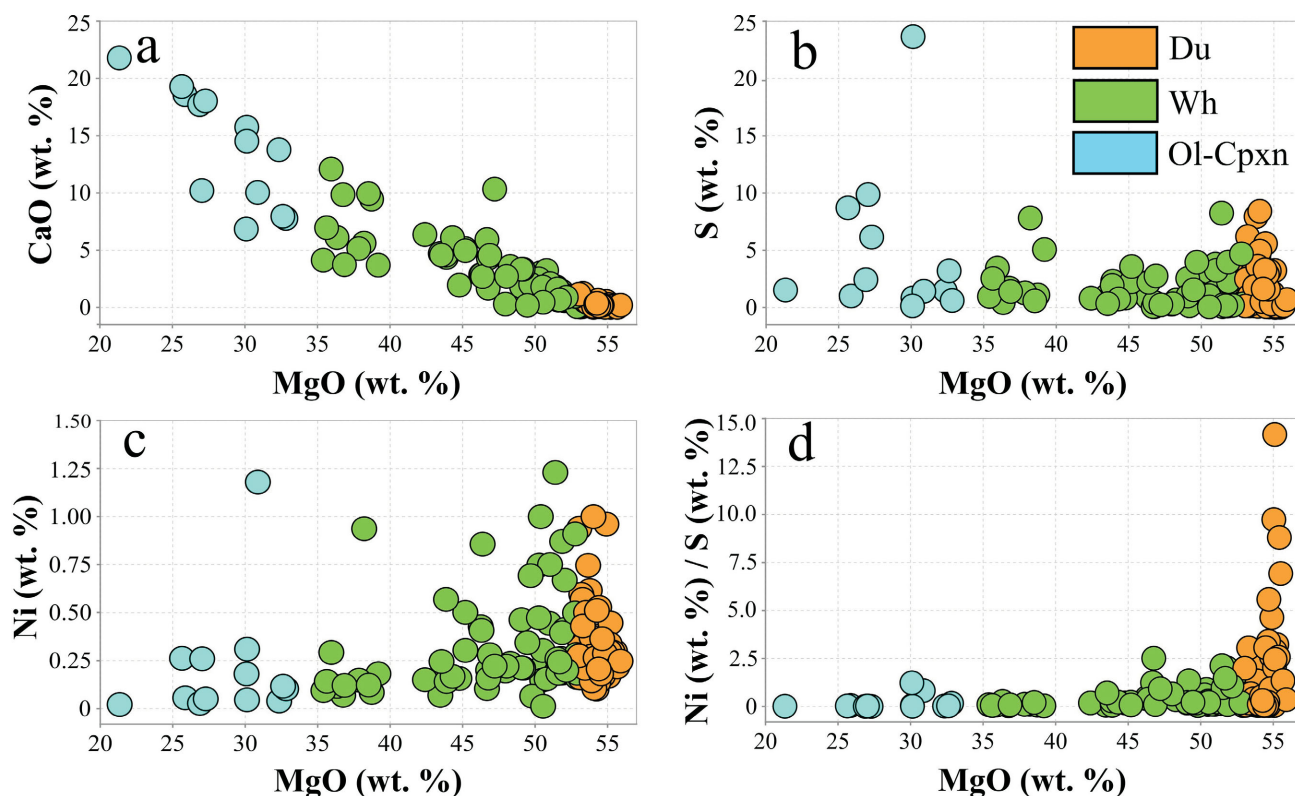


**Figure 4.** Binary plots of bulk-rock compositions of samples from the Turnagain deposit coloured according to rock type: **a)** CaO content versus MgO content; **b)** S content versus MgO content; **c)** Ni content versus MgO content; **d)** Ni to S ratio versus MgO content. The values of MgO and CaO are shown normalized to anhydrous values for the silicate fraction corrected for the Fe content of the sulphide fraction.

## Discussion

The Turnagain complex shares similarities with other Alaskan-type complexes with respect to mineralogy and the zonal distribution of the main intrusive rock types. However, the Turnagain complex notably contains a much greater volume of dunite and wehrlite which, coincidentally, host a potentially economic nickel-sulphide orebody.

Petrographic observations from this study indicate that the ultramafic rocks in the Horsetrail-Northwest zone consist of cumulate olivine and interstitial clinopyroxene, accompanied by minor cumulate clinopyroxene and cumulate chromite. Varying modal percentages of olivine and clinopyroxene, reflected in variations in MgO and CaO contents, describe a range of rock types from dunite to olivine clinopyroxenite (Figure 4a). The textural relationships indicate that olivine and chromite crystallized first, followed by interstitial clinopyroxene and, finally, cumulate clinopyroxene.

## Magmatic Sulphide

The presence of appreciable proportions of pyrrhotite and pentlandite interstitial to the cumulate olivine is consistent with magmatic sulphide formation. Pyrrhotite is interpreted as a product of the crystallization of sulphide liquid to monosulphide solid solution (MSS). The origin of the

pentlandite is less clear; lamellae of pentlandite in pyrrhotite indicate that at least some of the pentlandite exsolved from MSS (Figure 2a). Based on phase relations in the system Fe-Ni-S, this likely occurred at a temperature of approximately 610 °C (not corrected for pressure; Kullerud, 1963). However, the occurrence of large blocky crystals within pyrrhotite, and particularly the occurrence of isolated crystals of pentlandite, require another explanation (Figure 2b, c). The results of this study lead the authors to propose that, as shown experimentally by Sugaki and Kitakaze (1998) and Kitakaze et al. (2016), this pentlandite was the product of a peritectic reaction, in which the sulphide liquid reacted with earlier formed MSS to crystallize pentlandite (Figure 5). According to Sugaki and Kitakaze (1998) and Kitakaze et al. (2016), this would likely have occurred at a temperature in the range of 865 to 746 °C (not corrected for pressure). The occurrence of much of the pentlandite as inclusions within pyrrhotite aggregates implies that the peritectic reaction did not go to completion and that MSS continued to crystallize, eventually exsolving pentlandite at lower temperature.

In most cases the magmas forming these complexes are undersaturated in sulphide and do not contain significant nickel-sulphide mineralization. This is because sulphide solubility increases with decreasing pressure and because the magmas are oxidized, which further increases this solu-

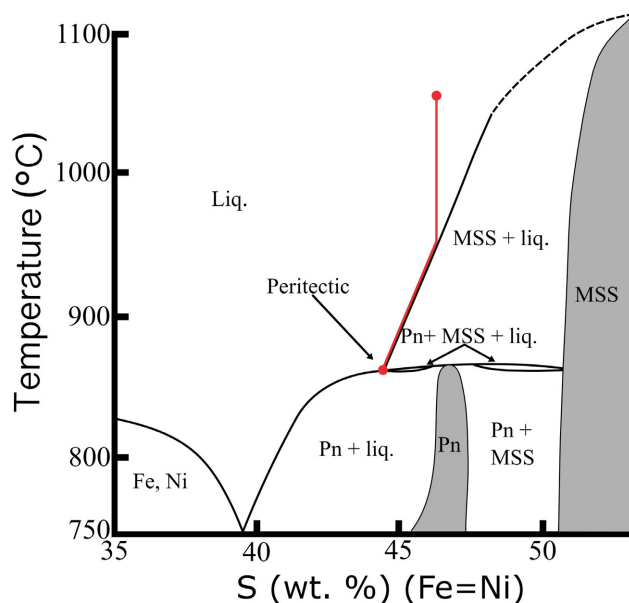
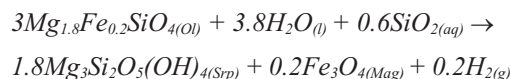


**Figure 5.** A binary diagram showing phase relationships (at Fe = Ni) in the Fe-Ni-S system from 750 to 1100 °C (modified from Kitakaze et al., 2016). The red line shows a possible crystallization path for a sulphide liquid (liq.) that initially crystallized a monosulphide solid solution (MSS) and then evolved to a peritectic point, where it reacted with the MSS to crystallize pentlandite (Pn). This continued until the consumption of the liquid, leaving behind a mixture of MSS and pentlandite.

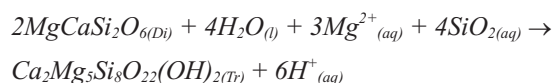
bility (Mavrogenes and O'Neill, 1999; Jugo, 2009). Therefore, an external source of sulphur at or near the site of emplacement of the magmas is required to enable saturation of the magma with sulphide. At the Turnagain deposit, this source could have been the pyrite-bearing graphitic phyllite enclaves within the Horsetrail-Northwest zone. Furthermore, the high oxygen fugacity of the magma may have promoted strong dissolution of the pyrite and the subsequent reduction of the magma by graphite could have led to its supersaturation in sulphide and the exsolution of a sulphide liquid, into which nickel partitioned preferentially (Naldrett, 2004).

### Hydrothermal Alteration

The silicate minerals of the Turnagain complex were variably altered by hydrothermal fluids. Thus, olivine (Ol) was replaced by serpentine group minerals (Srp) and magnetite (Mag) according to the reaction:

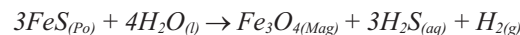


and clinopyroxene (as diopside [Di]) was altered to tremolite (Tr) according to the reaction:

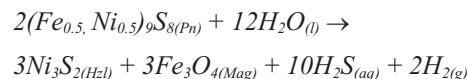


As the olivine contains significant nickel (300 to 2300 ppm), serpentinization would have released much of this nickel making it available to secondary nickel sulphides, such as heazlewoodite and millerite.

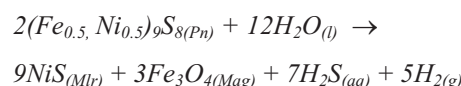
Hydrothermal alteration also affected the sulphide minerals with the replacement of pyrrhotite (Po) by magnetite according to the reaction:



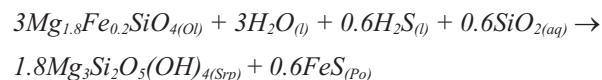
and the alteration of pentlandite (Pn) to heazlewoodite (Hzl) and millerite (Mlr) via the reactions:



and



These reactions both mobilized sulphur as  $H_2S$ , leading to the replacement of the iron component in olivine (containing between 10 to 15 mol. % of fayalite; Scheel, 2007) by pyrrhotite, and the magnesium-silicate component by a serpentine-group mineral according to the reaction:



The occurrence of pentlandite in the pyrrhotite of some samples (Figure 3d) could reflect the reaction of the  $H_2S$  with the nickel component of the olivine (Filippidis, 1982).

### Variability in Ni:S Ratios

A feature of the Horsetrail-Northwest zone is the extreme variability of the Ni:S ratios of the rocks (Figure 4d), which presents a major challenge for the economic recovery of the nickel. In principle, the nickel should be concentrated mainly in pentlandite and pyrrhotite, leading to a strong positive correlation between Ni and S, but because of the relative low proportion of sulphide relative to that of other magmatic sulphide deposits, the effect on the Ni:S ratio of the proportion of nickel hosted by olivine is considerable. Further complicating the issue is the fact that variable degrees of serpentinization led to variable proportions of this nickel being released to form secondary nickel-sulphide minerals. Finally, whereas in most nickel deposits the pentlandite exsolved from MSS, thus ensuring a close correlation between the proportion of pyrrhotite and the proportion of nickel, at the Turnagain deposit much of the pentlandite appears to have crystallized as a peritectic mineral, independently of pyrrhotite, leading to highly variable proportions of the two minerals. The relative importance of these processes and their effects on the Ni:S ratios are the subject of ongoing investigation.

## Future Work

Future research to understand these processes will include analyses of the major- and trace-element contents of rock-forming minerals using an electron microprobe and laser-ablation inductively coupled–mass spectrometry. The data collected will be used to evaluate the spatial and temporal variation in the compositions of the different minerals and, in the case of pentlandite, to determine whether there was a peritectic incorporation of palladium and other trace elements (Mansur et al., 2019). Sulphur isotope compositions will be analyzed using laser-ablation multiple-collector inductively coupled–mass spectrometry to evaluate the sulphur source and determine physicochemical parameters such as oxygen fugacity. Ultraviolet femtosecond laser-ablation multiple-collector inductively coupled–mass spectrometry will be used to analyze the in situ iron and nickel isotope compositions of the rock-forming minerals to evaluate the source of iron and nickel, and the isotopic fractionation of these metals between different minerals during the magmatic and hydrothermal processes (e.g., serpentinization). The resulting data will also be used to determine the temperature and redox conditions during magmatism and serpentinization (Rouxel et al., 2003; Scott et al., 2017).

## Conclusions

Magmatic pyrrhotite and pentlandite mineralization in the Horsetrail-Northwest zone of the Turnagain ultramafic complex occurs as disseminated-interstitial to net-textured sulphide in olivine-rich ultramafic rocks that formed through the assimilation of pyrite-bearing graphitic phyllite enclaves and the subsequent supersaturation of the melt with respect to sulphide. Pentlandite is the main nickel-ore mineral in the deposit and is present largely as a blocky variety that is either enclosed in pyrrhotite or forms isolated crystals. Some pentlandite occurs as lamellae in pyrrhotite. The blocky variety is interpreted as the product of a peritectic reaction between MSS and a sulphide liquid, whereas the lamellae are thought to have exsolved from MSS.

Hydrothermal alteration affected the distribution of nickel significantly by releasing it from olivine during serpentinization to form secondary minerals such as heazlewoodite and millerite, and altering pentlandite to these minerals. This alteration also led to the replacement of pyrrhotite by magnetite, which likely released additional nickel to secondary minerals.

The combination of magmatic processes and the mobilization of nickel and sulphur during hydrothermal alteration were likely responsible for the variable and unpredictable Ni:S ratios. A better understanding of these processes will help considerably in developing a comprehensive genetic model for the mineralization.

## Acknowledgments

Major funding for this project is being provided by the Natural Sciences and Engineering Research Council of Canada (NSERC) and Giga Metals Corporation. The lead author is grateful to Geoscience BC for its financial support through the Geoscience BC Scholarship program. Technical and logistical support provided by Giga Metals Corporation are gratefully acknowledged. The authors would also like to thank K. Rempel for insightful and constructive comments and suggestions during the review process.

## References

- Clark, T. (1980): Petrology of the Turnagain ultramafic complex, northwestern British Columbia; *Canadian Journal of Earth Sciences*, v. 17, no. 6, p. 744–757, URL <<https://doi.org/10.1139/e80-071>>.
- Filippidis, A. (1982): Experimental study of the serpentinization of Mg-Fe-Ni olivine in the presence of sulfur; *The Canadian Mineralogist*, v. 20, no. 4, p. 567–574.
- Giga Metals Corporation (2023): Mineral resource statement; Giga Metals Corporation, September 22, 2023, URL <[https://gigametals.com/site/assets/files/5329/giga\\_metals\\_resource\\_reserve\\_statement\\_september\\_2023.pdf](https://gigametals.com/site/assets/files/5329/giga_metals_resource_reserve_statement_september_2023.pdf)> [October 2023].
- Himmelberg, G.R. and Loney, R.A. (1995): Characteristics and petrogenesis of Alaskan-type ultramafic-mafic intrusions, southeastern Alaska; U.S. Geological Survey Professional Paper 1564, 47 p.
- Irvine, T.N. (1959): The ultramafic complex and related rocks of Duke Island, southeastern Alaska; Ph.D. thesis, California Institute of Technology, 320 p., URL <<https://doi.org/10.7907/KMR7-CC87>>.
- Irvine, T.N. (1963): Origin of the ultramafic complex at Duke Island, southeastern Alaska; *Mineralogical Society of America, Special Paper*, no. 1, p. 36–45.
- Irvine, T.N. (1974): Petrology of the Duke Island ultramafic complex southeastern Alaska; *Geological Society of America, Bulletin, Memoir* 138, 240 p., URL <<https://doi.org/10.1130/MEM138>>.
- Jackson-Brown, S. (2017): Origin of Cu-PGE-rich sulfide mineralization in the DJ/DB zone of the Turnagain Alaskan-type intrusion, British Columbia; M.Sc. thesis, The University of British Columbia, 272 p., URL <<https://doi.org/10.14288/1.0355222>>.
- Jugo, P.J. (2009): Sulfur content at sulfide saturation in oxidized magmas; *Geology*, v. 37, no. 5, p. 415–418.
- Kitakaze, A., Machida, T. and Komatsu, R. (2016): Phase relations in the Fe–Ni–S system from 875 to 650 °C; *The Canadian Mineralogist*, v. 54, no. 5, p. 1175–1186, URL <<https://doi.org/10.3749/canmin.1500087>>.
- Kullerud, G. (1963): Thermal stability of pentlandite; *The Canadian Mineralogist*, v. 7, p. 353–366.
- Mansur, E.T., Barnes, S.J. and Duran, C.J. (2019): Textural and compositional evidence for the formation of pentlandite via peritectic reaction: implications for the distribution of highly siderophile elements; *Geology*, v. 47, no. 4, p. 351–354.
- Mavrogenes, J.A. and O'Neill, H.S.C. (1999): The relative effects of pressure, temperature and oxygen fugacity on the solubil-

- ity of sulfide in mafic magmas; *Geochimica et Cosmochimica Acta*, v. 63, no. 7–8, p. 1173–1180.
- Naldrett, A.J. (2004): *Magmatic Sulfide Deposits—Geology, Geochemistry and Exploration*; Springer-Verlag Berlin, Heidelberg, Germany, 728 p., URL <<https://doi.org/10.1007/978-3-662-08444-1>>.
- Naldrett, A.J. and Cabri, L.J. (1976): Ultramafic and related mafic rocks; their classification and genesis with special reference to the concentration of nickel sulfides and platinum-group elements; *Economic Geology*, v. 71, no. 7, p. 1131–1158, URL <<https://doi.org/10.2113/gsecongeo.71.7.1131>>.
- Nixon, G.T., Scheel, J.E., Scoates, J.S., Friedman, R.M., Wall, C.J., Gabites, J. and Jackson-Brown, S. (2020): Syn-accretionary multistage assembly of an Early Jurassic Alaskan-type intrusion in the Canadian Cordillera: U-Pb and  $^{40}\text{Ar}/^{39}\text{Ar}$  geochronology of the Turnagain ultramafic-mafic intrusive complex, Yukon-Tanana terrane; *Canadian Journal of Earth Sciences*, v. 57, no. 5, p. 575–600, URL <<https://doi.org/10.1139/cjes-2019-0121>>.
- Rouxel, O., Dobbek, N., Ludden, J. and Fouquet, Y. (2003): Iron isotope fractionation during oceanic crust alteration; *Chemical Geology*, v. 202, no. 1–2, p. 155–182.
- Scheel, J.E. (2007): Age and origin of the Turnagain Alaskan-type intrusion and associated Ni-sulfide mineralization, north-central British Columbia, Canada; M.Sc. thesis, The University of British Columbia, 201 p., URL <<https://doi.org/10.14288/1.0052378>>.
- Scott, S.R., Sims, K.W., Frost, B.R., Kelemen, P.B., Evans, K.A. and Swapp, S.M. (2017): On the hydration of olivine in ultramafic rocks: implications from Fe isotopes in serpentinites; *Geochimica et Cosmochimica Acta*, v. 215, p. 105–121.
- Sugaki, A. and Kitakaze, A. (1998): High form of pentlandite and its thermal stability; *American Mineralogist*, v. 83, no. 1–2, p. 133–140, URL <<https://doi.org/10.2138/am-1998-1-213>>.
- Thakurta, J. (2018): Alaskan-type complexes and their associations with economic mineral deposits; Chapter 9 in *Processes and Ore Deposits of Ultramafic–Mafic Magmas through Space and Time*, Elsevier, Amsterdam, The Netherlands, p. 269–302, URL <<https://doi.org/10.1016/B978-0-12-811159-8.00010-X>>.
- Thakurta, J., Ripley, E.M. and Li, C. (2008): Geochemical constraints on the origin of sulfide mineralization in the Duke Island Complex, southeastern Alaska; *Geochemistry, Geophysics, Geosystems*, v. 9, no. 7, 34 p., URL <<https://doi.org/10.1029/2008GC001982>>.



# Stratigraphic Classification and Geochronology Within the Hazelton Group, Stewart Mining Camp, Northwestern British Columbia (Parts of NTS 104A, B)

**K.M. Powers<sup>1</sup>**, Department of Earth, Ocean and Atmospheric Sciences, The University of British Columbia, Vancouver, British Columbia, [kpowers@eoas.ubc.ca](mailto:kpowers@eoas.ubc.ca)

**K.E.L. Rubingh**, Department of Earth, Ocean and Atmospheric Sciences, The University of British Columbia, Vancouver, British Columbia

**S.L.L. Barker**, Department of Earth, Ocean and Atmospheric Sciences, The University of British Columbia, Vancouver, British Columbia

---

Powers, K.M., Rubingh, K.E.L. and Barker, S.L.L. (2024): Stratigraphic classification and geochronology within the Hazelton Group, Stewart mining camp, northwestern British Columbia (parts of NTS 104A, B); *in* Geoscience BC Summary of Activities 2023, Geoscience BC, Report 2024-01, p. 33–46.

## Introduction

The Stewart mining camp is a prolific historical region within the ‘Golden Triangle’, a mineral district in northwestern British Columbia (BC; Figure 1). Zinc-silver-lead-bearing volcanogenic massive-sulphide (VMS) deposits such as the BA occurrence and the Mountain Boy epithermal silver-copper-gold occurrence (K.M. Powers, K.E.L. Rubingh and S.L.L. Barker, unpublished poster, 2023), both properties owned and operated by MTB Metals Corp., and structurally controlled gold deposits (Scottie Resources Corp.) in the Stewart mining camp, are hosted within the Hazelton Group. The Hazelton Group is a package of volcanic, volcanoclastic and cogenetic sedimentary rocks of Jurassic age, which in regions remains relatively broadly lumped together as packages of undifferentiated volcanic rocks. A large part of the information gap is due to the rugged and remote nature of northwestern BC. Detailed geological descriptions of the volcanic rocks in the camp, as defined by previous researchers, are mafic to felsic intrusions, flows, pyroclastic and volcanoclastic rocks, as well as various clastic sediments ranging from mudstones to limestone, to boulder conglomerates (Marsden and Thorkelson, 1992; Alldrick, 1993; Gordee, 2006; Gagnon et al., 2012; Nelson and Kyba, 2014; Barresi et al., 2015; Nelson et al., 2022). Past work focused on the western portion of the camp, centring on larger past-producing mines such as the Premier mine that produced 56.7 million g Au and 1300 million g Ag; the Granduc mine that produced 190 million kg Cu, 124 million g Ag and 2 million g Au; and the Scottie Gold mine that yielded 3 million g Au (MINFILE 104B 021, BC Geological Survey, 2023b; Alldrick, 1993; Bird et al., 2020). The largest operating of

these is the Premier Gold project, with an indicated resource of 28 million g Au (Bird et al., 2020). Fieldwork in 2023 focused on Hazelton Group stratigraphy, away from previously described regions.

The objective of this study is to refine the Hazelton Group stratigraphy and to place within that stratigraphy the BA Zn-Ag-Pb VMS and Mountain Boy epithermal Ag-Cu-Zn occurrences (Figure 2). Of added interest is the stratigraphic variability between these two deposits, which are hosted in rocks that are broadly recognized as belonging to the Hazelton Group. Five lithostratigraphic sections were selected due to their excellent outcrop exposure along vertical cliff sections that could be studied, from the oldest to the youngest unit, along a 17 km strike that is perpendicular to the dip of the bedding. These sections were mapped at the 1:1000 scale (Figure 2), with the goal of collecting representative rock samples for geochemical and geochronological analyses from a broad section of the stratigraphic column. The stratigraphic sections were completed to help better define textural and chemical changes through detailed mapping across major contacts in the Hazelton Group. In previous regional mapping, such as the map at 1:50 000 scale of Alldrick (1994) or the maps at 1:250 000 scale and 1:100 000 scale of Grove (1973), these rocks were recognized as rocks of the Hazelton Group or were designated ‘undivided volcanic rocks’. Refinement within the stratigraphy will also allow for comparison of the host formation of the BA Zn-Ag-Pb VMS occurrence to that of the Eskay Creek Au-Ag-Zn-Cu-Pb VMS occurrence, which has been extensively studied and dated within the Iskut River formation, and is regionally equivalent to the Quock Formation of the upper Hazelton Group.

This study is part of a larger project focusing on improving the understanding of the Hazelton Group in the Golden Triangle through lithostratigraphy, geochemistry and geochronology to refine the relationship between volcanic stratigraphy and mineralization within the region. Three

---

<sup>1</sup>The lead author is a 2023 Geoscience BC Scholarship recipient.

This publication is also available, free of charge, as colour digital files in Adobe Acrobat® PDF format from the Geoscience BC website: <https://geosciencebc.com/updates/summary-of-activities/>.

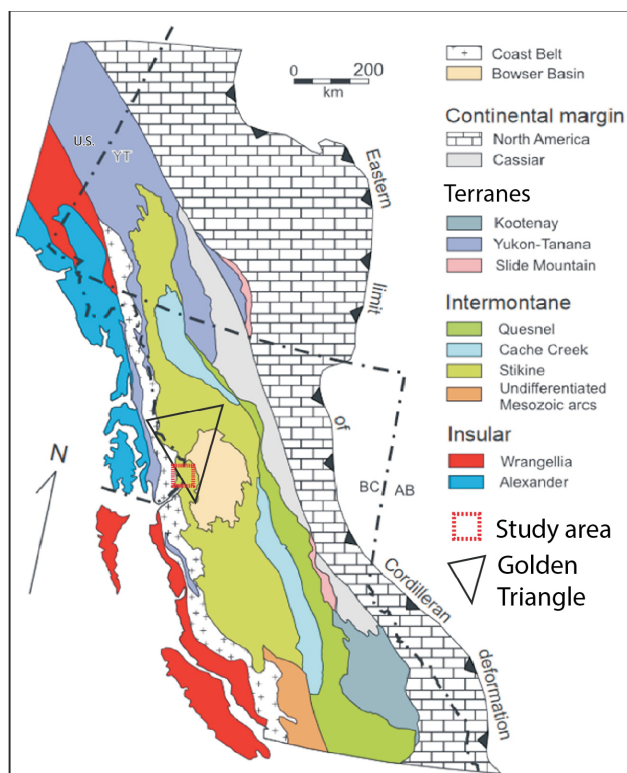


**Figure 1.** Major terranes of British Columbia and Yukon (modified from Gagnon et al., 2012). The red box indicates the location of the study area shown in Figure 2.

measured sections and the preliminary interpretations of the observed rock units, as well as their relationships to each other and to published literature, are presented in this paper.

## Background

### Regional Geology

The Stikine terrane of northwestern North America (Figure 1) makes up a portion of the Intermontane terranes that formed during the accretion of an outboard island arc onto the western margin of Laurentia in the Early to Late Jurassic (Anderson and Thorkelson, 1990). Stikine is one of three Intermontane terranes of western Laurentia, the others being the Quesnel and Cache Creek terranes (Gagnon et al., 2012). Stikinia has a tapered shape, with a width of less than 100 km at its northern boundary in the Yukon as well as at its southern boundary, just north of the border between Canada and the United States. Its maximum width is over 500 km in northern BC at the location of the Golden Triangle (Figure 1; Marsden and Thorkelson, 1992; Alldrick, 1993; Gordee, 2006; Gagnon et al., 2012; Nelson and Kyba, 2014; Barresi et al., 2015; Nelson et al., 2022). Three volcanic successions composed of volcanic rocks, volcanoclastic rocks and clastic sedimentary rocks make up Stikinia, with each succession separated by an unconformity. The oldest consists of Devonian to Permian arc-related vol-

canic and plutonic units and accompanying sedimentary strata, which make up the Stikine assemblage and Asitka Group. The next succession comprises arc-related magmatic units and accompanying sedimentary rocks of the Middle to Late Triassic Stuhini and Takla groups. The last succession, capping the Stikine terrane, is the Jurassic Hazelton Group (Alldrick, 1993; Nelson and Kyba, 2014). In the Stewart mining camp and further north (Figure 2), economically important mineral deposits, such as Scottie Gold and Premier, are hosted in the volcanic strata of the lower Hazelton Group, whereas deposits such as Eskay Creek are hosted within the volcano-sedimentary strata of the upper Hazelton Group (Mortensen et al., 2004).

### Hazelton Group Stratigraphy

The following section is a description of the Hazelton Group stratigraphy (Figure 3), from the oldest to the youngest unit, as defined by Marsden and Thorkelson (1992), Alldrick (1993), Gordee (2006), Gagnon et al. (2012), Nelson and Kyba (2014), Barresi et al. (2015), Nelson et al. (2018), Brueckner et al. (2021) and Nelson et al. (2022).

#### Jack Formation 205.5–201 Ma

The Jack Formation was first described as a ‘transitional unit’ (Anderson and Thorkelson, 1990) and is a largely sedimentary unit. This formation unconformably to disconformably overlies arc volcanism of the earlier Triassic Stuhini Group (Henderson et al., 1992). The Jack Formation, was originally defined as a purely siliciclastic unit composed of cobble to boulder conglomerates (Anderson and Thorkelson, 1990). More recently, Nelson and Kyba (2014) described quartz-bearing arkosic sandstone, granulestone, and thinly bedded siltstone and mudstone, along with andesitic volcanoclastic rocks, in direct gradational contact with identical siliciclastic strata above and below in sections in the Bruce glacier and Treaty glacier areas, which lie 110 km to the north of Stewart (Figure 1).

#### Betty Creek Formation 201–181.5 Ma

The lower members (Figure 3) constitute a volcanoclastic sequence of massive to well-bedded ash tuffs, turbidites, dust, lapilli and breccia tuffs, with varying abundances of plagioclase and hornblende. The upper tuffs in this succession, which has been referred to as the Unuk River andesite member, include fragmental units that contain lithic fragments and pumice, as well as crystal fragments. Overlying this package, most prominently within the Stewart mining camp area, are extrusive, locally coarse-grained flows and tuffs of the Premier porphyry intrusions (194 ± 2 Ma), as well as cogenetic intrusive units (Alldrick, 1985, 1993; Anderson and Thorkelson, 1990). These intrusive rocks are both economically and stratigraphically significant as they host the gold-rich Premier mine and are a distinctive marker unit in the region, respectively. (Alldrick, 1989, 1993; Anderson and Thorkelson, 1990; Marsden and Thor-

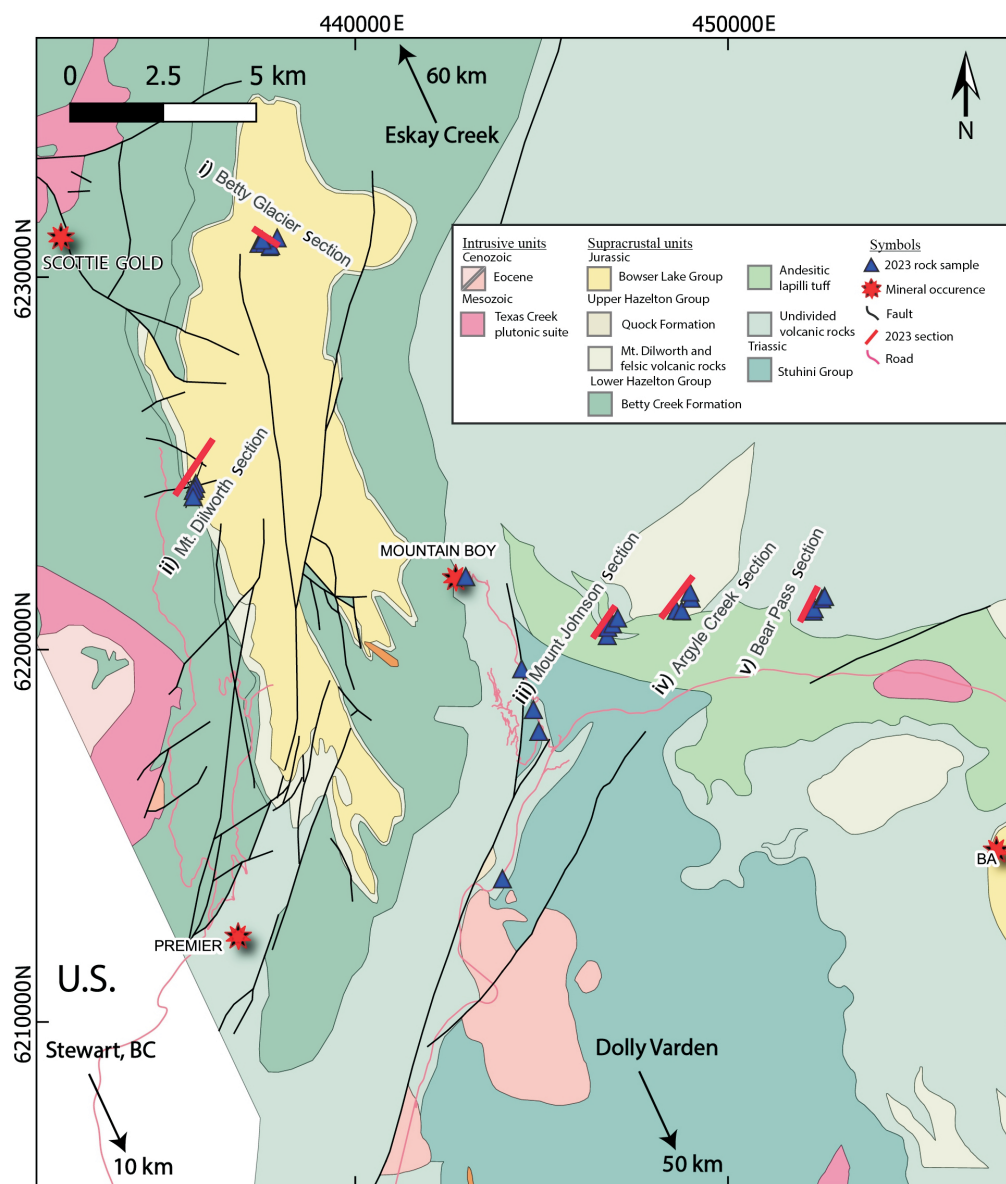


**Figure 2.** Regional geology of the Stewart mining camp study area (modified from BC Geological Survey, 2023a). The five sections studied are: i) Betty Glacier, ii) Mount Dilworth, iii) Mount Johnson and v) Bear Pass (labelled parallel to their length). Additional sample sites located outside of these sections are shown at the Mountain Boy silver prospect, as well as along roads. The distance between the Betty Glacier section and the Bear Pass section is 17 km. All co-ordinates are in UTM Zone 9, NAD 83.

kelson, 1992; Lewis et al., 2001; Gordee, 2006; Gagnon et al., 2012).

The upper members (Figure 3), which are distinguishable from the Unuk River andesite, can be divided into various mafic volcanic flows that may directly overlie the Jack Formation or the Premier porphyry intrusions of the Unuk River andesite. These flows consist of interbedded ‘dust’, lapilli, feldspar crystal tuffs and porphyritic felsic lava flows (Alldrick et al., 1993) overlain by pyroclastic flows consisting of pumice-rich rocks. Interbedded among these flows are volcaniclastic rocks characterized by way-up features such as load casts, ball-and-pillow structures, flame

structures, graded bedding, as well as centimetre-scale growth faults (Anderson and Thorkelson, 1990). Another sedimentary sequence caps the package; this sequence is distinctive due to its variably altered, brightly maroon and green sedimentary rocks that range from mudstone to coarse boulder conglomerate.

#### Mount Dilworth Formation 181.5–177 Ma

The contact with the underlying Betty Creek Formation (Figure 3) varies throughout the Golden Triangle and is either marked by limestone and chert beds or by the stratigraphic position where felsic volcanic lithofacies predominate

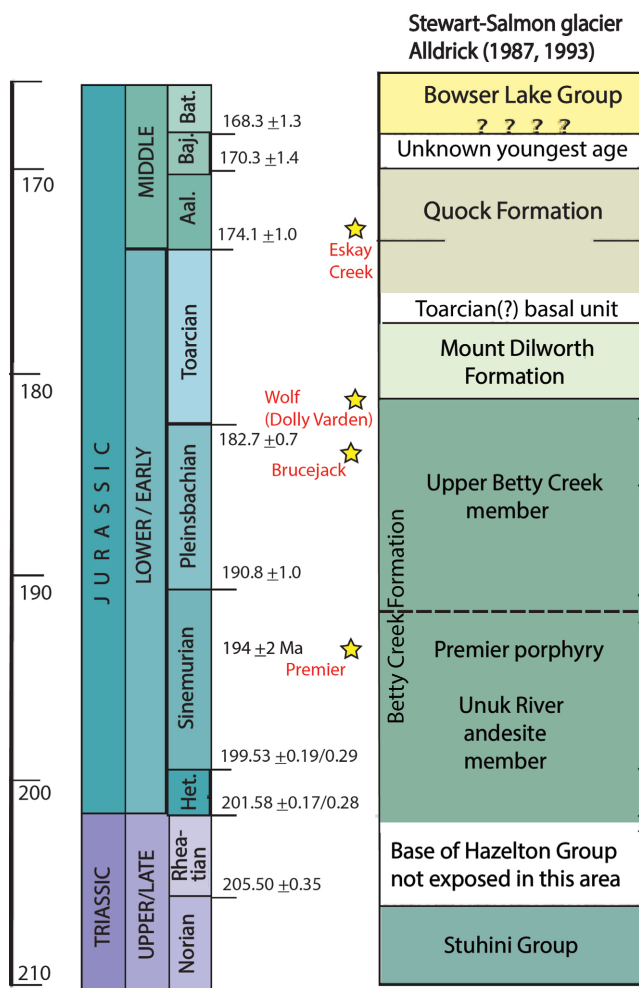


**Figure 3.** Generalized stratigraphy of the lower and upper units of the Hazelton Group in the Stewart mining camp (modified from Nelson et al., 2018 and Brueckner et al., 2021). Yellow stars indicate the U-Pb ages of major deposits in the Stewart camp and further north, such as at Brucejack and Eskay Creek. Premier U-Pb age from Alldrick (1985); Wolf U-Pb age (Dolly Varden) from Hunter and van Straaten (2020). Abbreviations: Aal., Aalenian; Baj., Bajocian; Bath., Bathonian; Het., Hettangian.

over more distal and intermediate compositions of the Betty Creek Formation (Alldrick, 1989, 1993; Anderson and Thorkelson, 1990; Marsden and Thorkelson, 1992; Lewis et al., 2001; Gordee, 2006; Gagnon, 2012). Anderson and Thorkelson (1990) described the variability within the Mount Dilworth Formation as characterized by felsic white, maroon or green flow-layered tuff, tuff breccia and dust tuff. These rock types show varying degrees of pumice welding and texturally range from aphyric to plagioclase-phyric.

### Quock Formation 177–170 Ma

The sedimentary rocks of the Quock Formation conformably to unconformably overlie the Mount Dilworth Formation (Figure 3). The Quock Formation is regionally extensive and consists of basal, limey, belemnite-rich sandstone and carbonate-cemented grit with limestone nodules (An-

derson and Thorkelson, 1990; Marsden and Thorkelson, 1992; Alldrick, 1993). Overlying this are ‘pyjama beds’, described by Tipper and Richards (1976) as thinly bedded siliceous mudstones and tuffs, which are distinctive due to their rhythmic beige and brown bands. In the Eskay mining camp, the Quock Formation is equivalent to the Iskut River formation, which overlies a series of rhyolite flow-dome complexes dated at  $175 \pm 2$  Ma. Here the Quock Formation (Iskut River formation) hosts the prolific Eskay Creek VMS deposit (Gagnon et al., 2012).

## Methodology

During the 2023 field season, detailed volcano-stratigraphic mapping was carried out along five vertical sections of Hazelton Group rocks (Figure 2). These sections were chosen due to their orientation perpendicular to bedding, which allowed mapping of individual lithofacies and lateral facies changes along strike; the sections were also chosen as they cover a large lateral map extent, with 17 km separating the easternmost from the westernmost section. Details on the map were recorded at the 1:1000 scale to effectively record major changes in the depositional environment, lithology and key field relationships between volcanic facies. The sections ranged in vertical thickness from 100 to >375 m.

Along with the mapping of these continuous outcrop sections, samples were strategically collected from key stratigraphic units. Three types of sample were collected during fieldwork: representative rocks, as well as samples for whole-rock geochemical and for geochronological analyses (sample locations shown in Figure 2). Representative samples will be used primarily as polished rock samples or to create petrographic thin sections, if more detailed descriptions of mineralogy are deemed necessary. The analysis results of the outcrop samples collected for whole-rock geochemistry will aid in the correlation of texturally similar rocks observed throughout the study area. The samples for whole-rock analyses were collected only from the visually least altered, most homogeneous and representative portions of the outcrop, thus reducing the risk of potential chemical contamination and increasing the level of confidence in geochemical correlations established within the stratigraphy. Different types of outcrop samples were collected for U-Pb geochronological analysis. The first type was collected from coherent volcanic flows, where the textural and field evidence allowed their classification as such. These samples will help determine the crystallization age of zircons within coherent sections of the Hazelton Group stratigraphy (Figure 3). The second type of U-Pb geochronological sample consists of detrital zircons. The results of the analyses of these samples selected from sandy layers within clastic units at the base of the Quock Formation will aid in confirming both the formation and the erosional period that this unconformity represents. To aid in the correla-

tion of studied sections, other samples for U-Pb detrital zircon radiometric dating were collected from sandy/silty layers of volcanoclastic sediments of the lower and upper Hazelton volcanic pile, which occur throughout the stratigraphy.

## Stratigraphic Sections

Three of the five studied sections shown on Figure 2 are described here in detail. These sections were chosen as representative of the lower through upper Hazelton Group stratigraphy that is present within the Stewart mining camp along a strike of 17 km. The sections are referred to on the map in Figure 2 as ‘Mount Johnson section’ (Figure 4), ‘Bear Pass section’ (Figure 5) and ‘Betty Glacier section’ (Figure 6).

### Mount Johnson Section

The Mount Johnson section (Figure 4) was chosen as the westernmost vertical section within the east-trending Bear River valley. The stratigraphy at this location has a general strike of 300° and dips moderately between 30 and 40°; there are flame structures in the fine sediments that show clear evidence of way-up features, with units identified as being upright.

#### Volcanoclastic and Clastic Sediments

The base of the measured section is dominated by a heterolithic volcanoclastic conglomerate. This unit weathers beige in outcrop and is green to grey on fresh surfaces. Aphanitic, matrix-supported, subangular to subrounded clasts make up 30% of the rock and range from 1 to 5 cm in size. These clasts (Figure 4a) consist of a mixture of light-coloured, pumice-rich felsic units and darker plagioclase-phyric mafic clasts. Interbedded within this massively bedded unit are sequences of coarse sand, one of which was sampled for U-Pb geochronology. The conglomerate unit grades into finely interbedded silt and sandstone. This unit has well-defined bedding and way-up-defining flame structures at the interface between the sand and silt layers.

#### Pumice-Rich Sediments

Conformably overlying the sedimentary package is a gradational transition into interbedded pumice and very coarse-grained sandstone (Figure 4b). Bedding within the darker bands of this package is defined by densely packed, clast-supported, flattened pumice that ranges from 0.1 to 1 cm in size. The lighter bands are beds of very coarse-grained, heterolithic, arkosic arenite sandstone containing clasts consisting of rounded volcanic granules with rare jasper. A geochronological sample was collected from a 10 m thick bed of this very coarse-grained sandstone, whereas a geochemical sample was collected from a pumice-rich bed and a massive section of sandy limestone. Topping this interbedded pumice and sandstone is a thin

unit of monolithic conglomerate comprising pebble-sized mudstone clasts (1–2 cm), which fines upward over 2 m. The upper 25 m of this member marks a distinct increase in the presence of sandy limestone, including a succession 5 m thick locally showing deformation defined by tight folding of the less competent limestone that caps the unit.

#### Pillow Basalts

The lime-rich sediments are disrupted sharply by 50 m of pillowed flows, which include pillow breccias. The best example of these pillowed flows and disaggregated breccias is in Figure 4c, where pillow lobes are draped by the same sand-rich limestone as below. Pillows are vesicle-rich, orbicular in shape and, on average, 30 cm in diameter. At the top of this pillow sequence are reworked pillows that show alignment with bedding supported by a limey mudstone and coarse-grained clastic sandstone. Within this outcrop, the density of pillows varies, with zones of densely stacked pillows interbedded with rubble zones of angular clasts of clastic and volcanic rocks. A pillow 30 cm in size was collected as a sample for whole-rock geochemistry.

#### Crystal-Rich Tuff

Overlaying the pillow rubble is a normally graded, pumice-rich conglomerate. At the base is a thin limestone and volcanoclastic matrix-supported angular boulder conglomerate 2 m thick, with clasts that reach up to 70 cm in size. Figure 4d shows the grading in bedding-aligned pumice that transitions from densely packed 20 cm clasts through to trace 1 cm flattened clasts over a 15 m vertical section. Capping the measured section is a white-weathering unit of crystal tuff that shows massive bedding for the first 15 m, then transitions into fine 1 cm laminations of coarse crystals. The rock consists of 20% plagioclase, 5% amphibole and 5% quartz, with a fine lithic groundmass. This unit is interpreted in field observations as a felsic crystal tuff that appears to continue at least another 50 m upsection to a point at which the mountain flattens out.

### Bear Pass Section

The Bear Pass section is located 5.5 km to the east of, and topographically above, the Mount Johnson section. Measurements in this area indicate bedding striking 265° and dipping 45°. As a result, just as at Mount Johnson, stratigraphy can be followed perpendicularly by walking uphill for a measured vertical section of 375 m. The observed stratigraphy, from bottom to top, is outlined below.

#### Volcanoclastic and Clastic Sediments

The base of this measured section generally constitutes the first half of the observed outcrop. It is primarily composed of interbedded sandstone and conglomerate units of varying thicknesses. The conglomerate consists of angular to subangular, aphanitic, matrix-supported heterolithic clasts (1–5 cm) of red vesicular volcanic rocks (20%), and

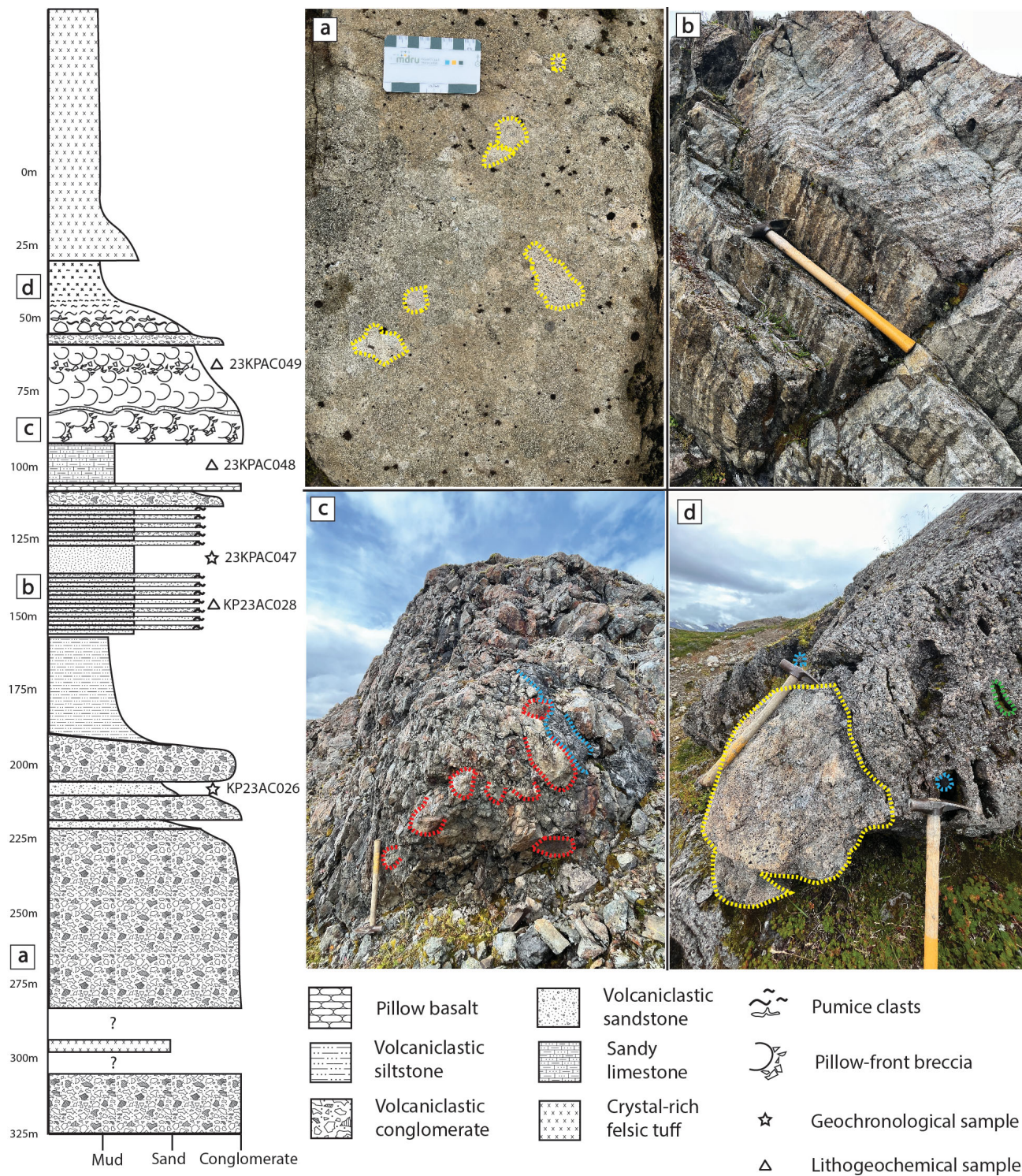


**Figure 4.** Stratigraphy of the Mount Johnson section, with corresponding field photographs of units showing **a)** clasts (outlined in yellow) supported in an aphanitic groundmass forming a massively bedded unit within the interpreted Betty Creek Formation; **b)** interbedded pumice-rich layers (dark) and lighter-coloured, coarse-grained volcaniclastic sandstone; **c)** pillows (outlined in red) cut in cross-section with spalling brecciation textures, draped by in situ sandy limestone (outlined in blue); **d)** large basal boulders (outlined in yellow) and in situ sandy limestone (outlined in blue) at the base of a coarse-grained, pumice-rich succession (outlined in green) that fines upward into fine pumice and ash.

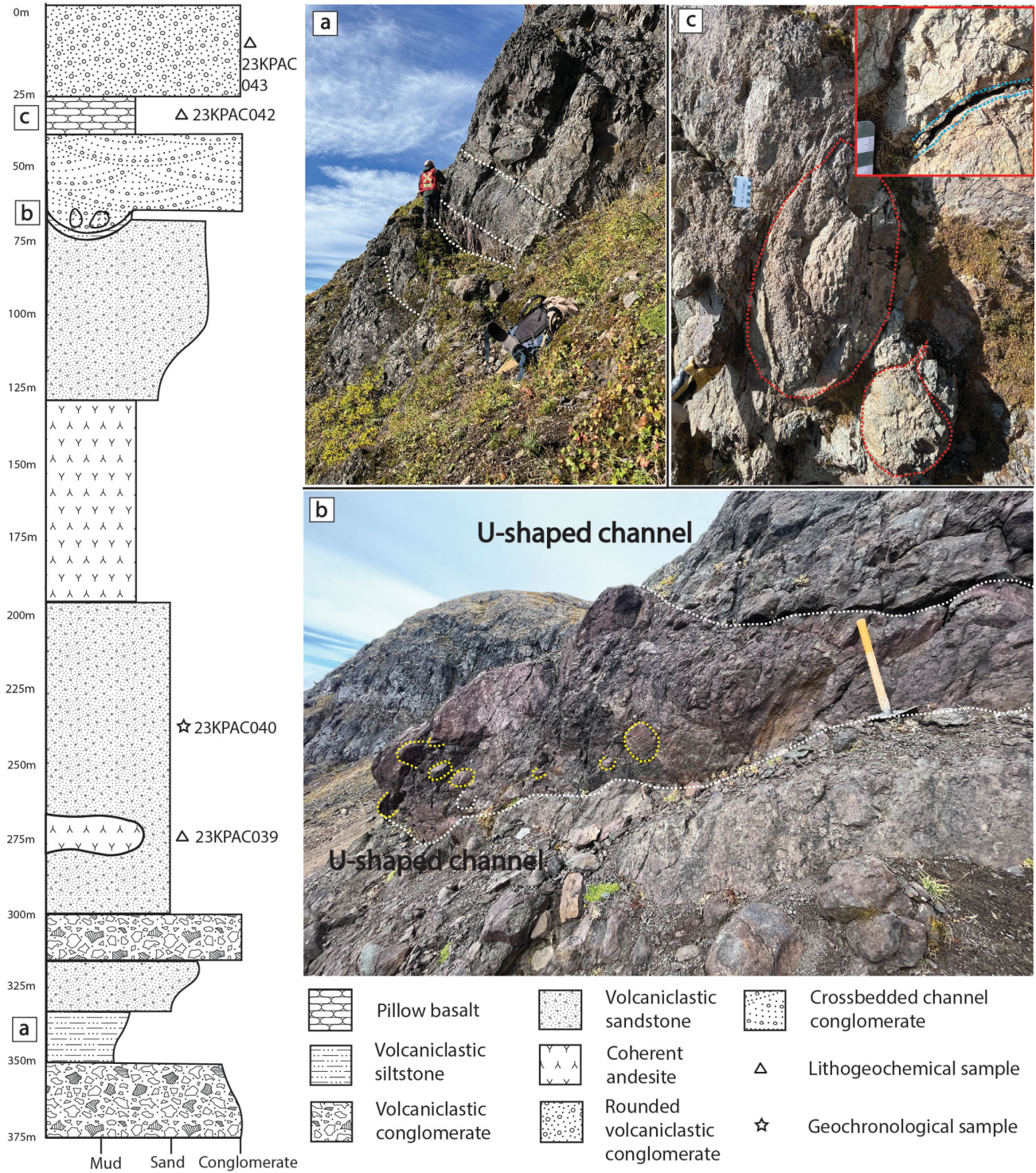


**Figure 5.** Stratigraphy of the Bear Pass section, with corresponding field photographs of units showing **a**) representative bedding dip within the lowermost 300 m of the measured section, in which the middle unit (indicated by dashed lines) is a fine volcaniclastic sandstone that has been disproportionately sheared; **b**) two stacked channel-cut deposits (lower limits outlined in white) displaying grading, with the largest rounded clasts (yellow) occupying the deepest portion of the channel and the fining, well-rounded clasts observed away from the channel base; and **c**) pillow-basalt lobes (outlined in red) that make up a narrow package (<10 m), with the glassy, weathered-out pillow-rind boundaries (outlined in blue) shown in the inset.

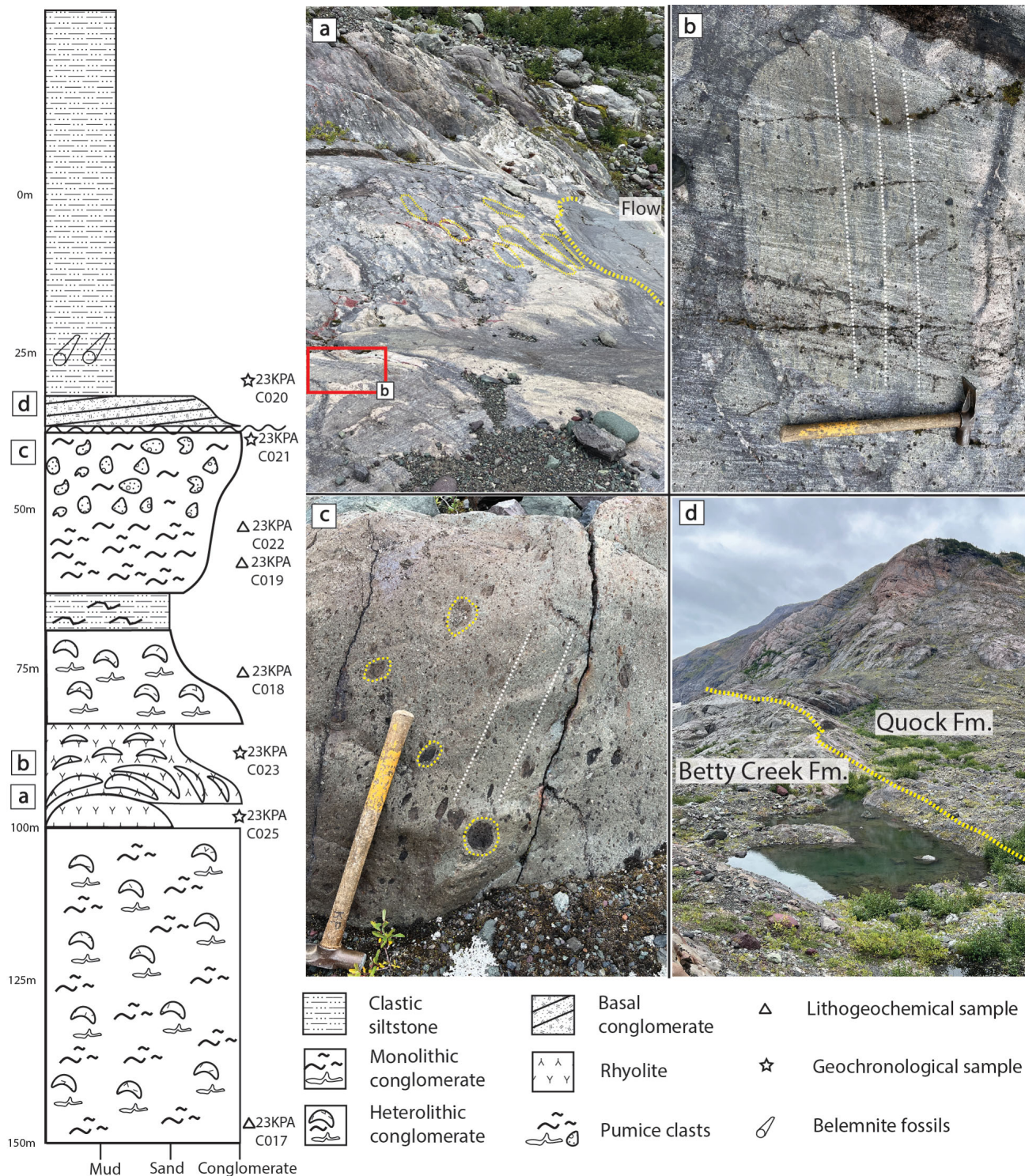


**Figure 6.** Stratigraphy of the Betty Glacier section, with corresponding field photographs of units showing **a**) a rhyolite flow with flow lobes and distinctive flow banding terminating initially in a jigsaw-fit monomictic breccia that transitions into rotated blocks of the same flow-banded rhyolite, the matrix of which is strongly altered to albite(?) that appears white in outcrop; **b**) a rotated clast of flow-banded (white) rhyolite; **c**) pumice clasts (outlined in yellow) and their alignment, roughly outlining bedding (dashed white lines), that are representative of most of the measured section; and **d**) the unconformable contact (dashed yellow line) between the Betty Creek Formation (lower Hazelton Group) and the Quock Formation (upper Hazelton Group), marking the transition between primarily volcanic rocks and clastic rocks.

pale-beige and green porphyritic volcanic rocks (80%). The massively bedded sandstone unit consists of coarse or granule-sized sand, comprising thick sections as well as finer (<1 m) interbeds within the conglomerate (Figure 5a). A small outcrop of coherent andesite was observed further upsection within the clastic sequence; the contacts defining this unit could not be observed in the outcrop. A section of coarse-grained sandstone was sampled for detrital zircon U-Pb geochronology.

#### **Coherent Andesite**

This cliff-forming, coherent unit shows patches of intense hydrothermal brecciation, which consists of angular clasts of porphyritic andesite, with a carbonate matrix that weathers distinctively. The unit is plagioclase- and hornblende-phyric, with millimetre-sized chlorite-filled amygdules set in a maroon groundmass. The andesite sits within the volcanoclastic/clastic sediments, where they are observed to continue upsection. This unit was sampled for whole-rock geochemistry analyses from a small outcrop of andesite hosted within the previously described sandstone unit shown on the stratigraphic column in Figure 5.

#### **Channel Sediments**

A distinctive set of channel deposits cut U-shaped erosional contacts into the underlying coarse sand and conglomerate unit, which is 3 m thick (Figure 5b). This unit is defined by a bed 10 cm thick of finely laminated, coarse sand that transitions sharply into a conglomerate, with well-rounded boulders and a lesser amount of subangular boulders; the largest of the rounded boulders are concentrated in the deepest part of the U shape. The upper contact of the coarse sand and conglomerate unit is cut by the erosional U-shaped contact of another channel deposit that has the same textures as the basal channel. The boulder conglomerate fines into a medium- to coarse-grained sandstone, which shows extensive crossbedding on the centimetre scale; this crossbedding shows that the units are facing upward.

#### **Pillow Basalt**

A narrow lens (10 m) of pillowed flows is observed in contact with the crossbedded sandstone. These pillows show porphyritic textures, the plagioclase phenocrysts (20%) and mafic crystals (20%) having been selectively altered to chlorite in a porphyritic groundmass (Figure 5c). The pillows lack obvious vesicles, but thin (2–3 mm) rinds can be observed rimming pillows 20–30 cm in size. A pillow was sampled for whole-rock geochemistry.

#### **Rounded Conglomerate**

The succession is capped by an outcrop of conglomerate weathered beige, which forms the plateau of the mountain. The conglomerate is matrix-supported and contains sub-rounded to rounded, pebble-sized clasts of felsic volcanic rocks. This unit was sampled for whole-rock geochemistry.

## **Betty Glacier Section**

The Betty Glacier section was selected in a location close to the type section of the Betty Creek Formation. Defining the stratigraphy and collecting both whole-rock geochemical and geochronological samples in this location allows for comparison with samples collected from outside the type area, such as those collected in the Mount Johnson and Bear Pass sections described above. Here again, stratigraphy was walked perpendicular to strike, allowing for a vertical section of 150 m to be described. The observed stratigraphy, from bottom to top, is outlined below.

#### **Heterolithic Conglomerate**

The base of the observed outcrop at the Betty Glacier section consists of a dark grey to black unit of heterolithic clasts of both unflattened pumice and rounded to sub-rounded porphyritic volcanic clasts between 0.1 and 5 cm in size. The alteration within this unit is patchy, ranging from pervasive chlorite to magnetite veining and flooding. Sorting and clast density vary through the 75 m section, ranging from domains of large (>20 cm) clasts of pumice to finer centimetre-sized lithic-dominated domains. The unit is consistently matrix-supported. Four samples were collected for whole rock geochemistry from this unit, covering the variability of the rock.

#### **Rhyolite Dome**

Hosted within the heterolithic conglomerate portion of the stratigraphy is a distinctive flow-banded felsic flow lobe. The lobe is cut parallel, or close to parallel, to its flow direction, which made it possible to describe its autobrecciated flow front. This breccia is characterized by its jigsaw fit immediately adjacent to the flow front, which then transitions into a mosaic of rotated flow-banded blocks cemented by an aphanitic, matrix-altered to pervasive, hard and white mineral, which is potentially albite, and bright red jasper (Figure 6a, b). A clast of this rhyolite within the autobreccia as well as a portion of the flow lobe itself were sampled for geochronological analyses.

#### **Pumice Conglomerate**

Overlying the heterolithic conglomerate unit, lithic clasts become fewer as pumice now dominates the unit. The pumice clasts show moderate flattening (Figure 6c) and increase in average size from 5 cm at the base of the unit to 30 cm at the top. Two whole-rock geochemical samples and one geochronological sample were collected from portions of this unit. The geochronological sample at the upper limit of the unit corresponds to the unconformity between the felsic volcanism of the Betty Creek Formation and the clastic sediments of the overlying Quock Formation of the upper Hazelton Group (Figure 6d).

## Clastic Sediments

The base of this unit is defined by a basal pebble conglomerate of rounded lithic clasts 1 m thick. This is overlain by a thick succession of rhythmically interbedded ‘pyjama beds’ consisting of medium-grained sand to mudstone. Within sandy interbeds, trace belemnites can be found. A detrital zircon geochronological sample was collected near the base of this unit.

## Discussion

The three stratigraphic sections described above are separated by a minimum of 5.5 km (Mount Johnson and Bear Pass sections) and a maximum of 17 km, between Betty Glacier and the Bear Pass sections. This large distance between sections allows for a broad correlation with observed facies and also allows for speculation about their potential depositional environment, with respect to their proximity to volcanic centres and paleoposition within the topography.

## Stratigraphic Units

### Volcaniclastic and Clastic Sediments

All three sections (Figures 4–6) describing the 17 km distance along strike show a package of volcaniclastic rocks that is at least 200 m thick. This unit can be described as a volcaniclastic conglomerate that consistently contained clasts of pumice, with consistent clast size, matrix composition and percentage of the whole rock throughout the sections. Locally, pumice showed varying degrees of flattening, along with variable lithic-fragment content and frequency of sandstone interbeds. Units matching this textural description correspond to either the lower or upper members of the Betty Creek Formation. Of the units observed during the 2023 field mapping, this volcaniclastic conglomerate unit is the most ambiguous, as the various ways in which it is described in reports of most of the members of the Hazelton Group make it difficult to clearly distinguish in the field. Samples collected for both whole-rock geochemical and geochronological analyses will aid in correlating this unit, as it is broadly described in the literature.

### Pumice-Rich Volcaniclastic Rocks

The distinctly pumice-rich units present within the two western sections, 12 km apart, are either thinly bedded (Mount Johnson section, Figure 4b) or massively bedded (Betty Glacier section, Figure 6c). Across the 12 km, these units vary in thickness from 80 m at the Mount Johnson section to 55 m at the Betty Glacier section. The difference between the two units lies in their textural and field relationships with their respective overlying units. The easternmost section, Bear Pass (Figure 5), shows rare to no pumice within its volcaniclastic rocks. This can be explained as either due to a change in the lateral facies or by the location of

that section vertically within the stratigraphy; geochronological and geochemical analyses will aid in answering this question.

The pumice-rich layers of the Mount Johnson section are consistent with descriptions from Gordee (2006) about similar layers from the upper Betty Creek Formation, referring to features such as pumice-rich pyroclastic units and flame structures in finely bedded sediments. The other key feature observed in the field is the increasing frequency in the occurrence of limestone, which has been described in the literature as occurring at the interface between the Betty Creek and Mount Dilworth formations (Alldrick, 1993).

The Betty Glacier section (Figure 6) appears to be consistent with the Mount Dilworth section as it consists of “white, maroon, or green, flow-layered, tuff that can be welded or unwelded” (Alldrick, 1993) and is also in contact with overlying sediments of the Quock Formation. Therefore, the Betty Glacier section may be interpreted as the upper limits of the Mount Dilworth Formation.

### Pillow Basalt

Pillow basalt at the Mount Johnson section (Figure 4) is intimately associated with the above-mentioned limestone units observed at the transition between the Betty Creek and Mount Dilworth formations. When this is considered in conjunction with the overlying crystal-rich, well-bedded felsic tuff that caps the section, it can be interpreted that these limestone-hosted pillowed flows are occurring at the contact between the Betty Creek and Mount Dilworth formations. These flows are texturally different than those observed further east at the Bear Pass section (Figure 5), where they are hosted within a volcanic, fine-grained porphyritic matrix, the upper contact of which is a continuation of volcaniclastic conglomerate units. The lack of sandy limestone that appears to mark the transition between the Betty Creek and Mount Dilworth formations, suggests the pillows seen at the Bear Pass section may occur stratigraphically deeper within the Betty Creek Formation, away from this observed contact relationship.

### Upper Hazelton Unconformity

The unconformity observed between the pumice-rich felsic volcanic rocks and the overlying rhythmically bedded clastic sediments at the Betty Glacier section (Figure 6) shares the same basal conglomerate, consisting of rounded pebbles grading into fossiliferous sandstone and mudstone, as the unconformity observed at the Zn-Ag-Pb VMS occurrence of the BA property (Figure 3; K.M. Powers, K.E.L. Rubingh and S.L.L. Barker, unpublished poster, 2023). Both show a unit of rounded pebble basal conglomerate <1 m thick along an irregular erosional contact, followed by fossiliferous beds of sandstone and siltstone. The significance of this correlation lies in the potential erosion of the upper portions of the VMS sulphides at BA, which

occur right up to the unconformity. Both of these unconformities have been sampled for geochronological and whole-rock geochemical analyses, the results of which will allow the reconstruction of differences in erosional history between the two sections along the top of this volcanic unit, thus establishing whether it is associated with the Betty Creek Formation or the younger Mount Dilworth Formation (K.M. Powers, K.E.L. Rubingh and S.L.L. Barker, unpublished poster, 2023).

### Placement of Sections into Regional Stratigraphy

The textural descriptions of outcrops and the field relationships between these outcrops are outlined below. The sections described in this study occur within the Betty Creek Formation of the lower Hazelton Group through to the Quock Formation of the upper Hazelton Group (Figure 7).

The Bear Pass section (Figure 5) represents the oldest of the measured sections, with the rocks primarily being classified as mafic, heterolithic, volcanoclastic or clastic conglomerates, characterized by the presence of minor mafic pillowed volcanic rocks and an overall lack of felsic pyroclastic units. The lack of felsic volcanic or volcanoclastic rocks places this section below the contact with the Mount Dilworth Formation, where a distinct increase in felsic content is observed. The Mount Johnson section (Figure 4) encompasses that transition zone between the Betty Creek volcanoclastic and clastic units and the basal limestone, felsic pumice-rich rocks and crystal-rich tuffs of the Mount Dilworth Formation. Lastly, the section measured in the Betty glacier area (Figure 6) represents the youngest of the sections. At this section, a rhyolite dome with flow-top breccias is observed, followed by a sequence of interbedded felsic pumice-rich conglomerate and tuff, which ulti-

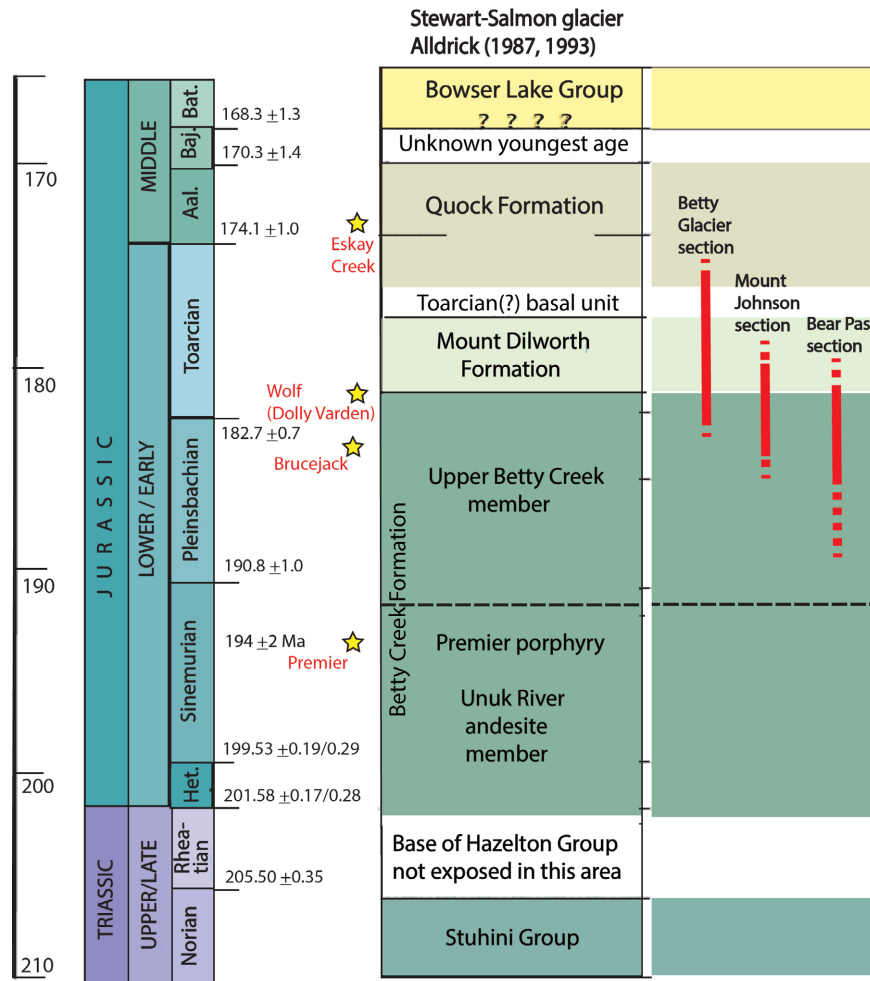


**Figure 7.** Generalized stratigraphy of the lower and upper units of the Hazelton Group in the Stewart mining camp (modified from Nelson et al., 2018 and Brueckner et al., 2021). Yellow stars indicate the U-Pb ages of major deposits in the Stewart camp and further north, such as at Brucejack and Eskay Creek. Premier U-Pb age from Alldrick (1985); Wolf U-Pb age (Dolly Varden) from Hunter and van Straaten (2020). The dashed lines showing the locations of the Bear Pass, Mount Johnson and Betty Glacier sections in the study area are indicative of interpreted continuation of the sections based on overlapping units observed during fieldwork. Abbreviations: Aal., Aalenian; Baj., Bajocian; Bath., Bathonian; Het., Hettangian.

mately terminates at the unconformity with sediments of the overlying clastic Quock Formation.

## Future Work

The work outlined in this paper represents one aspect of the work being conducted in this study. Paralleling the research being done on volcanic stratigraphy are studies investigating and classifying the mineralization at the BA Zn-Ag-Pb VMS and the Mountain Boy epithermal Ag deposits. Uranium-lead geochronological analysis of the samples collected during the 2023 season will aid in placing these deposits within the stratigraphic column and in reconstructing the local volcanic-arc environment. To properly define the mineralized units of this area, the following work will be undertaken:

- U-Pb geochronology, to determine both crystallization and detrital ages. The results will be processed through the 2023–2024 winter months, along with corresponding results from whole-rock geochemistry.
- Detailed petrographic descriptions of fine-grained and aphanitic volcanic and volcanoclastic rocks, to aid in further classifying the alteration, the mineralogy and, potentially, the origin of these rocks.
- Micro X-ray fluorescence analysis of representative samples that were collected from mineralized zones within the study area. These studies will focus on metal deportment, origin and geochemistry of the ore-hosting units.
- Further mapping of the region, with potential step-out fieldwork in the direction of the Dolly Varden silver deposit, where mineralization appears to draw some parallels to that observed within the study area.

## Conclusion

The Hazelton Group stratigraphy within the Stewart mining camp, and elsewhere within the Stikine terrane is highly variable and in regions units remain relatively broadly lumped together and described as packages of undifferentiated volcanic rocks. A wide range of textural and field-relationship descriptions apply to the Betty Creek Formation in particular; as a consequence, regional correlation of the members within the formation will benefit from geochemical and geochronological analyses undertaken in conjunction with descriptions recorded during fieldwork. This preliminary summary of field observations in 2023 makes it possible to tentatively place three stratigraphic sections (Figures 2, 4–6) within the Hazelton Group stratigraphy (Figure 7). The study sections have been interpreted to include rocks of the aforementioned Betty Creek and Mount Dilworth formations, as well as from the base of the Quock Formation, which represents potentially 18 m.y. of volcanic succession.

The three sections have laterally continuous units that share textural and field relationships, such as the extent and thickness (<200 m) of the units studied as well as volcanoclastic and clastic sediments, which appear to extend beyond this 17 km distance along strike. The sections, in particular the Bear Pass section, show distinct differences in both unit composition and depositional environment, which will be defined with the help of future geochemical and geochronological results. The oldest rocks (Figure 7), as determined from field relationships during 2023 mapping, are in the Bear Pass section (Figure 5), barring any unrecorded major fault displacement. In the Bear Pass section, volcanically derived conglomerate, sandstone-interfingered andesitic flows, channel deposits with clear U-shaped submarine erosional contacts (Figure 5b) and crossbedded sand, and finally pillowed basalts (Figure 5c) are primarily observed. These units, in combination with their field relationships, place the Bear Pass section within the Betty Creek Formation. The Mount Johnson section (Figure 4) is located both stratigraphically and geographically in the middle (Figure 6). In this section, there is a transition from lithic-rich conglomerate, and interbedded sand and pumice (Figure 4b) of the upper Betty Creek Formation to limestone-hosted pillow-basalt breccias (Figure 4c) at its upper contact. This transition from mafic volcanic rocks to felsic volcanic lithofacies and the presence of limestone units is consistent with previous descriptions of the Mount Dilworth Formation. Capping this section is a porphyritic, crystal-rich felsic tuff. Lastly, the youngest section (Figure 7) is the Betty Glacier section (Figure 6), which is located 17 km northwest of the Bear Pass section (Figure 2). In this section, the aforementioned laterally extensive volcanoclastic conglomerate, primarily felsic pumice-rich sediments (Figure 6c), a rhyolite dome (Figure 6b) and the unconformable contact with the clastic Quock Formation (Figure 6d) are observed. The majority of these, with the exception of the conglomerate at the base of the section and the Quock Formation, are consistent with earlier descriptions of the Mount Dilworth Formation.

The relationship between these areas will be fine-tuned and further defined based on the results from geochemical and geochronological analyses. The stratigraphic difference between the Mount Johnson (Figure 4) and Bear Pass sections (Figure 5) will require further work, as they are at the same elevation and share a similar strike and dip. These differences are likely a result of the combination of distance from the volcanic centre, structure and paleotopography at the time of deposition. Understanding the framework of depositional environments within the eastern Stewart mining camp will provide additional data to future explorers targeting known prospective stratigraphic intervals in the region.

## Acknowledgments

Funding and logistical support were generously provided by MTB Metals Corp., without whose co-operation none of this research would have been possible. Additional funding is provided by the Natural Sciences and Engineering Research Council of Canada (NSERC), Mitacs and Geoscience BC, through the Geoscience BC Scholarship program. The authors would also like to thank Scottie Resources Corp., Newcrest Mining Limited and Ascot Resources Ltd. for allowing access to their claim blocks. They also thank L. Theny for her review of the paper.

## References

- Alldrick, D.J. (1985): Stratigraphy and petrology of the Stewart mining camp (104B/1); *in* Geological Fieldwork 1984, BC Ministry of Energy, Mines and Low Carbon Innovation, BC Geological Survey, Paper 1985-1, p. 316–42.
- Alldrick, D.J. (1989): Volcanic centres in the Stewart Complex (103P and 104A, B); *in* Geological Fieldwork 1988, BC Ministry of Energy, Mines and Low Carbon Innovation, BC Geological Survey, Paper 1989-1, p. 233–240.
- Alldrick, D.J. (1993): Geology and metallogeny of the Stewart mining camp, northwestern British Columbia; BC Ministry of Energy, Mines and Low Carbon Innovation, BC Geological Survey, Bulletin 85, 113 p.
- Anderson, R.G. and Thorkelson, D.J. (1990): Mesozoic stratigraphy and setting for some mineral deposits in the Iskut River map area, northwestern British Columbia; *in* Current Research Part E, Cordillera and Pacific Margin, Geological Survey of Canada, Paper 90-1E, p. 131–139, URL <<https://doi.org/10.4095/131379>>.
- Barresi, T., Nelson, J.L., Dostal, J. and Friedman, R. (2015): Evolution of the Hazelton arc near Terrace, British Columbia: stratigraphic, geochronological, and geochemical constraints on a Late Triassic–Early Jurassic arc and Cu–Au porphyry belt; *Canadian Journal of Earth Sciences*, v. 52, no. 7, p. 466–494, URL <<https://doi.org/10.1139/cjes-2014-0155>>.
- BC Geological Survey (2023a): MapPlace GIS internet mapping system; BC Ministry of Energy, Mines and Low Carbon Innovation, BC Geological Survey, URL <<http://www.MapPlace.ca>> [October 2023].
- BC Geological Survey (2023b): MINFILE BC mineral deposits database; BC Ministry of Energy, Mines and Low Carbon Innovation, BC Geological Survey, URL <<https://minfile.gov.bc.ca/summary.aspx?minfilno=104B%20%200-21>> [October 2023].
- Bird, S., Arseneau, G., Petrovic, A., Palkovits, F., Fogarty, J., Jensen, S., Masson, B., Marsland, R., Teymouri, S., Grills, F. and Savage, K. (2020): Premier and Red Mountain Gold Project feasibility study NI 43-101 Technical Report British Columbia; technical report prepared for Ascot Resources Limited, 607 p.
- Brueckner, S.M., Johnson, G., Wafforn, S., Gibson, H., Sherlock, R., Anstey, C. and McNaughton, K. (2021): Potential for volcanogenic massive sulfide mineralization at the A6 anomaly, north-west British Columbia, Canada: stratigraphy, litho-geochemistry, and alteration mineralogy and chemistry; *Minerals*, v. 11, art. 867, URL <<https://doi.org/10.3390/min11080867>>.
- Gagnon, J.-F., Barresi, T., Waldron, J.W.F., Nelson, J.L., Poulton, T.P. and Cordey, F. (2012): Stratigraphy of the upper Hazelton Group and the Jurassic evolution of the Stikine terrane, British Columbia; *Canadian Journal of Earth Sciences*, v. 49, p. 1027–1052, URL <<https://doi.org/10.1139/e2012-042>>.
- Gordee, S.M. (2006): Volcanostratigraphy, age and geologic setting of the Lower–Middle Jurassic upper Hazelton Group west-central British Columbia; M.Sc. thesis, The University of British Columbia, 183 p.
- Grove, E.W. (1973): Detailed geological studies in the Stewart complex, northwestern British Columbia; Ph.D. thesis, The University of British Columbia, 522 p.
- Henderson, J.R., Kirkham, R.V., Henderson, M.N., Payne, J.G., Wright, T.O. and Wright, R.L. (1992): Stratigraphy and structure of the Sulphurets area, British Columbia; *in* Current Research, Part A, Cordillera and Pacific Margin, Geological Survey of Canada, Paper 92-1A, p. 323–332, URL <<https://doi.org/10.4095/132821>>.
- Hunter, R.C. and van Straaten, B.I. (2020): Preliminary stratigraphy and geochronology of the Hazelton Group, Kitsault River area, Stikine terrane, northwest British Columbia; *in* Geological Fieldwork 2019, BC Ministry of Energy, Mines and Low Carbon Innovation, BC Geological Survey, Paper 2020-01, p. 101–118.
- Lewis, P.D., Macdonald, A.J. and Bartsch, R.D. (2001): Hazelton Group/Bowser Lake Group stratigraphy in the Iskut River area—progress and problems; Chapter 2 *in* Metallogenesis of the Iskut River Area, Northwestern British Columbia, P.D. Lewis, A. Toma and R.M. Tosdal (ed.), Mineral Deposit Research Unit, Special Publication no. 1, p. 9–30.
- Marsden, H. and Thorkelson, D.J. (1992): Geology of the Hazelton volcanic belt in British Columbia: implications for the Early to Middle Jurassic evolution of Stikinia; *Tectonics*, v. 11, p. 1266–1287.
- Mortensen, J.K., Wojdak, P., Macdonald, R., Gordee, S.M. and Gabites, J.E. (2004): Regional studies of VMS mineralization and potential within the Early Jurassic Hazelton Group, British Columbia; *in* Geological Fieldwork 2004, BC Ministry of Energy, Mines and Low Carbon Innovation, BC Geological Survey, Paper 2005-1, p. 49–60.
- Nelson, J.A.L. and Kyba, J. (2014): Structural and stratigraphic control of porphyry and related mineralization in the Treaty Glacier–KSM–Brucejack–Stewart trend of western Stikinia; *in* Geological Fieldwork 2013, BC Ministry of Energy, Mines and Low Carbon Innovation, BC Geological Survey, Paper 2014-1, p. 111–140, URL <[https://cms-content.nrs.gov.bc.ca/geoscience/publicationcatalogue/Paper/BCGS\\_P2014-01-07\\_Nelson.pdf](https://cms-content.nrs.gov.bc.ca/geoscience/publicationcatalogue/Paper/BCGS_P2014-01-07_Nelson.pdf)> [October 2023].
- Nelson, J.L., Waldron, J., van Straaten, B., Zagorevski, A. and Rees, C. (2018): Revised stratigraphy of the Hazelton Group in the Iskut River region, northwestern British Columbia; *in* Geological Fieldwork 2017, BC Ministry of Energy, Mines and Low Carbon Innovation, BC Geological Survey, Paper 2018-1, p. 15–38.
- Nelson, J.L., van Straaten, B. and Friedman, R. (2022): Latest Triassic–Early Jurassic Stikine–Yukon–Tanana terrane collision and the onset of accretion in the Canadian Cordillera: insights from Hazelton Group detrital zircon provenance and arc–back-arc configuration; *Geosphere*, v. 18, no. 2, p. 670–696, URL <<https://doi.org/10.1130/GES02444.1>>.
- Tipper, H.W. and Richards, T.A. (1976): Jurassic stratigraphy and history of north-central British Columbia; *Geological Survey of Canada, Bulletin* 270, 82 p., URL <<https://doi.org/10.4095/103065>>.



# Trace-Element Mapping by Laser Ablation–Inductively Coupled Plasma–Mass Spectrometry of Sulphide Minerals from the Burgundy Ridge Copper-Gold Alkalic Porphyry Prospect in the Golden Triangle, Northwestern British Columbia (NTS 104B/14E)

**J. Dlugosz<sup>1</sup>**, Department of Earth, Environmental and Geographic Sciences, The University of British Columbia, Kelowna, British Columbia, joanna.dlugosz@ubc.ca

**K.P. Larson**, Department of Earth, Environmental and Geographic Sciences, The University of British Columbia, Kelowna, British Columbia

**C.J.M Lawley**, Natural Resources Canada, Geological Survey of Canada–Central, Ottawa, Ontario

**C.J. Beno**, Department of Earth, Environmental and Geographic Sciences, The University of British Columbia, Kelowna, British Columbia

**D.C. Petts**, Natural Resources Canada, Geological Survey of Canada–Central, Ottawa, Ontario

---

Dlugosz, J., Larson, K.P., Lawley, C.J.M., Beno, C.J. and Petts, D.C. (2024): Trace-element mapping by laser ablation–inductively coupled plasma–mass spectrometry of sulphide minerals from the Burgundy Ridge copper-gold alkalic porphyry prospect in the Golden Triangle, northwestern British Columbia (NTS 104B/14E); *in* Geoscience BC Summary of Activities 2023, Geoscience BC, Report 2024-01, p. 47–58.

## Introduction

Producing and advancing green technologies has become a topic of major interest in recent years due to the growing impact of humans on the environment. The geological materials that are susceptible to supply disruptions but are necessary for the production of these technologies have become known as ‘critical minerals’. Demand for critical minerals in manufacturing of consumer (e.g., smartphones, electric vehicles) and commercial (e.g., in healthcare and construction of green infrastructure) products continues to grow and is estimated to increase six-fold within the next 17 years (Government of Canada, 2022). To meet such demands, federal and provincial governments are investing in programs centred around the research and exploration for critical mineral deposits.

One such program is the Targeted Geoscience Initiative, which was established in 2000 by the Government of Canada. This program has funded and carried out studies in all provinces and territories, including projects focused on the Golden Triangle of northwestern British Columbia (BC; Figure 1). The Golden Triangle has attracted both the mineral exploration industry and researchers due to its gold and critical-mineral endowment, and the resulting abundance of ore deposits.

The Burgundy Ridge prospect is a silica-undersaturated copper-gold alkalic porphyry deposit on the Newmont Lake property, owned by Enduro Metals Corp., located in the Golden Triangle between well-known deposits at Galore Creek, 30 km northwest, and Eskay Creek, 30 km southeast (Figures 1, 2). Active exploration has occurred on the property only within the last approximately 5 years and, as such, there is a lack of geological information concerning the prospect’s petrogenesis and mineralization. Given the dearth of knowledge about the Burgundy Ridge prospect, The University of British Columbia, Okanagan, has partnered with Enduro Metals and the Geological Survey of Canada to begin characterizing the prospect in detail. Initial investigations have been focused on determining the timing of mineralization through rubidium-strontium geochronology, pyrite and chalcopyrite sulphur isotopes, and examination of trace elements within pyrite and chalcopyrite via micrometre-scale trace-element maps.

This paper presents the initial results and interpretations obtained from the laser ablation–inductively coupled plasma–mass spectrometry (LA-ICP-MS) chalcopyrite and pyrite trace-element maps. Such maps can be used to determine where critical minerals are hosted, as well as their abundances, and can inform interpretations about the conditions and origin of mineralization.

## Geological Background

The western margin of Laurentia (the North American craton) has been tectonically active since the Late Precambrian (Nelson and Colpron, 2007), culminating in the for-

---

<sup>1</sup>The lead author is a 2023 Geoscience BC Scholarship recipient.

This publication is also available, free of charge, as colour digital files in Adobe Acrobat® PDF format from the Geoscience BC website: <https://geosciencebc.com/updates/summary-of-activities/>.

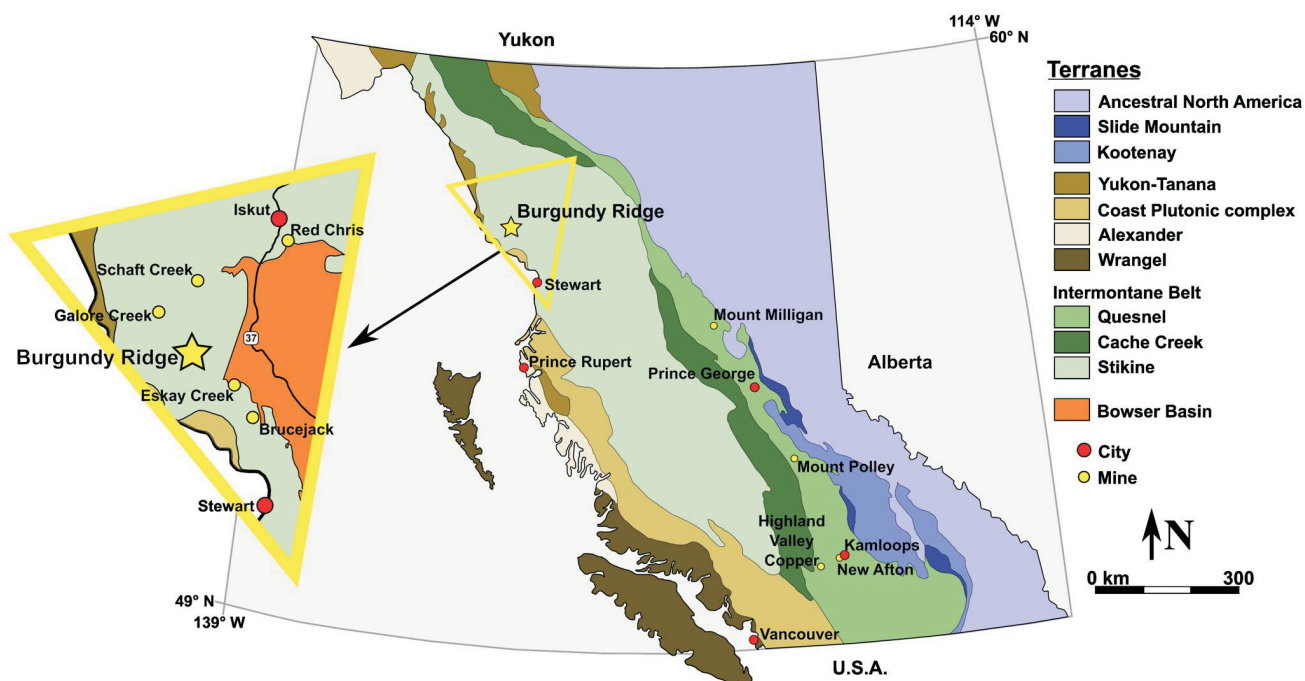


**Figure 1.** Terranes of British Columbia, the yellow triangle encompassing the area known as the ‘Golden Triangle’. The Bowser Basin is incorporated into the Golden Triangle map since it is the largest depocentre covering this part of the Stikine terrane (Logan and Mihalynuk, 2014). Modified from del Real et al. (2013) and BC Geological Survey (2015, 2018).

mation of the Canadian Cordillera. In BC, the Canadian Cordillera is dominated by a series of oceanic basin and island-arc terranes that were accreted during the early Mesozoic to early Cenozoic (Coney et al., 1980; Dickinson, 2004; Nelson and Colpron, 2007; Logan and Mihalynuk, 2014). The terranes were brought in contact with the Laurentian margin due to subduction and the westward movement of Laurentia that closed intervening basins (Nelson and Colpron, 2007; Logan and Mihalynuk, 2014; Monger and Gibson, 2019). The accretion process deformed rocks deposited on the western margin of the North American craton and displaced them eastward. Active tectonism along the western portion of the Cordillera post-accretion resulted in pluton emplacement, volcanism, orogen-parallel dismemberment and variable metamorphism (Nelson and Colpron, 2007; Logan and Mihalynuk, 2014; Tombe, 2020).

The Intermontane belt, one of five tectonometamorphic belts that constitute the Cordillera in BC, includes the Stikine, Quesnel and Cache Creek terranes (Figure 1; Nelson and Colpron, 2007; Tombe, 2020). The Stikine and Quesnel terranes consist of volcanosedimentary sequences produced by pre-accretion Devonian to Early Jurassic arc magmatism and further post-accretion continental-arc magmatism in the late Early Jurassic (Logan and Mihalynuk, 2014). Accretion of these terranes to the North American craton occurred around 180 Ma, with the Cache Creek terrane (oceanic affinity) becoming wedged between the Stikine and Quesnel terranes (Nelson and Colpron, 2007; Logan and Mihalynuk, 2014).

Much of the mineral wealth in BC is contained within porphyry deposits of the Stikine and Quesnel terranes (Logan and Mihalynuk, 2014). Many of the porphyry deposits within these two terranes formed during the late Triassic to Early Jurassic, with significant mineralization occurring during a 6 m.y. pulse between 202 and 208 Ma (Lang et al., 1995; Logan and Mihalynuk, 2014). The porphyry deposits can be subdivided into two main groups: calcalkaline and alkaline (Lang et al., 1995; Logan and Mihalynuk, 2014). Calcalkaline porphyry deposits are more abundant globally (Lang et al., 1995) and are almost twice as common in BC, with 904 known occurrences (Logan and Mihalynuk, 2014). Alkaline deposits are less common in BC, with 431 known occurrences, and globally, but are of interest because they can host economically significant amounts of copper, gold and other critical minerals (Deyell and Tosdal, 2005; Logan and Mihalynuk, 2014).

Alkalic porphyry deposits occur within the Golden Triangle of northwestern BC (Figure 1) in the Stikine terrane (Lang et al., 1995; Tombe, 2020), including one of the largest known alkalic porphyry deposits, Galore Creek (Micko, 2010; Tombe, 2020). The abundance of alkalic porphyries with economic potential in the Golden Triangle area provides an opportunity to enhance the understanding of these less-studied deposit types.

## Methods

Samples from the Burgundy Ridge prospect were collected from core drilled during the 2019 and 2021 seasons at the

Newmont Lake property (Figure 2). Alteration assemblages and sulphide mineralogy and textures were documented in thin sections using a petrographic microscope (Figure 3). Areas for further investigation were selected from each sample to include different sulphide textures, including mineral shape and inclusion density. Focus was placed on sulphides because critical minerals are found primarily in sulphide crystal structures or around sulphide grains. Areas with multiple sulphide minerals, such as pyrite, chalcopyrite and sphalerite, were targeted to determine what critical minerals were hosted in which sulphide. Rock types with high levels of chalcopyrite and pyrite mineralization were focused on, resulting in three samples being selected from hydrothermal-breccia zones, since these are interpreted as forming during the main mineralization event (Figure 3).

Three trace-element maps of representative portions of chalcopyrite and pyrite grains were obtained through in situ LA-ICP-MS analysis in May 2023 at the Geological Survey of Canada in Ottawa, Ontario. Polished thick sections

(100 µm) from samples 138.4, 212.4 and 212.7 were mapped using an Agilent 7700x quadrupole ICP-MS instrument coupled to a Photon Machines Analyte G2 193 nm excimer laser-ablation system (Cabri and Jackson, 2011). Data acquisition was separated into two runs. Each analytical run was calibrated with a doped synthetic basalt glass standard GSE-1G (Guillong et al., 2005) and synthetic sulphide standards (Po689, Po726). The NIST610 glass-reference material was analyzed as a secondary reference material to quantify accuracy and precision. Reference materials were analyzed at the start and end of each run and bracketing every 20 mapping lines. A circular laser spot with a diameter of 10 µm was used during the analysis of sample 212.7, whereas a smaller spot diameter of 8 µm was used for samples 138.4 and 212.4. Prior to the main ablation, the target surfaces were rastered to clear away any surficial adherents. Both analytical runs used a laser repetition rate of 20 Hz and fluence of 4.5 J/cm<sup>2</sup>.

Trace-element concentrations are reported in parts per million (ppm), whereas major elements expressed as oxides

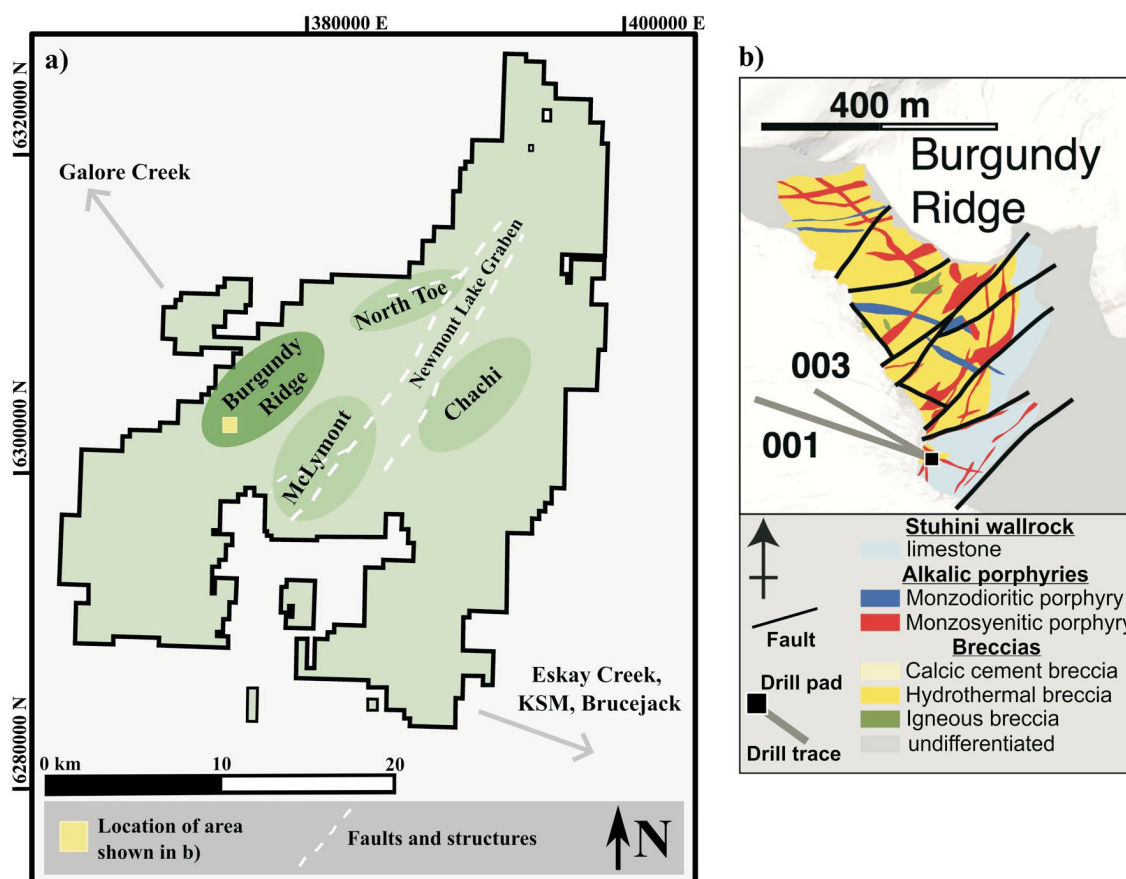


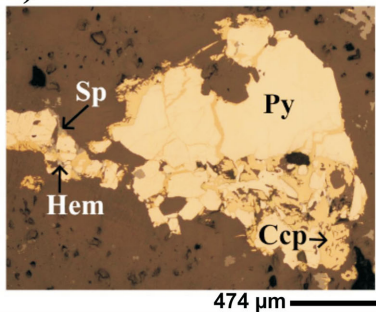
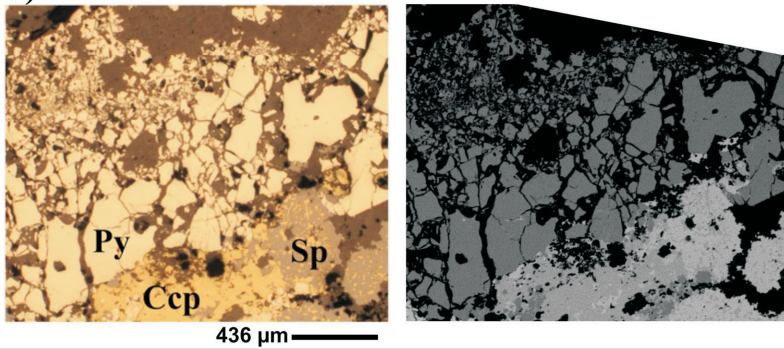
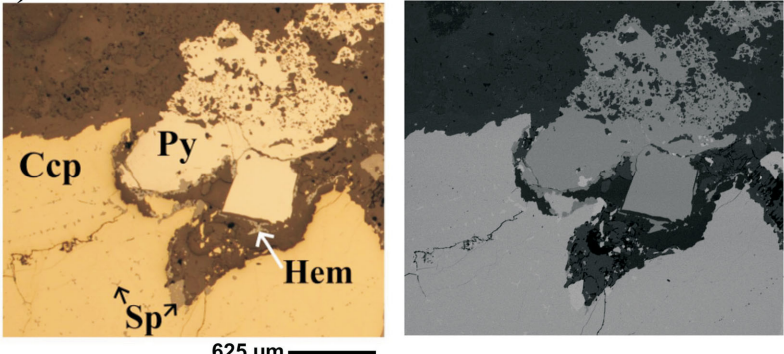
**Figure 2.** a) Enduro Metals Corp. Newmont Lake property and its prospects: Burgundy Ridge copper-gold porphyry, North Toe copper-gold porphyry, McLymont gold system and Chachi copper-gold-molybdenum anomaly. The prospects are hosted in the Golden Triangle of the Stikine terrane. The Galore Creek deposit is located 30 km northwest of the property, while the Eskay Creek past-producing mine, KSM deposit and Brucejack mine are all 30–50 km to the southeast. White dashed lines correspond to structural features on the property associated with the Newmont Lake graben. The yellow box represents the area shown in (b). b) Simplified map of the Burgundy Ridge prospect. Samples for trace-element maps were taken from drillholes 001 and 003. Modified from Ray et al. (1990) and Enduro Metals Corp. (2022, 2023).

are reported in weight percent (wt. %). Elements analyzed were  $^{13}\text{C}$ ,  $^{34}\text{S}$ ,  $^{45}\text{Sc}$ ,  $^{47}\text{Ti}$ ,  $^{51}\text{V}$ ,  $^{53}\text{Cr}$ ,  $^{55}\text{Mn}$ ,  $^{57}\text{Fe}$ ,  $^{59}\text{Co}$ ,  $^{60}\text{Ni}$ ,  $^{65}\text{Cu}$ ,  $^{66}\text{Zn}$ ,  $^{75}\text{As}$ ,  $^{77}\text{Se}$ ,  $^{85}\text{Rb}$ ,  $^{88}\text{Sr}$ ,  $^{89}\text{Y}$ ,  $^{90}\text{Zr}$ ,  $^{95}\text{Mo}$ ,  $^{105}\text{Pd}$ ,  $^{108}\text{Pd}$ ,  $^{109}\text{Ag}$ ,  $^{111}\text{Cd}$ ,  $^{118}\text{Sn}$ ,  $^{121}\text{Sb}$ ,  $^{125}\text{Te}$ ,  $^{137}\text{Ba}$ ,  $^{140}\text{Ce}$ ,  $^{157}\text{Gd}$ ,  $^{173}\text{Yb}$ ,  $^{178}\text{Hf}$ ,  $^{181}\text{Ta}$ ,  $^{182}\text{W}$ ,  $^{185}\text{Re}$ ,  $^{195}\text{Pt}$ ,  $^{197}\text{Au}$ ,  $^{205}\text{Tl}$ ,  $^{206}\text{Pb}$ ,  $^{207}\text{Pb}$ ,  $^{208}\text{Pb}$ ,  $^{209}\text{Bi}$  and  $^{238}\text{U}$ . Major elements reported as oxides were  $\text{Na}_2\text{O}$ ,  $\text{MgO}$ ,  $\text{Al}_2\text{O}_3$ ,  $\text{SiO}_2$ ,  $\text{P}_2\text{O}_5$ ,  $\text{K}_2\text{O}$ , and  $\text{CaO}$ .

To create the maps, raw LA-ICP-MS files were processed within the open-source R software (R Development Core Team, 2018) using the LAMTRACE data-reduction approach outlined in Jackson (2008). Data processing fol-

lowed the procedure outlined in Lawley et al. (2020) and included steps such as signal selection, background subtraction and conversion from continuous line scans to pixels to create the maps.

Further processing of the data from the trace-element maps was used to differentiate quantitative data from zones of differing compositions. Processing followed the methods outlined in Lawley et al. (2020) and utilized machine learning (R Development Core Team, 2018) in combination with multiple R packages such as robCompositions (Templ et al., 2011). First, to reduce problems when calculating a

		Description
<p><b>a) 138.4</b></p> 		<p>Hydrothermal breccia intruding Sparse Megacrystic Syenite zone</p> <p><u>Sulphides</u>: pyrite (Py), chalcocopyrite (Ccp), sphalerite (Sp)</p> <p><u>Alteration</u>: chlorite, carbonate, sericite, hematite (Hem)</p>
<p><b>b) 212.4</b></p> 		<p>Cement-dominant hydrothermal breccia intruding Limestone zone</p> <p><u>Sulphides</u>: pyrite (Py), chalcocopyrite (Ccp), sphalerite (Sp)</p> <p><u>Alteration</u>: K-feldspar, biotite, sericite, hematite</p>
<p><b>c) 212.7</b></p> 		<p>Hydrothermal breccia within a Biotite-Syenite zone</p> <p><u>Sulphides</u>: pyrite (Py), chalcocopyrite (Ccp), sphalerite (Sp)</p> <p><u>Alteration</u>: K-feldspar, biotite, sericite, calcite, hematite (Hem)</p>

**Figure 3.** Rock descriptions and identification of sulphides for samples **a)** 138.4, **b)** 212.4 and **c)** 212.7. Reflected-light images (left) and backscattered-electron images (right) were taken of the areas selected for LA-ICP-MS trace-element mapping. Brown areas in the reflected light images are silicate minerals. Sample number is based on the depth, in metres, of each sample. Samples 138.4 and 212.7 are from drillhole 001, while sample 212.4 is from drillhole 003. Drillhole locations in the Burgundy Ridge prospect are shown in Figure 2b.

covariance matrix, elements with large portions of missing values (due to detection limits) within the dataset were filtered out. Next, a reduction of variables was accomplished through principal-component analysis. With these analyses, the initial principal components relate to elements with the largest variance. Clusters of principal-component scores from biplots are due to variations in chemical compositions based on mineral content or zonation within minerals. The number of these clusters is subjective and changes for each map, depending on the complexity of the minerals within the sample. The resulting cluster maps were used, along with reflected-light photos of the mapped areas, to name clusters based on the corresponding mineral, primarily focusing on sulphide mineralization, and whether the zones were core or rim domains. Distinguishing between different minerals, and different zones within minerals, allows for further interpretations to be made from trace-element maps, such as which mineral phases are more likely to host critical minerals and when these critical minerals became enriched in the hydrothermal history.

## Results

### Pyrite Trace-Element Results

Zones within pyrite crystals from all three samples are distinguishable based on variations in trace-element concentrations (Figures 4, 5, 6). Pyrite grains are typically characterized by Co-, Ni-, Bi- and As-poor cores, and enrichment of these same elements in the rims. The rim and core domains within pyrite were determined by the presence or absence of trace elements (Figures 4, 5, 6). Core domains for all three samples had a more defined euhedral shape, whereas the rim domains were more anhedral (Figures 4, 5, 6). The elements Se and Te are depleted in the most central regions of the pyrite cores, increase toward the outer regions and yield homogeneous concentrations across rims (Figures 4, 5, 6). Gold and As typically occur in the matrix between, or fractures within, pyrite grains, with some mineralization also occurring within late pyrite rims in samples 138.4 and 212.7 (Figures 4, 6). In sample 212.4, blebs of Pt occur in the inclusion-rich pyrite rims (Figure 5). These Pt blebs are spatially associated with areas of high As and Co concentrations.

Tellurium and Bi, which are considered critical minerals, and Au are found primarily in pyrite in the three samples. Of the three samples, sample 138.4 yielded the lowest average concentrations of Au and Bi (0.18 and 0.85 ppm respectively) and an average concentration of 13 ppm for Te (Figure 4). Sample 212.4 returned average concentrations of 0.89 ppm Au, 2.6 ppm Bi and 17 ppm Te (Figure 5). Lastly, average concentrations from sample 212.7 were 0.32 ppm Au, 3.4 ppm Bi and 12 ppm Te (Figure 6).

Pyrite was found to be more enriched in Co (average of 2439 ppm) compared to chalcopyrite (average 170 ppm)

across the three samples. Pyrite from sample 138.4 returned lower average Co concentrations than from the other two samples, with core concentrations at approximately 1500 ppm and rim concentrations at 1330 ppm (Figure 4). Pyrite rims in samples 212.4 and 212.7 shared similar average Co concentrations of 3450 and 3432 ppm, respectively. Cobalt concentrations in the cores of these pyrite grains showed more variation, with samples 212.7 and 212.4 containing Co concentrations of 264 ppm and 1735 ppm, respectively (Figures 5, 6).

Sample 212.7 returned the highest average Ni concentration of 1367 ppm (Figure 6). The majority of Ni was hosted within the pyrite rims of this sample, with an average concentration of 1728 ppm compared to an average concentration of 12 ppm for the core domain (Figure 6). Sample 212.4 contained the second highest concentration, although average concentration was considerably less (252 ppm) compared to sample 212.7 (Figure 5). Pyrite associated with chalcopyrite mineralization contained an average Ni concentration of 529 ppm, whereas inclusion-rich pyrite rims returned an average concentration of 135 ppm and cores returned the lowest concentration of 62 ppm (Figure 5). Sample 138.4 returned an overall average Ni concentration of 205 ppm, more similar to sample 212.4 than 212.7 (Figure 4). Pyrite cores within sample 138.4 continued the trend of Ni poor cores, with an average concentration of 114 ppm compared to the rim-zone concentration of 282 ppm (Figure 4).

### Chalcopyrite Trace-Element Results

Chalcopyrite hosts the majority of Ag in the specimens analyzed, with samples 212.4 and 212.7 displaying a further enrichment of Ag along fractures within the chalcopyrite and at crystal boundaries (Figures 5, 6). In sample 138.4, both Ag and chalcopyrite occur in fractures within pyrite grains and immediately surrounding the grains (Figures 3a, 4). Concentration of Ag in chalcopyrite was the highest in sample 212.4 at 590 ppm, whereas samples 138.4 and 212.7 yielded 300 and 260 ppm, respectively.

## Discussion

The trace-element maps outline multiple phases of pyrite mineralization, as defined by distinct changes in the concentration of elements from core and rim domains (Figure 4, 5, 6). Early pyrite cores are characterized by a general lack of Co, Ni, Te, Bi and As, whereas the same elements are enriched in rim domains. Moreover, Co concentrations oscillate in pyrite rim domains, most clearly seen in sample 212.7 (Figure 6), perhaps reflecting fluctuations in the composition of hydrothermal fluids responsible for sulphide precipitation or the kinetics of pyrite crystallization. Late, inclusion-rich pyrite, which is present in samples 212.4 (Figure 5) and 212.7 (Figure 6), is associated with

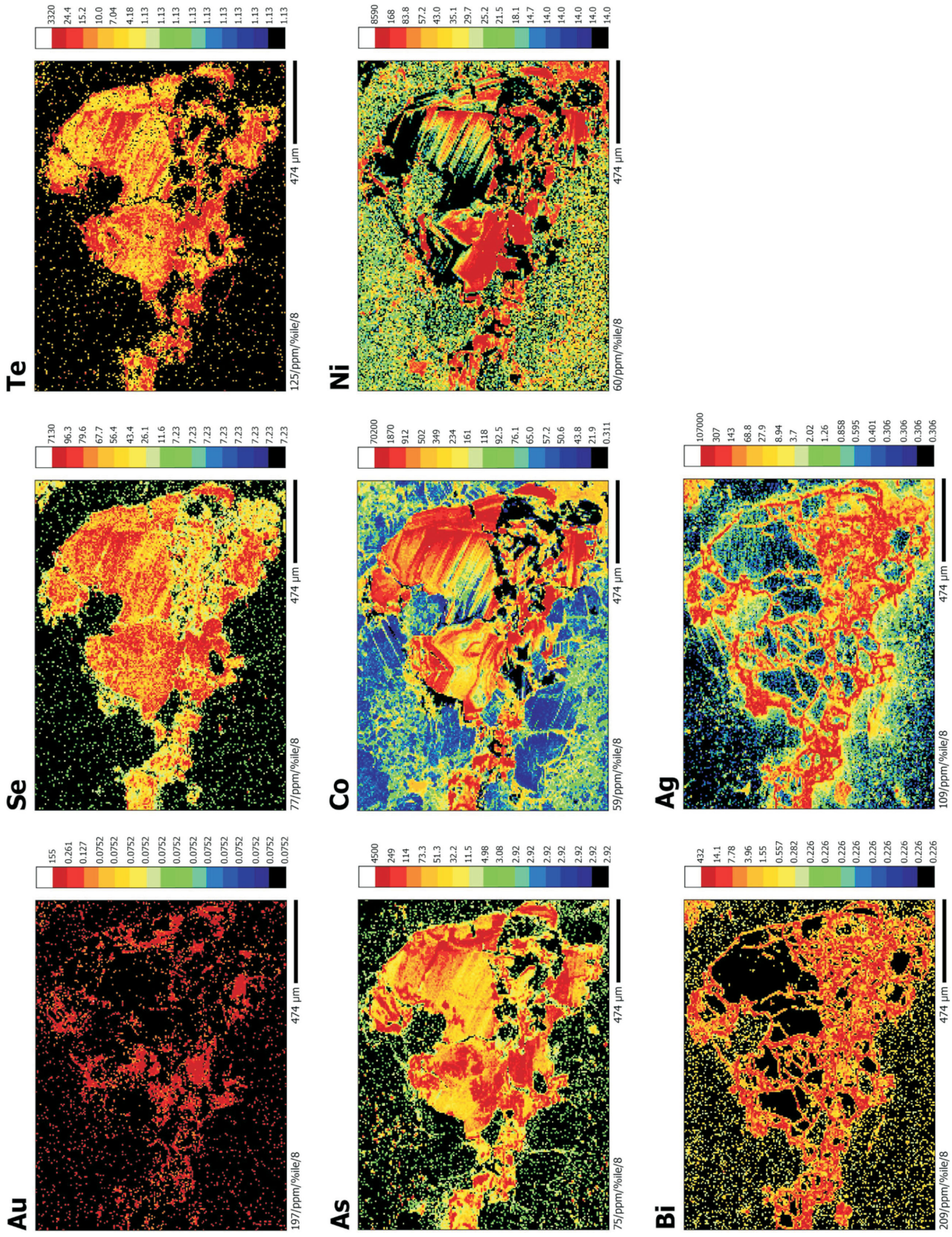


Figure 4. LA-ICP-MS trace-element maps of <sup>197</sup>Au, <sup>77</sup>Se, <sup>125</sup>Te, <sup>75</sup>As, <sup>59</sup>Co, <sup>60</sup>Ni, <sup>209</sup>Bi and <sup>109</sup>Ag in sulphide minerals from sample 138.4. Concentrations are in ppm.

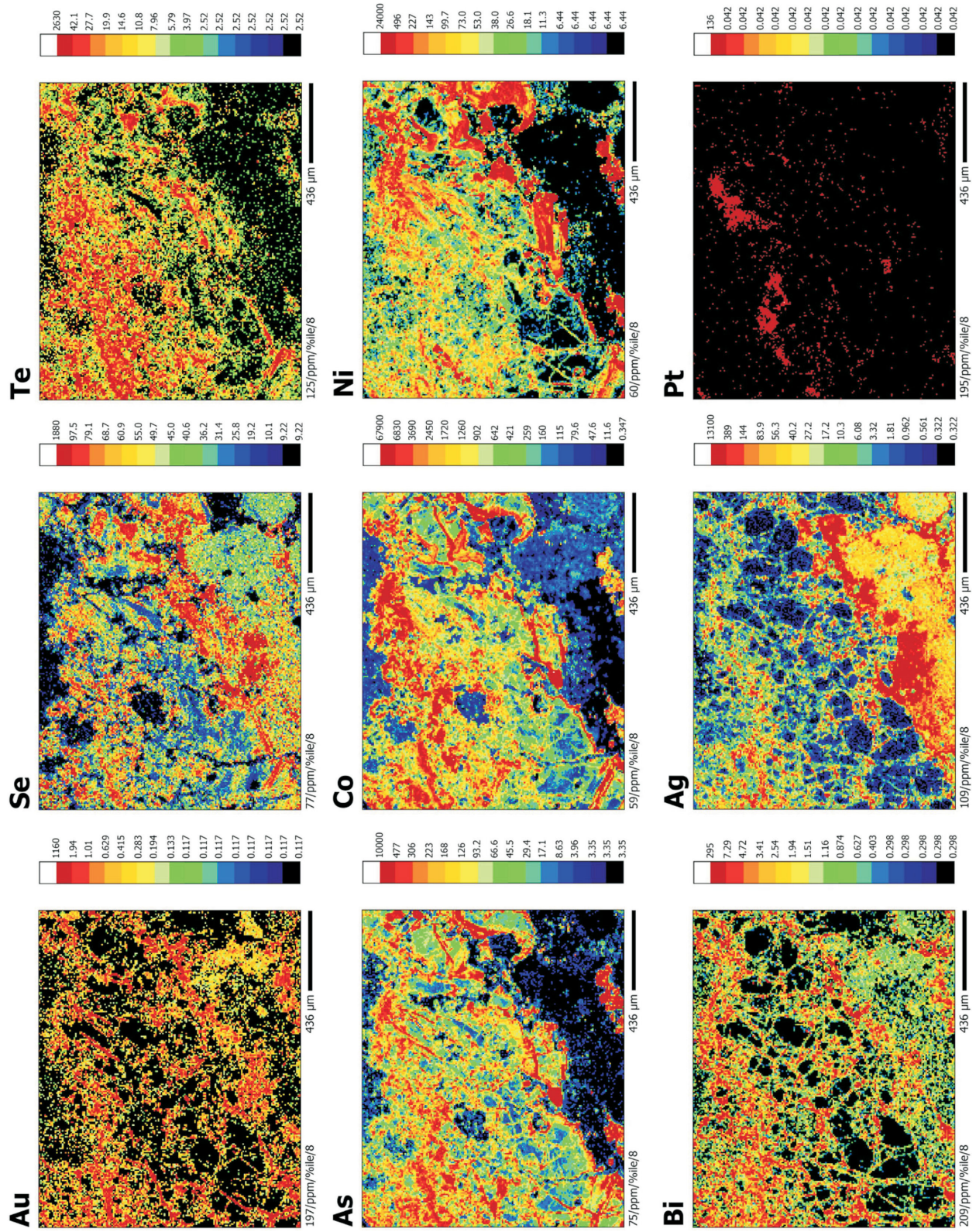


Figure 5. LA-ICP-MS trace-element maps of <sup>197</sup>Au, <sup>77</sup>Se, <sup>125</sup>Te, <sup>75</sup>As, <sup>59</sup>Co, <sup>60</sup>Ni, <sup>209</sup>Bi, <sup>109</sup>Ag and <sup>195</sup>Pt in sulphide minerals from sample 212.4. Concentrations are in ppm.

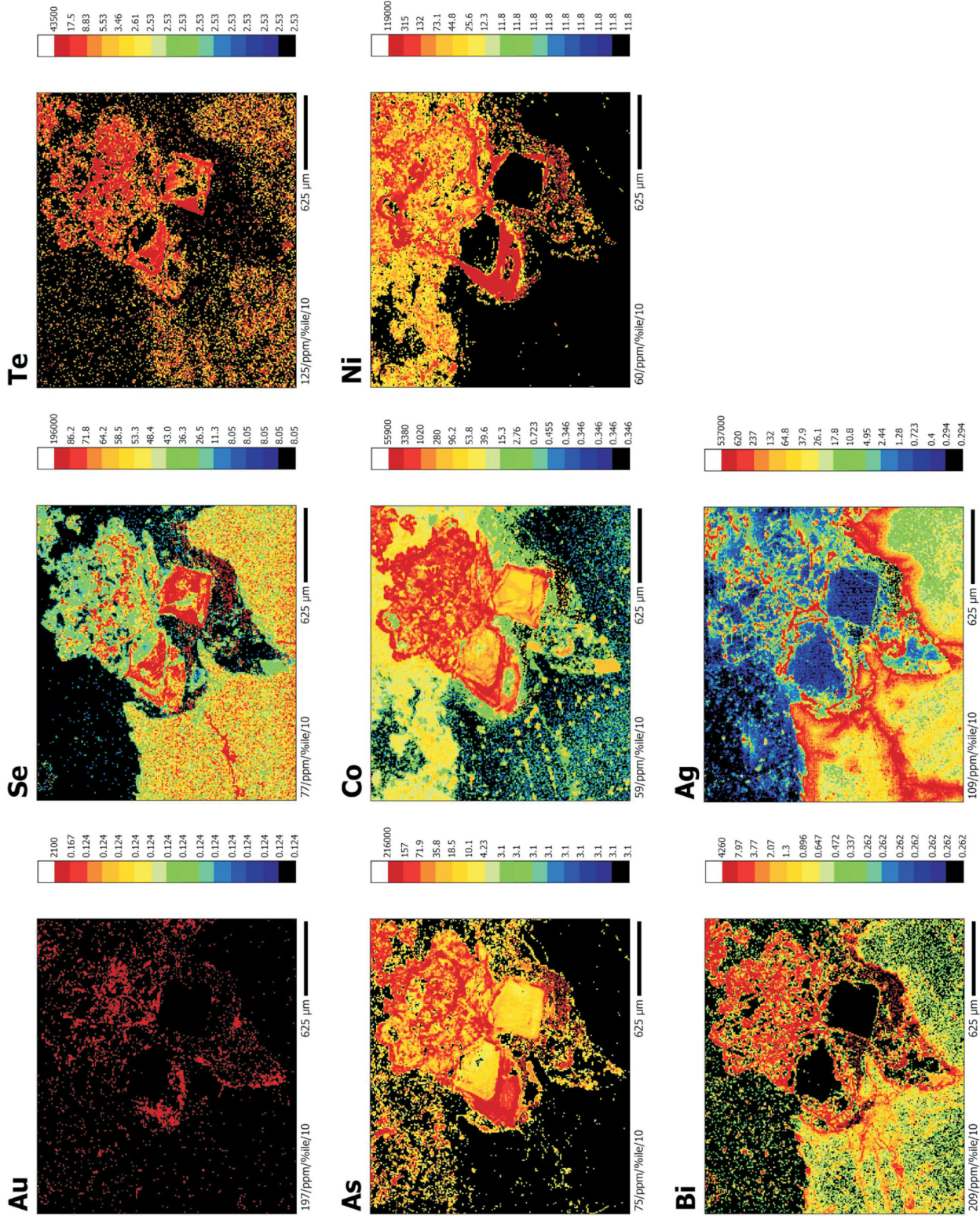


Figure 6. LA-ICP-MS trace-element maps of <sup>197</sup>Au, <sup>77</sup>Se, <sup>125</sup>Te, <sup>75</sup>As, <sup>59</sup>Co, <sup>60</sup>Ni, <sup>209</sup>Bi, and <sup>109</sup>Ag in sulphide minerals from sample 212.7. Concentrations are in ppm.

higher concentrations of Co, Bi, Te, As and Ag, with sample 212.4 additionally containing Pt in these zones.

Both Au and Ag mineralization appears to have been concentrated late in the hydrothermal evolution of the deposit. This is evident from the spatial trends in the trace-element maps, where both elements are absent from the innermost regions of pyrite and chalcopyrite. Instead, they are found primarily in late rims of pyrite or chalcopyrite grains, along fractures through grains or in the matrix between grains. Gold is absent from coarse crystalline pyrite cores in each sample but does occur within rim domains and as micro-inclusions associated with fractures, consistent with it entering the system prior to the latest fracture mineralization.

At the resolution of the analyses, Ag in chalcopyrite appears to occur in solid solution rather than as micro-inclusions. This is reflected by the broad, semicontinuous zones of Ag enrichment in chalcopyrite near grain boundaries and bordering fractures. These textures may indicate late replacement or reprecipitation reactions within chalcopyrite due to late Ag-rich fluids travelling through the system, resulting in the incorporation of Ag into the chalcopyrite crystal lattice.

Separation of quantitative data corresponding to pyrite mineralization through principal-component analysis allowed for further interpretations to be made. As shown in Figure 7, various plots of elements in pyrite can inform the conditions and processes behind mineralization, such as Co and Ni ratios. The Co and Ni ratios have been used to identify the processes responsible for pyrite mineralization, with  $Co/Ni > 1$  indicating hydrothermal processes,  $Co/Ni < 1$  indicating sedimentary processes and pyrite of volcanogenic origin having  $Co/Ni$  values between 5 and 50 (Bajwah et al., 1987). Pyrite formed from magmatic processes is characterized by high concentrations of Ni and Co compared to pyrite from other processes (Bajwah et al., 1987). However, the vast majority of pyrite analyses included as part of the current study yield lower Ni and Co concentrations that are more typical of volcanic and hydrothermal pyrite (Figure 7a). A smaller number of analyses yielded Ni and Co concentrations that are similar to those in pyrite of magmatic and sedimentary origin (Figure 7a). The pyrite cores in all three samples yield compositions that are most similar to volcanogenic pyrite (Figure 7a). Pyrite rims from samples 138.4 and 212.7 display Co-poor sedimentary characteristics, resulting in  $Co/Ni$  values below 1, and plot within the sedimentary field (Figure 7a). The latest pyrite rims in sample 212.7 plot primarily in the hydrothermal (above  $Co/Ni = 1$  line) and volcanogenic (above  $Co/Ni = 10$  line) fields (Figure 7a).

Trends of Ag/Co vs. Co/Cu recorded in pyrite have been used as a relative thermometer to differentiate distal low-temperature zones from proximal high-temperature zones

associated with high-grade mineralization in the core of porphyry deposits (Rivas-Romero et al., 2021). The material analyzed from all three samples generally overlaps the same range of temperature (Figure 7b), with the exception of pyrite-rim domains from sample 212.7 that are consistent with higher temperature pyrite mineralization. The pyrite rims that crystallized at higher apparent temperature may reflect infiltration of high-temperature hydrothermal fluid that accompanied the late mineralization event responsible for the crystallization of pyrite rims. Values of Co/Ni from the same domains plot primarily within the hydrothermal zone (Figure 7a), consistent with such an origin.

Relative Au solubility in pyrite can be visualized in As versus Au plots (Figure 7c). Above the line, Au is expected to occur as inclusions, whereas, below the line, Au may occur in solid solution (Reich et al., 2005). In pyrite, As can substitute for S within the pyrite lattice during periods of rapid pyrite precipitation (Abraitis et al., 2004). Zones with increased As concentration in pyrite are associated with higher concentrations of trace elements because As is typically incorporated into the pyrite lattice through coupled substitution (Abraitis et al., 2004; Lin et al., 2023). Gold is one element that is incorporated into the pyrite lattice through coupled substitution with As, which results in a positive correlation within pyrite (Abraitis et al., 2004; Lin et al., 2023). According to the plot in Figure 7c, the Au that occurs in late pyrite-rim domains, as opposed to fracture-infilling Au, is present primarily in solid solution rather than in inclusions. Although there is an overlap of As- and Au-rich zones in the three samples analyzed in this study, the appearance of Au within pyrite also displays a nugget-like texture (Figures 4, 5, 6, 7c). If Au was being incorporated into pyrite through solid solution, then more gradual homogeneous textures would be expected in the trace-element maps. The nugget-like texture and the As/Au plot indicate that Au is occurring in pyrite as both solid solution and inclusions. Regardless of texture, Au is associated with late pyrite rims and also within the surrounding matrix, indicating that Au mineralization occurred late in the hydrothermal evolution of the system.

The characteristics of the trace-element maps and discrimination plots are consistent with a depleted late-magmatic or post-emplacement hydrothermal event that resulted in the mineralization of pyrite cores depleted in Bi, Te, Co, Ni and Au. Later periods of hydrothermal activity appear to have introduced fluids enriched in Au and critical elements Bi, Te, Co and Ni. Consequently, as pyrite mineralized from these enriched fluids, Bi, Te, Co, Ni and Au were incorporated into rim domains, which the Ni/Co plot also indicates are hydrothermal in origin. The Ag/Co vs. Co/Cu plot indicates that late pyrite-rim mineralization occurred in a high-temperature environment with initial mineralization of Au; later accumulation followed in fractures within pyrite

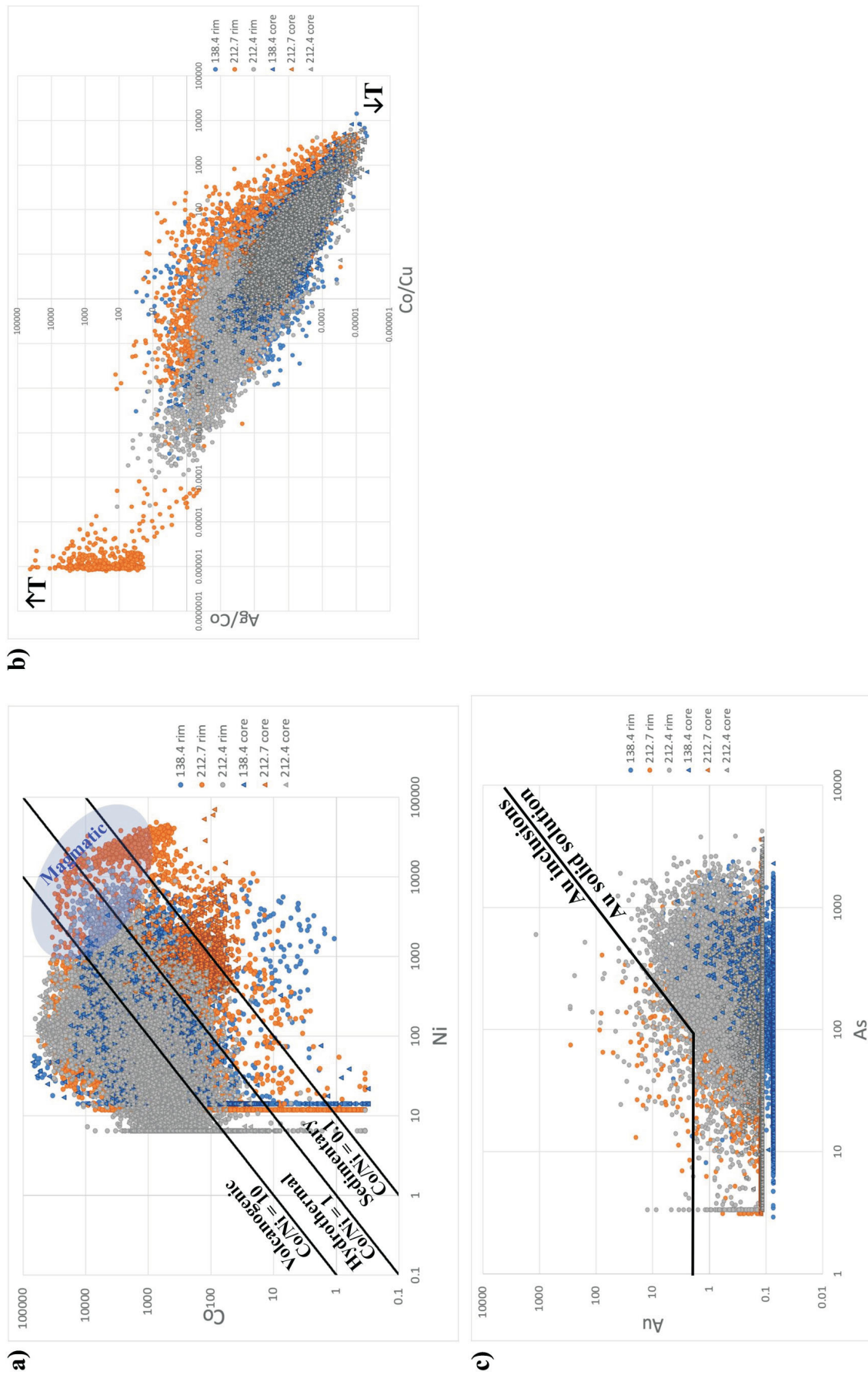


**Figure 7.** Scatterplots comparing trace-element concentrations in pyrite from samples 138.4 (blue), 212.7 (orange), and 212.4 (grey): **a)** Ni vs. Co to determine pyrite origin, the light blue ellipse indicating a magmatic origin; **b)** Co/Cu vs. Ag/Co plot showing temperature of mineralization; and **c)** As vs. Au plot to determine gold solubility in pyrite.

grains and the surrounding matrix. The late fluids also interacted with chalcopyrite within the system, resulting in the incorporation of Ag through either replacement or reprecipitation reactions along chalcopyrite-crystal boundaries and fractures.

### Preliminary Observations

Through trace-element mapping, interpretations have been made regarding the occurrence and abundance of Au, Ag and critical minerals of Bi, Te, Co, and Ni, and the processes that formed mineralization within the Burgundy Ridge prospect. Qualitative and quantitative data from trace-element mapping of sulphides have demonstrated the presence of

- multiple generations of mineralization;
- pyrite cores that have been depleted, and rims that have been enriched, with respect to critical minerals;
- late Ag and Au mineralization; and
- formation of pyrite due to hydrothermal and volcanogenic processes.

Overall, these data provide a detailed initial understanding of sulphide paragenesis within the deposit, with late high-temperature hydrothermal fluids forming the majority of mineralization within the Burgundy Ridge prospect.

### Future Work

The trace-element map data will be combined with in situ sulphur isotope and Rb-Sr geochronology analysis to support current preliminary observations. In situ Rb-Sr geochronology of mica cogenetic with sulphides in the system will be used to determine the timing of mineralization for the Burgundy Ridge prospect. Interpretations from in situ sulphur isotope analysis of chalcopyrite and pyrite from multiple samples throughout the deposit will be used to further determine the conditions of hydrothermal fluids relating to mineralization, such as temperature and pH. Through the Geological Survey of Canada's Targeted Geoscience Initiative, the findings from this study will be combined with other research on silica-undersaturated alkalic porphyry deposits in BC, such as Galore Creek. This will contribute to the overall understanding of these deposit types, which host economically significant amounts of critical minerals and other minerals, such as gold.

### Acknowledgments

Funding for this project has been provided by the Geological Survey of Canada (GSC) Targeted Geoscience Initiative (TGI) program, a GSC Research Assistant Program (RAP) Bursary and a Geoscience BC Scholarship. A. Wasilew, C. Evans and D. Hunko from Enduro Metals Corp., and J. Ryan are thanked for their collaboration and support on this project. The lead author would also like to

thank B. Dyck for reviewing the paper and providing valuable feedback.

### References

- Abratis, P.K., Patrick, R.A.D. and Vaughan, D.J. (2004): Variations in the compositional, textural and electrical properties of natural pyrite: a review; *International Journal of Mineral Processing*, v. 74, p. 41–59.
- Bajwah, Z.U., Seccombe, P.K. and Offler, R. (1987) Trace element distribution, Co:Ni ratios and genesis of the Big Cadia iron-copper deposit, New South Wales, Australia; *Mineralium Deposita*, v. 22, p. 292–300.
- BC Geological Survey (2015): Gold in British Columbia; BC Ministry of Energy, Mines and Low Carbon Innovation, BC Geological Survey, Information Circular 2015-06, URL <[https://www2.gov.bc.ca/assets/gov/farming-natural-resources-and-industry/mineral-exploration-mining/documents/mineral-development-office/gold\\_september\\_2015.pdf](https://www2.gov.bc.ca/assets/gov/farming-natural-resources-and-industry/mineral-exploration-mining/documents/mineral-development-office/gold_september_2015.pdf)> [October 2023].
- BC Geological Survey (2018): The Golden Triangle of northwestern British Columbia; BC Ministry of Energy, Mines and Low Carbon Innovation, BC Geological Survey, Information Circular 2018-05, URL <[https://cmscontent.nrs.gov.bc.ca/geoscience/publicationcatalogue/InformationCircular/BCGS\\_IC2018-05.pdf](https://cmscontent.nrs.gov.bc.ca/geoscience/publicationcatalogue/InformationCircular/BCGS_IC2018-05.pdf)> [October 2023].
- Cabri, L. and Jackson, S. (2011): New developments in characterization of sulfide refractory Au ores; World Gold 2011, 50th Conference of Metallurgists. MetSoc, October 2–5, Montreal, Quebec, p. 51–62.
- Coney, P.J., Jones, D.L. and Monger, J.W.H. (1980): Cordilleran suspect terranes; *Nature*, v. 288, p. 329–333.
- del Real, I., Hart, C.J.R., Bouzari, F., Blackwell, J.L., Rainbow, A., Sherlock, R. and Skinner, T. (2013): Paragenesis and alteration of the Southeast Zone and Deerhorn porphyry deposits, Woodjam property, central British Columbia (parts of 093A); *in* Geoscience BC Summary of Activities 2012, Geoscience BC, Report 2013-1, p. 79–90, URL <[https://cdn.geosciencebc.com/pdf/SummaryofActivities2013/SoA2013\\_delReal.pdf](https://cdn.geosciencebc.com/pdf/SummaryofActivities2013/SoA2013_delReal.pdf)> [November 2023].
- Deyell, C. L. and Tosdal, R. M. (2005): Alkalic Cu-Au deposits of British Columbia: sulfur isotope zonation as a guide to mineral exploration; *in* Geological Fieldwork 2004, BC Ministry of Energy, Mines and Low Carbon Innovation, BC Geological Survey, Paper 2005-1, p. 191–208, URL <[https://www.researchgate.net/publication/255586554\\_Alkalic\\_Cu-Au\\_Deposits\\_of\\_British\\_Columbia\\_Sulfur\\_Isotope\\_Zonation\\_as\\_a\\_Guide\\_to\\_Mineral\\_Exploration](https://www.researchgate.net/publication/255586554_Alkalic_Cu-Au_Deposits_of_British_Columbia_Sulfur_Isotope_Zonation_as_a_Guide_to_Mineral_Exploration)> [October 2023].
- Dickinson, W.R. (2004): Evolution of the North American Cordillera; *Annual Review of Earth and Planetary Sciences*, v. 32, p. 13–45.
- Enduro Metals Corp. (2022): Newmont Lake: our flagship project in British Columbia's Golden Triangle; Enduro Metals Corp., website, URL <<https://endurometals.com/newmont-lake/>> [October 2023].
- Enduro Metals Corp. (2023): Enduro outlines 20 km structural corridor controlling copper-gold mineralization at Newmont Lake; Enduro Metals Corp., press release, May 24, 2023, URL <<https://endurometals.com/enduro-outlines-20km-structural-corridor-controlling-copper-gold-mineralization-at-newmont-lake/>> [October 2023].

- Government of Canada (2022): The Canadian Critical Minerals Strategy; Government of Canada, online document, <<https://www.canada.ca/content/dam/nrcan-rncan/site/critical-minerals/Critical-minerals-strategyDec09.pdf>> [October 2023].
- Guillong, M., Hametner, K., Reusser, E., Wilson, S.A. and Günther, D. (2005): Preliminary characterisation of new glass reference materials (GSA-1G, GSC-1G, GSD-1G and GSE-1G) by laser ablation–inductively coupled plasma–mass spectrometry using 193 nm, 213 nm and 266 nm wavelengths; *Geostandards and Geoanalytical Research*, v. 29, p. 315–331, URL <<https://onlinelibrary.wiley.com/doi/abs/10.1111/j.1751-908X.2005.tb00903.x>> [November 2023].
- Jackson, S. (2008): LAMTRACE data reduction software for LA-ICP-MS; *in* Laser Ablation ICP-MS in the Earth Sciences: Current Practices and Outstanding Issues, P. Sylvester (ed.), Mineralogical Association of Canada, Short Course Series, v. 40, p. 305–307.
- Lang, J.R., Lueck, B., Mortensen, J.K., Kelly Russell, J., Stanley, C.R. and Thompson, J.F.H. (1995): Triassic-Jurassic silica-undersaturated and silica-saturated alkalic intrusions in the Cordillera of British Columbia: implications for arc magmatism; *Geology*, v. 23, p. 451–454.
- Lawley, C.J.M., Petts, D.C., Jackson, S.E., Zagorevski, A., Pearson, D.G., Kjarsgaard, B.A., Savard, D. and Tschirhart, V. (2020) Precious metal mobility during serpentinization and breakdown of base metal sulphide; *Lithos*, v. 354–355, URL <<https://doi.org/10.1016/j.lithos.2019.105278>>.
- Lin, S., Hu, K., Cao, J., Liu, Y., Liu, S. and Zhang, B. (2023): Coupling and decoupling of Au and As in pyrite from Carlin-type Au deposits, southwest China; *Journal of Asian Earth Sciences*, v. 246, URL <<https://doi.org/10.1016/j.jseaes.2023.105582>>.
- Logan, J.M. and Mihalyuk, M.G. (2014): Tectonic controls on Early Mesozoic paired alkaline porphyry deposit belts (Cu-Au ± Ag-Pt-Pd-Mo) within the Canadian Cordillera; *Economic Geology*, v. 109, no. 4, p. 827–858, URL <<https://doi.org/10.2113/econgeo.109.4.827>>.
- Micko, J. (2010): The geology and genesis of the Central Zone alkalic copper-gold porphyry deposit, Calgore Creek district, northwestern British Columbia, Canada; Ph.D. thesis, The University of British Columbia, 359 p.
- Monger, J.W.H. and Gibson, H.D. (2019): Mesozoic-Cenozoic deformation in the Canadian Cordillera: the record of a “Continental Bulldozer”?; *Tectonophysics*, v. 757, p. 153–169, URL <<https://doi.org/10.1016/j.tecto.2018.12.023>>.
- Nelson, J. and Colpron, M. (2007): Tectonics and metallogeny of the British Columbia, Yukon and Alaskan Cordillera, 1.8 Ga to the present; *in* Mineral Deposits of Canada: A Synthesis of Major Deposit-Types, District Metallogeny, the Evolution of Geological Provinces, and Exploration Methods; W.D. Goodfellow (ed.), Geological Association of Canada, Mineral Deposits Division, Special Publication No. 5, p. 755–791.
- Ray, G.E., Jaramillo, V.A. and Ettliger, A.D. (1990): The McLymont northwest zone, northwestern British Columbia: a gold-rich retrograde skarn? (104B); *in* Geological Fieldwork 1990, BC Ministry of Energy, Mines and Low Carbon Innovation, BC Geological Survey, Paper 1991-1, p. 255–262, URL <<https://citeseerx.ist.psu.edu/document?repid=rep1&type=pdf&doi=efa214a1887c945e4e40f25f20f5c27b6459030e>> [October 2023].
- R Development Core Team (2018): R: a language and environment for statistical computing; R Foundation for Statistical Computing, Vienna, Austria, URL <<https://www.R-project.org>> [October 2023].
- Reich, M., Kesler, S.E., Utsunomiya, S., Palenik, C.S., Chryssoulis, S.L. and Ewing, R.C. (2005): Solubility of gold in arsenian pyrite; *Geochimica et Cosmochimica Acta*, v. 69, no. 11, p. 2781–2796 URL <<https://doi.org/10.1016/j.gca.2005.01.011>>.
- Rivas-Romero, C., Reich, M., Barra, F., Gregory, D. and Pichott, S. (2021): The relation between trace element composition of Cu-(Fe) sulfides and hydrothermal alteration in a porphyry copper deposit: insights from the Chuquicamata underground mine, Chile; *Minerals*, v. 11, p. 1–29, URL <<https://doi.org/10.3390/min11070671>>.
- Templ, M., Hron, K. and Filzmoser, P. (2011): robCompositions: an R-package for robust statistical analysis of compositional data; *in* Compositional Data Analysis: Theory and Applications. V. Pawlowsky-Glahn and A. Buccianti, A. (ed.), John Wiley & Sons, Ltd, Chichester, UK, p. 341–355, URL <DOI:10.1002/9781119976462>.
- Tombe, S.P. (2020): Exploration and mining in the northwest region, British Columbia; provincial overview of exploration and mining in British Columbia, 2019; BC Ministry of Energy, Mines and Low Carbon Innovation, BC Geological Survey, Information Circular 2020-01, p. 41–58.

# Revisiting the Stratigraphy of the Alkalic Stuhini Group in the Galore Creek Area, Northwestern British Columbia (Parts of NTS 104G/03, 04)

R.J. Johnston<sup>1</sup>, The University of British Columbia, Vancouver, British Columbia, rjohnston@eoas.ubc.ca

L.A. Kennedy, The University of British Columbia, Vancouver, British Columbia

K.A. Hickey, The University of British Columbia, Vancouver, British Columbia

B.I. van Straaten, British Columbia Geological Survey, British Columbia Ministry of Energy, Mines and Low Carbon Innovation, Victoria, British Columbia

---

Johnston, R.J., Kennedy, L.A., Hickey, K.A. and van Straaten, B.I. (2024): Revisiting the stratigraphy of the alkalic Stuhini Group in the Galore Creek area, northwestern British Columbia (parts of NTS 104G/03, 04); in Geoscience BC Summary of Activities 2023, Geoscience BC, Report 2024-01, p. 59–66.

## Introduction

The Galore Creek alkalic porphyry Cu-Au-Ag deposit is one of several large porphyry systems in the prolific Golden Triangle of northwestern British Columbia (BC; Nelson and van Straaten, 2020; Figure 1), and it is the most silica-undersaturated alkalic porphyry system globally (Lang et al., 1995). Galore Creek is located within the Stikine island-arc terrane, in which volcano-sedimentary rocks of the Devonian–Permian Stikine assemblage are overlain by the Upper Triassic Stuhini Group and the Lower to Middle Jurassic Hazelton Group. At Galore Creek, porphyry-style alteration and mineralization is hosted in, and broadly coeval with, an alkalic volcanic sequence, cut by alkalic intrusive rocks (Enns et al., 1995; Schwab et al., 2008; Byrne and Tosdal, 2014; Micko et al., 2014). The alkalic volcanic rocks are part of the Stuhini Group, and orthoclase-phyric alkalic volcanic rocks have been dated at  $210.27 \pm 0.19$  Ma (van Straaten et al., 2023). The alkalic intrusions, typically orthoclase and/or feldspathoid phyric, are part of the Galore plutonic suite and have been dated between 210 and 208 Ma (Mortensen et al., 1995; Logan and Mihalynuk, 2014).

Across the Golden Triangle, the Stuhini Group is defined by thick mafic to intermediate volcanic rocks and well-stratified clastic sedimentary rocks (Logan and Koyanagi, 1994; Logan et al., 2000). These rock types are present throughout the Galore Creek area but at rare locations within the Golden Triangle (e.g., this study area) they are overlain by a distinctive alkalic volcanic sequence.

Within the Galore Creek deposit area, Enns et al. (1995), Micko (2010) and Micko et al. (2014) recognize lower

augite-phyric volcanic rocks overlain by pseudoleucite-bearing volcanic rocks and/or orthoclase-bearing volcanic rocks. Subsequently, Johnston et al. (2023) and van Straaten et al.'s (2023) work at sites surrounding the deposit identified the upper alkalic sequence overlying the lower intermediate to mafic volcano-sedimentary succession. Herein, the stratigraphy described by Johnston et al. (2023) is revisited and updated based on new field, petrographic and scanning electron microscope (SEM) data.

## Methods

Two field seasons of approximately 60 days each were conducted at Galore Creek in 2022 and 2023. Research focused on mapping deformation, stratigraphy and key crosscutting relationships. Several dozen thin sections from 2022 and 2023 samples were examined with an optical microscope at The University of British Columbia (UBC) in 2023. The SEM analyses were also completed at UBC (Vancouver, BC) in 2023.

## Stuhini Group Stratigraphy

The study area lies immediately west of the Galore Creek deposit area, and coincides with a large, 3 by 11 km, broadly north-south deformation corridor (termed here the Butte ridge deformation corridor) defined by folded and variably foliated volcano-sedimentary rocks of the Stuhini Group (Johnston et al., 2023; Figure 1). The fold axes in the volcano-sedimentary rocks plunge to the south-southwest. The foliation (primarily an axial-planar cleavage) dips to the west to southwest. Ductile penetrative strain of this intensity is rare outside this deformation corridor. Stratigraphic superposition was determined by detailed structural mapping of the deformation corridor, with a focus placed on recording way-up indicators, faults and folds. The Galore Creek region has been affected by several generations of faults, which juxtapose stratigraphy, alteration and earlier deformation features. Major sets of faults include north- and east-directed thrust faults, broadly north-

---

<sup>1</sup>The lead author is a 2023 Geoscience BC Scholarship recipient.

This publication is also available, free of charge, as colour digital files in Adobe Acrobat® PDF format from the Geoscience BC website: <https://geosciencebc.com/updates/summary-of-activities/>.

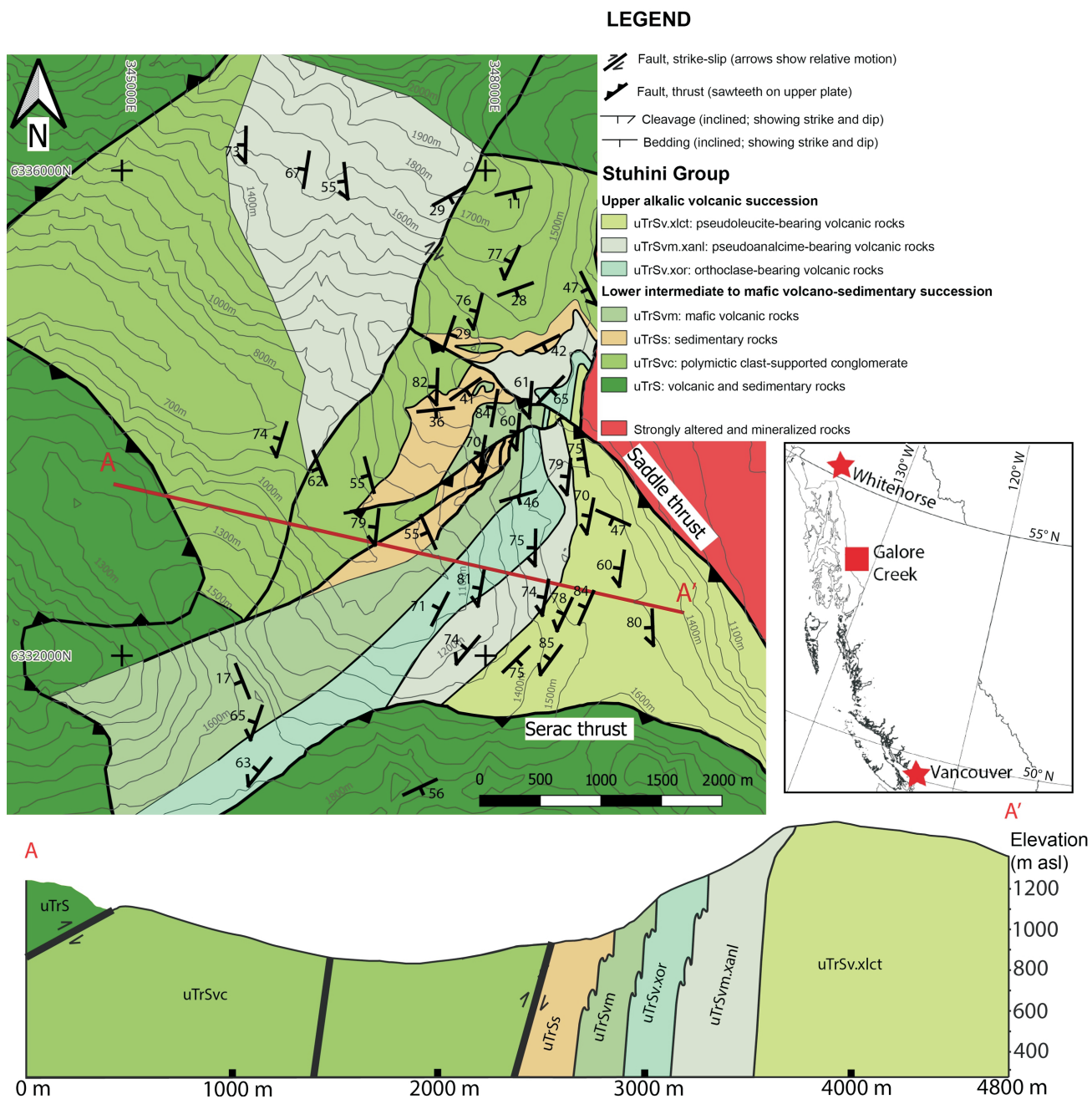


**Figure 1.** Map and cross-section of the Butte ridge deformation corridor west of Galore Creek, northwestern British Columbia (based on 2022 and 2023 field data). Elevation contours in m asl. All co-ordinates are in UTM Zone 9, NAD 83.

striking strike-slip faults and broadly north-striking normal faults.

Units of the Stuhini Group are described below from oldest to youngest.

## Lower Intermediate to Mafic Volcano-Sedimentary Succession

### Volcanic and Sedimentary Unit (uTrS)

Lower Stuhini Group rocks are exposed in the northern, western and southern portions of the study area (Figure 1). This unit is typically composed of thick (>10 m) packages of a) locally augite-bearing mafic volcanic rocks, b) ‘pin-striped’ sandstone and siltstone and c) polymictic pebble-boulder conglomerate.

### Volcanic-Clast-Bearing Conglomerate Unit (uTrSvc)

This unit (Figure 2) comprises polymictic pebble to boulder conglomerate and decimetre to metre thick sandstone beds. The conglomerate is clast supported, with distinct white-weathering intermediate volcanic clasts with feldspar and amphibole phenocrysts, and mafic volcanic clasts with augite phenocrysts up to 3 mm in size. Locally, where augite-bearing mafic volcanic clasts are absent, the conglomerate is matrix supported with pebble- to boulder-sized clasts of white-weathering intermediate volcanic rock set in a chloritized sandstone-siltstone matrix (Figure 3a). This unit is widespread across the northern and western extents of the study area (Figure 1).

### Sedimentary Unit (uTrSs)

A sedimentary unit (uTrSs) conformably overlies and is often interbedded with unit uTrSvc (Figure 2). It is composed of well-stratified siltstone, sandstone (Figure 3b) and locally limestone. Sandstone contains abundant feldspar and quartz grains in a fine-grained chloritized matrix. The unit is exposed in the central part of the study area.

### Mafic Volcanic Unit (uTrSvm)

The mafic volcanic unit (uTrSvm) is composed of augite-bearing mafic volcanic, volcanoclastic and reworked mafic volcanic rocks (Figures 2, 3c, d). Augite crystals are typically <2 mm in diameter. Augite is sparse in this unit and typically composes <10% of the rock by volume. Within the Butte ridge deformation corridor, the unit is mainly composed of reworked volcanic rocks. This contrasts with augite-phyric volcanic clasts in the volcanic and sedimentary unit (uTrS) and the volcanic-clast-bearing conglomerate unit (uTrSvc), which typically contain more abundant and coarser augite crystals. The groundmass of this unit has been metamorphosed and is dominated by actinolite, with minor chlorite and biotite, and plagioclase is present locally (Figure 3c, d). The primary composition of the protolith

groundmass is unclear. This unit is exposed in the western portion of the study area.

## Upper Alkalic Volcanic Succession

### Orthoclase-Phyric Volcanic Unit (uTrSv.xor)

The orthoclase-phyric volcanic unit (uTrSv.xor) contains tuff, crystal tuff, volcanic breccia and reworked volcanic rocks. All contain coarse orthoclase crystals (typically 5 mm in length). The groundmass composition is highly variable between lithofacies, but in the Butte ridge deformation corridor the unit is dominated by a chlorite-carbonate-biotite-white mica groundmass (Figure 3e, f). The SEM analysis shows that white mica contains both paragonite and muscovite. This unit is exposed as a broadly west-trending band north of the Saddle thrust, and a south-west-trending unit south of the Saddle thrust.

### Feldspathoid-Bearing Mafic Volcanic Unit (uTrSvm.xanl)

The augite-pseudoanalcime-phyric volcanic unit (uTrSvm.xanl) encompasses a wide range of lithofacies, including crystal tuff, lesser volcanic breccia and minor sedimentary rocks derived from this unit.

The volcanic rocks contain 10–50% white-weathering trapezohedral pseudoanalcime (3–7 mm) crystals and 10–30% augite (2–4 mm) crystals (Figure 4a). Pseudoanalcime refers to analcime crystals that have been pseudo-morphed into clusters of albite (Figure 4b). The albite clusters commonly form concentrically around the core of each crystal. In general, the groundmass is similar to that of unit uTrSvm and contains abundant actinolite and chlorite, with local plagioclase and biotite, however, groundmass composition is highly variable and is dependent on the lithofacies and augite abundance. This unit is widespread across the Galore Creek area, and within the study area it can be found north and south of the Saddle thrust.

### Coarse Feldspathoid-Phyric Volcanic Unit (uTrSv.xlct)

The coarse feldspathoid-phyric volcanic unit (uTrSv.xlct) is composed of tuff, crystal tuff, volcanic breccia, conglomerate derived from feldspathoid-bearing units, and local sandstone and siltstone.

The volcanic rocks contain 20–50% coarse, flattened and stretched feldspathoid phenocrysts (1 to >3 cm). Broken feldspathoid crystals are common and suggest an extrusive origin. In the field, two textural varieties of the rocks were observed: 1) black- or green-zoned crystals set in a white-weathering groundmass (Figure 4c, d) and 2) white-weathering crystals set in a dark grey to black aphanitic groundmass (Figure 4e, f). Petrographic observations and SEM analysis of the first textural variety indicate that the dark crystals have both orthoclase-dominated and muscovite-dominated zones. These crystals are set in a

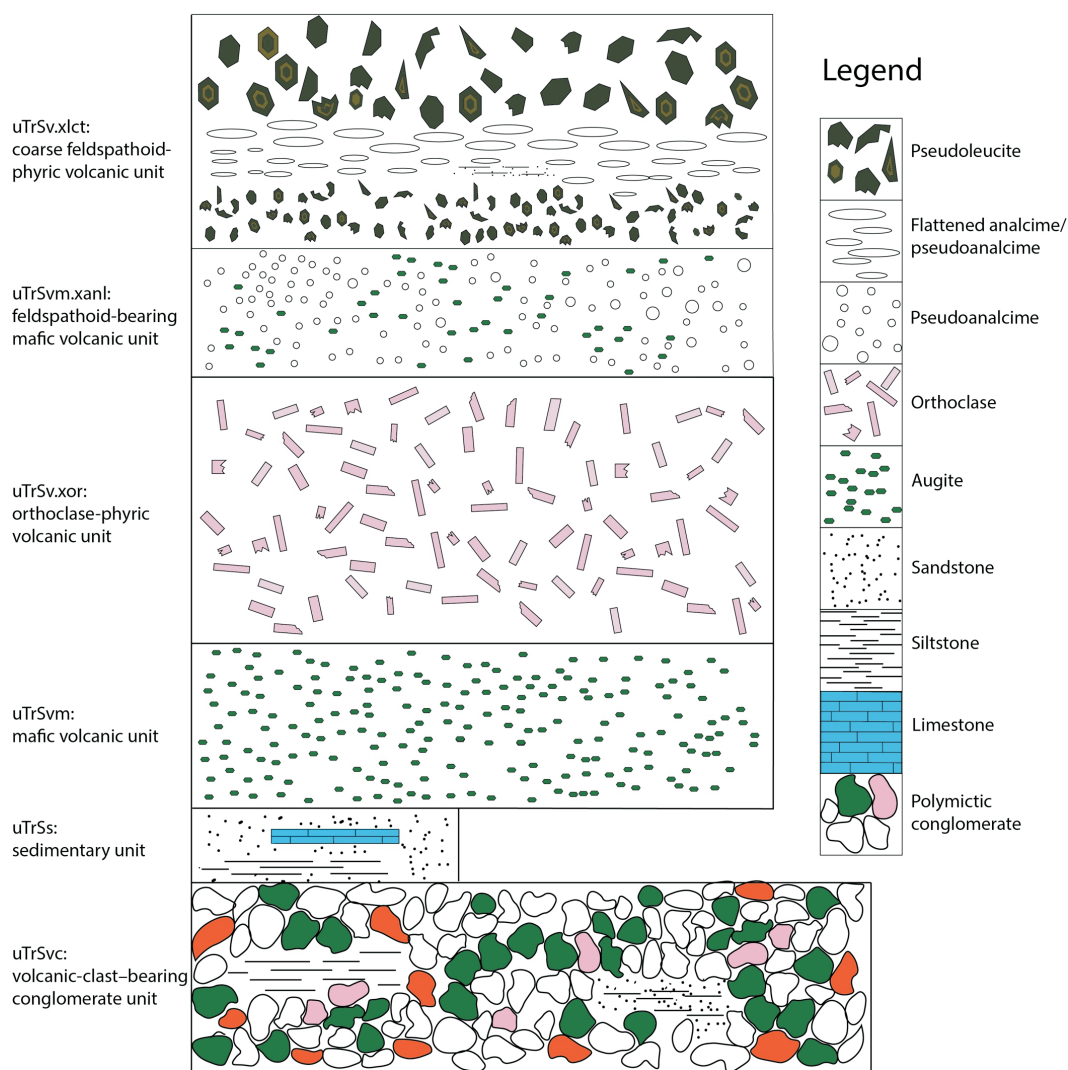


**Figure 2.** Stratigraphic column of the Butte ridge deformation corridor, showing the lower intermediate to mafic volcanic and sedimentary calcalkalic sequence and upper alkalic volcanic stratigraphy, derived from Johnston et al. (2023) and van Straaten et al. (2023). Relative thickness of the units is indicated.

fine-grained orthoclase and white mica groundmass or matrix (Figure 4d). The crystals in this textural variety are interpreted to be pseudoleucite. Petrographic observations and SEM analysis of the second textural variety show that albite ± white mica have pseudomorphed coarse feldspathoid crystals. Relict analcime is often present (Figure 4e, f). The coarse crystals in this textural variety are interpreted to be pseudoanalcime. The contacts between these textural varieties are irregular and cannot always be visually distinguished in the field. This unit is found as a very thick package in the southeastern part of the study area.

## Discussion

The lower calcalkalic stratigraphy seen in the study area is similar to what constitutes the Stuhini Group regionally. Thick packages of augite-bearing mafic volcanic rocks,

interbedded sandstone, siltstone and conglomerate are all common in the Stuhini Group (Logan and Koyanagi, 1994; Logan et al., 2000). Similar augite-bearing mafic volcanic clasts are seen within the volcanic-clast-bearing conglomerate unit (uTrSvc) and the volcanic and sedimentary unit (uTrS). These lower units are overlain by a sedimentary unit (uTrSs) and mafic volcanic unit (uTrSvm), the latter containing distinctly smaller and fewer augite crystals than the lower units.

The upper alkalic succession in the study area represents an unusual package of alkalic silica-saturated and silica-undersaturated rocks not commonly documented elsewhere in the Stuhini Group. The stratigraphic sequence is increasingly alkalic, with orthoclase-phyric volcanic rocks (unit uTrSv.xor) grading into silica-undersaturated, feldspathoid-bearing mafic volcanic rocks (unit uTrSvm.xanl), and finally grading into the uppermost coarse feldspathoid-

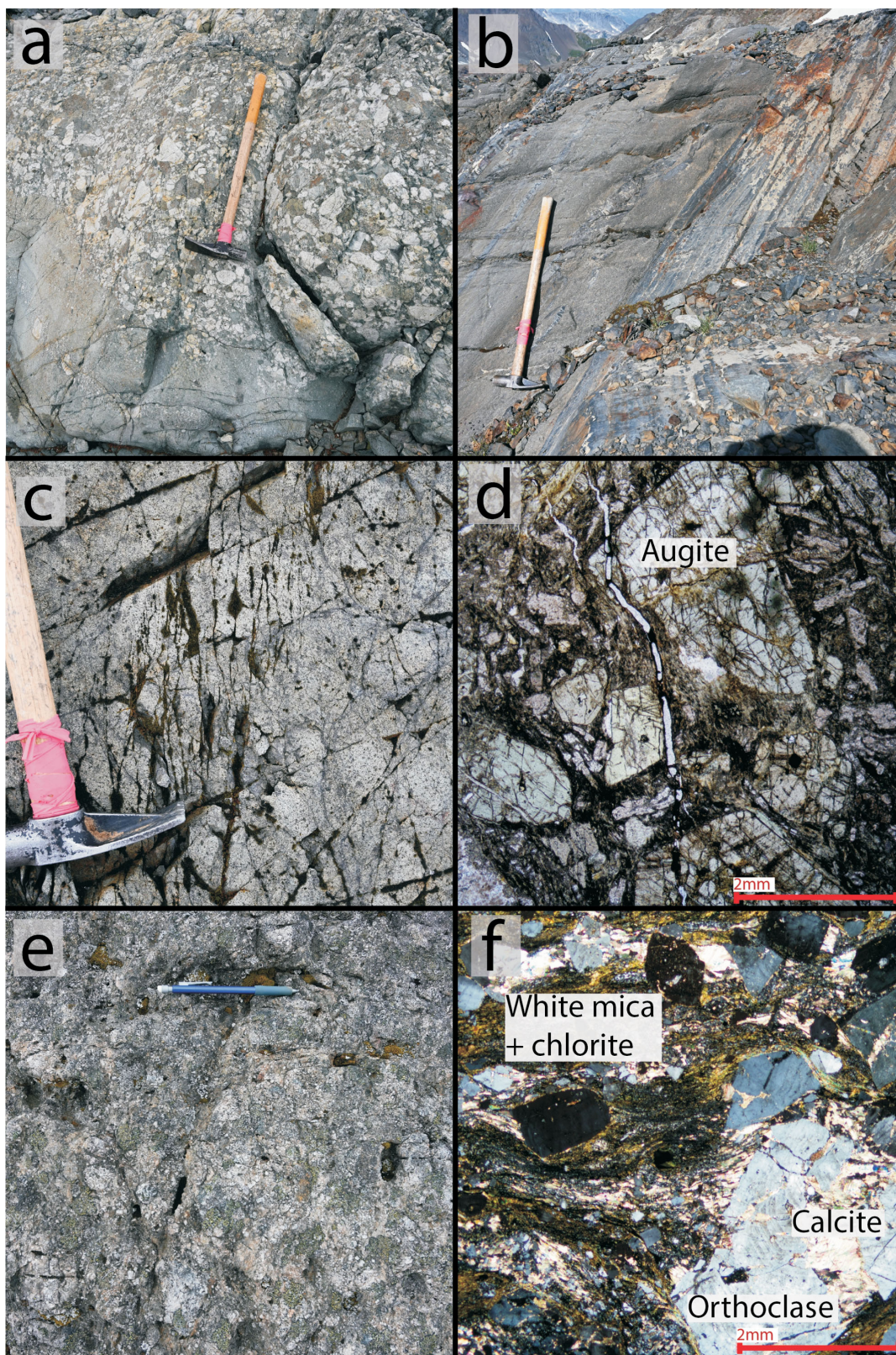


**Figure 3.** Photographs and photomicrographs of the lower intermediate to mafic volcanic and sedimentary succession of the Stuhini Group: a) field photograph of interbedded sandstone and polymictic conglomerate (unit uTrSvc); b) field photograph of interbedded sandstone and siltstone (unit uTrSs); c) field photograph of augite-phyric mafic volcanic rocks (unit uTrSvm); d) photomicrograph showing coarse augite crystals in a micaceous groundmass (unit uTrSvm); e) field photograph of orthoclase-bearing volcanic rocks (unit uTrSv.xor); f) photomicrograph of unit uTrSv.xor showing coarse orthoclase crystals set into a white mica-rich groundmass.

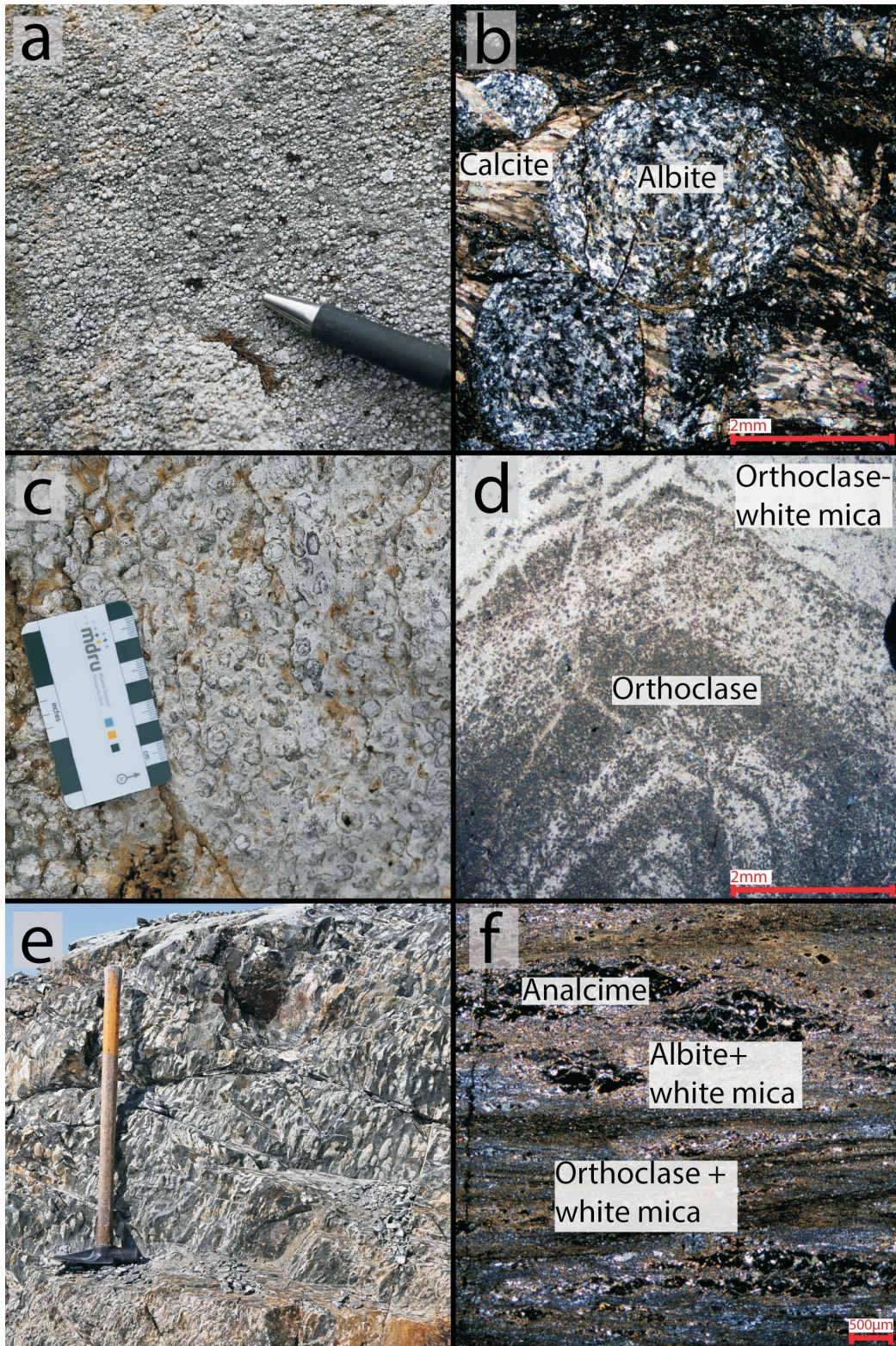


**Figure 4.** Photographs and photomicrographs of the upper alkalic volcanic succession of the Stuhini Group: a) field photograph of the feldspathoid-bearing mafic volcanic unit (uTrSvm.xanl); b) photomicrograph of the feldspathoid-bearing mafic volcanic unit (uTrSvm.xanl); c) field photograph of pseudoleucite crystals in the coarse feldspathoid-phyric volcanic unit (uTrSv.xlct), note the zonation in the crystals; d) photomicrograph of pseudoleucite crystals showing alternating orthoclase- and white mica-bearing zones (unit uTrSv.xlct); e) field photograph of stretched pseudoanalcite/analcite crystals in the coarse feldspathoid-phyric volcanic unit (uTrSv.xlct); f) photomicrograph of relict analcite (isometric minerals) in pseudoanalcite crystals, hosted in the coarse feldspathoid-phyric volcanic unit (uTrSv.xlct).

phyric volcanic unit (uTrSv.xlct). Due to the level of erosion, it is unknown if the coarse feldspathoid-phyric volcanic unit represents the final phase of deposition.

The feldspathoid-bearing rocks present at this site are not common in alkalic porphyry systems globally. This unusual composition has been attributed to a late pulse of Stuhini magmatism (Nelson and van Straaten, 2020).

### Future Work

The stratigraphic observations presented here will be integrated with data and observations from the BC Geological Survey and Galore Creek Mining Corporation. Additional microanalytical work on the upper alkalic volcanic units will be conducted to provide a more complete geological history. Lithochemical analysis of rocks and corresponding petrographic samples will be compared for the purposes of estimating a metamorphic history of the deformed and undeformed rocks.

### Conclusions

The upper alkalic volcanic sequence in the study area has only rarely been documented elsewhere in the Stuhini Group. In the study area, the volcanic stratigraphy of the Stuhini Group becomes increasingly alkalic upward, with the uppermost unit of coarse feldspathoid-phyric volcanic rocks being the most silica-undersaturated unit.

This work provides a revised stratigraphy for the Stuhini Group in the Galore Creek area. Regional explorers should be mindful of the unusual alkalic stratigraphy when exploring for Galore Creek-type porphyry systems in the region. Porphyry-style mineralization at Galore Creek is typically hosted in the upper alkalic stratigraphy (Enns et al., 1995; Schwab et al., 2008; Micko et al., 2014) and alkalic stratigraphy elsewhere may indicate the presence of similar alkalic intrusions that were responsible for mineralization.

### Acknowledgments

The authors would like to acknowledge Galore Creek Mining Corporation for their generous logistical support, and L. Bailey, N. Peterson and W.-S. Lee for their assistance, enthusiasm, helpful discussions and hospitality. The authors thank L. Bailey for a thorough and helpful review of the manuscript. Special thanks to W. Raleigh-Smith for his hard work and exceptional field assistance. This research is supported by a Natural Resources Canada Targeted Geoscience Initiative 5 grant to L.A. Kennedy and B.I. van Straaten. The lead author would like to thank Geoscience BC for providing financial support through the Geoscience BC Scholarship program.

### References

- Byrne, K. and Tosdal, R.M. (2014): Genesis of the Late Triassic southwest zone breccia-hosted alkalic porphyry Cu-Au deposit, Galore Creek, British Columbia, Canada; *Economic Geology*, v. 109, p. 915–938, URL <<https://doi.org/10.2113/econgeo.109.4.915>>.
- Enns, S.G., Thompson, J.F.H., Stanley, C.R. and Yarrow, E.W. (1995): The Galore Creek porphyry copper-gold deposits, northwestern British Columbia; *in* *Porphyry Deposits of the Northern Cordillera*, T.G. Schroeter (ed.), Canadian Institute of Mining and Metallurgy, Special Volume 46, p. 630–644.
- Johnston, R., Kennedy, L. and van Straaten, B.I. (2023): Preliminary observations of a high-strain zone along the western flank of the Galore Creek deposit area, northwestern British Columbia; *in* *Geological Fieldwork 2022*, BC Ministry of Energy, Mines and Low Carbon Innovation, BC Geological Survey, Paper 2023-01, p. 51–63, URL <[https://cmscontent.nrs.gov.bc.ca/geoscience/PublicationCatalogue/Paper/BCGS\\_P2023-01-05\\_Johnston.pdf](https://cmscontent.nrs.gov.bc.ca/geoscience/PublicationCatalogue/Paper/BCGS_P2023-01-05_Johnston.pdf)> [November 2023].
- Lang, J.R., Stanley, C.R. and Thompson, J.F.H. (1995): Porphyry copper-gold deposits related to alkaline igneous rocks in the Triassic-Jurassic arc terranes of British Columbia; *in* *Porphyry Copper Deposits of the American Cordillera*, F.W. Pierce and J.G. Bolm (ed.), Arizona Geological Society, Digest 20, p. 219–236.
- Logan, J.M. and Koyanagi, V.M. (1994): Geology and mineral deposits of the Galore Creek area; BC Ministry of Energy, Mines and Low Carbon Innovation, BC Geological Survey, Bulletin 92, 102 p.
- Logan, J.M. and Mihalynuk, M.G. (2014): Tectonic controls on early Mesozoic paired alkaline porphyry deposit belts (Cu-Au ±Ag-Pt-Pd-Mo) within the Canadian Cordillera; *Economic Geology*, v. 109, p. 827–858, URL <<https://doi.org/10.2113/econgeo.109.4.827>>.
- Logan, J.M., Drobe, J.R. and McClelland, W.C. (2000): Geology of the Forrest Kerr-Mess Creek area, northwestern British Columbia; BC Ministry of Energy, Mines and Low Carbon Innovation, BC Geological Survey, Bulletin 104, 132 p.
- Micko, J., Tosdal, R.M., Bissig, T., Chamberlain, C.M. and Simpson, K.A. (2014): Hydrothermal alteration and mineralization of the Galore Creek alkalic Cu-Au porphyry deposit, northwestern British Columbia, Canada; *Economic Geology*, v. 109, p. 891–914.
- Micko, M.J. (2010): The geology and genesis of the central zone alkalic copper-gold porphyry deposit, Galore Creek district, northwestern British Columbia, Canada; Ph.D. thesis, The University of British Columbia.
- Mortensen, J.K., Ghosh, D. and Ferri, F. (1995): U-Pb age constraints of intrusive rocks associated with copper-gold porphyry deposits in the Canadian Cordillera; *in* *Porphyry Deposits of the Northwestern Cordillera of North America*, T.G. Schroeter (ed.), Canadian Institute of Mining and Metallurgy, Special Volume 46, p. 142–158.
- Nelson, J.L. and van Straaten, B. (2020): Recurrent syn- to postsubduction mineralization along deep crustal corridors in the Iskut-Stewart-Kitsault region of western Stikinia, northwestern British Columbia; *in* *Porphyry Deposits of the Northwestern Cordillera of North America: A 25-Year Update*, E.R. Sharman, J.R. Lang and J.B. Chapman (ed.), Canadian Institute of Mining and Metallurgy, Special Volume 57, p. 194–211.

- Schwab, D.L., Petsel, S., Otto, B.R., Morris, S.K., Workman, E. and Tosdal, R.M. (2008): Overview of the Late Triassic Galore Creek copper-gold-silver porphyry system, northwestern British Columbia, Canada; *in* Ores and Orogenesis: Circum Pacific Tectonics, Geologic Evolution, and Ore Deposits, J.E. Spencer and S.R. Titley (ed.), Arizona Geological Society, Digest 22, p. 471–484.
- van Straaten, B.I., Friedman, R.M. and Camacho, A. (2023): Stratigraphy of the Stuhini Group (Upper Triassic) in the Galore Creek area, northwestern British Columbia; *in* Geological Fieldwork 2022, BC Ministry of Energy, Mines and Low Carbon Innovation, BC Geological Survey, Paper 2023-01, p. 33–49, URL <[https://cmscontent.nrs.gov.bc.ca/geoscience/PublicationCatalogue/Paper/BCGS\\_P2023-01-04\\_vanStraaten.pdf](https://cmscontent.nrs.gov.bc.ca/geoscience/PublicationCatalogue/Paper/BCGS_P2023-01-04_vanStraaten.pdf)> [November 2023].

# Effect of the Specific Pressing Force, Material Moisture Content and Roll Speed on Throughput of the High-Pressure Grinding Roll: Pilot-Scale Test on Copper Mountain Mine Ore, South-Central British Columbia (Part of NTS 92H/07)

**G. Pamparana<sup>1</sup>**, Norman B. Keevil Institute of Mining Engineering, The University of British Columbia, Vancouver, British Columbia, giovannipamparana@gmail.com

**B. Klein**, Norman B. Keevil Institute of Mining Engineering, The University of British Columbia, Vancouver, British Columbia

**M.G. Bergerman**, Department of Mining and Petroleum Engineering, University of São Paulo, São Paulo, Brazil

---

Pamparana, G., Klein, B. and Bergerman, M.G. (2024): Effect of the specific pressing force, material moisture content and roll speed on throughput of the high-pressure grinding roll: pilot-scale test on Copper Mountain mine ore, south-central British Columbia (part of NTS 92H/07); in Geoscience BC Summary of Activities 2023, Geoscience BC, Report 2024-01, p. 67–78.

## Introduction

High-pressure grinding roll (HPGR) technology has gained significant attention for the comminution of hard ores, primarily due to its energy efficiency compared to traditional autogenous (AG) and semi-autogenous grinding (SAG) mill circuits. Studies have demonstrated that HPGR circuits can decrease energy requirements by 10 to 40% (Schönert, 1988; Morell, 2022). Moreover, HPGR comminution also presents downstream benefits, such as improved mineral liberation and reduced particle strength, due to the creation of microfractures along grain boundaries (Ghorbani et al., 2013).

Manufacturers usually perform a series of pilot-scale HPGR tests to obtain the required information to set the standard parameters for industrial use (Rashidi et al., 2017). Pilot-scale testing can also be used to evaluate the performance of the HPGR under different operating conditions, allowing the development of models for purposes such as circuit simulation.

The optimal operation of HPGRs is essential to achieving the desired particle size reduction and product quality while minimizing energy consumption and operating costs. However, achieving the optimal operation of HPGRs can be challenging due to the complexity of the comminution process and the interaction between different operational variables, including properties of the feed material—such as the moisture content—the operating pressure, and the roll speed.

In 2008, a pilot-scale HPGR unit manufactured by the Köppern Group of Hattingen, Germany, was installed at the

Coal and Mineral Processing Laboratory of the Norman B. Keevil Institute of Mining Engineering at The University of British Columbia (UBC) in Vancouver, British Columbia. Over the last 15 years, more than 200 pilot-scale tests were performed with this unit on materials from a range of mineral deposits to assess HPGR comminution, determine design parameters for industrial-scale units, and support academic research.

The aim of this study is to investigate the usefulness of HPGR pilot-scale tests in understanding the relationship between operational variables. A ‘design of experiments’ (DOE) approach was employed, varying the pressing force, roll speed, and moisture content of the feed material, to determine their impact on the product size distribution, specific energy consumption, and overall performance of the HPGR.

## Methodology

### Test Facility and Set Up

The Köppern pilot-scale HPGR installed at UBC (Figure 1) was used to conduct the pilot-scale testing for this study. The rolls of the pilot unit have a Hexadur<sup>®</sup> liner, a diameter of 0.75 m, and a width of 0.22 m. Material to be tested is choke-fed into the unit from a feed hopper located above the rolls. The machine is equipped with a variable-speed drive and a hydraulic system that can apply a pressing force of up to 8 newtons per square millimetre (N/mm<sup>2</sup>). The HPGR programmable logic controller is connected to several sensors that record information from each test through a data-logger for data analysis, including the roller gap, applied pressure, power draw, torque, roll speed and testing time. Table 1 shows the specifications of the installed pilot-scale HPGR unit at UBC.

---

<sup>1</sup>The lead author is a 2023 Geoscience BC Scholarship recipient.

This publication is also available, free of charge, as colour digital files in Adobe Acrobat<sup>®</sup> PDF format from the Geoscience BC website: <https://geosciencebc.com/updates/summary-of-activities/>.



**Figure 1.** Photos of the Köppern pilot-scale high-pressure grinding roll (HPGR) unit installed at The University of British Columbia: **left)** the pilot-scale HPGR unit; **right)** close-up of the HPGR roll's liners.

**Table 1.** Specifications for the components of the Köppern pilot-scale high-pressure grinding roll unit installed at The University of British Columbia. Abbreviations: kN, kilonewtons; kW, kilowatts; N, newtons; rpm, revolutions per minute.

Component	Value
Roll diameter	0.75 m
Roll width	0.22 m
Press drive	Dual output shaft gear reducer
Feed system	Gravity
Wear surface (roll liner)	Hexadur® WTII
Installed power	200 kW
Maximum pressing force	1600 kN
Maximum specific pressing force	8.5 N/mm <sup>2</sup>
Static gap	9 mm
Variable speed drive	Up to 40 rpm (1.55 m/s)

**Table 2.** The three operational factors considered in the design of experiments for the pilot-scale high-pressure grinding roll tests, and the levels at which they were tested. Abbreviations: Max., maximum; Min., minimum; N, newtons.

Letter designator	Operational factor	Units	Min.	Max.	Mean	Standard deviation
A	Force	N/mm <sup>2</sup>	2.5	4.5	3.5	0.79
B	Roll speed	m/s	0.35	0.75	0.55	0.12
C	Moisture content	%	2.5	6	4.43	1.4

## Testing Material

Ore from the Copper Mountain mine near Princeton, in the southern interior of British Columbia, was supplied for HPGR testing. Approximately 5 t of material, from the same geometallurgical unit, was collected from Copper Mountain's SAG mill feed, which had been previously crushed with a gyratory crusher and a cone crusher. Once at UBC, the material was screened and crushed to a maximum particle size of 32 mm, then homogenized and split using a rotary splitter.

A complete exploratory analysis comprising 17 pilot-scale tests was performed on the material. Each pilot-scale HPGR test was run using approximately 300 kg of sample. The moisture content was adjusted and homogenized immediately before each test to avoid segregation of the moisture and evaporation.

## Experimental Program Design

For the HPGR, three operational factors can influence comminution: A—the specific pressing force, B—the roller speed, and C—the moisture content of the material being pressed. For the pilot-scale HPGR, these three variables can be changed relatively easily for each pilot run, allowing a controlled study of how each factor affects the responses of interest.

A custom DOE was developed to assess the effect of the three operating factors. Table 2 shows these three factors and the levels at which they were tested.

For each pilot-scale HPGR test, samples weighing at least 250 kg are required, therefore a total of 17 pilot-scale HPGR tests could be performed with the available material. The experimental design was developed so that most combinations of operational factors and levels could be tested, prioritizing assessing the specific pressing force thoroughly. Table 3 shows the combination of tested variables for each of the 17 tests carried out. Table 3 shows the levels of the factors tested as codes, where -1 corresponds to the minimum level tested for each factor, 0 corresponds to the mean level, and 1 corresponds to the maximum level, as specified in Table 2. Coding the levels of the variables allows for an easy and direct analysis of the effect of each factor independently of their scale.

Each of the 'blocks' shown in Table 3 corresponds to a different part of the experimental design, and each 'block' of tests focuses on different variables. Block 1 is a two-factor DOE, varying the pressing force and roll speed while main-

**Table 3.** Details of the complete experimental design, showing the coded factor levels for each test run, where -1 is the minimum level tested for that factor, 0 is the mean level, and 1 is the maximum level. Each 'DOE block' corresponds to a separate experimental design, in which one of the factors is fixed. Abbreviations: DOE, design of experiments; N, newtons.

Test no.	DOE block no.	Factor A Force (N/mm <sup>2</sup> )	Factor B Roll speed (m/s)	Factor C Moisture content (%)
1	1	-1	-1	-1
2	1	1	-1	-1
3	1	-1	1	-1
4	1	1	1	-1
5	1	0	0	-1
6	1	0	0	-1
7	1	0	0	-1
8	2	-1	0	-1
9	2	1	0	-1
10	2	0	-1	-1
11	2	0	1	-1
12	3	0	0	1
13	3	0	0	0
14	3	-1	0	1
15	3	1	0	0
16	3	1	0	1
17	3	-1	0	0

taining the moisture content at a typical HPGR operational level (2.5% moisture content). This block contains three repeats at mean values (runs 5 to 7) to assess for response variability. Block 2 enhances block 1, testing mean levels of the pressing force and roll speed. Block 3 is another two-factor DOE that varies the pressing force and moisture content while maintaining the roll speed at a typical testing level (0.55 m/s), which expands the testing at mean levels. It must be noted that runs 8 and 9 of test block 2 also include this two-factor design but were not repeated due to limited material availability.

### Responses Tested in the Experimental Program

The following eight responses were recorded during each of the 17 test runs:

- 1) Average operating gap (mm)
- 2) Specific energy consumption (kWh/t)
- 3) Throughput (t/h)
- 4) Specific throughput, or m-dot (tonnes per hour per cubic metre per second [ts/hm<sup>3</sup>])
- 5) Reduction ratio of 50%
- 6) Reduction ratio of 80%
- 7) Flake density (g/cm<sup>3</sup>)
- 8) Flake thickness (mm)

The operating gap is the distance between the rolls when no pressure is applied. It is a critical parameter that affects the product particle size distribution. The specific energy consumption is the amount of energy required to comminute a unit of ore and is an indicator of the circuit's energy effi-

ciency. Throughput is the amount of material processed by unit of time, whereas the specific throughput is the material processed per unitary roll dimensions (a roll of 1 m diameter, 1 m width and rolling at 1 m/s). Both are essential for circuit design and optimization. The 80% and 50% reduction ratios refer to the ratio between the feed ( $F_{80}$  or  $F_{50}$ ) and the product ( $P_{80}$  or  $P_{50}$ ; particle size at which 80% or 50% of the material will pass when screened), indicating the degree of particle size reduction. Flake density and thickness are measured directly from the flakes collected during the HPGR operation. They represent the physical characteristics of the HPGR product and are related to the product size distribution and properties of the ore.

By measuring these particular responses, a holistic view of the HPGR process can be obtained, enabling the identification of optimal conditions for operation and the development of predictive models for scale-up and simulation.

## Results

### Results From the Experimental Design

The results from the 17 pilot-scale HPGR tests performed are summarized in Table 4.

Each of the eight responses recorded during the test runs was modelled individually, to study how each variable affects the operation and outcome of the HPGR. For this study, an initial quadratic model was considered, and then, using the p-value criterion, an elimination process was performed to develop the final model. An 'analysis of variance' was performed on the resulting model to assess the significance of each predictor and the model and if the lack of fit was significant. The resulting coded coefficients and p-values are summarized in Table 5.

The coded coefficients are useful for directly comparing the influence of each predictor over the ranges of predictor levels tested since they are all on the same scale (-1, 0 and 1), meaning that the larger the absolute value of the coded coefficient, the more significant the effect of the predictor on the response (either positive or negative). A model term is considered significant if the p-value is less than 0.05, whereas p-values over 0.1 are considered not significant for the model. The model terms included in the final model with p-values over 0.1 support hierarchy due to interactions or quadratic terms present that include them.

### Analysis of the Results of the Experimental Program

#### Operating Gap

Figure 2 shows how the three operational factors affected the operating gap. As expected, the specific pressing force has the most significant effect. A higher applied force will generate a larger compression of the material and, thus, re-

duce the operating gap. The second largest effect is the moisture content, significantly reducing the operating gap as the moisture content increases. Increased moisture contents can lubricate the physical particle interactions, reducing the overall strength of the particle bed and enabling the gap to collapse. The roll speed has the lowest effect, where an increase reduces the gap.

### Specific Energy Consumption

Figure 3 shows how the three operational factors affect the specific energy consumption. Optimizing energy consumption to obtain the best particle size reduction using the least energy possible is of great interest. As expected, increasing the specific pressing force increases the specific energy consumption due to an increase in the machine's

**Table 4.** Summary of the results of the pilot-scale high-pressure grinding roll tests. Abbreviations: kWh/t, kilowatt-hours per tonne; N, newtons; RR, reduction ratio; t/h, tonnes per hour; ts/hm<sup>3</sup>, tonnes per hour per cubic metre per second.

Test no.	Factor A Force [N/mm <sup>2</sup> ]	Factor B Roll speed [m/s]	Factor C Moisture content [%]	Operating gap [mm]	Specific energy [kWh/t]	Throughput [t/h]	Specific throughput [ts/hm <sup>3</sup> ]	RR <sub>80</sub>	RR <sub>50</sub>	Flake density [g/L]	Flake thickness [mm]
1	2.5	0.35	2.5	22.5	1.51	15.8	268.4	2.39	3.09	2.39	27.4
2	4.5	0.35	2.5	19.9	2.64	14.3	243.3	3.33	4.37	2.39	24.7
3	2.5	0.75	2.5	21.7	1.53	31.6	253.4	2.41	3.39	2.39	25.6
4	4.5	0.75	2.5	19.1	2.71	29	231.8	3.34	4.57	2.39	23.9
5	3.5	0.55	2.5	21.8	1.95	23.8	256.6	3	4.03	2.39	26.2
6	3.5	0.55	2.5	21.4	1.97	23.3	252.5	3.04	3.76	2.38	25.4
7	3.5	0.55	2.5	20.3	2.09	22.8	247.3	2.9	3.49	2.38	25.4
8	2.5	0.55	2.5	21.8	1.49	23.9	258.6	2.46	3.73	2.38	27.4
9	4.5	0.55	2.5	19.4	2.68	21.8	236.9	3.28	4.59	2.38	23.5
10	3.5	0.35	2.5	21.1	2.03	14.8	253.6	3.13	4.42	2.36	25.9
11	3.5	0.75	2.5	19.9	2.12	29.7	237.8	3.08	4.24	2.39	23.8
12	3.5	0.55	6	18.5	2.5	21.8	236.6	2.95	4.34	2.32	22.7
13	3.5	0.55	4.25	19.6	2.27	22.5	244.6	2.85	3.51	2.35	24.7
14	2.5	0.55	6	20.3	1.66	23.6	256.5	2.45	3.23	2.37	25
15	4.5	0.55	4.25	17.7	3.02	20.4	220.2	3.51	4.36	2.33	21.9
16	4.5	0.55	6	16.6	3.1	20	219.8	3.22	4	2.31	20.4
17	2.5	0.55	4.25	21.4	1.55	24.1	260.9	2.71	3.95	2.35	26.7

**Table 5.** Summary of the coded linear regression (intercept and coefficients) and p-values for each of the eight responses measured in the pilot-scale tests. Factor A is the specific pressing force, factor B is the roll speed, and factor C is the moisture content.

Response	Intercept	Factor A	Factor B	Factor C	Factor A x factor C
Operating gap	19.65	-1.51	-0.46	-1.07	
<i>p-values</i>		< 0.0001	0.03	0.02	
Specific energy consumption	2.23	0.67		0.14	0.08
<i>p-values</i>		< 0.0001		0.03	0.02
Throughput	22.25	-1.51	7.57	-0.53	-0.44
<i>p-values</i>		< 0.0001	< 0.0001	0.21	0.04
Specific throughput	243.52	-16.26	-7.06	-4.25	-4.17
<i>p-values</i>		< 0.0001	0	0.17	0.01
Reduction ratio 80%	2.95	0.43			
<i>p-values</i>		< 0.0001			
Reduction ratio 50%	3.99	0.45			
<i>p-values</i>		0			
Flake density	2.36	-0.02		-0.01	-0.02
<i>p-values</i>		0		0.13	0
Flake thickness	23.88	-1.77	-0.77	-1.73	
<i>p-values</i>		< 0.0001	0.01	0.01	

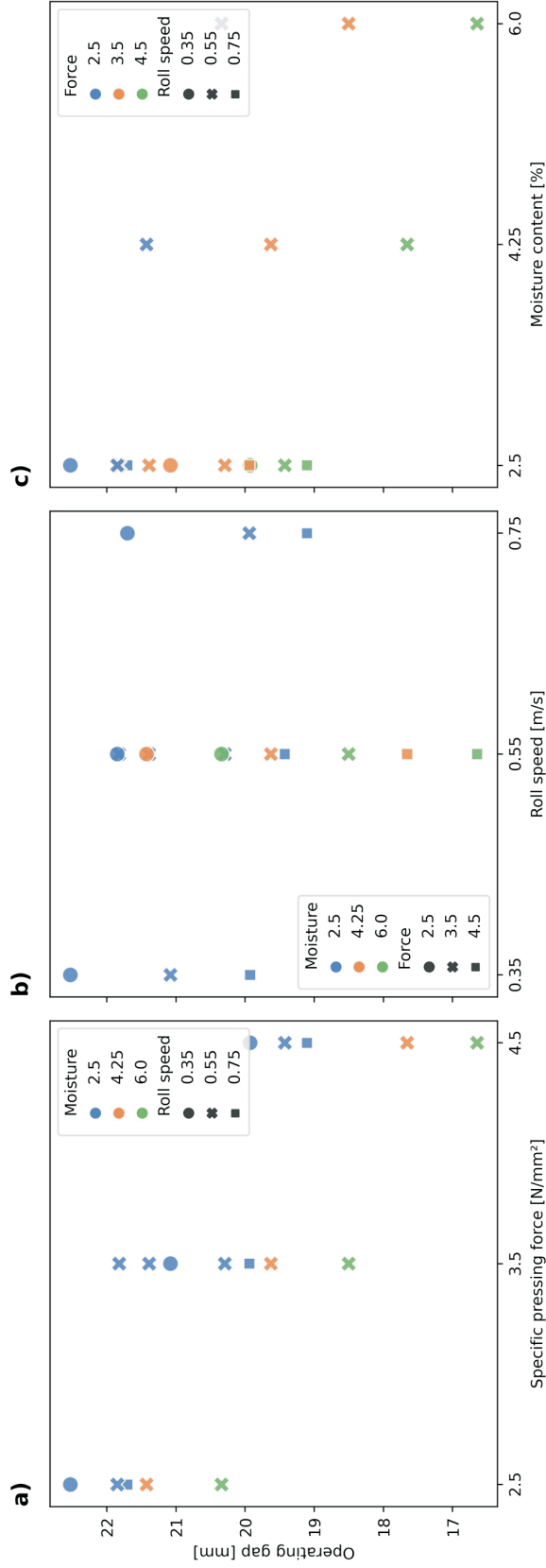


**Figure 2.** Effect of the operational factors—**a**) specific pressing force, **b**) roll speed, and **c**) moisture content—on the operating gap. Abbreviation: N, newtons.

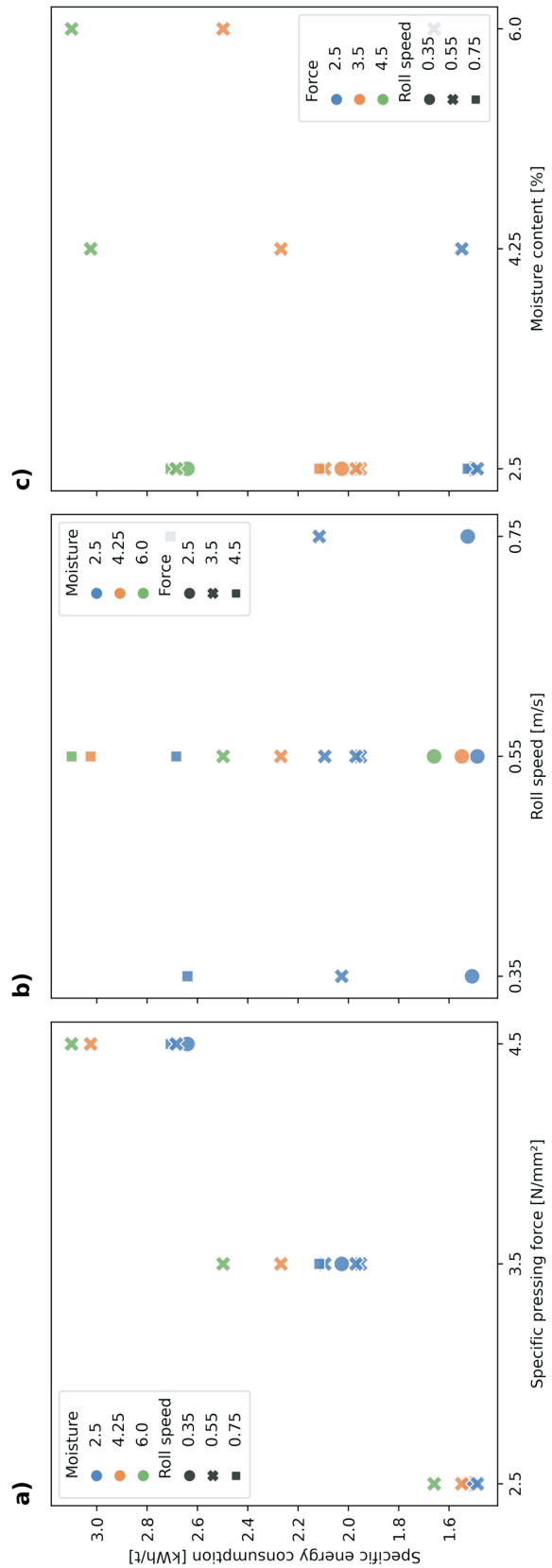


**Figure 3.** Effect of the operational factors—**a**) specific pressing force, **b**) roll speed, and **c**) moisture content—on the specific energy consumption. Abbreviations: kWh/t, kilowatt-hours per tonne; N, newtons.

power to apply more force. The roll speed does not affect the specific energy consumption. The moisture content has a small impact on the specific energy consumption, indicating that higher moisture content will consume more energy.

### Throughput

Figure 4 shows how the three operational factors affect the HPGR throughput. The roller speed highly affects the throughput, which sets the trend. If little or no slippage is assumed at the operating gap (Lim et al., 1997), the particle bed flows at the same speed as the rolls. The specific pressing force also has a significant effect, such that with increasing specific pressing force, the throughput decreases due to the reduction of the operating gap. The moisture content does not significantly influence throughput, but the interaction between the moisture content and specific pressing force is significant. A combination of the specific pressing force and moisture content can be associated with increased slippage at the rolls, leading to a decrease in the throughput.

### Specific Throughput

Figure 5 shows the effect of the three operational factors on the specific throughput. The specific throughput (referred to as ‘m-dot’) is calculated by dividing the throughput by the roll speed, width and diameter, generating a parameter that can be used for scale-up. Due to this, the specific throughput decreases with an increase of the roll speed, indicating that the best performance is not obtained by running the HPGR the fastest. The specific pressing force also leads to a decrease in the specific throughput, so a balance between the best breakage of the material being pressed and the highest throughput must be achieved when optimizing the HPGR operation. The moisture content has an insignificant effect on the specific throughput, but its interaction with the specific pressing force is significant, similar to the results observed with the throughput.

### Reduction Ratios of 80% and 50%

Figures 6 and 7 shows the effect of the three operational factors on the reduction ratio for the  $P_{80}$  and  $P_{50}$  particle sizes, respectively. The only significant factor is the specific pressing force, which is expected. The roll speed and moisture content are not significant. No interactions or quadratic terms were found to be significant for the modelling.

### Flake Density

Figure 8 shows the effects of the three operational factors on flake density. The flake density is associated with how compact the material gets as it flows through the rolls. As expected, the specific pressing force plays an important role in increasing the compression and is a significant variable. The interaction of the specific pressing force with the moisture content was also significant. Increasing the moisture content allows an enhancement of compression by re-

ducing the friction between the particles. The roll speed had no significant effect on the flake density.

### Flake Thickness

Figure 9 shows how the three operational factors affect the flake thickness. The operating gap is highly correlated to the flake thickness. The flakes serve as a physical indication of the operating gap, with the difference that the flakes expand after being expelled from the rolls. Also, it is important to note that the flake thickness is a manual measurement, subject to higher errors, especially when flakes are uneven. As with the operating gap, the three operational factors had a significant effect on the thickness of the flakes, with the specific pressing force and moisture content having the most significant effect.

### Final Models Based on Measured Responses

Table 6 shows the uncoded coefficients for the linear regression equations that serve to predict the responses over the range of the operational factor levels tested, and Table 7 summarizes the fit statistics for the models, including the coefficient of determination ( $R^2$ ) and standard deviations. The predicted  $R^2$  shows how the model performs when predicting the actual results.

Almost all the models perform very well, with  $R^2$  values of over 0.9, except for the 50% reduction ratio ( $RR_{50}$ ) and flake density predictions. The poor performance of the 50% reduction ratio is due to the simplicity of the model since it only considers the specific pressing force. Figure 7 shows that although there is a trend of the  $RR_{50}$  with the specific pressing force, the dispersion of points for each force level is high, indicating that there has to be another predictor that helps to reduce the prediction error.

The block effect can explain the poor prediction of the flake density. The data is grouped for the tests belonging to blocks 1 and 2, where the flake density is almost the same for all. The data from block 3 deviates from this value due to the change in moisture content. More tests with higher moisture content should be performed to conclude the changes in the modelling. Regardless, the model performs well for low moisture contents, obtaining an error of 0.6%.

### Conclusions

This study presents the results of a pilot-scale high-pressure grinding roll test program conducted on ore from the Copper Mountain mine. A ‘design of experiments’ was performed, which involved varying three operational factors—the specific pressing force, roll speed, and feed moisture content—in 17 tests. Eight responses were recorded during each of the test runs, and for each response, linear regression models were developed, indicating the relative significance of the three operational factors on the eight responses. Operation of the high-pressure grinding roll can

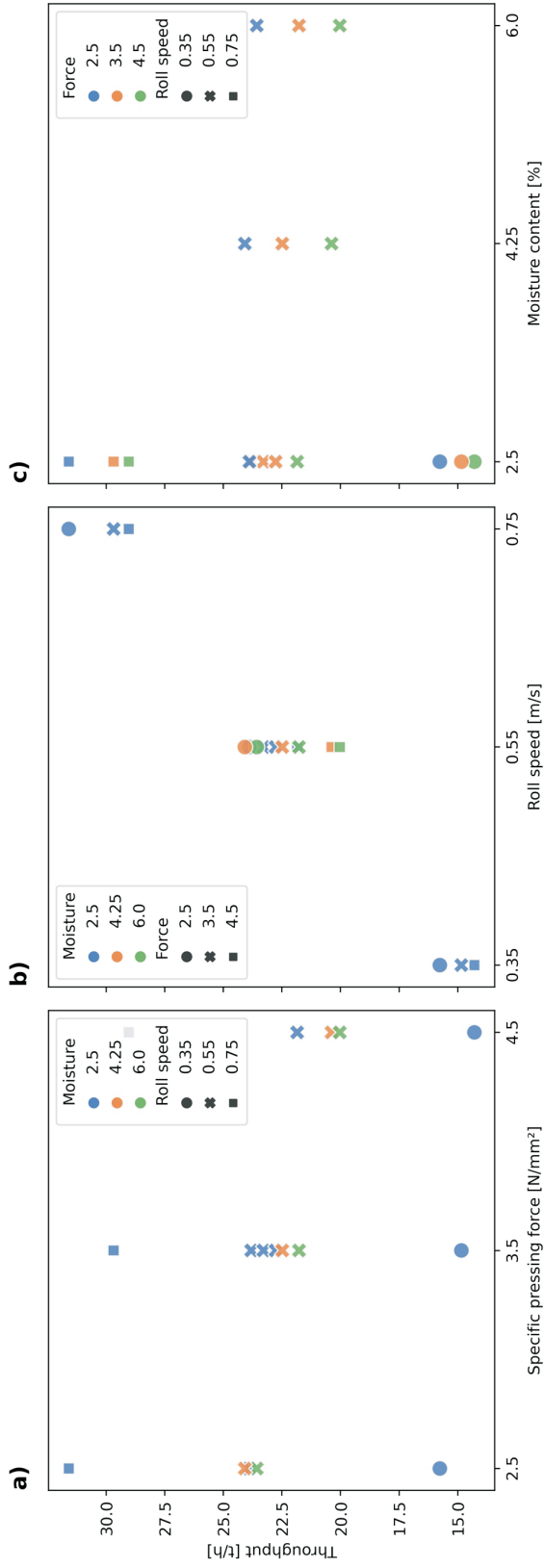


**Figure 4.** Effect of the operational factors—**a**) specific pressing force, **b**) roll speed, and **c**) moisture content—on the throughput. Abbreviations: N, newtons; t/h, tonnes per hour.

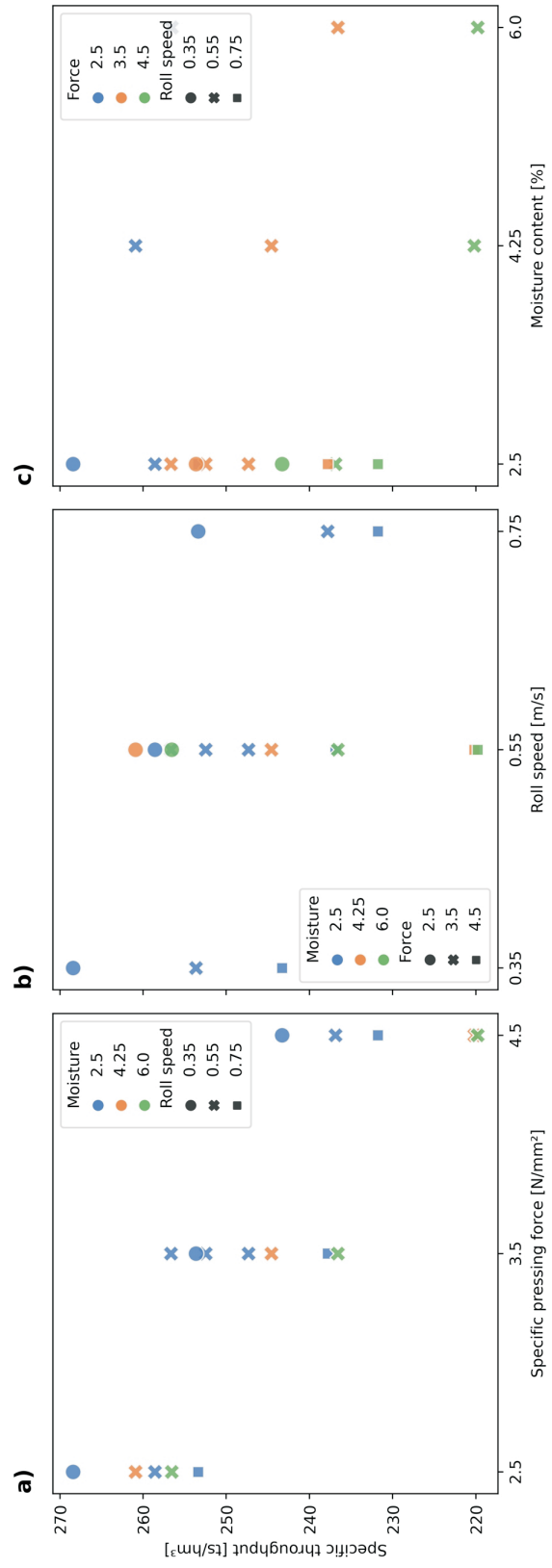


**Figure 5.** Effect of the operational factors—**a**) specific pressing force, **b**) roll speed, and **c**) moisture content—on the specific throughput. Abbreviations: N, newtons; ts/hm<sup>3</sup>, tonnes per hour per cubic metre per second.

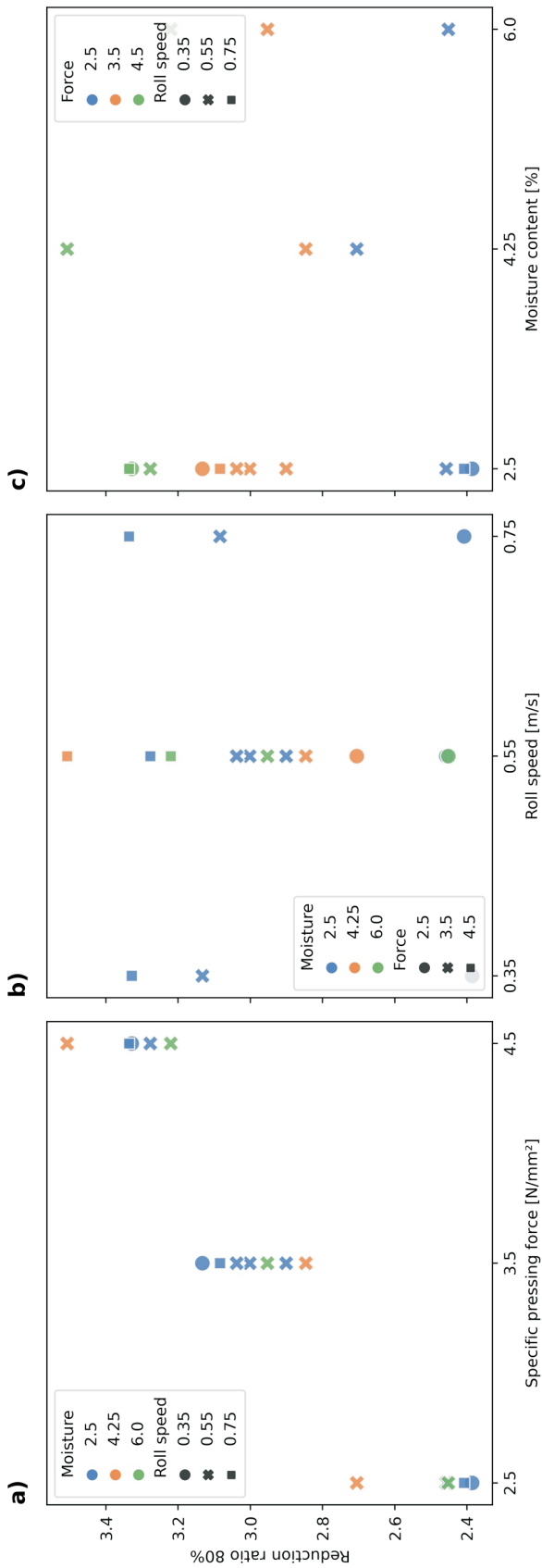


**Figure 6.** Effect of the operational factors—**a)** specific pressing force, **b)** roll speed, and **c)** moisture content—on the 80% reduction ratio. Abbreviation: N, newtons.

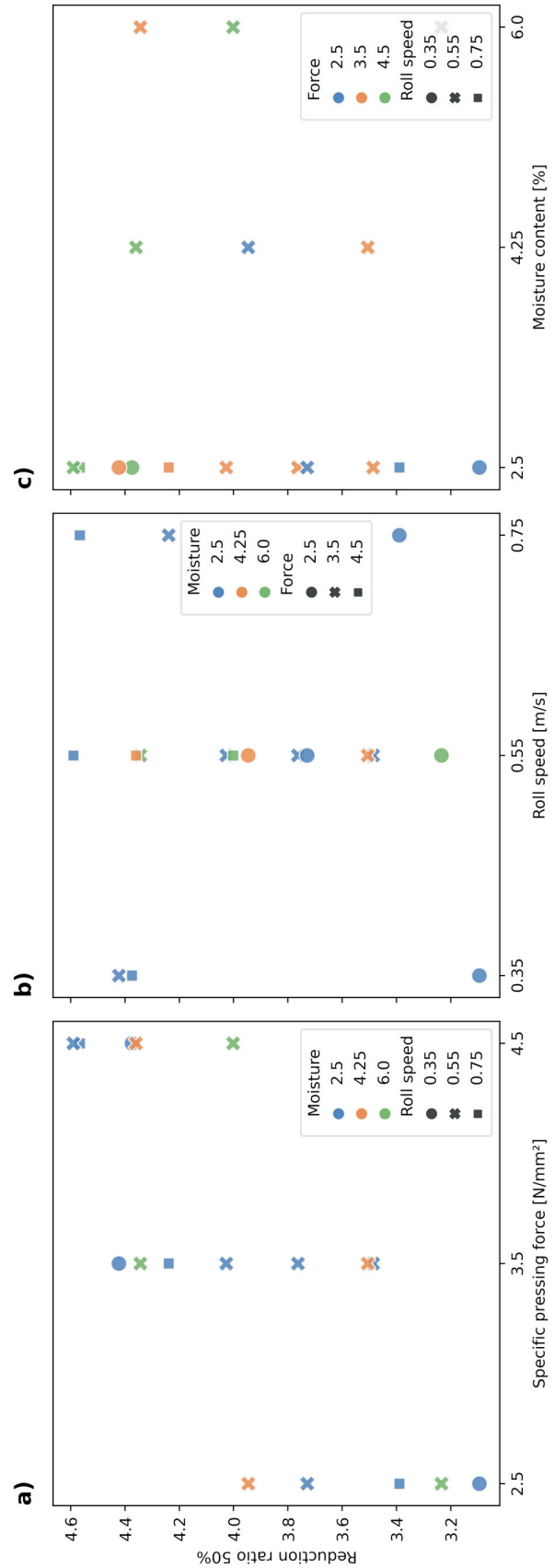


**Figure 7.** Effect of the operational factors—**a)** specific pressing force, **b)** roll speed, and **c)** moisture content—on the 50% reduction ratio.

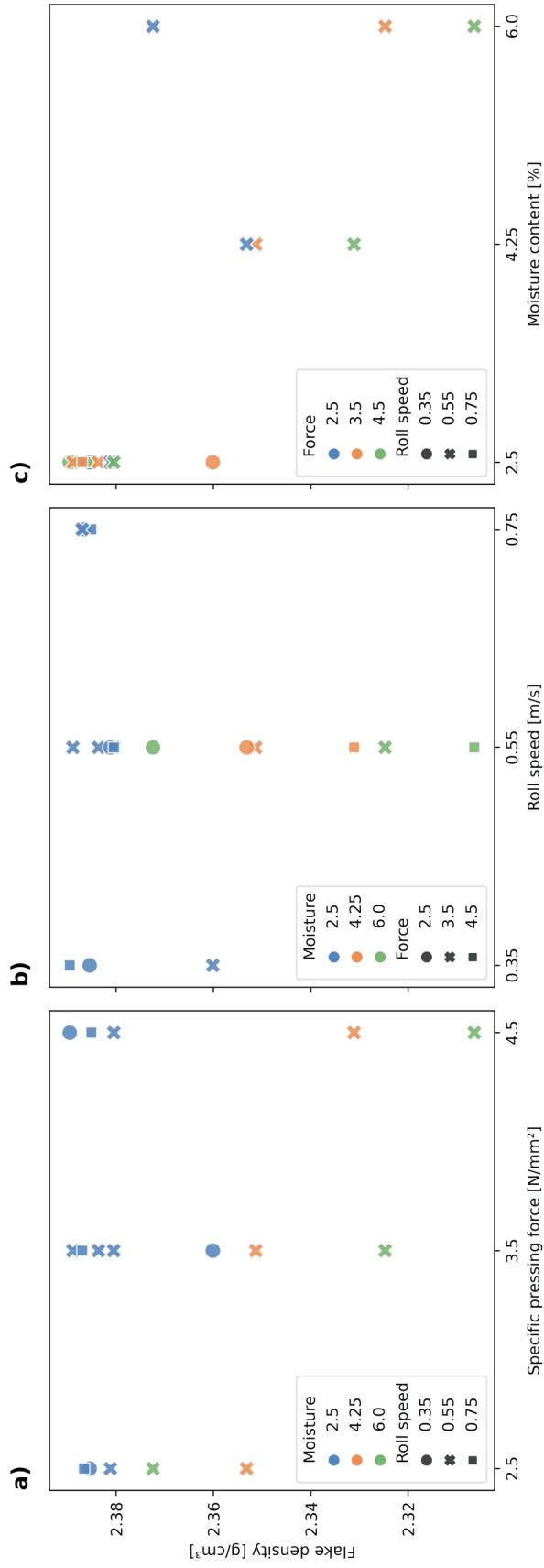


**Figure 8. Effect of the operational factors—**a) specific pressing force, **b)** roll speed, and **c)** moisture content—on flake density. Abbreviation: N, newtons.

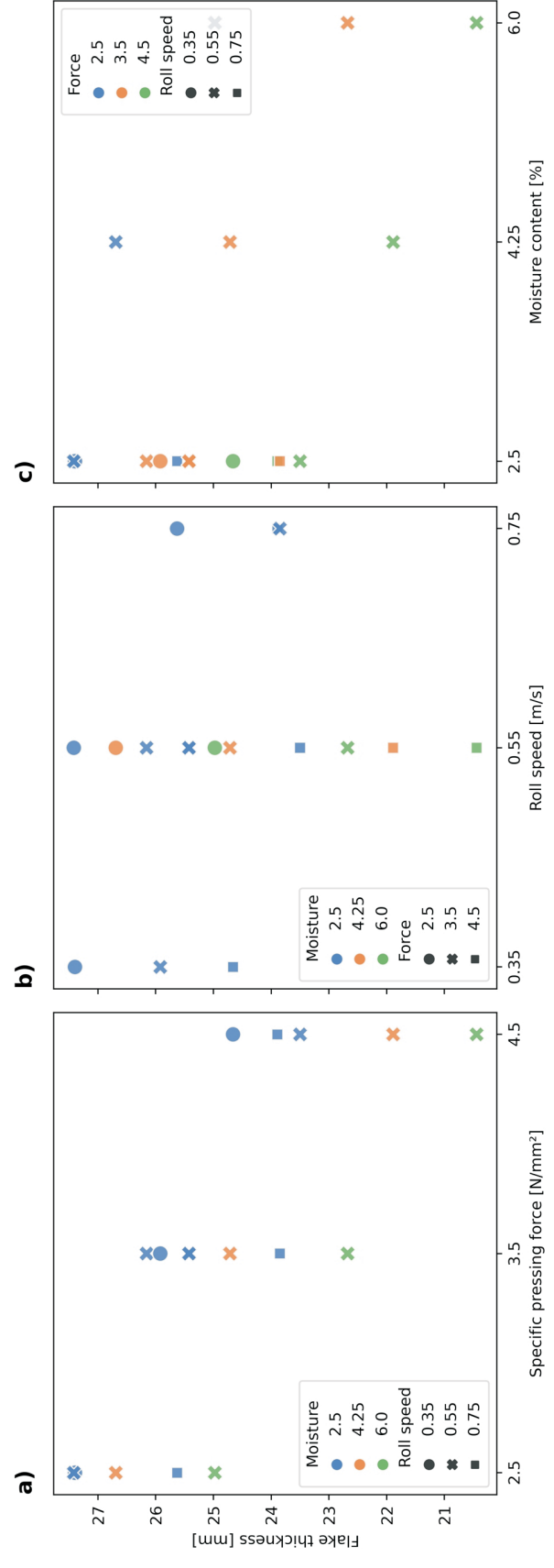


**Figure 9. Effect of the operational factors—**a) specific pressing force, **b)** roll speed, and **c)** moisture content—on flake thickness. Abbreviation: N, newtons.

**Table 6.** Actual (uncoded) linear regression equations (intercept and coefficients) for the measured responses.

Response	Intercept	Force	Roll speed	Moisture content	Force x moisture content
Operating gap	28.82	-1.51	-2.32	-0.61	
Specific energy consumption	0.2	0.48		-0.08	0.04
Throughput	4.28	-0.45	37.84	0.57	-0.25
Specific throughput	294.7	-6.12	-35.32	5.92	-2.39
Reduction ratio 80%	1.46	0.43			
Reduction ratio 50%	2.41	0.45			
Flake density	2.3	0.02		0.03	-0.01
Flake thickness	36.41	-1.77	-3.84	-0.99	

**Table 7.** Fit statistics for the linear regression models developed for each of the responses. Abbreviation: R<sup>2</sup>, coefficient of determination.

Response	Standard deviation	Mean	Coefficient of variance (%)	R <sup>2</sup>	Predicted R <sup>2</sup>	Mean absolute error
Operating gap	0.46	20.19	2.3	0.92	0.83	1.60%
Specific energy consumption	0.07	2.17	3.21	0.99	0.96	2.20%
Throughput	0.48	22.54	2.12	0.99	0.98	1.40%
Specific throughput	3.55	245.81	1.44	0.95	0.85	1.00%
Reduction ratio 80%	0.12	2.94	4.11	0.91	0.83	3.40%
Reduction ratio 50%	0.3	3.95	7.52	0.64	0.4	7.20%
Flake density	0.01	2.37	0.34	0.78	0.34	0.60%
Flake thickness	0.64	24.74	2.58	0.9	0.72	2.10%

be optimized using this data to maximize the throughput while minimizing energy consumption to achieve a specific product particle size target. It was found that the best moisture content for the feed was the lowest possible, at 2.5%. Higher moisture contents led to a decrease in throughput and increased energy consumption.

The results of the experimental program revealed that the roll speed only affects the operating gap and throughput, so the breakage and energy consumption should be kept similar when testing other materials from the same deposit. To keep the breakage constant throughout different geometallurgical units, optimizing the pressing force alongside the roll speed is necessary, since it will also affect the throughput. Due to the poor-performing reduction ratio models, it is not possible to make any conclusions on this aspect of the optimization.

This study highlights the importance of conducting pilot-scale tests and experimenting to optimize the operation of a high-pressure grinding roll in mining operations. The results presented can be used as a tool to enhance the efficiency of high-pressure grinding roll operation and reduce operating costs. The models developed in this study can also be extended to other geometallurgical units with similar mineralogical characteristics, such as the ones within the same deposit.

Future work involves prediction of the high-pressure grinding roll response to the same material by using a piston-and-die press test, which utilizes small quantities of material compared to a pilot-scale test. Ongoing research involves using less than 10 kg of material to predict the specific throughput, specific energy consumption, and size reduction of the high-pressure grinding roll. The results presented in this paper are crucial to understanding the behaviour of the high-pressure grinding roll under different factors. This knowledge will be applied in future modelling using a small-scale test.

## Acknowledgments

The authors would like to acknowledge M. Westendorf, M. Devicente and I. Atutxa for reviewing the paper, and the staff at the Copper Mountain mine (HudBay Minerals Inc.) and Ingeteam for supporting the research. The lead author would like to thank Geoscience BC for providing financial support through the Geoscience BC Scholarship program.

## References

- Ghorbani, Y., Mainza, A., Petersen, J., Becker, M., Franzidis, J.P. and Kalala, J. (2013): Investigation of particles with high crack density produced by HPGR and its effect on the redistribution of the particle size fraction in heaps; *Minerals Engineering*, v. 43–44, p. 44–51, URL <<https://doi.org/10.1016/j.mineng.2012.08.010>>.

- Lim, W.I.L., Campbell, J.J. and Tondo, L.A. (1997): The effect of rolls speed and rolls surface pattern on high pressure grinding rolls performance; *Minerals Engineering*, v. 10, p. 401–419, URL <[https://doi.10.1016/S0892-6875\(97\)00017-4](https://doi.10.1016/S0892-6875(97)00017-4)>.
- Morrell, S. (2022): Helping to reduce mining industry carbon emissions: a step-by-step guide to sizing and selection of energy efficient high pressure grinding rolls circuits; *Minerals Engineering*, v. 179, art. 107431, URL <<https://doi.10.1016/j.mineng.2012.08.010>>.
- Rashidi, S., Rajamani, R.K. and Fuerstenau, D.W. (2017): A review of the modeling of high pressure grinding rolls; *KONA Powder and Particle Journal*, v. 34, p. 125–140, URL <<https://doi.10.14356/kona.2017017>>.
- Schönert, K. (1988): A first survey of grinding with high-compression roller mills; *International Journal of Mineral Processing*, v. 22, p. 401–412, URL <[https://doi.10.1016/0301-7516\(88\)90075-0](https://doi.10.1016/0301-7516(88)90075-0)>.



# Application of Zeolite, Leonardite and Compost as a Tool for Mine Reclamation: A Greenhouse Study Using Tailings from the Historical Afton Mine in South-Central British Columbia (Part of NTS 92I/09)

**B. Bahroudi<sup>1</sup>**, Department of Natural Resource Sciences, Thompson Rivers University, Kamloops, British Columbia, bahroudi.behnaz@yahoo.com

**J. Singh**, Department of Natural Resource Sciences, Thompson Rivers University, Kamloops, British Columbia

**L.H. Fraser**, Department of Natural Resource Sciences, Thompson Rivers University, Kamloops, British Columbia

---

Bahroudi, B., Singh, J. and Fraser, L.H. (2024): Application of zeolite, leonardite and compost as a tool for mine reclamation: a greenhouse study using tailings from the historical Afton mine in south-central British Columbia (part of NTS 92I/09); in Geoscience BC Summary of Activities 2023, Geoscience BC, Report 2024-01, p. 79–92.

## Introduction

The global consumption of mineral resources is on the rise, with a key driver being the shift toward a low-carbon future (Church and Crawford, 2020). This transition is notably fueled by the demand for essential minerals such as copper, crucial for electricity transmission, and other precious metals required for batteries and electric vehicles (Gielen, 2021). This results in more mining excavation to extract the desired minerals, and production of mine waste materials (Plante et al., 2023). Tailings are one type of mine waste material produced during the processing of minerals, which are obtained from a mine source and separated from the ore through a mill, washery or concentrator (Lottermoser, 2010). These materials may contain heavy metals and are required to be deposited in tailings storage facilities (TSFs; Cacciuttolo et al., 2023). The contemporary best practice in constructing TSFs emphasizes the preservation of soils, with the aim of facilitating their future reuse for reclamation purposes. In the TSF construction process, topsoil, subsoil and other materials are typically extracted from land that may extend over several square kilometres and reach tens of metres in depth (Schoenberger, 2016).

Relying on natural processes for the ecological restoration of TSFs filled with mine tailings may take several hundred years (Bradshaw, 1987). Therefore, it is necessary to implement sustainable reclamation practices to facilitate the restoration of TSFs. Studies have shown that improperly managed (e.g., not effectively reclaimed) mine tailings pose an environmental and health risk (Cacciuttolo et al., 2023). In recent decades, significant policies have been put in place and actions have been taken to minimize the environmental

footprint of mining operations by improving reclamation practices. Reclamation is crucial for mining companies and stakeholders aiming to create a functional and sustainable post-mining landscape (Hendrychová et al., 2020). A vital component of this process involves building and enriching the soil, as well as encouraging the establishment of plant and animal communities (Adesipo et al., 2021). However, reclamation of mine tailings is a challenge because of their inferior soil structure due to the lack of nutrients and organic matter (Gardner et al., 2010), and high levels of heavy metals (Hayes et al., 2009).

To reduce the environmental effect of mine tailings and promote vegetation growth and ecosystem development, placing topsoil and subsoil covers on top of the tailings has become a common and direct way of reclamation following mine closure. The topsoil and subsoil that were removed prior to the construction of TSFs can be reapplied and levelled to provide a planting medium (Zhu et al., 1999). However, the disturbed topsoil and subsoil may not be as nutrient-rich as they were prior to removal (Fischer et al., 2022). The act of disturbing the surface layer of soil through stripping, long-time stockpiling and reinstatement can induce notable transformations and movement of nitrogen (N), ultimately leading to substantial loss of nitrogen and significant degradation of the soil over time (Stroh-mayer, 1999; Sheoran et al., 2010; Fischer et al., 2022). Incorporating appropriate amendments to the soil can improve the structure of the microbial community; it can also provide the soil with the necessary organic material and carbon source for reactivating the nutrient cycle, which is the positive interaction between soil and plants where plants use the nutrients stored in the soil and distribute them on the surface as organic matter, and therefore soil can become suitable for the establishment of plants (Bradshaw, 1997; Asemaninejad et al., 2021).

---

<sup>1</sup>The lead author is a 2023 Geoscience BC Scholarship recipient.

This publication is also available, free of charge, as colour digital files in Adobe Acrobat® PDF format from the Geoscience BC website: <https://geosciencebc.com/updates/summary-of-activities/>.

Although there are different types of amendments that can assist with the reclamation of contaminated sites, the use of natural zeolites has gained attention due to their low cost, widespread availability in the world and unique physico-chemical properties (Manu et al., 2022). Natural zeolites are crystalline aluminosilicates that originated from volcanic rocks, and are known for their ion-exchange properties and ability to enhance plant growth, improve soil properties, reduce drought effects and nutrient leachate, mitigate soil contaminations, and increase water retention capacity of the soil (Kesraoui-Ouki et al., 1994; Misaelides, 2011). Another amendment with potential use for mine reclamation is leonardite. Leonardite is a naturally occurring type of oxidized lignite, rich in humic and fulvic acids (Ozdoba et al., 2001). Research findings indicate that the presence of humic substances can lead to favourable outcomes in plant growth. This is attributed to their ability to indirectly influence soil properties, thereby enhancing the absorption of nutrients, promoting soil aggregation, improving aeration, and increasing permeability (Piccolo et al., 1996; Chen et al., 2004). Based on the individual properties of zeolite and leonardite, the combination of these amendments can provide benefits in soil remediation and reclamation. The addition of carbon-rich materials like leonardite has proven highly effective in stimulating microbial activity, whereas zeolite can increase soil sorption capacity and increase the number of micro-organisms in soil because it is porous and acts as an ideal habitat for micro-organisms (Szerement et al., 2023). Furthermore, as the porosity of zeolite absorbs nutrients and the high humic substance in leonardite can improve soil, the mix of these amendments can have the potential to ameliorate degraded soil. More specifically, the findings of a study on agricultural soil in 2014 demonstrated that a slow-release fertilizer derived from leonardite and zeolite exhibited lower nutrient-releasing rates compared to a commercially available fertilizer (Chawakitchareon et al., 2014).

Another beneficial amendment to improve the soil properties of contaminated sites is compost. Compost amendment can improve soil health and foster pollutant degradation. By introducing active micro-organisms, compost enhances the soil's microbial activity and nutrient content, stimulating the natural degradation of hazardous compounds. Additionally, the organic matter in compost can act as a sorbent, reducing the bioavailability of contaminants and preventing their migration (Kästner and Miltner, 2016). Research has shown that even small amounts of compost added to the soil can have a significant impact on the level of organic matter present, especially in the initial growing season (Heiskanen et al., 2022).

It is worth mentioning that the return of these disturbed lands to a sustainable and functional state similar to pre-mining conditions is a regulatory and social licence requirement. In particular, the reclamation of grassland eco-

systems that were disturbed during mining activities is of great importance. Grasslands, specifically in British Columbia (BC), are an endangered ecosystem due to human activities, livestock and invasive plants (Iverson, 2004). As grasslands provide numerous benefits to communities, including erosion protection, habitat for species at risk, carbon sequestration and climate stability, losing grasslands can negatively impact human health and the different communities that live in them (Wetland Stewardship Partnership, 2010). Bluebunch wheatgrass (*Pseudoroegneria spicata*), a perennial native grass, is one of the dominant species in BC grasslands, and its exceptional drought tolerance makes it a great species in semi-arid regions of BC (Tisdale, 1947; Wikeem and Wikeem, 2004).

Despite the potential benefits of these amendments, there is a lack of comprehensive research on their combined application in the context of mine reclamation and the specific impacts on bluebunch wheatgrass growth. Moreover, the influence of compost amendment on these treatments and its role in enhancing soil fertility remains underexplored. Addressing this knowledge gap is crucial for developing effective and sustainable strategies to reclaim TSFs and degraded mine soils, and mitigate the environmental impact of mining operations.

Considering the current environmental challenges and the need for sustainable mine reclamation practices, this paper summarizes the results of a greenhouse study that was designed to 1) investigate the influence of amendments such as zeolite, leonardite and their combination, in two different concentrations, on bluebunch wheatgrass (*Pseudoroegneria spicata*) growth and soil improvement; and 2) examine the effect of the addition of compost in conjunction with the aforementioned treatments on tailings from the historical Afton mine, to assess their combined potential for improving plant growth and soil fertility. Understanding how various amendments and their interactions impact plant growth and soil properties will contribute to the development of innovative and environmentally friendly approaches for the reclamation of the historical Afton tailings storage facility and similar sites.

## Materials and Methods

### Mine Tailings and Amendments

Samples of bulk tailings were obtained from the historical Afton tailings storage facility, and samples of topsoil and subsoil were collected from stockpiles at New Afton mine. New Afton mine is a Canadian gold and copper mine located approximately 350 km northeast of Vancouver and 10 km west of the city of Kamloops, in the south-central interior of BC (latitude 50°39'N, longitude 120°32'W, elevation 700 m; Figure 1). The historical Afton tailings exhibit a coarse texture accompanied by a medium bulk density. The

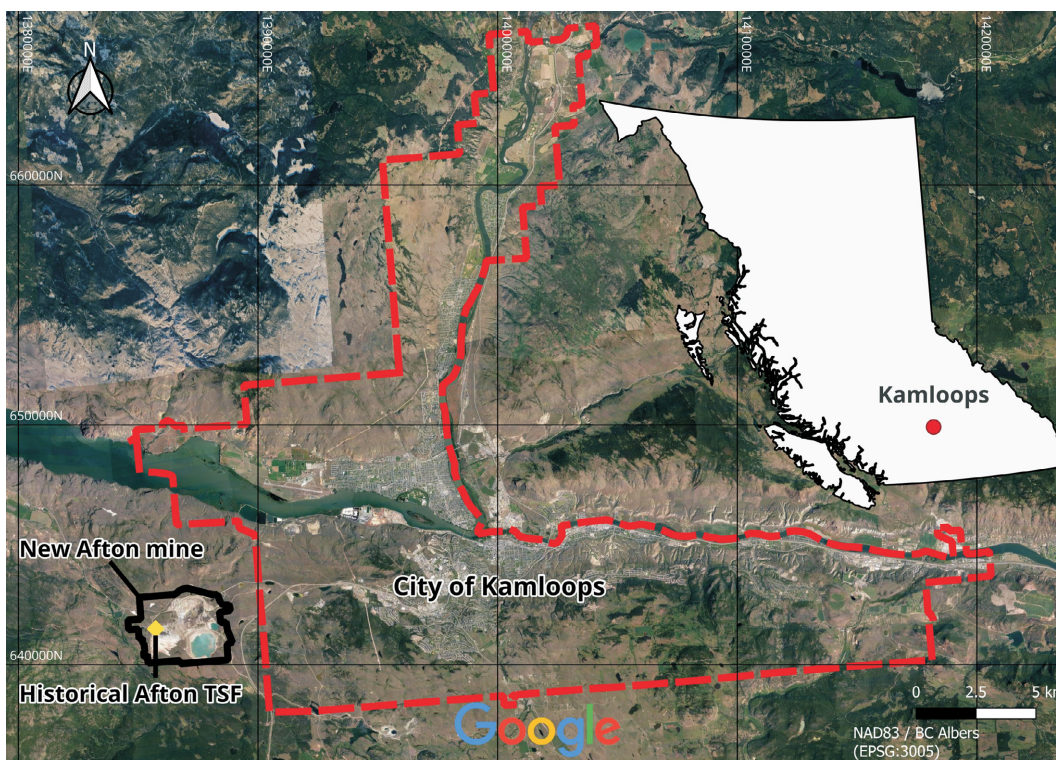


**Figure 1.** Location of the historical Afton tailings storage facility (TSF) and New Afton mine, from which the material used in this study was obtained. New Afton mine is 10 km west of the centre point of the city of Kamloops, British Columbia. Inset shows the location of Kamloops within the province.

tailings are characterized by a moderately alkaline pH and low amount of organic matter, total carbon and total nitrogen (Table 1; Munshower, 1994). Topsoil and subsoil from the New Afton stockpile also had a coarse soil texture, a moderately alkaline pH and low organic matter.

The compost used in this study was made of wood waste, with no soil present (class A compost), and contained a mix of urea and a blend of composting microbes and some fungi and bacteria that are more adept at absorbing hydrocarbons. Leonardite was sourced from the Red Lake deposit, located approximately 40 km northwest of Kamloops, and zeolite from the Bromley Creek mine, approximately 7.5 km southwest of the town of Princeton, also in the south-central interior of BC.

### Design of the Greenhouse Experiment

The greenhouse experiment was carried out at the Thompson Rivers University Research Greenhouse, located in Kamloops, BC, from December 2021 to March 2022. Pots with a diameter of 10.19 cm and a length of 60 cm, connected to water collection drainages, were first filled with 30 cm of tailings, followed by 20 cm of subsoil and 10 cm of topsoil (Figure 2a). Depending on the treatment, zeolite (Z), leonardite (L) or a combination of the two (ZL) were mixed into topsoil at a high (0.0448 kg/m<sup>3</sup>) or low (0.0224 kg/m<sup>3</sup>) ratio of amendments to topsoil. Then, com-

**Table 1.** Chemical and physical parameters of the mine tailings, subsoil and topsoil used in this study. Abbreviations: dS/m, deci-Siemens per metre; EC, electrical conductivity; OM, organic matter; TC, total carbon; TKN, total Kjeldahl nitrogen. The unit of measurement for pH refers to the soil-to-water ratio (1:2).

Substrate/ materials	pH (1:2)	OM (%)	TC (%)	TKN (%)	EC (dS/m)	Bulk density (kg/m <sup>3</sup> )
Tailings	8.38	1.7	0.93	<0.01	3.33	1340
Subsoil	7.98	0.6	1.04	0.0117	5.14	1460
Topsoil	7.98	2.7	1.15	0.0317	3.51	1640

post at a ratio of 1:1 (compost:topsoil) was applied on top of the topsoil to half of the pots. In addition, there were two control pots, both filled with tailings covered by 20 cm of subsoil and 10 cm of topsoil, but one amended with compost and one without compost added. There were, therefore, in total, 12 combinations of Z, L and ZL with and without compost, in addition to the two control treatments. The 14 treatments were replicated six times for a total of 84 pots (Figure 2b).

Ten bluebunch wheatgrass seeds (*Pseudoroegneria spicata*) were planted per pot at approximately 0.5 cm depth in the topsoil, and the pots were randomly placed (Figure 2b) in the research greenhouse. After three weeks of germination, nine of the planted bluebunch wheatgrass seedlings were removed from each pot, leaving one healthy-growing bluebunch wheatgrass seedling in each pot (Figure 3a, b).

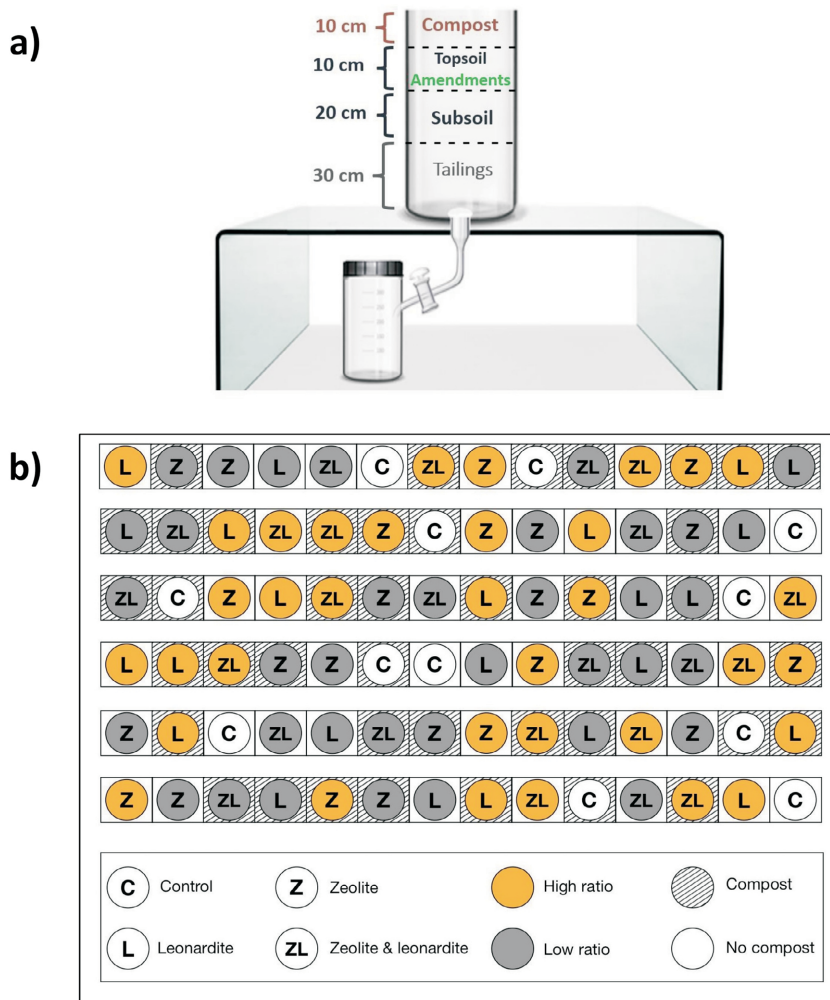


**Figure 2. a)** Example of a study pot. The pots were filled with 30 cm of tailings, 20 cm of subsoil and 10 cm of topsoil. Three different compositions of amendment were mixed into the topsoil (zeolite, leonardite, and a combination of zeolite and leonardite). Additionally, the effect of the presence or absence of compost was examined by placing 10 cm of compost on top of the topsoil in half of the pots. **b)** The design of the study: the variables are the three amendments (i.e., zeolite, leonardite, a combination of zeolite and leonardite) mixed into topsoil in a high ratio ( $0.0448 \text{ kg/m}^3$ ) or a low ratio ( $0.0224 \text{ kg/m}^3$ ) of amendments to topsoil, either with or without the addition of compost (i.e., Compost and No compost) on top of the topsoil. The control treatments are meant to examine the effect of the presence or absence of compost without the addition of the other amendments. The 14 treatments were replicated six times, for a total of 84 pots.

During the experiment, the soil moisture level was measured in each pot at a depth of 20 cm, using a Spectrum® Technologies, Inc. FieldScout TDR 300 soil moisture probe, to ensure a soil moisture balance of 20% in each pot. This moisture balance was maintained by watering every 2–3 days. Growth over the 120 days of the experiment was conducted under controlled conditions meant to replicate the climate of a semi-arid region in south-central BC. These conditions were: natural and artificial light—18 hours of daylight/6 hours of night; temperature—25° C during the day/22° C at night; humidity—40 to 70%; and are based on data recorded at the Kamloops climate station between 1990 and 2012 (Rayne and Forest, 2015).

### Soil, Plant Biomass and Sampling

After the 120 day growth period of the experiment, samples of soil (topsoil and subsoil) were extracted from a depth of 10–20 cm from each of the 84 pots using a stainless-steel soil sampling probe with a core diameter of 2 cm. The soil samples were analyzed for total carbon (TC) and total nitrogen (TN) using a Thermo Scientific™ FlashSmart™ elemental analyzer. Soil preparation for elemental analysis included passing the soil through a 2 mm sieve and air drying within a Yamato™ drying oven (model DKN812) for 48 hours at 85° C to remove moisture. Next, approximately 10–15 mg of the sieved and dried soil were weighed, placed

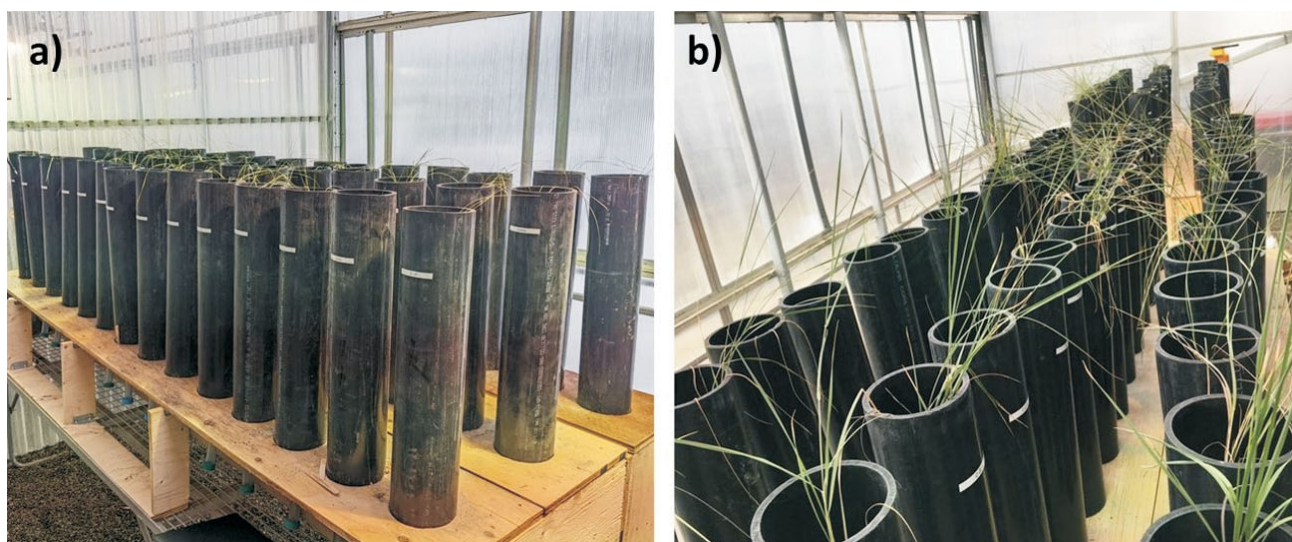


**Figure 3.** Photos of the experimental pots in the greenhouse: **a)** the arrangement shown demonstrates three replicates of the treatments; **b)** close-up of the experimental pots with only one healthy bluebunch wheatgrass seedling retained in each pot.

in small tin capsules and loaded sequentially into the elemental analyzer sample wheel (Gavlak et al., 2005; ThermoFisher Scientific, 2017). Soil organic matter (SOM) content was also determined for all samples by analyzing for loss-on-ignition at 550° C for 4 hours (Singh et al., 2019).

The bluebunch wheatgrass shoots were clipped at the soil surface, and the roots were retrieved from the amended soil and tailings substrate. Plant tissue samples were washed and dried at 65° C for 48 hours, then weighed on an analytical scale to determine root and shoot biomass (Bayliff, 2022).

### Statistical Analysis

All statistical analyses and resultant figures were produced using R version 4.2.3 (The R Foundation for Statistical Computing). In all cases, the experimental treatments were grouped and ranked using Tukey’s HSD (Honestly Significant Difference) test ( $P$  [probability] <0.05). Plant biomass data were checked for normality both visually and using the Shapiro-Wilk test. Homogeneity of variance was assessed using Levene’s test, and, when necessary, the data were transformed using a square root function (Levene, 1960; Shapiro and Wilk, 1965). Furthermore, an aligned rank transformation was applied to the soil data in order to properly run a two-way analysis of variances, as the soil data were not normal prior to analysis (Wobbrock et al., 2011).

## Results

### Soil Total Carbon and Nitrogen

The analysis of total carbon revealed that the addition of both compost and amendments had significant effects on the total carbon content of the soil (Figure 4a). Compost ad-

dition in all treatments exhibited a considerable positive impact, resulting in a substantial increase in total carbon content. Furthermore, a comparison between the Z, L and ZL treatments indicated that the Z treatment made a more significant contribution to the increase of total carbon content in the soil. Similarly, the data for total nitrogen demonstrated that the addition of compost had a significant positive impact across all treatments (Figure 4b). As observed with total carbon, the Z treatments exhibited significantly higher total nitrogen content in the soil compared to the L treatment (Figure 4a, b).

The results of analysis of the C/N ratio highlighted the significant effect of the addition of compost on soil fertility. Differences in C/N ratios were evident between the L and ZL treatments, and also between the Z and ZL treatments (Figure 4c). Both the L and Z treatments exhibited a more positive impact on the C/N ratio compared to the ZL treatments. Notably, the ratio of amendments to topsoil (i.e., high [0.0448 kg/m<sup>3</sup>] or low [0.0224 kg/m<sup>3</sup>]) did not appear to have any significant effect on the carbon or nitrogen content, or the C/N ratio in any of the analyses, therefore this variation in the treatments is not presented in the plots.

These results convincingly demonstrate that the addition of compost has a consistently positive influence on soil carbon and nitrogen content, irrespective of the types of amendments and the ratios of amendments to topsoil. The Z treatment, in particular, proved to be especially effective in enhancing the soil’s total carbon and nitrogen levels.

### Soil Organic Matter

The results of analysis for soil organic matter (SOM) content suggest that both the addition of compost (Figure 5a) and the application of amendment treatments (Figure 5b)

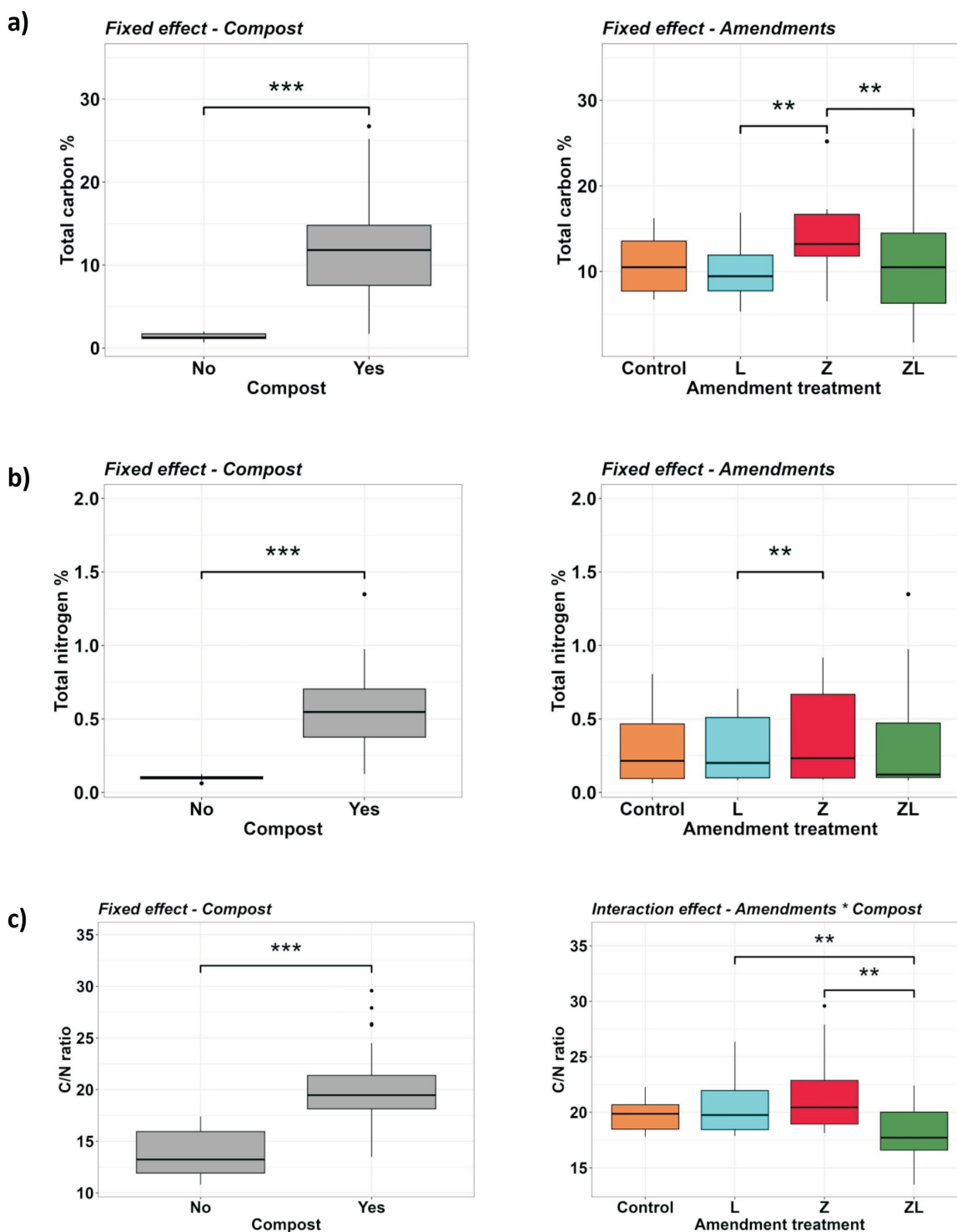


**Figure 4.** Results of analysis for (a) total carbon, (b) total nitrogen, and (c) the carbon to nitrogen (C/N) ratio. The graphs for total carbon and total nitrogen show a significant impact due to the addition of compost (represented as the "Fixed effect – Compost") and amendments (indicated as the "Fixed effect – Amendments"). The C/N ratio was significantly influenced by the addition of compost (represented as the "Fixed effect – Compost") and the interaction between compost and amendments (indicated as the "Interaction effect – Amendments \* Compost"). In all the graphs, pairwise comparisons were conducted within each group that were then compared to the control pots and adjusted with Benjamini-Hochberg corrections. Significance levels were denoted as '\*\*\*' for  $P$  (probability)  $<0.01$  and '\*\*\*\*' for  $P <0.001$ . Non-significant values were omitted from the plots. The main rectangular box represents the interquartile range, and the vertical line inside the box indicates the median. The whisker lines provide a visual representation of the spread of the data. In all the graphs No and Yes mean the absence and presence of compost, respectively. The two different ratios of amendments to topsoil did not significantly influence the total carbon, total nitrogen or C/N ratio; therefore, these results are not presented in the graphs. Abbreviations: L, leonardite; Z, zeolite; ZL, a combination of zeolite and leonardite.

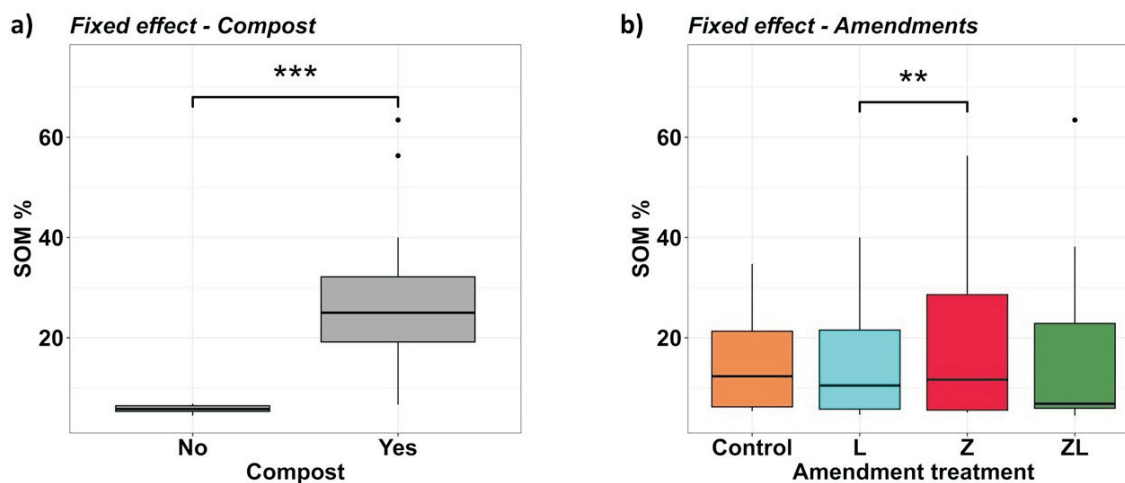


**Figure 5.** Effects of (a) addition of compost (shown as the “Fixed effect – Compost”) and (b) amendments (represented as the “Fixed effect – Amendments”) on the percentage of soil organic matter in the samples. In the graph in (a), No and Yes mean the absence and presence of compost, respectively. In all the graphs, significance levels were denoted as “\*\*\*” for  $P$  (probability)  $<0.01$  and “\*\*\*\*” for  $P <0.001$ . Non-significant values were omitted from the plots. The main rectangular box represents the interquartile range, and the vertical line inside the box indicates the median. The whisker lines provide a visual representation of the spread of the data. The two different ratios of amendments to topsoil, and the interaction of amendments and compost did not significantly influence the percentage of soil organic matter; therefore, these results are not presented in the graphs. Abbreviations: L, leonardite; SOM, soil organic matter; Z, zeolite; ZL, a combination of zeolite and leonardite.

significantly influenced the SOM content. The addition of compost to the soil resulted in a substantial increase in SOM compared to the control and other treatments. Moreover, the results show that pots with the Z treatment exhibited higher SOM content than pots with the L treatment. As with the analyses for carbon and nitrogen, the different ratios of amendments to topsoil did not appear to have any significant effect on the SOM content.

### Plant Productivity

The results of analysis of the biomass in the samples indicate that treatments using compost had a significant positive impact on the growth of bluebunch wheatgrass, resulting in a significantly higher total biomass content than the other treatments (Figure 6a–c), at a confidence level of 95%. However, the addition of Z, L or a combination of the two (ZL) did not result in significant statistical differences in biomass production. Similarly, no significant differences were observed between the different ratios of the amendments to topsoil.

Interestingly, in the compost-amended treatments, the root-to-shoot biomass ratio was less than one. As shown in Figure 7a, the root-to-shoot ratio of plants amended with compost was below the reference line (where the root-to-shoot ratio is one, meaning roots and shoots are present in equal proportions), whereas treatments without the addition of compost were above the reference line. This suggests that compost played a crucial role in promoting the root-to-shoot biomass ratio. Figure 7b further supports this observation, as treatments with compost added showed higher

shoot biomass than root biomass, whereas treatments without compost resulted in higher root biomass than shoot biomass.

These findings highlight the significant influence of compost on bluebunch wheatgrass productivity, particularly in enhancing aboveground biomass. The absence of significant differences among treatments using different ratios of amendments to topsoil indicates that the type and proportion of amendments tested did not exert a notable influence on plant productivity.

## Discussion

### Effects of Amendments on Soil Fertility

The carbon-to-nitrogen ratio analysis in this research resulted in a C/N ratio between 18:1 to 21:1 for treatments with compost, and a C/N ratio ranging from 13:1 to 14:1 for the ones without. Compost significantly impacted soil carbon and nitrogen content by increasing carbon content by approximately nine times and nitrogen content by six times compared to treatments without compost. This is because the compost contains labile organic matter, i.e., wood chips, and beneficial fungi and bacteria that can improve the soil’s organic matter. These findings align with previous studies that have shown the addition of compost leads to improvements in carbon and nitrogen levels and, consequently, an increase in plant growth (Chalker-Scott, 2007; Scharenbroch, 2009; Solís-Dominguez et al., 2012; Scharenbroch and Watson, 2014; Antonelli, 2018). The current research also found that treatments containing zeo-

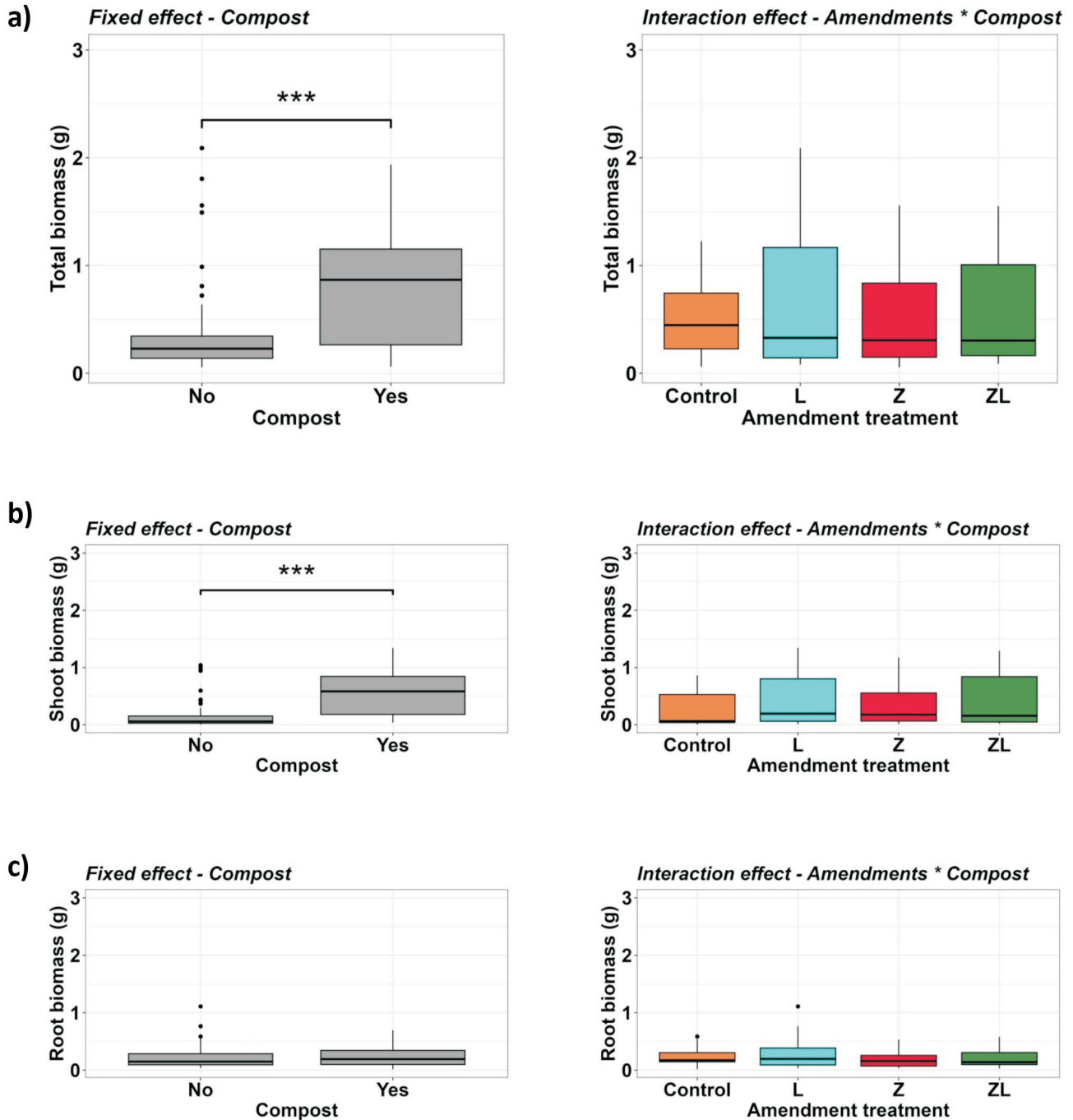


**Figure 6.** Effect of the addition of compost (shown as “Fixed effect – Compost”) and amendments plus compost (shown as “Interaction effect – Amendments \* Compost”) on (a) total biomass, (b) shoot biomass, and (c) root biomass. The graphs show that the compost factor alone significantly influenced total biomass and shoot biomass; however, no significant effects of compost addition, amendments type or ratio to topsoil were observed in the root biomass, but the data are plotted in (c) to be consistent with the other two plots. Although the influence of the amendments was not significant for the shoot biomass, the data are plotted in (b) to be consistent with the total biomass plot. In all the graphs, pairwise comparisons were performed and subjected to Benjamini-Hochberg corrections. Significance levels were denoted as “\*\*\*” for  $P$  (probability) < 0.01 and “\*\*\*\*” for  $P$  < 0.001. Non-significant values were omitted from the plots. The main rectangular box represents the interquartile range, and the vertical line inside the box indicates the median. The whisker lines provide a visual representation of the spread of the data. In the graphs showing results of addition of compost, No and Yes mean the absence and presence and compost, respectively. The two different ratios of amendments to topsoil did not significantly influence the total biomass, shoot biomass or root biomass; therefore, these results are not presented in the graphs. Abbreviations: L, leonardite; Z, zeolite; ZL, a combination of zeolite and leonardite.

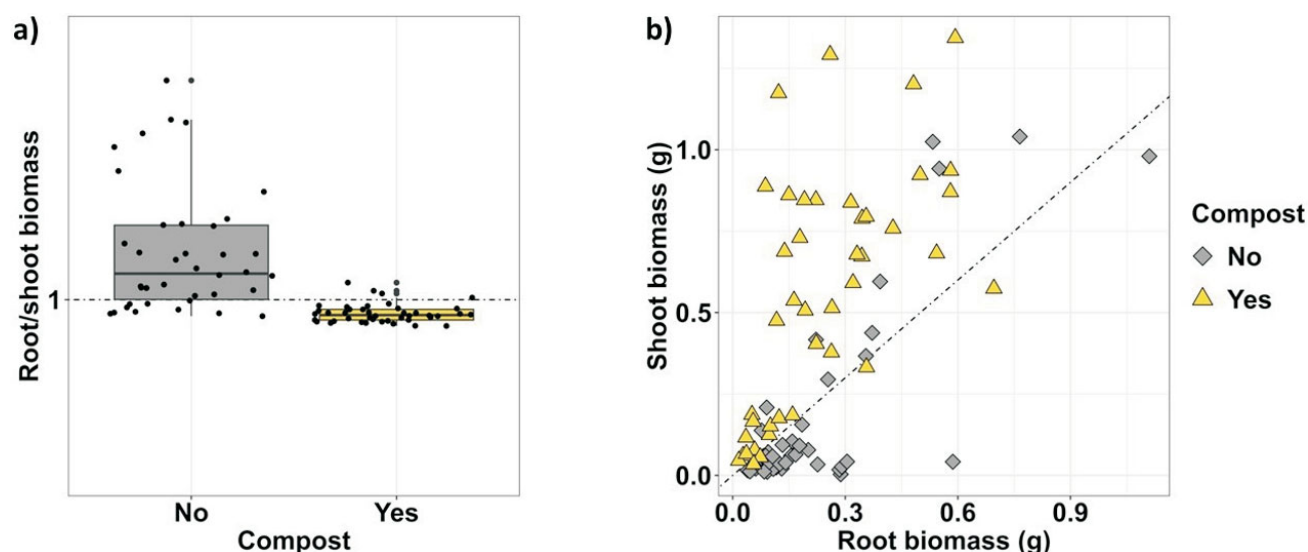


**Figure 7. a)** The root-to-shoot biomass ratio in treatments supplemented with compost (designated as “Yes”) and those without compost (designated as “No”). The main rectangular box represents the interquartile range, and the vertical line inside the box indicates the median. The whisker lines provide a visual representation of the spread of the data. **b)** Root and shoot biomass relationship: the amount of root-to-shoot biomass was significantly influenced by the presence or absence of compost (shown as Yes and No, respectively). Values above the equilibrium line (reference line) indicate a higher root-to-shoot ratio, whereas values below the line suggest a lower root-to-shoot ratio. Graph (a) showcases a greater shoot production in compost-amended treatments (highlighted in yellow) and a reduced production in treatments without compost (highlighted in grey).

lite (Z) had significantly higher nitrogen levels than the leonardite (L) treatments, and higher carbon levels than both the L and ZL treatments. This may be because of zeolite’s ability to absorb, store and slowly release nutrients, mainly when recharged with nitrogen and carbon (Jarosz et al., 2022).

The primary organic components of soil are carbon (C) and nitrogen (N), both of which contribute to soil fertility (Swangjang, 2015). As a function of the C/N ratio, C and N status can have a significant impact on SOM mineralization. In addition, the C/N ratio can be used to predict the release of nutrients (Larney and Angers, 2012) and to establish whether carbon or nitrogen deficiencies are limiting soil microbial processes (Shrestha et al., 2009). As evidenced in a previous study, rapid mineralization occurs when a substrate’s C/N ratio falls between 1 and 15, which means more nitrogen can be available for plants to absorb (Brust, 2019). In other words, a lower C/N ratio leads to a faster release of nitrogen because there is more nitrogen available in comparison to carbon in the soil (Watson et al., 2002; Brust, 2019). On the other hand, when the ratio is over 35, microbial immobilization occurs, which means that micro-organisms in the soil consume nitrogen rather than releasing it for plant use. Achieving a C/N ratio of between 20 and 30 results in a balance between mineralization and immobilization (Brust, 2019). It is necessary for soil micro-organisms to receive sufficient carbon and nitrogen from the soil in order to remain viable, and a C/N ratio of 24 has been found to facilitate their best performance (Brust, 2019). This ratio seems to balance mineralization

and immobilization and has a significant impact on the nitrogen cycle and overall soil health.

It is important to consider the role of ecosystems in the context of the C/N ratio in soil fertility. According to Mulder and Elser (2009), an abandoned grassland had an average C/N ratio of 18.5. Swangjang (2015) also examined the C/N ratios in various ecosystems, including horticultural and agricultural systems, establishing a C/N ratio ranging from 10:1 to 18:1. Another study showed a C/N ratio between 13.4 to 14.2 on grasslands, and a ratio ranging from 13.3 to 15.7 in a forest ecosystem (Cleveland and Liptzin, 2007).

### Amendments and Soil Organic Matter Properties

The presence and structure of soil organic matter have a significant impact on various processes that occur within the terrestrial ecosystem. Soil organic matter acts as a reservoir and receiver of essential nutrients required for plant growth, and plays a crucial role in maintaining soil structure, water retention, and preventing erosion (Gregorich et al., 1993; Batjes, 1996). In comparison to the control treatments in this study, compost-amended treatments showed a significantly higher SOM content. The addition of compost resulted in a mean SOM of 26.5%, whereas treatments without compost had a mean SOM of 5.85%. Based on the suggested ranking by Munshower (1994), the compost-amended treatments are ranked as very high, whereas the ones without compost are ranked as medium to high in terms of SOM. The positive effect of compost containing

wood chips on SOM content is consistent with results demonstrated in previous studies (e.g., Antonelli, 2018). This is because compost increases the total carbon and nitrogen content, which can directly affect the increase of soil organic matter. Moreover, treatments amended with zeolite showed a higher mean SOM of 18.4%, significantly higher than treatments with leonardite (SOM of 14.9%). The carbon and nitrogen results also showed that treatments with zeolite had higher values in both parameters compared to treatments with leonardite.

### Effect of Amendments on Plant Productivity

It has been observed that changes in plant productivity are often linked to variations in soil carbon levels. This is because aboveground productivity acts as a crucial source of soil carbon (Kunkel et al., 2011; Abraha et al., 2018). In this study, the significant increase in biomass in compost-amended treatments can be directly related to nutrient improvement and microbial and fungi activity in the soil (Eisenhauer et al., 2012). Surprisingly, the addition of other amendments did not result in any significant improvement, which may be related to the limited duration of the greenhouse trial (Coghill, 2021).

The results of this study also show that plants grown with compost had a root-to-shoot ratio of less than 1, indicating an abundance of nutrients in the amended substrate, resulting in increased aboveground biomass production (Wilsey and Polley, 2006). However, according to Ågren and Franklin (2003), a lack of nutrients can lead plants to allocate more resources to their root, and, consequently, increase root-to-shoot biomass in the growing medium. Therefore, the higher root-to-shoot ratios observed in this study in treatments without compost (mean root-to-shoot ratio of 5.36 g/g) can be attributed to insufficient organic matter, and, more specifically, insufficient nitrogen. This nitrogen deficiency may have compelled the plants to prioritize root production over shoot production. Conversely, greater shoot biomass was produced in the treatments with compost, which is consistent with previous studies (e.g., Antonelli, 2018).

It is worth mentioning that trace element analysis is underway to test the concentration of heavy metals in the leachate, soil and plant uptakes. These data will provide a comprehensive understanding of each treatment in reducing and eliminating trace elements.

### Conclusion

In conclusion, this research underscores the vital role of compost amendment in promoting plant growth and ameliorating soil fertility within the context of degraded mine topsoil and subsoil. The investigation provides valuable insights into the efficacy of distinct amendments, namely zeolite and leonardite, both individually and in synergy, with

and without the addition of fortified compost, as a tool for facilitating mine reclamation endeavours. The discerning exploration of these amendments not only advances our current understanding but also illuminates their potential synergistic effects. These findings provide insight to support the mining sector in more effective reclamation efforts on tailings storage facilities. It is imperative to acknowledge that while the controlled greenhouse environment offers valuable insights, the translation of these outcomes into real-world scenarios necessitates conducting field experiments. Thus, further research is needed to validate the trends observed in the controlled setting, while also probing various zeolite amendment ratios under field conditions to find an optimal ratio.

### Acknowledgments

Funding for this project was provided through the Natural Science and Engineering Research Council of Canada – Industrial Research Chair in Ecosystem Reclamation, with industry partners Geoscience BC, Genome British Columbia, Arrow Transportation Systems Inc., the Real Estate Foundation of BC, New Afton mine, Highland Valley Copper mine, Kinder Morgan Canada Limited, Metro Vancouver, and British Columbia Cattlemen’s Association. Scholarship funding was also provided in support of this project from Geoscience BC, and an in-kind contribution of zeolite and leonardite amendments came from Progressive Planet Company. Special thanks to M. Coghill, K. Baker, L. Munoz and A. Sutherland, fellow graduate students and student researchers who helped in the field and Fraser lab. Also, special thanks to peer reviewer J. Kang.

### References

- Abraha, M., Hamilton, S.K., Chen, J. and Robertson, G.P. (2018): Ecosystem carbon exchange on conversion of Conservation Reserve Program grasslands to annual and perennial cropping systems; *Agricultural and Forest Meteorology*, v. 253–254, p. 151–160, URL <<https://doi.org/10.1016/j.agrformet.2018.02.016>>.
- Adesipo, A.A., Freese, D., Zerbe, S. and Wiegler, G. (2021): An approach to thresholds for evaluating post-mining site reclamation; *Sustainability*, v. 13, no. 10, art. 5618, URL <<https://doi.org/10.3390/su13105618>>.
- Ågren, G.I. and Franklin, O. (2003): Root:shoot ratios, optimization and nitrogen productivity; *Annals of Botany*, v. 92, p. 795–800, URL <<https://doi.org/10.1093/aob/mcg203>>.
- Antonelli, P.M. (2018): Facilitating native plant recovery on copper mine tailings in the semiarid grasslands of southern interior British Columbia; M.Sc. thesis, Thompson Rivers University, 118 p., URL <[https://www.tru.ca/\\_shared/assets/Paul\\_Antonelli\\_Thesis45148.pdf](https://www.tru.ca/_shared/assets/Paul_Antonelli_Thesis45148.pdf)> [November 2023].
- Asemaninejad, A., Langley, S., Mackinnon, T., Spiers, G., Beckett, P., Mykytczuk, N. and Basiliko, N. (2021): Blended municipal compost and biosolids materials for mine reclamation: long-term field studies to explore metal mobility, soil fertility and microbial communities; *Science of The To-*

- tal Environment, v. 760, art. 143393, URL <<https://doi.org/10.1016/j.scitotenv.2020.143393>>.
- Batjes, N.H. (1996): Total carbon and nitrogen in the soils of the world; *European Journal of Soil Science*, v. 47, no. 2, p. 151–163, URL <<https://doi.org/10.1111/j.1365-2389.1996.tb01386.x>>.
- Bayliff, S. (2022): Examining the effects of mowing, irrigation, and fertilization on plant productivity and soil carbon levels of perennial cropping systems; M.Sc. thesis, Thompson Rivers University, 110 p., URL <[https://www.tru.ca/\\_shared/assets/Sarah\\_Bayliff\\_thesis55755.pdf](https://www.tru.ca/_shared/assets/Sarah_Bayliff_thesis55755.pdf)> [November 2023].
- Bradshaw, A.D. (1987): The reclamation of derelict land and the ecology of ecosystems; *in* Restoration Ecology: A Synthetic Approach to Ecological Research, W.R. Jordan, M.E. Gilpin and J.D. Aber (ed.), Cambridge University Press, Cambridge, United Kingdom, p. 53–74.
- Bradshaw, A.D. (1997): Restoration of mined lands—using natural processes; *Ecological Engineering*, v. 8, no. 4, p. 255–269, URL <[https://doi.org/10.1016/S0925-8574\(97\)00022-0](https://doi.org/10.1016/S0925-8574(97)00022-0)>.
- Brust, G.E. (2019): Management strategies for organic vegetable fertility; Chapter 9 *in* Safety and Practice for Organic Food, D. Biswas and S.A. Micaleff (ed.), Academic Press, London, England, p. 193–212, URL <<https://doi.org/10.1016/B978-0-12-812060-6.00009-X>>.
- Cacciuttolo, C., Cano, D. and Custodio, M. (2023): Socio-environmental risks linked with mine tailings chemical composition: promoting responsible and safe mine tailings management considering copper and gold mining experiences from Chile and Peru; *Toxics*, v. 11, no. 5, art. 462, part of Special Issue “Migration and Transformation Law and Risk Assessment of Industrial and Mining Pollutants”, URL <<https://doi.org/10.3390/toxics11050462>>.
- Chalker-Scott, L. (2007): Impact of mulches on landscape plants and the environment – a review; *Journal of Environmental Horticulture*, v. 25, p. 239–249, URL <<https://doi.org/10.24266/0738-2898-25.4.239>>.
- Chawakitchareon, P., Poovuttikul, P. and Chantanurak, T. (2014): Slow-release fertilizer prepared from leonardite and zeolite; *Advanced Materials Research*, v. 931–932, p. 758–761, URL <<https://doi.org/10.4028/www.scientific.net/amr.931-932.758>>.
- Chen, Y., Clapp, C. and Magen, H. (2004): Mechanisms of plant growth stimulation by humic substances: the role of organo-iron complexes; *Soil Science and Plant Nutrition*, v. 50, no. 7, p. 1089–1095, URL <<https://doi.org/10.1080/00380768.2004.10408579>>.
- Church, C. and Crawford, A. (2020): Minerals and the metals for the energy transition: exploring the conflict implications for mineral-rich, fragile states; Chapter 12 *in* The Geopolitics of the Global Energy Transition, M. Hafner and S. Tagliapietra (ed.), v. 73 in the series “Lecture Notes in Energy”, Springer Nature, Switzerland, p. 279–304, URL <[https://doi.org/10.1007/978-3-030-39066-2\\_12](https://doi.org/10.1007/978-3-030-39066-2_12)>.
- Cleveland, C.C. and Liptzin, D.C. (2007): C:N:P stoichiometry in soil: is there a “Redfield ratio” for the microbial biomass?; *Biogeochemistry*, v. 85, p. 235–252, URL <<https://doi.org/10.1007/s10533-007-9132-0>>.
- Coghill, M.G. (2021): Examining the soil legacy effects of spotted knapweed (*Centaurea stoebe*); M.Sc. thesis, Thompson Rivers University, 96 p., URL <[https://www.tru.ca/\\_shared/assets/Matthew\\_Coghill\\_Thesis53561.pdf](https://www.tru.ca/_shared/assets/Matthew_Coghill_Thesis53561.pdf)> [November 2023].
- Eisenhauer, N., Scheu, S. and Jousset, A. (2012): Bacterial diversity stabilizes community productivity; *PLOS ONE*, v. 7, no. 3, art. e34517, URL <<https://doi.org/10.1371/journal.pone.0034517>>.
- Fischer, A.M., Van Hamme, J.D., Gardner, W.C. and Fraser, L.H. (2022): Impacts from topsoil stockpile height on soil geochemical properties in two mining operations in British Columbia: implications for restoration practices; *Mining*, v. 2, no. 2, p. 315–329, URL <<https://doi.org/10.3390/mining2020017>>.
- Gardner, W.C., Broersma, K., Naeth, A., Chanasyk, D. and Jobson, A. (2010): Influence of biosolids and fertilizer amendments on physical, chemical and microbiological properties of copper mine tailings; *Canadian Journal of Soil Sciences*, v. 90, p. 571–583, URL <<https://doi.org/10.4141/cjss09067>>.
- Gavlak, R., Horneck, D. and Miller, R.O. (2005): Soil, Plant and Water Reference Methods for the Western Region, WREP-125 (3rd edition); Western Coordinating Committee on Nutrient Management, 207 p., URL <<https://www.napt-program.org/files/napt/western-states-method-manual-2005.pdf>> [November 2023].
- Gielen, D. (2021): Critical materials for the energy transition; International Renewable Energy Agency, Technical Paper 5/2021, Abu Dhabi, 42 p., URL <[https://www.irena.org/-/media/Files/IRENA/Agency/Technical-Papers/IRENA\\_Critical\\_Materials\\_2021.pdf](https://www.irena.org/-/media/Files/IRENA/Agency/Technical-Papers/IRENA_Critical_Materials_2021.pdf)> [November 2023].
- Gregorich, E.G., Reynolds, W.D., Culley, J.L.B., McGovern, M.A. and Curnoe, W.E. (1993): Changes in soil physical properties with depth in a conventionally tilled soil after no-tillage; *Soil and Tillage Research*, v. 26, no. 4, p. 289–299, URL <[https://doi.org/10.1016/0167-1987\(93\)90002-7](https://doi.org/10.1016/0167-1987(93)90002-7)>.
- Hayes, S.M., White, S.A., Thompson, T.L., Maier, R.M. and Chorover, J. (2009): Changes in lead and zinc lability during weathering-induced acidification of desert mine tailings: coupling chemical and micro-scale analyses; *Applied Geochemistry*, v. 24, p. 2234–2245, URL <<https://doi.org/10.1016/j.apgeochem.2009.09.010>>.
- Heiskanen, J., Ruhanen, H. and Hagner, M. (2022): Effects of compost, biochar and ash mixed in till soil cover of mine tailings on plant growth and bioaccumulation of elements: a growing test in a greenhouse; *Heliyon*, v. 2, no. 8, art. e08838, URL <<https://doi.org/10.1016/j.heliyon.2022.e08838>>.
- Hendrychová, M., Svobodova, K. and Kabrna, M. (2020): Mine reclamation planning and management: integrating natural habitats into post-mining land use; *Resources Policy*, v. 69, art. 101882, URL <<https://doi.org/10.1016/j.resourpol.2020.101882>>.
- Iverson, K. (2004): Grasslands of the Southern Interior; BC Ministry of Sustainable Resource Management and BC Ministry of Water, Land and Air Protection, Ecosystems at Risk brochure, 6 p., URL <[https://www2.gov.bc.ca/assets/gov/environment/plants-animals-and-ecosystems/species-ecosystems-at-risk/brochures/grasslands\\_southern\\_interior.pdf](https://www2.gov.bc.ca/assets/gov/environment/plants-animals-and-ecosystems/species-ecosystems-at-risk/brochures/grasslands_southern_interior.pdf)> [November 2023].
- Jarosz, R., Szerement, J., Gondek, K. and Mierzwa-Hersztek, M. (2022): The use of zeolites as an addition to fertilisers—a review; *CATENA*, v. 213, art. 106125, URL <<https://doi.org/10.1016/j.catena.2022.106125>>.

- Kästner, M. and Miltner, A. (2016): Application of compost for effective bioremediation of organic contaminants and pollutants in soil; *Applied Microbiology and Biotechnology*, v. 100, no. 8, p. 3433–3449, URL <<https://doi.org/10.1007/s00253-016-7378-y>>.
- Kesraoui-Ouki, S., Cheeseman, C.R. and Perry, R. (1994): Natural zeolite utilisation in pollution control: a review of applications to metals' effluents; *Journal of Chemical Technology and Biotechnology*, v. 59, no. 2, p. 121–126, URL <<https://doi.org/10.1002/jctb.280590202>>.
- Kunkel, M.L., Flores, A.N., Smith, T.J., McNamara, J.P. and Benner, S.G. (2011): A simplified approach for estimating soil carbon and nitrogen stocks in semi-arid complex terrain; *Geoderma*, v. 165, no. 1, p. 1–11, URL <<https://doi.org/10.1016/j.geoderma.2011.06.011>>.
- Larney, F.J. and Angers, D.A. (2012): The role of organic amendments in soil reclamation: a review; *Canadian Journal of Soil Science*, v. 92, no. 1, p. 19–38, URL <<https://doi.org/10.4141/cjss2010-064>>.
- Levene, H. (1960): Robust tests for equality of variances; in *Contributions to Probability and Statistics*, I. Olkin (ed.), Stanford University Press, Palo Alto, California, p. 278–292.
- Lottermoser, B.G. (2010): *Mine Wastes: Characterization, Treatment and Environmental Impacts* (3<sup>rd</sup> edition); Springer, Berlin, Heidelberg, 404 p., URL <<https://link.springer.com/book/10.1007/978-3-642-12419-8>> [November 2023].
- Manu, M., Wang, C., Li, D., Varjani, S. and Wong, J.W. (2022): Impact of zeolite amendment on composting of food waste digestate; *Journal of Cleaner Production*, v. 371, art. 133408, URL <<https://doi.org/10.1016/j.jclepro.2022.133408>>.
- Misaelides, P. (2011): Application of natural zeolites in environmental remediation: a short review; *Microporous and Mesoporous Materials*, v. 144, no. 1–3, p. 15–18, URL <<https://doi.org/10.1016/j.micromeso.2011.03.024>>.
- Mulder, C. and Elser, J.J. (2009): Soil acidity, ecological stoichiometry and allometric scaling in grassland food webs; *Global Change Biology*, v. 15, no. 11, p. 2730–2738, URL <<https://doi.org/10.1111/j.1365-2486.2009.01899.x>>.
- Munshower, F.F. (1994): *Practical Handbook of Disturbed Land Revegetation*; Lewis Publishers, Boca Raton, Florida, 265 p.
- Ozdoba, D.M., Blyth, J.C., Engler, R.F., Dinel, H. and Schnitzer, M. (2001): Leonardite and humified organic matter; in *Humic Substances: Structures, Models and Functions*, E.A. Ghabbour and G. Davies (ed.), Royal Society of Chemistry, Special Publication No. 273, p. 309–314.
- Piccolo, A., Pietramellara, G. and Mbagwu, J. (1996): Effects of coal derived humic substances on water retention and structural stability of Mediterranean soils; *Soil Use and Management*, v. 12, no. 4, p. 209–213, URL <<https://doi.org/10.1111/j.1475-2743.1996.tb00545.x>>.
- Plante, B., Pabst, T. and Wilson, D. (2023): Editorial for special issue “Environmental Geochemistry in the Mining Environment”; *Minerals*, v. 13, no. 1, art. 112, URL <<https://doi.org/10.3390/min13010112>>.
- Rayne, S. and Forest, K. (2015): Declining relative humidity in the Thompson River Valley near Kamloops, British Columbia, Canada: 1990–2012; *bioRxiv*, preprint, URL <<https://doi.org/10.1101/028894>>.
- Scharenbroch, B.C. (2009): A meta-analysis of studies published in *Arboriculture & Urban Forestry* relating to organic materials and impacts on soil, tree, and environmental properties; *Arboriculture & Urban Forestry*, v. 35, p. 221–231, URL <<https://doi.org/10.48044/jauf.2009.036>>.
- Scharenbroch, B.C. and Watson, G.W. (2014): Wood chips and compost improve soil quality and increase growth of *Acer rubrum* and *Betula nigra* in compacted urban soil; *Arboriculture & Urban Forestry*, v. 40, no. 6, p. 319–331, URL <<https://doi.org/10.48044/jauf.2014.030>>.
- Schoenberger, E. (2016): Environmentally sustainable mining: the case of tailings storage facilities; *Resources Policy*, v. 49, p. 119–128, URL <<https://doi.org/10.1016/j.resourpol.2016.04.009>>.
- Shapiro, S.S. and Wilk, M.B. (1965): An analysis of variance test for normality (complete samples); *Biometrika*, v. 52, no. 3–4, p. 591–611, URL <<https://doi.org/10.1093/biomet/52.3-4.591>>.
- Sheoran, V., Sheoran, A.S. and Poonia, P. (2010): Soil reclamation of abandoned mine land by revegetation: a review; *International Journal of Soil, Sediment and Water*, v. 3, no. 2, art. 13, URL <<https://scholarworks.umass.edu/intljssw/vol3/iss2/13>> [November 2023].
- Shrestha, R.K., Lal, R. and Jacinthe, A. (2009): Enhancing carbon and nitrogen sequestration in reclaimed soils through organic amendments and chiseling; *Soil Science Society of America Journal*, v. 73, no. 3, p. 1004–1011, URL <<https://doi.org/10.2136/sssaj2008.0216>>.
- Singh, J.P., Vaidya, B.P., Goodey, N.M. and Krumins, J.A. (2019): Soil microbial response to metal contamination in a vegetated and urban brownfield; *Journal of Environmental Management*, v. 244, p. 313–319, URL <<https://doi.org/10.1016/j.jenvman.2019.04.111>>.
- Solis-Dominguez, F.A., White, S.A., Hutter, T.B., Amistadi, M.K., Root, R.A., Chorover, J. and Maier, R.M. (2012): Response of key soil parameters during compost-assisted phytostabilization in extremely acidic tailings: effect of plant species; *Environmental Science and Technology*, v. 46, no. 2, p. 1019–1027, URL <<https://doi.org/10.1021/es202846n>>.
- Strohmayr, P. (1999): Soil stockpiling for reclamation and restoration activities after mining and construction; *Restoration and Reclamation Review*, v. 4, no. 7, 6 p., URL <<https://conservancy.umn.edu/bitstream/handle/11299/59360/4.7.Strohmayr.pdf?sequence=1>> [November 2023].
- Swangjang, K. (2015): Soil carbon and nitrogen ratio in different land use; *International Conference on Advances in Environment Research*, v. 87, no. 7, p. 36–40, URL <[https://www.researchgate.net/publication/335378514\\_Soil\\_Carbon\\_and\\_Nitrogen\\_Ratio\\_in\\_Different\\_Land\\_Use](https://www.researchgate.net/publication/335378514_Soil_Carbon_and_Nitrogen_Ratio_in_Different_Land_Use)> [November 2023].
- Szerement, J., Jurek, K., Mokrzycki, J., Jarosz, R., Oleszczuk, P. and Mierzwa-Hersztek, M. (2023): Zeolite composites from fly ashes mixed with leonardite as a useful addition to fertilizer for accelerating the PAHs degradation in soil; *Soil and Tillage Research*, v. 230, art. 105701, URL <<https://doi.org/10.1016/j.still.2023.105701>>.
- ThermoFisher Scientific (2017): *FlashSmart<sup>TM</sup> elemental analyzers*; ThermoFisher Scientific, 94 p.
- Tisdale, E.W. (1947): The grasslands of the Southern Interior of British Columbia; *Ecology*, v. 28, no. 4, p. 346–382, URL <<https://doi.org/10.2307/1931227>>.
- Watson, C.A., Atkinson, D., Gosling, P., Jackson, L.R. and Rayns, F.W. (2002): Managing soil fertility in organic farm-

- ing systems; *Soil Use and Management*, v. 18, p. 239–247, URL <<https://doi.org/10.1111/j.1475-2743.2002.tb00265.x>>.
- Wetland Stewardship Partnership (2010): *Grasslands in British Columbia: A Primer for Local Governments*; Wetland Stewardship Partnership, 16 p., URL <[https://bcwetlandsca.files.wordpress.com/2016/11/grasslands-primer\\_wsp\\_2010.pdf](https://bcwetlandsca.files.wordpress.com/2016/11/grasslands-primer_wsp_2010.pdf)> [November 2023].
- Wikeem, B. and Wikeem, S. (2004): *The Grasslands of British Columbia*; Grasslands Conservation Council of British Columbia, 497 p., URL <[https://bcgrasslands.org/wp-content/uploads/2017/06/gcc\\_e-book\\_grasslands-of-bc.pdf](https://bcgrasslands.org/wp-content/uploads/2017/06/gcc_e-book_grasslands-of-bc.pdf)> [November 2023].
- Wilsey, B.J. and Polley, H.W. (2006): Aboveground productivity and root-shoot allocation differ between native and introduced grass species; *Oecologia*, v. 150, no. 2, p. 300–309, URL <<https://doi.org/10.1007/s00442-006-0515-z>>.
- Wobbrock, J.O., Findlater, L., Gergle, D. and Higgins, J.J. (2011): The aligned rank transform for nonparametric factorial analyses using only anova procedures; *in CHI '11: Proceedings of the SIGCHI Conference on Human Factors in Computing Systems*, May 7–12, 2011, Vancouver BC, Association for Computing Machinery, p. 143–146, URL <<https://doi.org/10.1145/1978942.1978963>>.
- Zhu, D., Schwab, A.P. and Banks, M.K. (1999): Heavy metal leaching from mine tailings as affected by plants; *Journal of Environmental Quality*, v. 28, no. 6, p. 1727–1732, URL <<https://doi.org/10.2134/jeq1999.00472425002800060006x>>.



# Petrophysical Analysis of Geothermal Systems at Mount Meager, Southwestern British Columbia (Part of NTS 092J)

**F. Hormozzade Ghalati<sup>1</sup>**, Department of Earth Sciences, Carleton University, Ottawa, Ontario,  
fatemehormozzadeghal@cmail.carleton.ca

**J.A. Craven**, Natural Resources Canada, Geological Survey of Canada–Central, Ottawa, Ontario

**D. Motazedian**, Department of Earth Sciences, Carleton University, Ottawa, Ontario

**S.E. Grasby**, Natural Resources Canada, Geological Survey of Canada–Calgary, Calgary, Alberta

---

Hormozzade Ghalati, F., Craven, J.A., Motazedian, D. and Grasby, S.E. (2024): Petrophysical analysis of geothermal systems at Mount Meager, southwestern British Columbia (part of NTS 092J); in *Geoscience BC Summary of Activities 2023*, Geoscience BC, Report 2024-01, p. 93–100.

## Introduction

An essential aspect of geothermal energy utilization is the knowledge of factors influencing fluid flow pathways (Li, 2020). Fluid flow pathways are predominantly shaped by permeable geological elements, such as fractures, joints and faults, which are the key factors influencing the distribution of fluids within reservoirs and heat conduction in geothermal systems (Hanano, 2000). Researchers have employed diverse methods to investigate fluid flow pathways and their governing parameters in geothermal reservoirs. These methodologies involve numerical modeling (e.g., Strehlow et al., 2015), laboratory experiments and structural analyses (e.g., Farquharson et al., 2015; Eggertsson et al., 2020), geochemical studies (e.g., Libbey and Williams-Jones, 2016) and geophysical techniques (e.g., Heise et al., 2016; Cordell et al., 2019; Miller et al., 2022), each providing unique insights into flow pathways at various depths of investigation.

The Mount Meager Volcanic Complex (MMVC) in southwestern British Columbia (BC) stands as a prominent geothermal resource in Canada (Grasby et al., 2012). Its abundant thermal springs and high enthalpy geothermal potential (based on borehole temperature data) suggest the presence of permeable conduits channelling fluids to the near surface (Grasby et al., 2021). To expand the understanding of the potential geothermal reservoir beneath the MMVC, a comprehensive project was initiated in 2019, which includes a gravity survey, passive seismic analysis, deep and shallow magnetotelluric (MT) studies and bedrock mapping (Grasby et al., 2020, 2021, 2023).

The MT method is a passive electromagnetic exploration technique that measures the magnetic and electric fields on the Earth's surface (Chave and Jones, 2012). Natural electromagnetic signals span a broad frequency range of 0.001 to 40 000 hertz (Hz). The audio-magnetotelluric (AMT) method measures the natural electromagnetic fields at the higher frequencies (1 to 40 000 Hz), which permits mapping of relatively shallower subsurface electrical resistivity structures than those mapped by the MT method. Electrical resistivity, a fundamental physical property influenced by factors such as pore geometry, rock composition, fluid content and temperature, offers a means of reservoir assessment in geothermal systems (Muñoz, 2014). Resistivity models derived from the inversion of MT data enable the modelling of subsurface structures by analyzing natural perturbations in the Earth's electric and magnetic fields. Prior MT studies at Mount Meager identified a deep magma body beneath the volcano and its possible connection to the geothermal system (Jones and Dumas, 1993; Candy, 2001; Hanneson and Unsworth, 2022). A more comprehensive dataset, gathered using the AMT method in 2019, explores subsurface structures within the top hundred metres and up to a few kilometres beneath the MMVC (Figure 1; Craven et al., 2020).

This project establishes empirical relationships between laboratory petrophysical data (porosity and permeability) and the AMT-derived resistivity model. The goal is to comprehensively assess the spatial relationships between geological structures and fluid circulation within the potential geothermal reservoir beneath the MMVC.

## Study Area

Mount Meager (an active volcano within the Garibaldi volcanic belt) is situated about 150 km north of Vancouver, BC, and displays rugged topography forged through uplift and erosion over the past 2.5 million years (Figure 1; Huang, 2019). Its geological composition predominantly

---

<sup>1</sup>The lead author is a 2023 Geoscience BC Scholarship recipient.

This publication is also available, free of charge, as colour digital files in Adobe Acrobat® PDF format from the Geoscience BC website: <https://geosciencebc.com/updates/summary-of-activities/>.

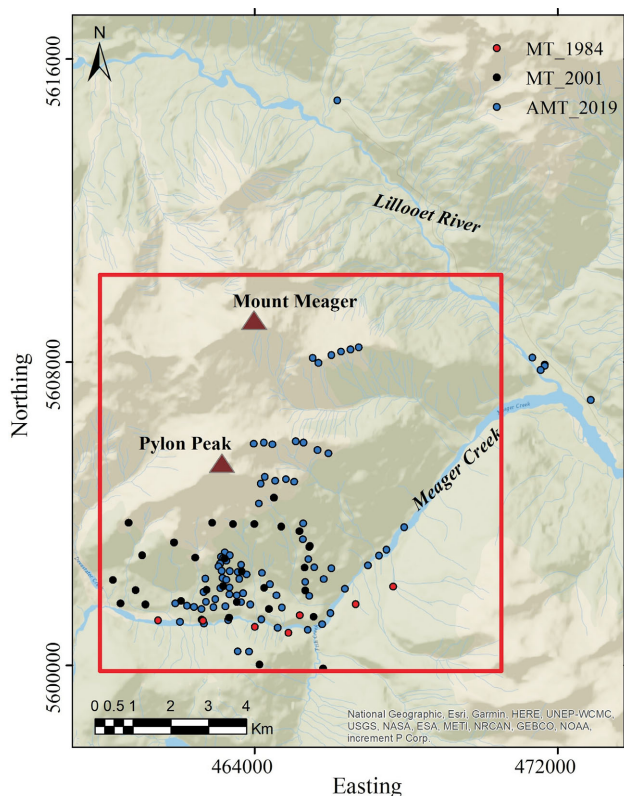


**Figure 1.** Overview of the Mount Meager Volcanic Complex study area. Locations of the magnetotelluric (MT) / audio-magnetotelluric (AMT) stations are shown. The 1984 MT stations are from Jones and Dumas (1993) and the 2001 MT stations are from Candy (2001). The red outlined area is shown in Figure 2. All co-ordinates are in UTM Zone 10N, NAD 83.

features Mesozoic fractured crystalline and metamorphic rocks, including quartz diorite, granodiorite, dacite and gneiss. The hydraulic conductivity and permeability at Mount Meager primarily depend on fracture porosity, as evidenced by observed fluid loss during drilling of the basement rock. Furthermore, the distribution of upward fluid flow is influenced by fault and fracture zones, dikes and hydrothermal brecciation associated with volcanic activities (Adams and Moore, 1987).

Notable fault zones within the MMVC region include the Meager Creek fault (MCF), No-Good fault (NGF), Camp fault and Carbonate fault. The MCF, a key structure in controlling the geothermal system, exhibits an east-striking normal fault with an approximately 45–50° northward dip. It plays a sealing role, preventing fluid flow across the fault, and is considered the southern boundary of the reservoir. The NGF, Camp and Carbonate faults intersect the MCF and exhibit varying strike directions and dips, adding complexity to the fault system (Figure 2). Additionally, steeply dipping regional fractures and local fractures contribute to the structural heterogeneity of the MMVC’s granodiorite (Balfour et al., 2011).

The distribution of thermal springs in southwestern BC is linked to major crustal-scale faults that provide permeable pathways for hot water seepage to the surface. These springs are spatially correlated with fractured rocks dissected by faults. For example, the Meager Creek hot springs discharge hot water due to a topographic rise in the

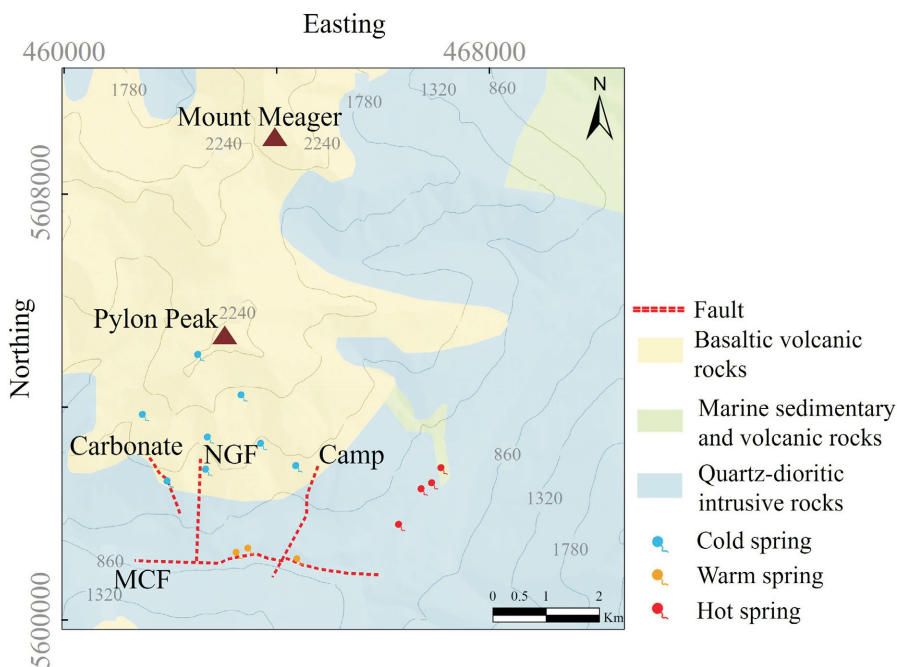


**Figure 2.** Geological map of the Mount Meager Volcanic Complex. Background geology modified after Proenza (2012). Elevations are shown as contour lines (in m asl) and all co-ordinates are in UTM Zone 10N, NAD 83. Abbreviations: Camp, Camp fault; Carbonate, Carbonate fault; MCF, Meager Creek fault; NGF, No-Good fault.

bedrock, whereas warm springs align with the trace of the MCF, indicative of permeable zones allowing thermal fluid outflow (Jamieson, 1981; Bernard, 2020; Hormozzade Ghlati et al., 2022).

## Data and Methodology

Understanding fluid flow in a reservoir depends on the rocks' physical properties, including porosity, permeability and pore connectedness. Porosity reflects the volume of pore space in a medium, whereas permeability measures the medium's capacity to allow fluid flow (Bernabé et al., 2010). Evaluating these fundamental properties is essential in assessing hydraulic conductivity and flow characteristics within a geothermal reservoir.

This project analyzed 21 surface core samples collected from various locations within the MMVC, including both volcanic and basement rocks. Porosity and permeability were measured using the Coretest Systems, Inc. AP-608 Gas combined permeameter and porosimeter at the Institut national de la recherche scientifique (INRS; Québec, Québec). Additionally, aside from rock matrix porosity, fracture porosity was identified in the studied rocks. Quantitative insight into the impact of fractures on porosity and permeability was gained by employing theoretical models that consider various fracture attributes. The characteristics of these fractures, including dip angle, dip direction, orientation, length, spacing and aperture, were essential in assessing the fracture networks. Fracture data were collected from surface outcrops in the study area at locations where fresh bedrock was exposed. Fracture porosity ( $\phi_f$ ; fraction) is calculated as

$$\phi_f = w_f \times \left( \frac{1}{D_i} + \frac{1}{D_j} \right) \quad (1)$$

where  $w_f$  is fracture aperture (m), and  $D$  is spacing (m) in  $i$  and  $j$  directions. Moreover, permeability through a set of fractures ( $k_f$  in mD; 1 millidarcy =  $9.869233 \times 10^{-16}$  m<sup>2</sup>) can be expressed using the following equation, where the fracture aperture is in  $\mu$ m and porosity is in % (Tiab and Donaldson, 2016):

$$k_f = 8.33 \times 10^{-4} \times w_f \times \phi_f \quad (2)$$

Moreover, porosity relates to the electrical resistivity of bulk rock and fluid. This relationship can be defined through petrophysical models like Archie's law (Equation 3; Archie, 1942), modified Archie's law (MAL; Equation 4; Glover et al., 2000), Hashin Shtrikman (HS) model (Equation 5; Hashin and Shtrikman, 1962) and Waxman Smits model (Waxman and Smits, 1968).

$$\sigma_f = \sigma_b \phi^{-m} \quad (3)$$

$$\sigma_b = \sigma_f \phi^m + \sigma_s (1-\phi)^p \quad (4)$$

$$p = \frac{\log(1-\phi^m)}{\log(1-\phi)}$$

$$\sigma_s + \frac{\phi}{\frac{1}{\sigma_f - \sigma_s} + \frac{1-\phi}{3\sigma_s}} = \sigma_b^{HS-} \leq \sigma_b \leq \sigma_b^{HS+} = \sigma_f + \frac{1-\phi}{\frac{1}{\sigma_s - \sigma_f} + \frac{\phi}{3\sigma_f}} \quad (5)$$

In these equations,  $\phi$  is porosity,  $m$  is an empirical constant for the cementation factor,  $\sigma_b$  is the bulk electrical conductivity of the hostrock (Siemens/metre [S/m]),  $\sigma_f$  is the fluid electrical conductivity (S/m),  $\sigma_s$  is the solid phase conductivity of the material (S/m),  $HS^+$  is the upper Hashin-Shtrikman bound of the bulk electrical conductivity and  $HS^-$  is the lower Hashin-Shtrikman bound of the bulk electrical conductivity. These models help in defining porosity at the locations where the electrical conductivity measurements are available.

In addition to petrophysical data, geophysical data provides valuable insights into the composition and physical properties of rocks and fluids around boreholes. To expand the understanding of rock properties on a larger scale, the AMT method was used to infer subsurface electrical resistivity. The impedance tensor ( $Z$ ; Equation 6; Chave and Jones, 2012) and geomagnetic transfer function (or tipper,  $T$ ; Equation 7; Simpson and Bahr, 2005) were employed to interpret resistivity structures. The  $Z$  defines a relationship between the horizontal components of the Earth's electric ( $E_x$  and  $E_y$ ) and magnetic ( $H_x$  and  $H_y$ ) fields considering the angular frequency ( $\omega$ ). The  $T$  defines the relationship between the horizontal ( $H_x$  and  $H_y$ ) and vertical ( $H_z$ ) components of the Earth's magnetic field.

$$\begin{bmatrix} E_x \\ E_y \end{bmatrix} = \begin{bmatrix} Z_{xx} & Z_{xy} \\ Z_{yx} & Z_{yy} \end{bmatrix} \begin{bmatrix} H_x \\ H_y \end{bmatrix} \quad (6)$$

$$H_z(\omega) = (T_x(\omega) \quad T_y(\omega)) \begin{pmatrix} H_x(\omega) \\ H_y(\omega) \end{pmatrix} \quad (7)$$

Additionally, temperature, pressure, and geological logs are available for all boreholes in this project. The combination of geochemical, petrophysical and geophysical data sources contribute significantly to the comprehensive assessment of the MMVC's subsurface properties and fluid dynamics.

## Results

The results of the 3-D AMT data inversion and petrophysical evaluation of the MMVC is published in Hormozzade

Ghalati et al. (2022, 2023). An overview of the published results is provided here.

The final model was acquired after 35 iterations and a root mean square (RMS) of 1.4 using CGG’s RLM-3D modeling code (Soyer et al., 2018). Most of the stations have an overall RMS misfit of less than one, which shows the acceptance of the model.

The main features in the model include two major conductors (C1 and C2), which exhibit an average resistivity of around 15 ohm ( $\Omega$ )·m and are embedded within a background resistivity of approximately 100  $\Omega$ ·m. These relatively shallow conductive zones are interpreted to represent the low-permeability clay-rich layers found in various boreholes; layers that maintain measured temperatures ranging from 70 to 160 °C. These clay-rich layers function as caprocks, enabling the accumulation of deeper fluids. Within the boreholes, the shallow conductive zones are associated with argillic alteration minerals, characterized by the presence of smectite, illite and, occasionally, kaolinite (Hormozzade Ghalati et al., 2023).

The geological structures influencing thermal activity in the Mount Meager region are the MCF and NGF, which have east-west and north-south orientations, respectively. According to this AMT resistivity model, surfaces inclined

at angles of 50–60° and 80–90° are representative of the MCF and NGF, respectively. These angles align with available structural geology data. In this model, the intersection of the NGF and MCF corresponds to conductive zones and potential paths for fluid movement (Figure 3). This correlation is substantiated by noticeable changes in electrical resistivity occurring at the fault locations. The average electrical resistivity of the pathways in the AMT model is between 40 and 300  $\Omega$ ·m. These resistivity shifts are evident along the western and southern boundaries of the model, coinciding with the fault indications represented by the planes and lines in Figure 3.

In order to assess the fluid pathways shown within the AMT model using petrophysical models (Equations 3 to 5), the initial step involved computing the electrical resistivity of the fluid samples from boreholes and thermal springs. Due to the effects of temperature on electrical resistivity, the fluid sample resistivities were adjusted to the reservoir temperature using Equation 8:

$$R_{wT2} = R_{wT1} \left( \frac{T1 + x}{T2 + x} \right) \quad (8)$$

$$x = 10^{-((0.3404 \times \log_{10} R_{wT1}) - 0.6414)}$$

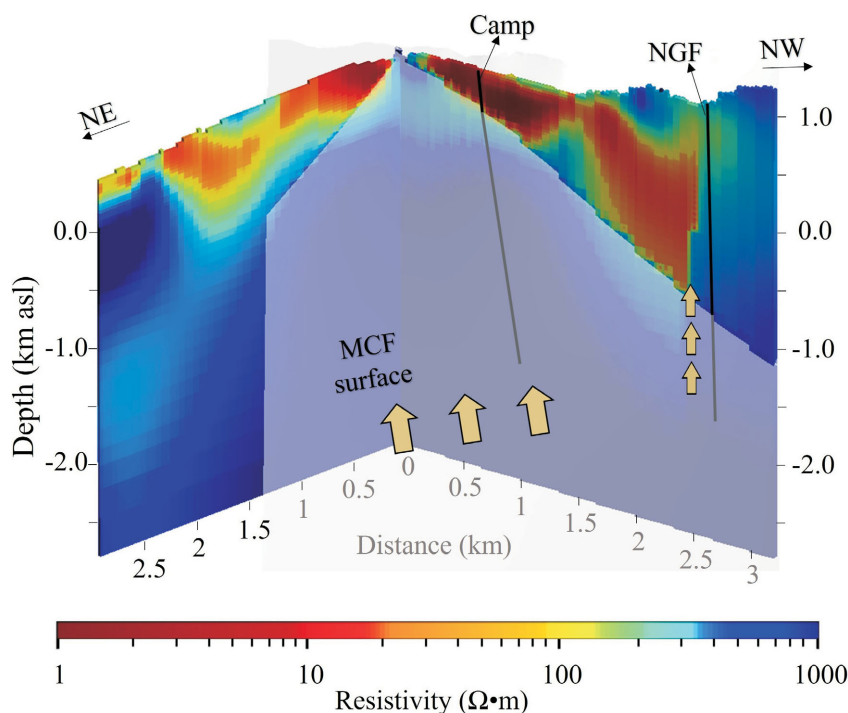


**Figure 3.** Cross-sectional view through the 3-D electrical resistivity model of the southern part of Pylon Peak (Hormozzade Ghalati et al., 2023). Local faults (Meager Creek fault [MCF], Camp fault [Camp] and No-Good fault [NGF]) are illustrated as surfaces. Yellow arrows show the potential direction of fluid flow. The view for these sections is from the north, hence east corresponds to the left of the figures, and west corresponds to the right. Abbreviation:  $\Omega$ , ohm; NE, northeast; NW, northwest.

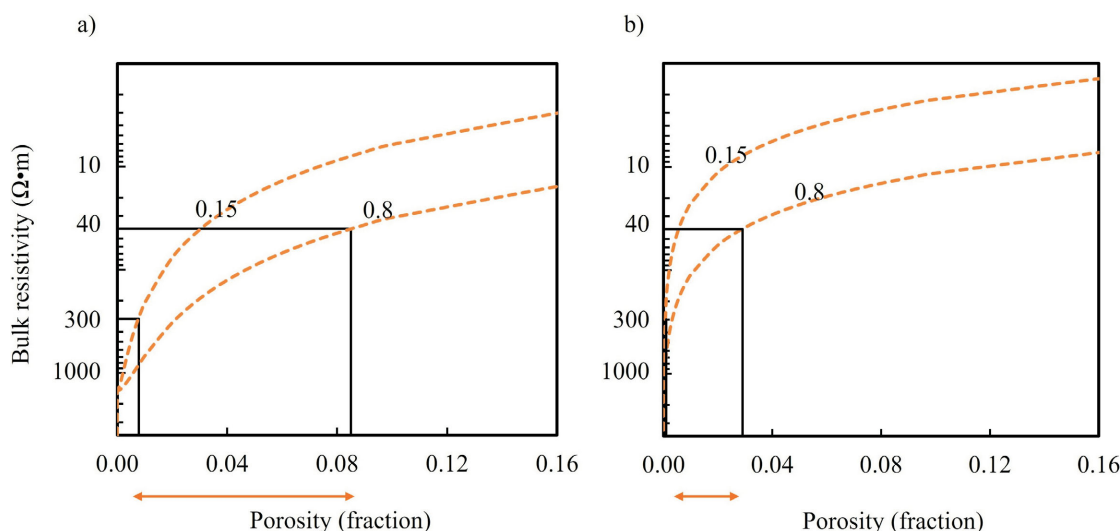


**Figure 4.** Interpretation of the electrical resistivity model of the Mount Meager Volcanic Complex. Dashed lines show different fluid resistivities with the fluid resistivity values annotating the lines. The changes in fluid resistivity between 0.15 and 0.8  $\Omega\cdot\text{m}$  are highlighted. The fluid fraction is estimated for the potential reservoir zone, using **a)** modified Archie's law (MAL) and **b)** an upper Hashin and Shtrikman bound ( $\text{HS}^*$ ). A two-phase medium with a pore connectedness of 1.6 and hostrock conductivity of 0.0007 Siemens/metre (S/m) is assumed to define the electrical resistivity versus porosity.

where  $R_{wT1}$  and  $R_{wT2}$  are the electrical resistivity ( $\Omega\cdot\text{m}$ ) of the fluid at temperatures of T1 and T2 in  $^{\circ}\text{C}$  (Tiab and Donaldson, 2016). Fluid resistivity calculations show a range of values from 0.15 to 0.80  $\Omega\cdot\text{m}$  for the borehole fluid samples at the reservoir temperature. These corrected electrical resistivity values were then used in further porosity-permeability calculations. Considering the MAL and HS models, a porosity range of 0.1–8.5% is expected for the range of bulk electrical resistivity obtained from the AMT model (Figure 4).

Taking into account the porosity-permeability relationship based on laboratory measurements of the MMVC rock samples, it is anticipated that the permeability for the indicated fluid pathways of the AMT model falls within the range of 0 to 0.249 mD (0 to  $2.46 \times 10^{-16} \text{ m}^2$ ). For natural geothermal convection at reservoir temperatures ranging from 200 to 250  $^{\circ}\text{C}$ , a permeability on the order of 1.01 mD ( $9.97 \times 10^{-16} \text{ m}^2$ ) is typically required (as indicated by Straus and Schubert, 1977). However, as the temperature increases, resulting in a reduction in fluid viscosity, the minimum permeability needed for fluid flow can be lowered to around 0.1 mD ( $9.97 \times 10^{-17} \text{ m}^2$ ), particularly at higher reservoir temperatures (350  $^{\circ}\text{C}$ ; e.g., Hanano, 2000). Because permeability measurements of the core samples depend on the physical sample size, macroscopic fractures might not be captured and considered in the studied core samples. Moreover, the geology mainly consists of Mesozoic fractured crystalline and metamorphic rocks and fractures were detected by high amounts of fluid loss during drilling of the basement rocks. Therefore, fracture networks at the MMVC should be studied. Fracture porosity and permeability was calculated for surface fracture data

(Equations 1 and 2). It was estimated that the porosity and permeability of the fracture zones can increase up to 40% and 666 mD ( $6.57 \times 10^{-13} \text{ m}^2$ ), respectively.

## Summary

This paper summarizes the integration of laboratory core measurements of porosity and permeability and fluid chemistry data with the 3-D electrical resistivity model. This integrated approach enabled the development of new petrophysical models linking porosity and permeability to electrical resistivity. By calibrating these models using well log and laboratory-based rock physical data, porosity and permeability values were derived from the resistivity model. Moreover, potential fracture zones within the study area were characterized, which helped in explaining the permeable pathways governing the upflow of thermal fluids within the Mount Meager Volcanic Complex.

The Mount Meager Volcanic Complex was studied due to the abundance of historical data, which is attributed to the presence of warm and hot springs, pre-existing drilled boreholes and nearby communities that are enthusiastic about embracing alternative energy sources. The outcomes of this research enhance the understanding of the geological aspects of geothermal resources and will contribute to the broader objectives of mitigating the economic risks associated with geothermal exploration within the Garibaldi volcanic belt.

## Acknowledgments

This project was funded by Natural Resources Canada and Geoscience BC and benefited from support of the Natural

Sciences and Engineering Research Council of Canada through Carleton University. The authors would like to thank S.M. Ansari for reviewing this manuscript. The authors would also like to thank E. Roots for providing pyMT code; V. Tschirhart, R. Bryant and S.M. Ansari for helping during the field survey; T. Jenkins from the Lil'wat First Nation for ensuring wildlife were undisturbed; M. Accurso, D. Vincent and R. Slinger for piloting (No Limits Helicopters); and Innergex Renewable Energy Inc. for providing significant access to their field bunkhouse. The authors also thank Meager Creek Development Corporation for providing water chemistry data and CGG for providing RLM-3D and Geotools software.

## References

- Adams, M.C. and Moore, J.N. (1987): Hydrothermal alteration and fluid geochemistry of the Meager Mountain Geothermal System, British Columbia; *American Journal of Science*, v. 287, no. 7, p. 720–755.
- Archie, G.E. (1942): The electrical resistivity log as an aid in determining some reservoir characteristics; *Transactions of the AIME*, v. 146, no. 1, p. 54–62, URL <<https://doi.org/10.2118/942054-G>>.
- Balfour, N.J., Cassidy, J.F., Dosso, S.E. and Mazzotti, S. (2011): Mapping crustal stress and strain in southwest British Columbia; *Journal of Geophysical Research*, v. 116, art. B03314, 11 p., URL <<https://doi.org/10.1029/2010JB008003>>.
- Bernabé, Y., Li, M. and Mainault, A. (2010): Permeability and pore connectivity: a new model based on network simulations; *Journal of Geophysical Research*, v. 115, art. B10203, 14 p., URL <<https://doi.org/10.1029/2010JB007444>>.
- Bernard, K. (2020): Epithermal clast coating inside the rock avalanche-debris flow deposits from Mount Meager Volcanic Complex, British Columbia (Canada); *Journal of Volcanology and Geothermal Research*, v. 402, art. 106994, URL <<https://doi.org/10.1016/j.jvolgeores.2020.106994>>.
- Candy, C. (2001): Crew development corporation report on a magnetotelluric survey, South Meager geothermal project, Pemberton, British Columbia; Frontier Geosciences Inc., unpublished report for Frontier Geosciences project FG1-581.
- Chave, A.D. and Jones, A.G. (2012): *The Magnetotelluric Method: Theory and Practice*; Cambridge University Press, New York, New York, 552 p., URL <<https://www.cambridge.org/core/books/magnetotelluric-method/magnetotelluric-method/C7110AAC1567259EC65172C35B5F16EA>> [October 2023].
- Cordell, D., Unsworth, M.J., Diaz, D., Reyes-Wagner, V., Currie, C.A. and Hicks, S.P. (2019): Fluid and melt pathways in the central Chilean subduction zone near the 2010 Maule earthquake (35–36 °S) as inferred from magnetotelluric data; *Geochemistry, Geophysics, Geosystems*, v. 20, no. 4, p. 18–35, URL <<https://doi.org/10.1029/2018GC008167>>.
- Craven, J.A., Hormozzade, F., Tschirhart, V., Ansari, M., Bryant, R. and Montezadian, D. (2020): Overview of the 2019 audiomagnetotelluric survey of the Mount Meager geothermal reservoir; Chapter 6 in *Garibaldi Geothermal Energy Project, Mount Meager 2019 - Field Report*, Geoscience BC, Report 2020-09, p. 126–147, URL <[https://www.geosciencebc.com/i/project\\_data/GBCReport2020-09/GeoscienceBCReport%202020-09.pdf](https://www.geosciencebc.com/i/project_data/GBCReport2020-09/GeoscienceBCReport%202020-09.pdf)> [March 2021].
- Eggertsson, G.H., Lavallée, Y., Kendrick, J.E. and Markússon, S.H. (2020): Improving fluid flow in geothermal reservoirs by thermal and mechanical stimulation: the case of Krafla volcano, Iceland; *Journal of Volcanology and Geothermal Research*, v. 391, art. 106351, URL <<https://doi.org/10.1016/j.jvolgeores.2018.04.008>>.
- Farquharson, J., Heap, M.J., Varley, N.R., Baud, P. and Reuschlé, T. (2015): Permeability and porosity relationships of edifice-forming andesites: a combined field and laboratory study; *Journal of Volcanology and Geothermal Research*, v. 297, p. 52–68, URL <<https://doi.org/10.1016/j.jvolgeores.2015.03.016>>.
- Glover, P.W.J., Hole, M.J. and Pous, J. (2000): A modified Archie's law for two conducting phases; *Earth and Planetary Science Letters*, v. 180, no. 3, p. 369–383, URL <[https://doi.org/10.1016/S0012-821X\(00\)00168-0](https://doi.org/10.1016/S0012-821X(00)00168-0)>.
- Grasby, S.E., Allen, D.M., Bell, S., Chen, Z., Ferguson, G., Jessop, A., Kelman, M., Ko, M., Majorowicz, J., Moore, M., Raymond, J. and Therrien, R. (2012): Geothermal energy resource potential of Canada; *Geological Survey of Canada, Open File 6914*, 322 p., URL <<https://doi.org/10.4095/291488>>.
- Grasby, S.E., Ansari, S.M., Barendregt, R.W., Borch, A., Calahorrano-DiPatre, A., Chen, Z., Craven, J.A., Dettmer, J., Gilbert, H., Hanneson, C., Harris, M., Hormozzade, F., Leiter, S., Liu, J., Muhammad, M., Quane, S.L., Russell, J.K., Salvage, R.O., Savard, G., Tschirhart, V. et al. (2021): *Garibaldi Geothermal Energy Project – phase 1 – final report*; Geoscience BC, Report 2021–08, 276 p., URL <[https://www.geosciencebc.com/i/project\\_data/GBCReport2021-08/GBCR%202021-08%20Garibaldi%20Geothermal%20Energy%20Project%20-%20Phase%201.pdf](https://www.geosciencebc.com/i/project_data/GBCReport2021-08/GBCR%202021-08%20Garibaldi%20Geothermal%20Energy%20Project%20-%20Phase%201.pdf)> [February 2022].
- Grasby, S.E., Ansari, S.M., Calahorrano-DiPatre, A., Chen, Z., Craven, J.A., Dettmer, J., Gilbert, H., Hanneson, C., Harris, M., Liu, J., Muhammad, M., Russell, K., Salvage, R.O., Savard, G., Tschirhart, V., Unsworth, M.J., Vigouroux-Caillibot, N. and Williams-Jones, G. (2020): Geothermal resource potential of the Garibaldi volcanic belt, southwestern British Columbia (part of NTS 092J); in *Geoscience BC Summary of Activities 2019: Energy and Water*, Geoscience BC, Report 2020-02, p. 103–108, URL <[https://www.geosciencebc.com/i/pdf/SummaryofActivities2019/EW/Project%202018-004\\_EW\\_SOA2019.pdf](https://www.geosciencebc.com/i/pdf/SummaryofActivities2019/EW/Project%202018-004_EW_SOA2019.pdf)> [February 2022].
- Grasby, S.E., Borch, A., Calahorrano-DiPatre, A., Chen, Z., Craven, J., Liu, X., Muhammad, M., Russell, J.K., Tschirhart, V., Unsworth, M.J., Williams-Jones, G. and Yuan, W. (2023): *Garibaldi Geothermal Volcanic Belt Assessment Project, southwestern British Columbia (part of NTS 092J), phase 2: 2022 field report*; in *Geoscience BC Summary of Activities 2022: Energy and Water*, Geoscience BC, Report 2023-02, p. 47–54, URL <[https://www.geosciencebc.com/i/project\\_data/GBCReport2023-02/P2018-004\\_Grasby\\_EnergyWaterSoA2022.pdf](https://www.geosciencebc.com/i/project_data/GBCReport2023-02/P2018-004_Grasby_EnergyWaterSoA2022.pdf)> [October 2023].
- Hanano, M. (2000): Two different roles of fractures in geothermal development; in *Proceedings of the World Geothermal Congress 2000, May 28–June 10, 2000, Kyushu-Tohoku, Japan*, International Geothermal Association, p. 2597–2602.
- Hanneson, C. and Unsworth, M. (2022): Magnetotelluric investigations of geothermal systems centred in southern British

- Columbia (parts of NTS 082, 083, 092, 093); in *Geoscience BC Summary of Activities 2021: Energy and Water*, Geoscience BC, Report 2022-02, p. 81–94, URL <[https://www.geosciencebc.com/i/pdf/SummaryofActivities2021/EW/Sch\\_Hanneson\\_EWSOA2021.pdf](https://www.geosciencebc.com/i/pdf/SummaryofActivities2021/EW/Sch_Hanneson_EWSOA2021.pdf)> [October 2023].
- Hashin, Z. and Shtrikman, S. (1962): A variational approach to theory of effective magnetic permeability of multiphase materials; *Journal of Applied Physics*, v. 33, no. 10, p. 3125–3131, URL <<https://doi.org/10.1063/1.1728579>>.
- Heise, W., Caldwell, T.G., Bertrand, E.A., Hill, G.J., Bennie, S.L. and Palmer, N.G. (2016): Imaging the deep source of the Rotorua and Waimangu geothermal fields, Taupo Volcanic Zone, New Zealand; *Journal of Volcanology and Geothermal Research*, v. 314, p. 39–48, URL <<https://doi.org/10.1016/j.jvolgeores.2015.10.017>>.
- Hormozzade Ghalati, F., Craven, J.A., Motazedian, D., Grasby, S.E., Roots, E., Tschirhart, V., Chen, Z. and Liu, X. (2023): Analysis of fluid flow pathways in the Mount Meager Volcanic Complex, southwestern Canada, utilizing AMT and petrophysical data; *Geochemistry, Geophysics, Geosystems*, v. 24, no. 3, art. e2022GC010814, 20 p., URL <<https://doi.org/10.1029/2022GC010814>>.
- Hormozzade Ghalati, F., Craven, J.A., Motazedian, D., Grasby, S.E. and Tschirhart, V. (2022): Modeling a fractured geothermal reservoir using 3-D AMT data inversion: insights from Garibaldi volcanic belt, British Columbia, Canada; *Geothermics*, v. 105, art. 102528, URL <<https://doi.org/10.1016/j.geothermics.2022.102528>>.
- Huang, K. (2019): Geochemical analysis of thermal fluids from southern Mount Meager, British Columbia, Canada; M.Sc. thesis, University of Iceland, 92 p.
- Jamieson, G.R. (1981): A preliminary study of the regional groundwater flow in the Meager Mountain geothermal area, British Columbia; M.Sc. thesis, The University of British Columbia, 163 p., URL <<http://hdl.handle.net/2429/22494>> [May 2020].
- Jones, A.G. and Dumas, I. (1993): Electromagnetic images of a volcanic zone; *Physics of the Earth and Planetary Interiors*, v. 81, p. 289–314, URL <[https://doi.org/10.1016/0031-9201\(93\)90137-X](https://doi.org/10.1016/0031-9201(93)90137-X)>.
- Li, J. (2020): Investigations of fluid flow through fractures in enhanced geothermal systems; Ph.D. thesis, University of Queensland, 127 p., URL <<https://doi.org/10.14264/uql.2020.973>>.
- Libbey, R.B. and Williams-Jones, A.E. (2016): Compositions of hydrothermal silicates and carbonates as indicators of physicochemical conditions in the Reykjanes geothermal system, Iceland; *Geothermics*, v. 64, p. 15–27, URL <<https://doi.org/10.1016/j.geothermics.2016.04.007>>.
- Miller, C.A., Barretto, J., Stagpoole, V., Caratori-Tontini, F., Brakenrig, T. and Bertrand, E. (2022): The integrated history of repeated caldera formation and infill at the Okataina Volcanic Centre: insights from 3D gravity and magnetic models; *Journal of Volcanology and Geothermal Research*, v. 427, art. 107555, URL <<https://doi.org/10.1016/j.jvolgeores.2022.107555>>.
- Muñoz, G. (2014): Exploring for geothermal resources with electromagnetic methods; *Surveys in Geophysics*, v. 35, no. 1, p. 101–22, URL <<https://doi.org/10.1007/s10712-013-9236-0>>.
- Proenza, Y. (2012): Geothermal data compilation and analysis of Alterra Power’s upper Lillooet property; M.Eng. thesis, University of British Columbia, 47 p., URL <[https://www.geosciencebc.com/i/project\\_data/GBC2017-006/Yuliana%20Proenza%20MEng%20Project.zip](https://www.geosciencebc.com/i/project_data/GBC2017-006/Yuliana%20Proenza%20MEng%20Project.zip)> [September 2023].
- Simpson, F. and Bahr, K. (2005): *Practical Magnetotellurics*; Cambridge University Press, Cambridge, United Kingdom, 270 p., URL <<https://www.cambridge.org/core/books/practical-magnetotellurics/FB76CCD1DB4A49AB48429A22E7D4E5D8>> [October 2023].
- Soyer, W., Mackie, R. and Miorelli, F. (2018): Optimizing the estimation of distortion parameters in magnetotelluric 3d inversion; 80th EAGE Conference and Exhibition, June 11–14, 2018, Copenhagen, Denmark, European Association of Geoscientists & Engineers, v. 2018, p. 1–5, URL <<https://doi.org/10.3997/2214-4609.201801399>>.
- Straus, J.M. and Schubert, G. (1977): Thermal convection of water in a porous medium: effects of temperature- and pressure-dependent thermodynamic and transport properties; *Journal of Geophysical Research*, v. 82, p. 325–333, URL <<https://doi.org/10.1029/JB082i002p00325>>.
- Strehlow, K., Gottsmann, J.H. and Rust, A.C. (2015): Poroelastic responses of confined aquifers to subsurface strain and their use for volcano monitoring; *Solid Earth Discussions*, v. 7, no. 2, p. 1673–1729, URL <<https://doi.org/10.5194/sed-7-1673-2015>>.
- Tiab, D. and Donaldson, E.C. (2016): Naturally fractured reservoirs; Chapter 8 in *Petrophysics* (4<sup>th</sup> edition), Gulf Professional Publishing, Boston, Massachusetts, p. 415–481, URL <<https://doi.org/10.1016/B978-0-12-803188-9.00008-5>>.
- Waxman, M.H. and Smits, L.J.M. (1968): Electrical conductivities in oil-bearing shaly sands; *Society of Petroleum Engineers Journal*, v. 8, no. 2, p. 107–122.



# Key Considerations for Carbon Dioxide Sequestration in the Lower Mainland, Southwestern British Columbia (Parts of NTS 092G/01–03)

M. Nazemi<sup>1</sup>, Department of Earth Sciences, Simon Fraser University, Burnaby, British Columbia, maziyar\_nazemi@sfu.ca

---

Nazemi, M. (2024): Key considerations for carbon dioxide sequestration in the Lower Mainland, southwestern British Columbia (parts of NTS 092/G01–03); in Geoscience BC Summary of Activities 2023, Geoscience BC, Report 2024-01, p. 101–114.

## Introduction

The continuous rise in atmospheric carbon dioxide (CO<sub>2</sub>) levels, initially observed by Keeling in 1960 (Keeling, 1960), has persisted over time, with annual peak concentrations showing a consistent upward trend (Ewald, 2013; Keighley and Maher, 2015). Although CO<sub>2</sub> is naturally generated, the predominant cause of recent increases, spanning from the 1800s to the present, is largely attributed to human activities, specifically the use of carbon-based resources such as coal, oil and methane-rich natural gas (Keighley and Maher, 2015). Elevated CO<sub>2</sub> concentrations alter the Earth's atmospheric composition by amplifying the natural greenhouse effect, resulting in a warming influence on the planet's surface (Bachu, 2003). As the Earth's climate continues to warm, the frequency and intensity of extreme weather events, including phenomena like heat domes, tropical cyclones, increased precipitation and heightened instances of flooding, are expected to rise (Flannigan and Wagner, 1991). Given the substantial risks these events pose to critical societal infrastructure, concerns regarding the societal impacts of climate change have understandably intensified (Bratu et al., 2022). Nevertheless, it is important to acknowledge that CO<sub>2</sub> emissions are anticipated to continue their upward trajectory, as the global transition toward a carbon-neutral economy is projected to extend over several decades (U.S. Energy Information Administration, 2021).

Discovering practical solutions for reducing carbon emissions while maintaining the current standard of living and improving the quality of life in developing nations necessitates cost-effective and innovative approaches. In this context, the most promising strategy for promptly and moderately reducing CO<sub>2</sub> emissions is CO<sub>2</sub> capture and underground sequestration (Intergovernmental Panel on Climate Change, 2014). Carbon capture and storage (CCS) involves the extraction of CO<sub>2</sub> from industrial sources, followed by its injection into suitable geological formations.

Numerous studies (Kaszuba et al., 2003; Bachu and Gunter, 2005; Kharaka et al., 2006; Shukla et al., 2010; Stephenson et al., 2019; Pearce et al., 2021) have explored and validated the feasibility of CCS. Typically, CCS implementation is concentrated in regions with significant hydrocarbon production (Lane et al., 2021). Conversely, areas with limited oil and gas exploration tend to overlook CCS assessment and opportunities, often due to the presumption that underground storage is impractical.

The Lower Mainland of British Columbia (LMBC) has previously undergone assessments related to its hydrocarbon potential and suitability for natural gas storage, suggesting that it could serve as an accessible and potentially economically viable site for CO<sub>2</sub> storage (Gordy, 1988; Hannigan et al., 2001). However, to date, there has been limited effort directed toward evaluating the feasibility of CCS in the LMBC. The sedimentary layers beneath the LMBC remain inadequately understood, particularly at greater depths, and a detailed examination of the geological context, including the interpretation of depositional environments and facies analysis, has not been undertaken. To address this significant knowledge gap, this research provides a concise overview of the essential considerations involved in the assessment of CO<sub>2</sub> sequestration potential within saline aquifers situated in the LMBC. These considerations encompass factors such as geothermal gradient and pressure, reservoir thickness, salinity, mineral composition, porosity and permeability characteristics, seismic activity and fault distribution.

## Study Area

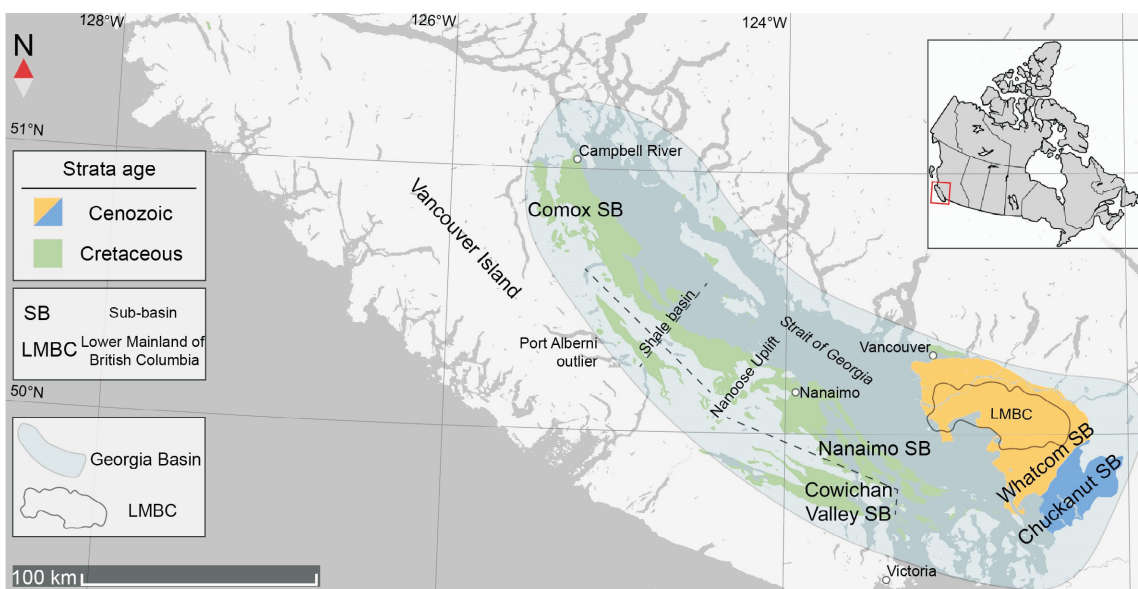
The geological strata beneath the LMBC are part of the broader geological feature known as the Georgia Basin, which is characterized by a northwest-southeast orientation and is marked by a structural and topographic depression. The Georgia Basin spans an extensive area of approximately 18 000 km<sup>2</sup> and includes the Strait of Georgia, eastern Vancouver Island, the Fraser River Lowland and the northwestern region of the State of Washington, United States (Figure 1; Molnar et al., 2010).

The sedimentary deposits within the Georgia Basin can be categorized into three primary tectonostratigraphic clastic

---

<sup>1</sup>The lead author is a 2023 Geoscience BC Scholarship recipient.

This publication is also available, free of charge, as colour digital files in Adobe Acrobat® PDF format from the Geoscience BC website: <https://geosciencebc.com/updates/summary-of-activities/>.



Copyright 2019, with permission from Elsevier (<https://www.sciencedirect.com/journal/earth-science-reviews>).

**Figure 1.** Location map of the Georgia Basin and Lower Mainland of British Columbia (LMBC), and simplified geological map of southwestern British Columbia, Canada. Outcrop areas in the Georgia Basin include Upper Cretaceous Nanaimo Group strata exposed in the Comox, Nanaimo and Cowichan Valley sub-basins (green); Paleogene and Neogene strata in the Whatcom sub-basin (orange); and Paleogene and Neogene strata in the Chuckanut sub-basin (blue). The inset figure shows the location of the larger map within the context of the province of British Columbia and the rest of Canada. Figure reprinted from Huang et al. (2022).

sedimentary units: firstly, the predominantly Upper Cretaceous Nanaimo Group; secondly, the Paleogene Huntingdon Formation; and, thirdly, the Neogene Boundary Bay Formation (Figure 1; Monger, 1990; Groulx and Mustard, 2004; Molnar et al., 2010). The LMBC includes Metro Vancouver, the Fraser River Lowland and the adjacent mountainous areas. This region is home to more than 60% of British Columbia's (BC) population, exceeding 3 million residents, making it the third-largest urban area in Canada. The LMBC is geographically defined by the Coast Mountains to the north, the Cascade Mountains to the east and the international border separating Canada and the United States to the south. Furthermore, the LMBC features prominent population centres that also serve as significant industrial hubs, housing numerous large carbon-emitting facilities.

## Geological Background

### Tectonic Setting and Basin Type

The Canadian Cordillera is geologically categorized into five distinct morphological belts, arranged from west to east: the Insular, Coast, Intermontane, Omineca and Foreland belts (Figure 2; Monger and Price, 2002). Each of these belts is characterized by a unique combination of geological features, including landforms, rock types, metamorphic grade and structural characteristics (Gabrielse and Yorath, 1991). The formation of the southern Canadian Cordillera can be attributed to the amalgamation of two superterranes, which also correspond to two of the morpho-

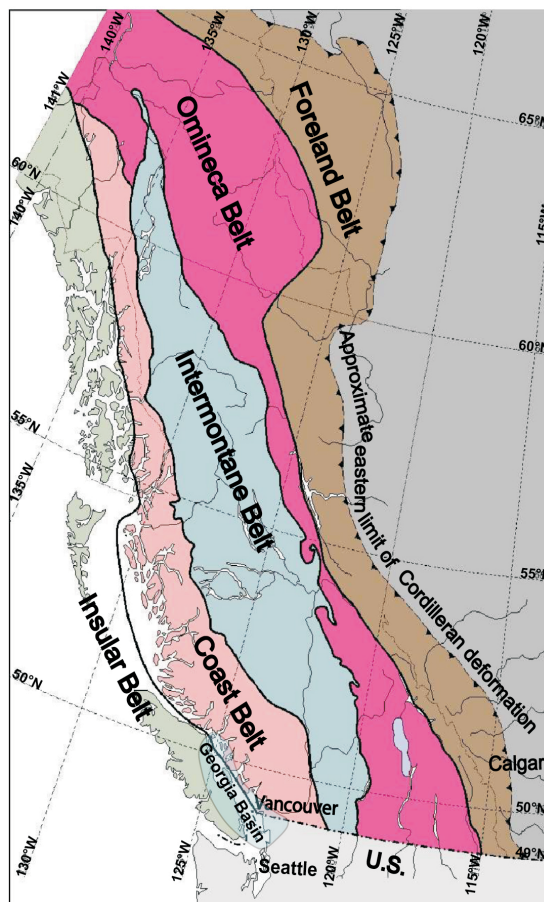


**Figure 2.** Morphogeological belts of the Canadian Cordillera (from Wheeler et al., 1991).

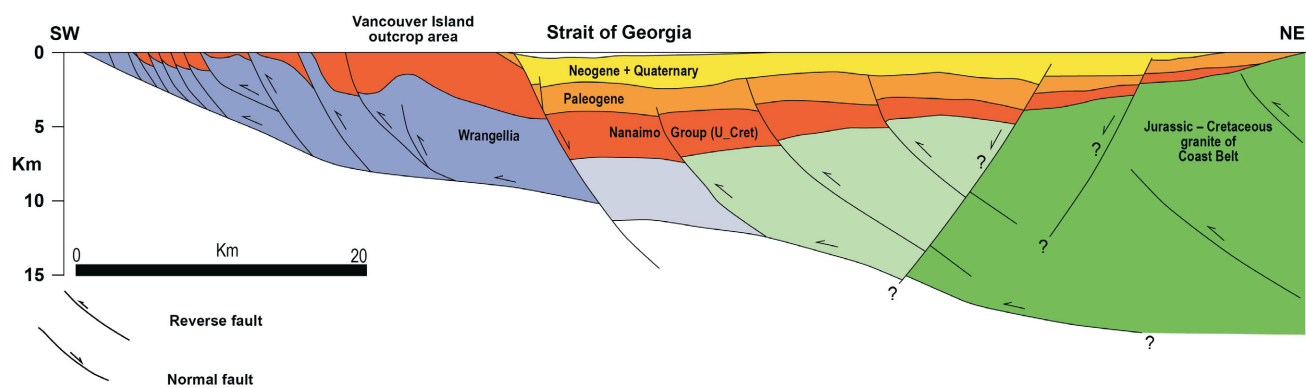


**Figure 3.** Idealized structural cross-section of the southern Georgia Basin based on LITHOPROBE data, modified after England and Bustin (1998), England and Calon (1991) and Gordy (1988). Question marks along the fault surfaces indicate interpreted locations. Paler shades of purple and green are used on the strata below the Strait of Georgia, but they are still part of the Wrangellia (purple) and Jurassic-Cretaceous (green) sequences. Abbreviations: NE, northeast; SW, southwest; U\_Cret, Upper Cretaceous.

logical belts (Figures 2, 3). Specifically, the eastern Intermontane Superterrane was accreted during the Middle Jurassic, whereas the western Insular Superterrane was accreted during the Early Cretaceous (Monger, 1991a, b; Zelt et al., 2001). These two superterrane are separated by the Coast Belt or Coast Plutonic Complex (CPC), which represents a region characterized by high-grade metamorphic rocks and intrusive plutonic formations. It is believed that the Coast Belt or CPC formed during the Early Cretaceous when the Insular Superterrane accreted to the western margin of North America (Monger et al., 1994).

The Georgia Basin is a Cretaceous to Cenozoic fore-arc basin that straddles the boundary between the Insular Superterrane and the CPC (Figures 1, 2; England, 1991; England and Bustin, 1998; Monger and Price, 2002). Based on the structural evolution of the Canadian Cordillera, previous workers have posited that the Georgia Basin was developed in the arc-trench gap between Wrangellia and North America and overlies the eastern portion of Wrangellia and the western portion of the CPC (Figure 1; Muller and Jeletzky, 1970; Bustin and England, 1991; England, 1991; England and Calon, 1991).

The preserved thick successions of shallow-marine proximal facies could reflect a more oblique convergent character for the Georgia Basin. However, recent studies of fore-arc basins globally have identified thick basal successions of terrestrial and shallow-marine strata in similar fore-arc settings, suggesting shallow-marine strata are common in these basins and particularly in ridged fore arcs (Takano et al., 2013; Jones, 2016; Takano and Tsuji, 2017; Kent et al., 2020).

The siliciclastic sedimentary fill within the Georgia Basin can locally reach a thickness exceeding 6 km (England and Bustin, 1998). This sedimentary fill consists of Late Cretaceous through to modern strata (Figure 3; Hannigan et al., 2001). The Georgia Basin is subdivided into five distinct

sub-basins (Figure 1; Mustard and Monger, 1994; England and Bustin, 1998; Hannigan et al., 2001; Huang et al., 2019, 2022; Kent et al., 2020; Giroto, 2022). The Nanaimo sub-basin encompasses the southeastern coast of Vancouver Island, the adjacent Strait of Georgia and the Gulf Islands. The Comox sub-basin is located farther north, along the east-central coast of Vancouver Island and the adjacent Strait of Georgia. The Cowichan Valley sub-basin was initially designated as a separate sub-basin due to uncertainties regarding its relationship with the rest of the Nanaimo Group. Subsequently, later studies incorporated the Cowichan Valley sub-basin into the Nanaimo sub-basin without providing a specific rationale for this revision (Clapp, 1913). The Cowichan Valley sub-basin was subsequently redefined as a distinct sub-basin by Huang et al. (2022) and Giroto (2022). This redefinition was based on differences in detrital zircon age populations and maximum depositional ages observed in strata near the basal unconformity compared to strata in the Comox and Nanaimo sub-basins.

The Chuckanut and Whatcom sub-basins encompass specific geographic regions, with the Whatcom sub-basin covering the Fraser Delta and the Chuckanut sub-basin encompassing northwestern Washington (Figure 1; Hannigan et al., 2001; Kent et al., 2020). The Whatcom sub-basin hosts sedimentary strata of the Nanaimo Group. These strata underlie sedimentary layers, including Paleogene sedimentary rocks of the Huntingdon Formation, Neogene sedimentary rocks of the Boundary Bay Formation and Quaternary sediments from the Fraser River (Figure 4; Zelt et al., 2001).

The Chuckanut sub-basin is separated from the Whatcom sub-basin by the Lummi Island fault, which has experienced more than 1.5 km of southward displacement (Miller, 1963; Johnson, 1985). The sedimentary fill within the Chuckanut sub-basin comprises the Chuckanut Formation,

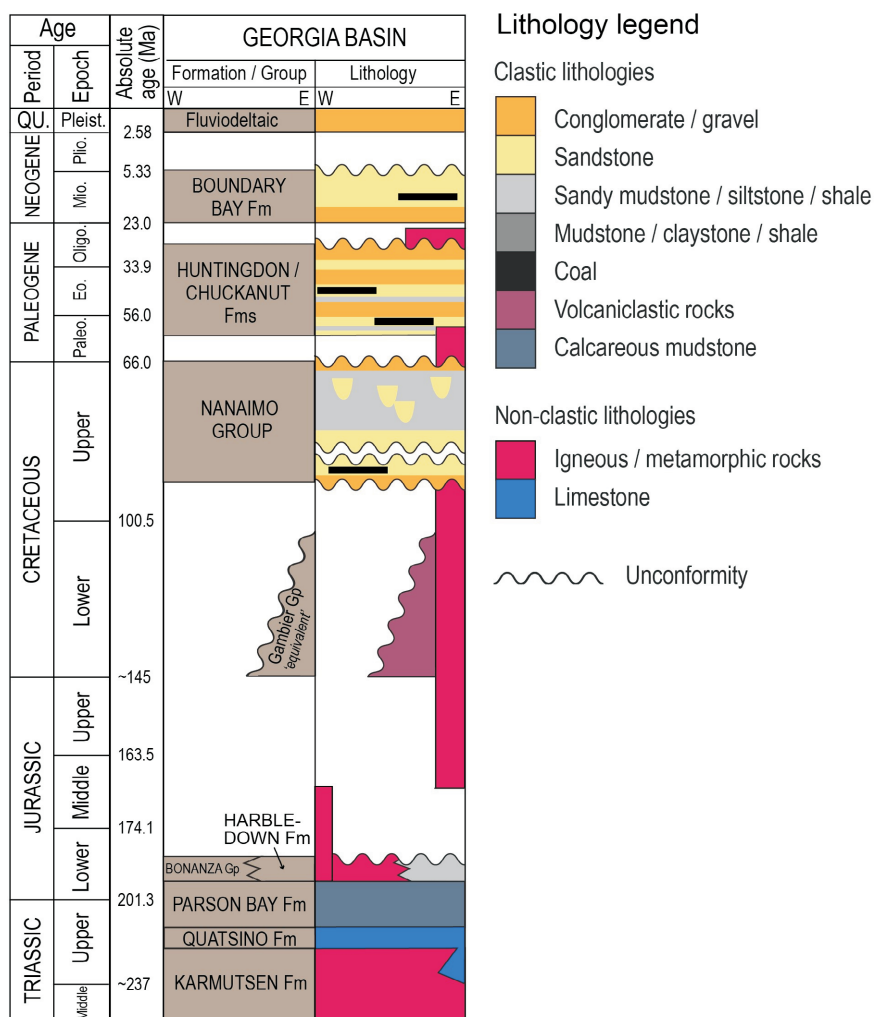


**Figure 4.** Simplified stratigraphic column for the Georgia Basin (with data from Haggart, 1992, 1993; Hannigan et al., 2001; Bain and Hubbard, 2016; Englert et al., 2018; Huang et al., 2019; Kent et al., 2020). Potential reservoir strata occur in coarse clastic rocks of the Huntingdon and Boundary Bay formations and the Nanaimo Group. Abbreviations: E, east; Eo., Eocene; Fm, Formation; Gp, Group; Mio., Miocene; Oligo., Oligocene; Paleo., Paleocene; Pleist., Pleistocene; Plio., Pliocene; QU., Quaternary; W, west.

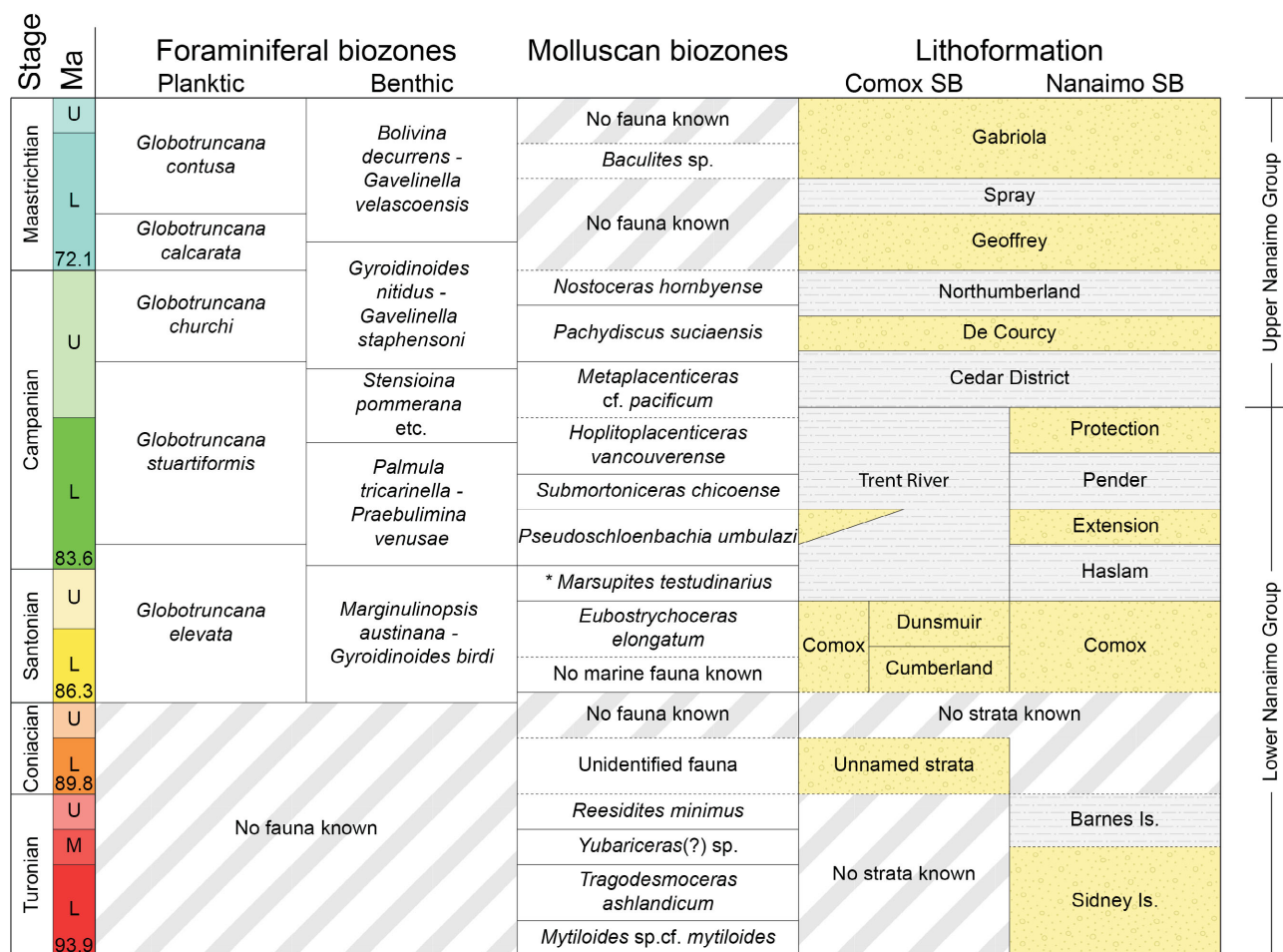
Boundary Bay Formation and overlying Quaternary deposits (Figures 1, 4).

### General Stratigraphy

The basement underlying the Georgia Basin is primarily composed of Wrangellia terrane, which consists of several geological components. These include the Sicker arc, formed during the Silurian to Devonian as an island arc; a Triassic mid-ocean basalt plateau (the Karmutsen Formation); the Bonanza arc, a Jurassic bimodal arc; and sedimentary rocks associated with these features (Huang et al., 2022). In the eastern part of the Georgia Basin, the basement comprises CPC, a continental arc that spanned from the Middle Jurassic to the Eocene (Monger and Journeay, 1994). Additionally, the Gambier Group, a sequence of Lower Cretaceous volcanogenic sedimentary and volcani-

clastic rocks, forms part of the basement in this region (Figure 4; Lynch, 1991, 1992; Monger and Journeay, 1994). The sedimentary fill of the Georgia Basin, which ranges from mainly Upper Cretaceous to the lowermost Paleocene, is primarily composed of the Nanaimo Group, with a thickness of approximately 4 km (Figures 3, 4; Mustard, 1991; Mustard et al., 1994; England and Bustin, 1998; Huang et al., 2022).

The Nanaimo Group is informally subdivided into two main units, known as the lower and upper Nanaimo Group. The lower Nanaimo Group primarily consists of continental to shallow-marine strata and is found in sedimentologically isolated sub-basins, including the Comox, Nanaimo and Cowichan Valley sub-basins (Figure 1; Giroto, 2022; Huang et al., 2022). Within the Comox and Nanaimo sub-basins, the lower Nanaimo Group is further divided into



Copyright 2019, with permission from Elsevier (<https://www.sciencedirect.com/journal/earth-science-reviews>).

**Figure 5.** Nanaimo Group lithostratigraphy in the Nanaimo and Comox sub-basins (Mustard et al., 1994; Haggart et al., 2005) including foraminiferal (Sliter, 1973; McGugan, 1979) and molluscan biozones (Muller and Jeletzky, 1970; Haggart et al., 2005; Ward et al., 2012; Haggart and Graham, 2018). In the formation column, yellow indicates strata that comprise dominantly sandstone and/or conglomeratic intervals, and grey indicates dominantly mudstone and shale. Figure reprinted from Huang et al. (2022). Abbreviations: Is., Island; L, Lower; M, Middle; SB, sub-basin; U, Upper.

lithostratigraphic formations. These formations alternate between predominantly coarse- and fine-grained strata. In the Comox sub-basin, the lower Nanaimo Group comprises the Comox and Trent River formations. The Nanaimo sub-basin includes the Sidney Island, Barnes Island, Comox, Haslam, Extension, Pender and Protection formations (Figure 5; Giroto, 2022).

The transition from the lower to the upper Nanaimo Group marks the consolidation of the previously isolated sub-basins into a unified basin, initiating deep-marine sedimentation across the entire basin (England, 1991; Mustard, 1991; Mustard and Monger, 1994; Kent et al., 2020; Giroto, 2022). The upper Nanaimo Group comprises formations such as the Cedar District, De Courcy, Northumberland, Geoffrey, Spray and Gabriola formations (Figure 5; Mustard and Monger, 1994; Huang et al., 2019, 2022; Kent et al., 2020). Although the Nanaimo Group is predominantly exposed in eastern Vancouver Island, these

strata also extend into the subsurface beneath the Strait of Georgia and the LMBC (Figures 3, 4). However, the understanding of the subsurface distribution and characteristics of the Nanaimo Group strata remains limited due to a lack of comprehensive data.

The Huntingdon Formation in British Columbia and the Chuckanut Formation in Washington represent the primary sedimentary fill during the Paleogene within the Georgia Basin (Figure 4; Vance, 1975; Johnson, 1984; England and Hiscott, 1992; Hannigan et al., 2001). In both the Canadian and American portions of the Georgia Basin, Paleogene strata are characterized predominantly by continental deposits (Johnson, 1984, 1991; Mustard and Monger, 1994; Hannigan et al., 2001). Intrusive Oligocene dikes and sills are locally observed in the Vancouver area, penetrating both Paleogene and Cretaceous strata (Figure 4; Mustard et al., 1994). Within the LMBC, the Huntingdon Formation is disconformably situated over the upper Nanaimo Group

(Figures 3, 4; Mustard et al., 1994). Within the Whatcom sub-basin, there exists a substantial and distinctive succession of mainly Miocene sedimentary rocks that differ from the older Cenozoic sedimentary rocks (Hopkins, 1966, 1968; Rouse et al., 1990; Mustard and Rouse, 1991; Mustard et al., 1994). These sedimentary rocks are referred to as the Boundary Bay Formation (Mustard et al., 1994) and are primarily exposed in scattered outcrops along the lower Fraser River valley and to the east and northeast of Bellingham in Washington (Figure 1; Hannigan et al., 2001).

## Exploration History and Regional Studies

The scientific exploration of the Georgia Basin has a rich history spanning over 140 years, initially driven by the discovery of substantial bituminous coal reserves in the region between 1850 and the early 1900s. Subsequently, the basin garnered scientific attention due to its potential for significant hydrocarbon deposits (Bustin and England, 1991; Bustin, 1995).

Exploration surveys (e.g., geological, seismic, gravimetric, magnetic) and drilling for hydrocarbons have been conducted intermittently in the basin since the early 1920s, with little tangible success. The first petroleum exploration wells were drilled prior to the acquisition of the first seismic lines, with the first well drilled in Whatcom County, Washington, in 1901, and the first well in the Fraser Valley, Canada, drilled in 1906 (Johnston, 1923; McFarland, 1983). Of all 118 wells drilled for oil and gas exploration within the Georgia Basin (particularly in the Canadian part), only 44 wells have known location and drilling information (Figure 6). Twenty-four of the drilled wells within the Canadian part of the Georgia Basin have wireline log data (11 wells in the LMBC and 13 wells on Vancouver Island; Figure 6).

The first basin-scale exploration survey was a regional aeromagnetic geophysical survey, led by the Geological Survey of Canada in 1955. In 1959, a gravity survey was conducted by Petcal Ltd., which encompassed most of the Fraser Valley and west of Abbotsford. In 1959, the first large-scale seismic reflection survey was conducted by Richfield Oil Corporation. The coverage of the seismic reflection survey extended from Abbotsford to the Strait of Georgia, and between the Fraser River and the United States border. In 1977, a seismic program was conducted by BC Gas (now FortisBC) to assess the potential for underground gas storage in the LMBC; this program involved acquiring 322 km of two-dimensional (2-D) seismic lines. Geophysical surveys outside of the LMBC include surveys in the United States, the Strait of Georgia and Vancouver Island. In the United States, CGG (Companie Général Géophysique) acquired seismic reflection data in 1985 in Whatcom County. In 1962, Canadian Superior Oil Ltd. acquired roughly 245 km of gas-exploder seismic data in the

Strait of Georgia. Soon after, the British American Oil Company Limited acquired 1150 km of gas-exploder marine seismic data in the Strait of Georgia. An extensive marine seismic program was performed by Texaco Exploration Canada Ltd. in the Strait of Georgia from 1968 to 1969, which acquired 300 km of marine seismic data. In 1987, British Petroleum Resources Canada Ltd. acquired 160 km of seismic data on eastern Vancouver Island. Following that survey, two wells were drilled into seismically defined structures. Offshore seismic data remain difficult to obtain in the Strait of Georgia.

## Petroleum Geology

### Reservoir Potential of Mesozoic and Cenozoic Strata in the LMBC

The Nanaimo Group contains the oldest strata in the Georgia Basin that are inferred to have significant reservoir potential (England, 1991; Hannigan et al., 2001). Generally, the lithoformations within the Nanaimo Group consist of alternating sequences of coarse-grained units dominated by sandstone and conglomerate and fine-grained units dominated by mudstone (Figure 5; England and Bustin, 1998; Kent et al., 2020; Huang et al., 2022). This simplified stratigraphy remains reasonably accurate when considering the lower Nanaimo Group in recently developed genetic stratigraphic frameworks (Kent et al., 2020; Giroto, 2022; Huang et al., 2022). However, in the upper Nanaimo Group, the positioning of lithoformations depends more on the architecture of the interpreted turbidite system, leading to greater variability (Bain and Hubbard, 2016; Englert et al., 2018; Huang et al., 2022).

The Nanaimo Group encompasses a diverse range of depositional environments. It includes neritic to bathyal marine settings represented by deep-marine turbidites, submarine fans and slope facies. Additionally, there are shallow marine and littoral facies that document marginal marine deposition (Mustard et al., 1994; Katnick and Mustard, 2003; Johnstone et al., 2006; Hamblin, 2012; Giroto, 2022). Specifically, the lower Nanaimo Group is characterized by coastal, paralic and nonmarine deposition, whereas the upper Nanaimo Group is dominated by deep-marine and submarine-fan complexes due to the tectonic deepening of the basin at the end of the deposition of the lower Nanaimo Group (Giroto, 2022; Huang et al., 2022).

The Paleogene Huntingdon Formation and its Chuckanut Formation equivalent are composed of clastic deposits of fluvial and alluvial origins (Johnson, 1984; Gilley, 2003). In the subsurface, the Huntingdon Formation is interpreted as a substantial fluvial sequence featuring laterally accreting meandering channels within a floodplain dominated by sand (Mustard et al., 1994; Gilley, 2003). The primary rock types found within these formations are medium- to coarse-grained sandstone and conglomerate, with lesser

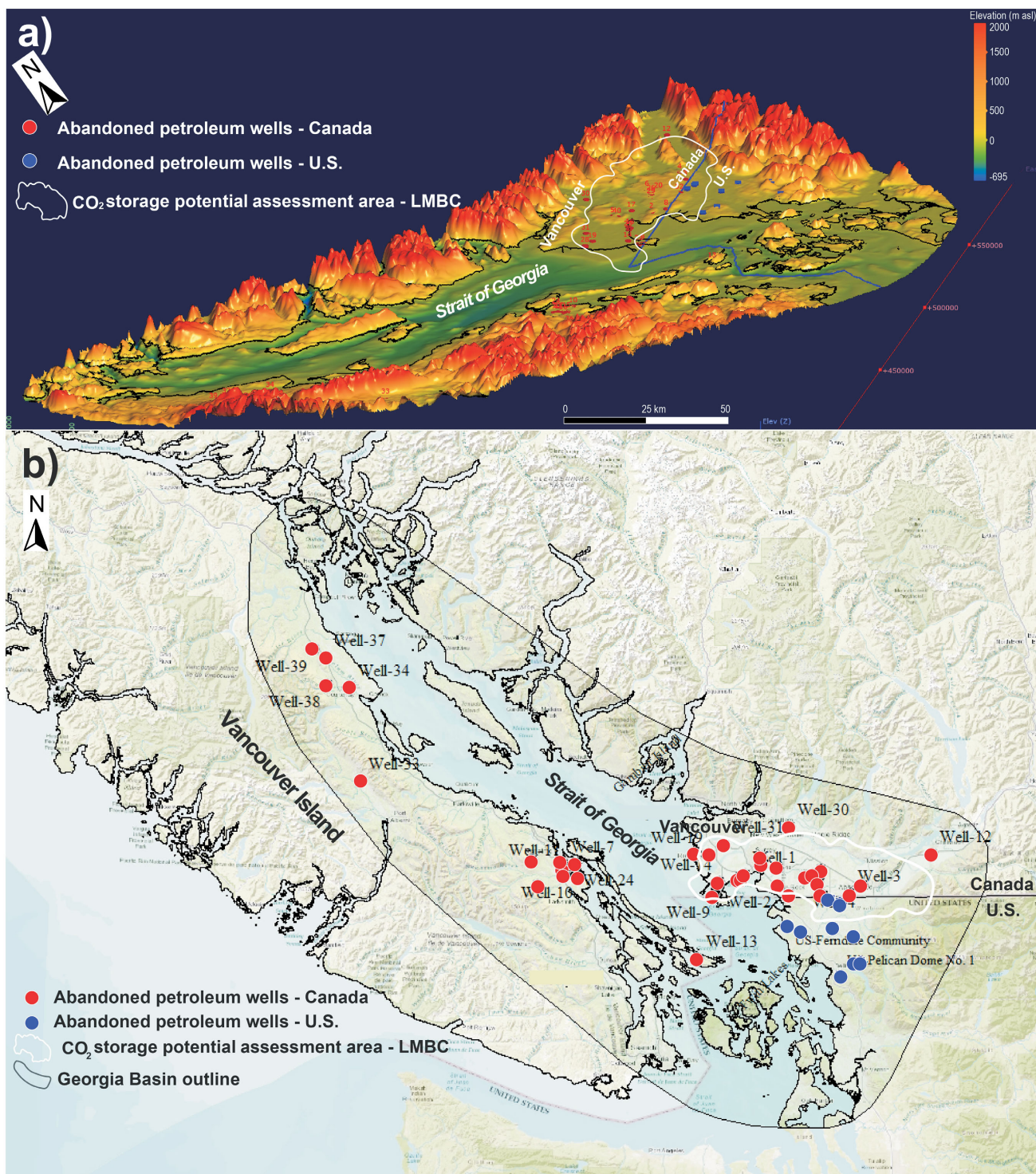


**Figure 6. a)** Digital elevation model and bathymetry of the Georgia Basin (Natural Resources Canada, 2021). **b)** Location of drilled wells in the Georgia Basin for which drilling data (e.g., hole location, kelly bushing, depth, etc.) are available. Among the 44 wells in the Georgia Basin with drilling data, only 24 have wireline log data: 11 in the Lower Mainland of British Columbia (LMBC) and 13 on Vancouver Island.

occurrences of shale, mudstone, siltstone and lignite (Gilley, 2003).

Notably, potential reservoir facies are associated with the coarse clastic deposits present in these formations

(Hannigan et al., 2001). In comparison to sandstones in the Nanaimo Group, the Paleogene sandstones display less degradation, contain less silica cement and exhibit lower compaction levels (Hannigan et al., 2001; Gilley, 2003). As a result, rocks with reservoir-quality properties are more

likely to be found in Cenozoic sedimentary rocks than in the Nanaimo Group (Hannigan et al., 2001).

Gordy (1988) noted that potential sandstone reservoirs in southwestern British Columbia exhibit porosities varying from 8 to 34%, with an average of 15%, and in Washington, porous sandstone displays an average porosity range of 12 to 15%. Additionally, there is evidence of secondary fracture porosity, likely resulting from substantial water and gas flows at depths exceeding 2000 m, especially in cases where primary matrix porosity is minimal.

### Seal Potential of Mesozoic and Cenozoic Strata

The geological storage of CO<sub>2</sub> demands meticulous design to ensure the containment of CO<sub>2</sub> within porous rock formations, thus preventing unintended leakage. In this context, the concept of structural trapping assumes paramount significance. To achieve secure storage, the injection of CO<sub>2</sub> into porous and permeable geological strata should be executed beneath a stratigraphic layer characterized by extensive lateral distribution, substantial thickness and low permeability properties, which serve as an effective impermeable seal. This stratigraphic sealing layer plays a pivotal role in halting the buoyant upward movement of CO<sub>2</sub>. Generally, Cretaceous reservoirs benefit from adequate lateral and upper sealing provided by the presence of multiple interbedded shale and mudstone units within the Georgia Basin, as detailed by Hannigan et al. (2001). Furthermore, structural sealing mechanisms are observed in the LMBC, potentially serving as seals in situations where sandstone and shale units intersect along fault lines. However, it is important to note that the sealing potential may be diminished for Paleogene strata, primarily due to their high sand content (England, 1991).

### Suitable Characteristics for CO<sub>2</sub> Sequestration in Saline Aquifers in LMBC

The most suitable basins for the storage of gaseous or supercritical CO<sub>2</sub> possess specific characteristics (Keighley and Maher, 2015). Ideally, these basins comprise sedimentary strata (referred to as reservoirs) that are water-saturated and permeable, overlain by laterally extensive layers of low-permeability rocks. Furthermore, these basins tend to exhibit structural simplicity, characterized by a scarcity of continuous faults, both laterally and vertically. Such basins are typically found in mid-continent locations, exemplified by the Western Canada Sedimentary Basin.

The following sections will detail the essential characteristics of sedimentary basins and sedimentary strata that are crucial for the successful implementation of CO<sub>2</sub> storage in regions marked by tectonic activity. These key characteristics encompass the geothermal gradient and pressure, reservoir thickness, porosity and permeability, salinity, mineralogy, seismicity and faults.

## Geothermal Gradient and Pressure

The behaviour of CO<sub>2</sub> with respect to its phase is significantly influenced by the geothermal gradient and pressure conditions in geological formations (Bachu, 2003; Bachu and Adams, 2003). This interplay is a determining factor for the effective storage and dissolution of CO<sub>2</sub> (Keighley and Maher, 2015). In a scenario with a typical geothermal gradient of 25 °C/km, and under normal hydrostatic pressure conditions, CO<sub>2</sub> transitions into a supercritical state at an approximate depth of 800 m (Holloway and Savage, 1993). However, it's important to note that the depth at which CO<sub>2</sub> achieves supercritical conditions can vary based on factors such as local surface temperature, the specific geothermal gradient of the region and the local hydrostatic and lithostatic pressures (Bachu, 2003). In most sedimentary basins, the pressure conditions conform closely to hydrostatic conditions. However, in cases of lithostatic conditions where pressure is solely attributed to the weight of the overlying rock, the density of water-saturated overburden is employed instead of water density (Bachu and Adams, 2003).

Surface temperatures within sedimentary basins display significant global variations, with arctic and sub-arctic basins experiencing average annual temperatures around 0 °C, whereas low-altitude tropical basins may exhibit average annual temperatures of approximately 30 °C (Bachu, 2003). Under standard pressure gradient conditions in sedimentary basins, the maximum attainable CO<sub>2</sub> density is approximately 850 kg/m<sup>3</sup> (Bachu, 2003). Consequently, it becomes evident that in warmer basins (higher temperature gradient), higher pressures (or depths) are required to attain elevated CO<sub>2</sub> density when compared to colder basins (lower temperature gradient).

### Reservoir Thickness

The required minimum thickness of a saline aquifer for effective CO<sub>2</sub> storage is typically around 30 m (Intergovernmental Panel on Climate Change, 2005). However, it's important to note that the actual reservoir thickness needed can vary significantly depending on factors such as heterogeneity, reservoir geometry, porosity, permeability and fluid properties. Therefore, conducting site-specific geological assessments and engineering evaluations is crucial to determining the precise minimum reservoir thickness for CO<sub>2</sub> storage in any given location. This approach ensures that the storage site meets the necessary criteria for effective and efficient carbon storage.

### Porosity and Permeability

The volume of CO<sub>2</sub> that can be effectively stored in a reservoir and the efficiency of storage depends on several key factors, including effective porosity, reservoir area, thickness, lithology and injectivity, which is primarily con-

trolled by permeability. When supercritical CO<sub>2</sub> or CO<sub>2</sub>-rich brine is injected into a reservoir, it displaces much of the existing pore fluid. Storage efficiency, a critical parameter, represents the ratio of the volume of CO<sub>2</sub> stored to the maximum pore volume available for CO<sub>2</sub> storage.

Permeability, the ability of a rock to transmit fluids, plays a fundamental role in the injection and dispersion of supercritical or gaseous CO<sub>2</sub> or CO<sub>2</sub>-rich brine mixtures within the reservoir. High-permeability reservoirs facilitate more efficient injection processes. In contrast, insufficient permeability or the presence of flow barriers like faults or fine-grained layers can result in increased fluid pressure near the injection point, limiting injection rates and the overall amount of CO<sub>2</sub> that can be stored (Bentham and Kirby, 2005).

Porosity and permeability parameters collectively determine the suitability of a reservoir for CO<sub>2</sub> storage, as they influence storage capacity and injectivity. Successful CCS projects require careful assessment of these geological and reservoir characteristics to ensure effective and efficient storage of CO<sub>2</sub>.

## Salinity

Salinity, often expressed as the concentration of total dissolved solids (TDS in ppm), encompasses a wide array of dissolved substances, including minerals, salts, metals and organic compounds in subsurface fluids.

The impact of salinity on CO<sub>2</sub> storage within saline aquifers is noteworthy. Saline water can dissolve more CO<sub>2</sub> compared to freshwater, thereby increasing the potential for CO<sub>2</sub> storage (Bachu, 2008). Nevertheless, elevated salinity levels can also trigger the formation of carbonates when CO<sub>2</sub> reacts with minerals in the water, particularly in proximity to injection wells. This mineralization process can reduce permeability and, consequently, CO<sub>2</sub> storage capacity (Bachu and Adams, 2003).

In the context of supercritical or gaseous CO<sub>2</sub> sequestration, formation water with higher salinity can cause separate-phase CO<sub>2</sub> to migrate upwards within the aquifer, potentially escaping through weaknesses in overlying rock layers. The salinity range conducive to CO<sub>2</sub> dissolution in saline aquifers is typically considered to be between 30 000 and 100 000 ppm. Salinity levels below 30 000 ppm tend to diminish the CO<sub>2</sub> carrying capacity of formation water, whereas salinity exceeding 100 000 ppm may contain high concentrations of minerals that react with CO<sub>2</sub>, leading to mineralization and a subsequent reduction in permeability. Careful consideration of salinity levels is crucial for optimizing CO<sub>2</sub> storage and minimizing potential migration risks.

## Mineralogy

The interaction of CO<sub>2</sub> with brine in aquifers can have multiple effects, including alterations in the mineral composition of the reservoir, changes in pH levels, modifications in the isotopic composition and adjustments in the ion concentration of the brine (Pearce et al., 2021). Saline reservoirs composed of siliciclastic materials are typically sandstone with varying proportions of clay and silicate minerals. The reactivity of these minerals with CO<sub>2</sub> is variable, with quartz and clay demonstrating lower reactivity, whereas carbonate, plagioclase feldspar and mafic minerals tending to be more reactive (Gunter et al., 1993, 1997; Knauss et al., 2005; Rosenbauer and Thomas, 2010).

The injection of CO<sub>2</sub>-rich brine mixtures into saline aquifers can induce the dissolution of feldspar and unstable minerals, subsequently leading to the precipitation of quartz and/or calcite cement within pore spaces. These cementitious materials can diminish injectivity, affecting the efficiency of injection processes (Ang et al., 2022). However, CO<sub>2</sub> injection into siliciclastic formations containing carbonate minerals (e.g., calcium and magnesium) and mafic minerals (e.g., basalt-rich strata) can result in significant sequestration through mineral trapping over extended periods, ranging from hundreds to thousands of years (Amin et al., 2014). These complex interactions underscore the importance of understanding reservoir fluid chemistry and mineralogical changes in aquifers during CO<sub>2</sub> storage operations.

## Seismicity

The injection of supercritical/gaseous CO<sub>2</sub> or CO<sub>2</sub>-rich brine mixtures into deep saline aquifers carries the potential risk of inducing seismic activity if the injected fluids lead to overpressurization (McGarr et al., 2002; Zoback and Gorelick, 2012). Elevated injection pressures can enhance injectivity but also result in increased mechanical stress and deformation, potentially triggering microseismic events, reactivating faults, creating new fractures, causing ground surface uplift and even generating earthquakes (Rutqvist et al., 2007; Ferronato et al., 2010; Cappa and Rutqvist, 2011). It is important to note that even relatively minor earthquakes, such as those with a magnitude of 3 or less, can pose a significant threat to the integrity of CO<sub>2</sub> storage projects (Zoback and Gorelick, 2012).

Therefore, it is imperative to identify pre-existing faults and take measures to prevent the injection of supercritical/gaseous CO<sub>2</sub> or CO<sub>2</sub>-rich brine mixtures in close proximity to these structural features.

## Faults

Faults that are either sealed or partially sealed can intersect potential CO<sub>2</sub> storage aquifers leading to complications in

CO<sub>2</sub> storage. These faults may compartmentalize the target reservoir, adding complexity and cost to the storage project (Keighley and Maher, 2015). Alternatively, if some of these faults remain unsealed, they significantly elevate the risk of fluid leakage. Basins that have undergone multiple tectonic or deformation events tend to be more heavily faulted and, as a result, are less suitable for CO<sub>2</sub> storage, especially for supercritical/gaseous CO<sub>2</sub> storage (Celia et al., 2015). Therefore, conducting a structural analysis is imperative for assessing the potential for fluid leakage throughout the life cycle of a storage project (Keighley and Maher, 2015).

## Conclusions

The increasing concentration of CO<sub>2</sub> in the Earth's atmosphere is significantly impacting the planet by intensifying the natural greenhouse effect, leading to a warming influence on the Earth's surface. This warming trend is associated with more frequent and intense extreme weather events, such as heatwaves, tropical cyclones, heavy precipitation and flooding, raising concerns among individuals and communities. Addressing the challenge of reducing carbon emissions while sustaining and improving living standards, especially in developing countries, necessitates cost-effective and innovative solutions. Consequently, the capture and underground sequestration of CO<sub>2</sub> emerges as one of the most practical and feasible approaches for reducing CO<sub>2</sub> emissions in the short to medium term.

The Lower Mainland of British Columbia (LMBC) has previously undergone assessments for its hydrocarbon potential and natural gas storage capacity, revealing it as a promising and potentially viable site for CO<sub>2</sub> storage. However, despite these initial assessments, there has been a lack of substantial effort to thoroughly evaluate the feasibility of carbon capture and storage in the LMBC. The sedimentary strata located beneath the LMBC, particularly at greater depths, remain poorly understood, with limited insights into their geological context, such as interpretations of depositional environments and facies analysis. Considering these gaps in knowledge, the objective of this research is to assess the feasibility of carbon capture and storage in the LMBC, by investigating several interconnected reservoir characteristics, including geothermal gradient and pressure, reservoir thickness, porosity and permeability characteristics, salinity, mineral composition, seismic activity and fault distribution. A comprehensive evaluation of these factors is imperative to ensure the safe and effective implementation of CO<sub>2</sub> sequestration projects in such regions.

## Acknowledgments

This study was funded through grants to S.E. Dashtgard from the BC Ministry of Energy, Mines and Low Carbon Innovation and the Natural Sciences and Engineering Re-

search Council of Canada (RGPIN-2019-04528). The author would like to thank Geoscience BC for providing financial support through the Geoscience BC scholarship program. A special thank you to S. Dashtgard for providing comments that improved the quality of this paper.

## References

- Amin, S.M., Weiss, D. and Blunt, M. (2014): Reactive transport modelling of geologic CO<sub>2</sub> sequestration in saline aquifers: the influence of pure CO<sub>2</sub> and of mixtures of CO<sub>2</sub> with CH<sub>4</sub> on the sealing capacity of cap rock at 37 C and 100 bar; *Chemical Geology*, v. 367, p. 39–50.
- Ang, L., Yongming, L., Xi, C., Zhongyi, Z. and Yu, P. (2022): Review of CO<sub>2</sub> sequestration mechanism in saline aquifers; *Natural Gas Industry B*, v. 9, no. 4, p. 383–393.
- Bachu, S. (2003): Screening and ranking of sedimentary basins for sequestration of CO<sub>2</sub> in geological media in response to climate change; *Environmental Geology*, v. 44, no. 3, p. 277–289.
- Bachu, S. (2008): CO<sub>2</sub> storage in geological media: role, means, status and barriers to deployment; *Progress in Energy and Combustion Science*, v. 34, no. 2, p. 254–273.
- Bachu, S. and Adams, J.J. (2003): Sequestration of CO<sub>2</sub> in geological media in response to climate change: capacity of deep saline aquifers to sequester CO<sub>2</sub> in solution; *Energy Conversion and Management*, v. 44, no. 20, p. 3151–3175.
- Bachu, S. and Gunter, W.D. (2005): Overview of acid-gas injection operations in western Canada; *in Proceedings of the 7<sup>th</sup> International Conference on Greenhouse Gas Control Technologies*, E.S. Rubin, D.W. Keith and C.F. Gilboy (ed.), September 5–9, 2004, Vancouver, British Columbia, Elsevier, p. 443–448.
- Bain, H.A. and Hubbard, S.M. (2016): Stratigraphic evolution of a long-lived submarine channel system in the Late Cretaceous Nanaimo Group, British Columbia, Canada; *Sedimentary Geology*, v. 337, p. 113–132.
- Bentham, M. and Kirby, M. (2005): CO<sub>2</sub> storage in saline aquifers; *Oil & Gas Science and Technology*, v. 60, no. 3, p. 559–567.
- Bratu, A., Card, K.G., Closson, K., Aran, N., Marshall, C., Clayton, S., Gislason, M.K., Samji, H., Martin, G., Lem, M., Logie, C.H., Takaro, T.K. and Hogg, R.S. (2022): The 2021 western North American heat dome increased climate change anxiety among British Columbians: results from a natural experiment; *The Journal of Climate Change and Health*, v. 6, art. 100116.
- Bustin, R. (1995): Organic maturation and petroleum source rock potential of Tofino Basin, southwestern British Columbia; *Bulletin of Canadian Petroleum Geology*, v. 43, no. 2, p. 177–186.
- Bustin, R. and England, T. (1991): Petroleum source rock potential of the Nanaimo Group, western margin of the Georgia Basin, southwestern British Columbia; *in Current Research, Part A, Geological Survey of Canada, Paper 91-1A*, p. 143–145.
- Cappa, F. and Rutqvist, J. (2011): Impact of CO<sub>2</sub> geological sequestration on the nucleation of earthquakes; *Geophysical Research Letters*, v. 38, no. 17, art. L17313, 6 p.
- Celia, M.A., Bachu, S., Nordbotten, J.M. and Bandilla, K.W. (2015): Status of CO<sub>2</sub> storage in deep saline aquifers with emphasis on modeling approaches and practical simulations; *Water Resources Research*, v. 51, no. 9, p. 6846–6892.

- Clapp, C.H. (1913): Geology of the Victoria and Saanich map areas, Vancouver Island, British Columbia; Geological Survey of Canada, Memoir 36, 143 p.
- England, T. (1991): Late Cretaceous to Paleogene structural and stratigraphic evolution of Georgia Basin, southwestern British Columbia: implications for hydrocarbon potential; *Washington Geology*, v. 19, no. 4, p. 10–11.
- England, T. and Bustin, R. (1998): Architecture of the Georgia Basin, southwestern British Columbia; *Bulletin of Canadian Petroleum Geology*, v. 46, no. 2, p. 288–320.
- England, T. and Calon, T. (1991): The Cowichan fold and thrust system, Vancouver Island, southwestern British Columbia; *Geological Society of America Bulletin*, v. 103, no. 3, p. 336–362.
- England, T. and Hiscott, R. (1992): Lithostratigraphy and deep-water setting of the upper Nanaimo Group (Upper Cretaceous), outer Gulf Islands of southwestern British Columbia; *Canadian Journal of Earth Sciences*, v. 29, no. 3, p. 574–595.
- Englert, R.G., Hubbard, S.M., Coutts, D.S. and Matthews, W.A. (2018): Tectonically controlled initiation of contemporaneous deep-water channel systems along a Late Cretaceous continental margin, western British Columbia, Canada; *Sedimentology*, v. 65, no. 7, p. 2404–2438.
- Ewald, J. (2013): CO<sub>2</sub> at NOAA's Mauna Loa Observatory reaches new milestone: tops 400 ppm; National Oceanic and Atmospheric Administration, U.S. Department of Commerce, NOAA Research News, May 10, 2013, URL <<https://gml.noaa.gov/news/pdfs/7074.pdf>> [September 2022].
- Ferronato, M., Gambolati, G., Janna, C. and Teatini, P. (2010): Geomechanical issues of anthropogenic CO<sub>2</sub> sequestration in exploited gas fields; *Energy Conversion and Management*, v. 51, no. 10, p. 1918–1928.
- Flannigan, M. and Wagner, C.V. (1991): Climate change and wildfire in Canada; *Canadian Journal of Forest Research*, v. 21, no. 1, p. 66–72.
- Gabrielse, H. and Yorath, C.J., editors (1991): Geology of the Cordilleran Orogen in Canada; Geological Survey of Canada, Geology of Canada, no. 4, 844 p. (also Geological Society of America, Geology of North America, v. G-2).
- Gilley, B.H.T. (2003): Facies architecture and stratigraphy of the Paleogene Huntingdon Formation at Abbotsford, British Columbia; M.Sc. thesis, Simon Fraser University, 152 p.
- Giroto, K. (2022): Tectono-stratigraphic model for the early evolution of the Late Cretaceous Nanaimo Group: Georgia Basin, British Columbia, Canada; M.Sc. thesis, Simon Fraser University, 145 p.
- Gordy, P.L. (1988): Evaluation of the hydrocarbon potential of the Georgia depression; BC Ministry of Energy, Mines and Low Carbon Innovation, Geological Report 88–03.
- Groulx, B.J. and Mustard, P.S. (2004): Understanding the geological development of the Lower Mainland: the first step to informed land-use decisions; *in* Fraser River Delta, British Columbia: Issues of an Urban Estuary, B.J. Groulx, D.C. Mosher, J.L. Luternauer and D.E. Bilderback (ed.), Geological Survey of Canada, Bulletin 567, p. 1–22.
- Gunter, W.D., Perkins, E.H. and McCann, T.J. (1993): Aquifer disposal of CO<sub>2</sub>-rich gases: reaction design for added capacity; *Energy Conversion and Management*, v. 34, no. 9–11, p. 941–948.
- Gunter, W.D., Wiwehar, B. and Perkins, E.H. (1997): Aquifer disposal of CO<sub>2</sub>-rich greenhouse gases: extension of the time scale of experiment for CO<sub>2</sub>-sequestering reactions by geochemical modelling; *Mineralogy and Petrology*, v. 59, no. 1–2, p. 121–140.
- Haggart, J.W. (1992): Progress in Jurassic and Cretaceous stratigraphy, Queen Charlotte Islands, British Columbia; *in* Current Research, Part A, Geological Survey of Canada, Paper 92-1A, p. 361–365.
- Haggart, J.W. (1993): Latest Jurassic and Cretaceous paleogeography of the northern Insular Belt, British Columbia; *in* Mesozoic Paleogeography of the Western United States - II, G.C. Dunne and K.A. McDougall (ed.), Society of Economic Paleontologists and Mineralogists, Pacific Section, Book 71, p. 463–475.
- Haggart, J.W. and Graham, R. (2018): The crinoid *Marsupites* in the Upper Cretaceous Nanaimo Group, British Columbia: resolution of the Santonian–Campanian boundary in the North Pacific Province; *Cretaceous Research*, v. 87, p. 277–295.
- Haggart, J.W., Ward, P.D. and Orr, W. (2005): Turonian (Upper Cretaceous) lithostratigraphy and biochronology, southern Gulf Islands, British Columbia, and northern San Juan Islands, Washington State; *Canadian Journal of Earth Sciences*, v. 42, no. 11, p. 2001–2020.
- Hamblin, A. (2012): Upper Cretaceous Nanaimo Group of Vancouver Island as a potential bedrock aquifer zone: summary of previous literature and concepts; Geological Survey of Canada, Open File 7265, 20 p.
- Hannigan, P.K., Dietrich, J.R., Lee, P.J. and Osadetz, K.G. (2001): Petroleum resource potential of sedimentary basins on the Pacific margin of Canada; Geological Survey of Canada, Bulletin 564, 73 p., URL <<https://emrlibrary.gov.yk.ca/gsc/bulletins/564.pdf>> [September 2022].
- Holloway, S. and Savage, D. (1993): The potential for aquifer disposal of carbon dioxide in the UK; *Energy Conversion and Management*, v. 34, no. 9–11, p. 925–932.
- Hopkins, W.S. (1966): Palynology of Tertiary rocks of the Whatcom Basin, southwestern British Columbia and northwestern Washington; Ph.D. thesis, The University of British Columbia, 169 p.
- Hopkins, W.S. (1968): Subsurface Miocene rocks, British Columbia–Washington, a palynological investigation; *Geological Society of America Bulletin*, v. 79, no. 6, p. 763–768.
- Huang, C., Dashtgard, S.E., Haggart, J.W. and Giroto, K. (2022): Synthesis of chronostratigraphic data and methods in the Georgia Basin, Canada, with implications for convergent-margin basin chronology; *Earth-Science Reviews*, v. 231, art. 104076.
- Huang, C., Dashtgard, S.E., Kent, B.A., Gibson, H.D. and Matthews, W.A. (2019): Resolving the architecture and early evolution of a forearc basin (Georgia Basin, Canada) using detrital zircon; *Scientific Reports*, v. 9, no. 1, p. 1–12.
- Intergovernmental Panel on Climate Change (2005): IPCC Special Report on Carbon Dioxide Capture and Storage; prepared by Working Group III of the Intergovernmental Panel on Climate Change, B. Metz, O. Davidson, H.C. de Coninck, M. Loos and L.A. Meyer (ed.), Intergovernmental Panel on Climate Change, Cambridge University Press, Cambridge, United Kingdom, and New York, New York, 442 p.
- Intergovernmental Panel on Climate Change (2014): Climate Change 2014: Synthesis Report, Contribution of Working Groups I, II and III to the Fifth Assessment Report of the In-

- tergovernmental Panel on Climate Change; R.K. Pachauri and L.A. Meyer (ed.), Core Writing Team, Intergovernmental Panel on Climate Change, Cambridge University Press, Cambridge, United Kingdom, and New York, New York, 151 p.
- Johnson, S. (1991): Sedimentation and tectonic setting of the Chuckanut Formation, northwest Washington; *Washington Geology*, v. 19, no. 4, p. 12–13.
- Johnson, S.Y. (1984): Stratigraphy, age, and paleogeography of the Eocene Chuckanut Formation, northwest Washington; *Canadian Journal of Earth Sciences*, v. 21, no. 1, p. 92–106.
- Johnson, S.Y. (1985): Eocene strike-slip faulting and nonmarine basin formation in Washington; Chapter 3 in *Strike-Slip Deformation, Basin Formation and Sedimentation*, K.T. Biddle and N. Christie-Blick (ed.), Society of Economic Paleontologists and Mineralogists, Special Publication No. 37, p. 78–90.
- Johnston, W.A. (1923): Geology of Fraser River Delta map area; Geological Survey of Canada, Memoir 135, 87 p., 1 map.
- Johnstone, P., Mustard, P. and MacEachern, J. (2006): The basal unconformity of the Nanaimo Group, southwestern British Columbia: a Late Cretaceous storm-swept rocky shoreline; *Canadian Journal of Earth Sciences*, v. 43, no. 8, p. 1165–1181.
- Jones, M.T. (2016): Stratigraphy and architecture of shallow-marine strata on an active margin, lower Nanaimo Group, Vancouver Island, BC; M.Sc. thesis, Simon Fraser University, 85 p.
- Kaszuba, J.P., Janecky, D.R. and Snow, M.G. (2003): Carbon dioxide reaction processes in a model brine aquifer at 200 C and 200 bars: implications for geologic sequestration of carbon; *Applied Geochemistry*, v. 18, no. 7, p. 1065–1080.
- Katnick, D.C. and Mustard, P.S. (2003): Geology of Denman and Hornby islands, British Columbia: implications for Nanaimo Basin evolution and formal definition of the Geoffrey and Spray formations, Upper Cretaceous Nanaimo Group; *Canadian Journal of Earth Sciences*, v. 40, no. 3, p. 375–393.
- Keeling, C.D. (1960): The concentration and isotopic abundances of carbon dioxide in the atmosphere; *Tellus*, v. 12, no. 2, p. 200–203.
- Keighley, D. and Maher, C. (2015): A preliminary assessment of carbon storage suitability in deep underground geological formations of New Brunswick, Canada; *Atlantic Geology*, v. 51, p. 269–286.
- Kent, B.A., Dashtgard, S.E., Huang, C., MacEachern, J.A., Gibson, H.D. and Cathyl-Huhn, G. (2020): Initiation and early evolution of a forearc basin: Georgia Basin, Canada; *Basin Research*, v. 32, no. 1, p. 163–185.
- Kharaka, Y.K., Cole, D.R., Hovorka, S.D., Gunter, W., Knauss, K.G. and Freifeld, B. (2006): Gas-water-rock interactions in Frio Formation following CO<sub>2</sub> injection: implications for the storage of greenhouse gases in sedimentary basins; *Geology*, v. 34, no. 7, p. 577–580.
- Knauss, K.G., Johnson, J.W. and Steefel, C.I. (2005): Evaluation of the impact of CO<sub>2</sub>, co-contaminant gas, aqueous fluid and reservoir rock interactions on the geologic sequestration of CO<sub>2</sub>; *Chemical Geology*, v. 217, no. 3–4, p. 339–350.
- Lane, J., Greig, C. and Garnett, A. (2021): Uncertain storage prospects create a conundrum for carbon capture and storage ambitions; *Nature Climate Change*, v. 11, no. 11, p. 925–936.
- Lynch, G. (1992): Deformation of Early Cretaceous volcanic-arc assemblages, southern Coast Belt, British Columbia; *Canadian Journal of Earth Sciences*, v. 29, no. 12, p. 2706–2721.
- Lynch, J.V.G. (1991): Georgia Basin Project: stratigraphy and structure of Gambier Group rocks in the Howe Sound-Mamquam River area, southwest Coast Belt, British Columbia; *in Current Research, Part A, Geological Survey of Canada, Paper 91-1A*, p. 49–58.
- McFarland, C.R. (1983): Oil and gas exploration in Washington, 1900–1982; State of Washington, Department of Natural Resources, Division of Geology and Earth Resources, Information Circular 75, 119 p.
- McGarr, A., Simpson, D. and Seeber, L. (2002): Case histories of induced and triggered seismicity; *in International Handbook of Earthquake and Engineering Seismology*, W.H.K. Lee, H. Kanamori, P.C. Jennings and C. Kisslinger (ed.), International Geophysics Series, v. 81, pt. A, p. 647–664.
- McGugan, A. (1979): Biostratigraphy and paleoecology of Upper Cretaceous (Campanian and Maestrichtian) foraminifera from the upper Lambert, Northumberland, and Spray formations, Gulf Islands, British Columbia, Canada; *Canadian Journal of Earth Sciences*, v. 16, no. 12, p. 2263–2274.
- Miller, G.M. (1963): Early Eocene angular unconformity at western front of Northern Cascades, Whatcom County, Washington; *Erratum; AAPG Bulletin*, v. 47, no. 8, p. 1627.
- Molnar, S., Cassidy, J.F., Dosso, S.E. and Olsen, K.B. (2010): 3D ground motion in the Georgia Basin region of SW British Columbia for Pacific Northwest scenario earthquakes; *in Proceedings of the 9<sup>th</sup> US National and 10<sup>th</sup> Canadian Conference on Earthquake Engineering 2010, July 25–29, 2010, Toronto, Ontario*, v. 9, p. 7466–7475.
- Monger, J. (1990): Georgia Basin: regional setting and adjacent Coast Mountains geology, British Columbia; *in Current Research, Part F, Geological Survey of Canada, Paper 90-1F*, p. 95–102.
- Monger, J. (1991a): Georgia Basin Project: structural evolution of parts of southern Insular and southwestern Coast belts; *in Current Research, Part A, Geological Survey of Canada, Paper 91-1A*, p. 219–228.
- Monger, J. (1991b): Late Mesozoic to Recent evolution of the Georgia Strait–Puget Sound region, British Columbia and Washington; *Washington Geology*, v. 19, no. 4, p. 3–9.
- Monger, J. and Price, R. (2002): The Canadian Cordillera: geology and tectonic evolution; *CSEG Recorder*, v. 27, no. 2, p. 17–36.
- Monger, J., Van der Heyden, P., Journeay, J., Evenchick, C. and Mahoney, J. (1994): Jurassic-Cretaceous basins along the Canadian Coast Belt: their bearing on pre-mid-Cretaceous sinistral displacements; *Geology*, v. 22, no. 2, p. 175–178.
- Monger, J.W.H. and Journeay, J.M. (1994): Basement geology and tectonic evolution of the Vancouver region; *in Geology and Geological Hazards of the Vancouver Region, Southwestern British Columbia*, J.W.H. Monger (ed.), Geological Survey of Canada, Bulletin 481, p. 3–25.
- Muller, J.E. and Jeletzky, J.A. (1970): Geology of the Upper Cretaceous Nanaimo Group, Vancouver Island and Gulf Islands, British Columbia; Geological Survey of Canada, Paper 69-25, 84 p.
- Mustard, P. (1991): Stratigraphy and sedimentology of the Georgia Basin, British Columbia and Washington State; *Washington Geology*, v. 19, p. 4.

- Mustard, P.S. and Monger, J. (1994): The Upper Cretaceous Nanaimo group, Georgia Basin; *in* *Geology and Geological Hazards of the Vancouver Region*, Southwestern British Columbia, J.W.H. Monger (ed.), Geological Survey of Canada, Bulletin 481, p. 27–95.
- Mustard, P.S. and Rouse, G.E. (1991): Sedimentary outliers of the eastern Georgia Basin margin, British Columbia; *in* *Current Research, Part A*, Geological Survey of Canada, Paper 91-1A, p. 229–240.
- Mustard, P.S., Rouse, G.E. and Monger, J. (1994): Stratigraphy and evolution of Tertiary Georgia Basin and adjacent Upper Cretaceous sedimentary rocks, southwestern British Columbia and northwestern Washington State; *in* *Geology and Geological Hazards of the Vancouver Region*, Southwestern British Columbia, Geological Survey of Canada, Bulletin 481, p. 97–169.
- Natural Resources Canada (2021): Canadian Digital Elevation Model; Natural Resources Canada, URL <<https://open.canada.ca/data/en/dataset/7f245e4d-76c2-4caa-951a-45d1d2051333>> [November 2023].
- Pearce, J., La Croix, A., Brink, F., Hayes, P. and Underschultz, J. (2021): CO<sub>2</sub> mineral trapping comparison in different regions: predicted geochemical reactivity of the Precipice Sandstone reservoir and overlying Evergreen Formation; *Petroleum Geoscience*, v. 27, no. 3, URL <<https://www.earthdoc.org/content/journals/10.1144/ptgeo2020-106>> [September 2022].
- Rosenbauer, R.J. and Thomas, B. (2010): Carbon dioxide (CO<sub>2</sub>) sequestration in deep saline aquifers and formations; Chapter 3 *in* *Developments and Innovation in Carbon Dioxide (CO<sub>2</sub>) Capture and Storage Technology, Volume 2: Carbon Dioxide (CO<sub>2</sub>) Storage and Utilisation*, M. Mercedes Maroto-Valer (ed.), CRC Press LLC, Boca Raton, Florida, p. 57–103.
- Rouse, G.E., Lesack, K.A. and White, J.M. (1990): Palynology of Cretaceous and Tertiary strata of Georgia Basin, southwestern British Columbia; *in* *Current Research, Part F*, Geological Survey of Canada, Paper 90-1F, p. 109–113.
- Rutqvist, J., Birkholzer, J., Cappa, F. and Tsang, C.-F. (2007): Estimating maximum sustainable injection pressure during geological sequestration of CO<sub>2</sub> using coupled fluid flow and geomechanical fault-slip analysis; *Energy Conversion and Management*, v. 48, no. 6, p. 1798–1807.
- Shukla, R., Ranjith, P., Haque, A. and Choi, X. (2010): A review of studies on CO<sub>2</sub> sequestration and caprock integrity; *Fuel*, v. 89, no. 10, p. 2651–2664.
- Sliter, W.V. (1973): Upper Cretaceous foraminifers from the Vancouver Island area, British Columbia, Canada; *The Journal of Foraminiferal Research*, v. 3, no. 4, p. 167–186.
- Stephenson, M.H., Ringrose, P., Geiger, S., Bridden, M. and Schofield, D. (2019): Geoscience and decarbonization: current status and future directions; *Petroleum Geoscience*, v. 25, no. 4, p. 501–508.
- Takano, O. and Tsuji, T. (2017): Fluvial to bay sequence stratigraphy and seismic facies of the Cretaceous to Paleogene successions in the MITI Sanriku-oki well and the vicinities, the Sanriku-oki forearc basin, northeast Japan; *Island Arc*, v. 26, no. 4, art. e12184.
- Takano, O., Itoh, Y. and Kusumoto, S. (2013): Variation in forearc basin configuration and basin-filling depositional systems as a function of trench slope break development and strike-slip movement: examples from the Cenozoic Ishikari–Sanriku-Oki and Tokai-Oki–Kumano-Nada forearc basins, Japan; Chapter 1 *in* *Mechanism of Sedimentary Basin Formation - Multidisciplinary Approach on Active Plate Margins*, Y. Itoh (ed.), Intech, p. 3–25.
- U.S. Energy Information Administration (2021): International energy outlook 2021; U.S. Energy Information Administration, URL <<https://www.eia.gov/outlooks/ieo/>> [September 2022].
- Vance, J.A. (1975): Bedrock geology of San Juan County; *in* *Geology and Water Resources of the San Juan Islands*, San Juan County, Washington, R.H. Russell (ed.), Washington Department of Ecology, Office of Technical Services, Water Supply Bulletin No. 46, p. 3–19.
- Ward, P.D., Haggart, J.W., Mitchell, R., Kirschvink, J.L. and Tobin, T. (2012): Integration of macrofossil biostratigraphy and magnetostratigraphy for the Pacific Coast Upper Cretaceous (Campanian–Maastrichtian) of North America and implications for correlation with the Western Interior and Tethys; *Geological Society of America Bulletin*, v. 124, no. 5–6, p. 957–974.
- Wheeler, J.O., Brookfield, A.J., Gabrielse, H., Monger, J.W.H., Tipper, H.W. and Woodworth, G.J., compilers (1991): Terrane map of the Canadian Cordillera; Geological Survey of Canada, Map 1713A, scale 1:2 000 000, URL <<https://doi.org/10.4095/133550>>.
- Zelt, B., Ellis, R., Zelt, C., Hyndman, R., Lowe, C., Spence, G. and Fisher, M. (2001): Three-dimensional crustal velocity structure beneath the Strait of Georgia, British Columbia; *Geophysical Journal International*, v. 144, no. 3, p. 695–712.
- Zoback, M.D. and Gorelick, S.M. (2012): Earthquake triggering and large-scale geologic storage of carbon dioxide; *Proceedings of the National Academy of Sciences*, v. 109, no. 26, p. 10164–10168.







**Geoscience BC**

SUITE 1101-750 WEST PENDER ST  
VANCOUVER, BC V6C 2T7 CANADA

604 662 4147  
info@geosciencebc.com  
**geosciencebc.com**

